ABSTRACT

Title of Document: ADVANCED RECEPTOR MODELS FOR EXPLOITING HIGHLY TIME RESOLVED DATA ACQUIRED IN THE EPA SUPERSITE PROJECT

Haohao Ke, Ph.D., 2012

Directed By: Professor John M. Ondov
Department of Chemistry and Biochemistry

Receptor models have been widely used in air quality studies to identify pollution sources and estimate their contributions. A common problem for most current receptor models is insufficient consideration of realistic constraints such as can be obtained from emission inventories, chemical composition profiles of the sources, and the physics of plume dispersion. In addition, poor resolving of collinear sources was often found. With the high quality time-, composition-, and size-resolved measurements during the EPA Supersite project, efforts towards resolving nearby industrial sources were made by combinative use of Positive Matrix Factorization (PMF) and the Pseudo-Deterministic Receptor Model (PDRM).

The PMF modeling of Baltimore data in September 2001 revealed coal-fired and oil-fired power plants (CFPP and OFPP, respectively) with significant cross contamination, as indicated by the high Se/Ni ratio in the OFPP profile. Nevertheless, the PMF results provided a good estimate of background and the PMF-constrained

emission rates well seeded the trajectory-driven PDRM modeling. Using NO_x as the tracer gas for χ/Q tuning, ultimately resolved emissions from individual stacks exhibited acceptable tracer ratios and the emission rates of metals generally agreed with the TRI estimates. This approach was later applied to two metal pollution episodes in St. Louis during in November 2001 and March 2002 and met a similar success. As NO_x measurements were unavailable at those metal-production facilities, highly-specific tracer metals (i.e., Cd, Zn, and Cu) for the corresponding units were used to tune χ/Qs and their contributions were well resolved with the PMF-seeded PDRM.

Opportunistically a $PM_{2.5}$ excursion during a windless morning in November 2002 allowed the extraction of an *in-situ* profile of vehicular emissions in Baltimore. The profiles obtained by direct peak observation, windless model linear regression (WMA), PMF, and UNMIX were comparable and the WMA profile showed the best predictions for non-traffic tracers. Besides, an approach to evaluate vehicular emission factors was developed by receptor measurements under windless conditions. Using SVOC tracers, seasonal variations of traffic and other sources including coal burning, heating, biomass burning, and vegetation were investigated by PMF and in particular the November traffic profile was consistent with the WMA profile obtained earlier.

ADVANCED RECEPTOR MODELS FOR EXPLOITING HIGHLY TIME-RESOLVED DATA ACQUIRED IN THE EPA SUPERSITE PREJECT

By

Haohao Ke

Dissertation submitted to the Faculty of the Graduate School of the
University of Maryland, College Park, in partial fulfillment
of the requirements for the degree of
Doctor of Philosophy
2012

Advisory Committee:
Professor John M. Ondov, Advisor
Professor Ross J. Salawitch, Chair
Professor Neil Blough
Professor Alice Mignerey
Professor Russell Dickerson
Professor Rachel Pinker (Dean's Representative)

Acknowledgements

I would like to express my sincerest gratitude to my advisor, Professor John M. Ondov for his thoughtful guidance and tremendous help throughout my research.

Special thanks are due to my thesis committee members, Professor Ross Salawitch, Professor Neil Blough, Professor Alice Mignerey, Professor Russell Dickerson, and Professor Rachel Pinker for all their helpful discussions, comments, and suggestions.

I would also like to thank all my friends for their continuous support, and especially Ms. Natalia White, with whom it was an honor to work for the last three years.

Lastly, I would thank my family for providing me the motivation without which I was unable to accomplish my study.

Table of Contents

List of Tables

List of Figures

Chapter 1: Introduction

The establishment of effective pollution control strategies relies on the understanding of relationships between emissions from various sources and ambient concentrations. In general, source apportionment models are either source- or receptor-based. Source-based models, such as the Community Multi-scale Air Quality (CMAQ) model (Byun and Schere 2006) and the Comprehensive Air-quality Model with extensions (CAMx) (Koo et al. 2009), use both known source emissions and dispersion characteristics as input to calculate ambient concentrations. In contrast, receptor models make use of ambient concentrations measured at receptor site(s) and some known characteristics of sources or dispersion to "condition" predicted source impacts (Watson et al. 2002, Hopke and Cohen 2011). All source apportionment models, no matter source- or receptor-based, follow the same expression:

$$c_{ik} = \sum_j F_{ij} \cdot T_{ijk} \cdot D_{jk} \cdot Q_{jk} \qquad (1.1)$$

where c_{ik} is the i^{th} species concentration (g m^{-3}) measured at the receptor site during the k^{th} time interval, F_{ij} is the fraction quantity (dimensionless) of the i^{th} species in the emissions from the j^{th} source, T_{ijk} is the transformation factor (dimensionless) of the i^{th} species during transport through the atmosphere, $D_{jk}$is the dispersion factor (s m^{-3}) between the j^{th} source and the receptor during the k^{th} time period, and Q_{jk} is the emission rate (g s^{-1}) from the j^{th} source during the k^{th} time period.

In a typical source (or deterministic) model, T_{ijk} is calculated by chemical model, D_{jk} is obtained by meteorological model, F_{ij} and Q_{jk} are either measured at sources

or estimated from existing source inventory, and c_{ik} can thus be determined. The performance of source-based models relies excessively on the mathematical modeling of plume dispersion, which often exhibits poor accuracy partially due to the paucity of meteorological measurements needed to characterize the wind fields in both the vertical and horizontal directions. In addition, lack of *apriori* knowledge of emission rates, which is not unusual, can limit the application of deterministic models as well.

Receptor models often inexplicitly treat atmospheric processes and ignore temporal variability in F_{ij}, and thus their formulations are simplified. Despite their different mathematics, the underlying philosophy of receptor models is common, that is, to let the data speak for itself by "forcing" predictions towards physical realities (Watson 1984), e.g., observed concentrations and meteorological facts. In the following section, several common receptor modeling techniques are reviewed.

1.1 Current Receptor Models

Current EPA-recommended (www.epa.gov/ttn/scram/receptorindex.htm) receptor models include chemical mass balance (CMB) (U.S.EPA 2004c), positive matrix factorization (PMF) (U.S.EPA 2008), and UNMIX (U.S.EPA 2007). Besides, principal component analysis (PCA) (Thurston and Spengler 1985), the multi-linear engine (ME) (Paatero 1999), and multiple linear regression (MLR) (Kleinman et al. 1980) are other commonly-used tools.

In CMB applications, F_{ij}s in Equation 1.1 are retrieved by source measurements; T_{ijk}s are often set to unity as a result of the ignorance of chemical transformation and mass loss during transport; the products of D_{jk}s and Q_{jk}s are source contribution

estimates (SCE) and denoted as S_{jk}s (g m^{-3}); and c_{ik}s are measured at the receptor site. Hence the CMB equation can be simplified as:

$$c_{ik} = \sum_j F_{ij} \cdot S_{jk} + e_{ik} \quad (1.2)$$

where e_{ik} is the residual term (i.e., the unaccountable mass concentration, g m^{-3}). For each time period k, the CMB model seeks the S_{jk} solution of i linear equations with the minimum scaled residual (χ^2_k, defined in Equation 1.3) by using an inverse variance (V_{ik}, defined in Equation 1.4) weighted least-squares linear regression (Watson et al. 1990).

$$\chi^2_k = \frac{1}{i-j} \sum_{i=1}^{m} \left[\frac{\left(c_{ik} - \sum_{j=1}^{p} F_{ij} S_{jk}\right)^2}{V_{ik}} \right] \quad (1.3)$$

$$V_{ik} = \sigma^2_{ik} + \sum_{j=1}^{p} (S_{jk})^2 \sigma^2_{F_{ij}} \quad (1.4)$$

where σ_{ik} is the uncertainty (or standard deviation, g m^{-3}) of the measured concentration of species i within observation period k, and $\sigma_{F_{ij}}$ is the standard deviation of the fraction of species i in emissions from source j.

Two major problems have been found for CMB modeling. First, the CMB model is inherently unable to handle collinearity in source emissions, e.g., negative estimated contributions of nearly collinear sources could be obtained (Henry 1992). Second, the emission profiles used for modeling may be inaccurate, as they were usually acquired by sampling over an insufficient period of time. Moreover, obtaining abundance profiles for all sources is impractical in many circumstances. Although source profiles published in the SPECIATE database (U.S.EPA 2006) or other references have often been used as surrogates in the absence of on-site source

information, those generic source profiles may not well represent the actual source emissions during the time of study. Nevertheless, as species with low precisions in the source profiles and receptor measurements are down-weighted (Equations 1.3 and 1.4), the CMB solution is self-rectified to some extent.

Unlike CMB modeling which requires a detailed knowledge of sources (i.e., types of sources and their emission profiles), PMF modeling (Paatero and Tapper 1994) simultaneously solves for both source contributions (g matrix) and compositions (f matrix) for a given number of factors (N sources) following Equation 1.5 and non-negativity constraints are imposed on PMF solutions (Paatero 1997, Paatero and Tapper 1994). However, due to the weak constraining force of non-negative constraints (Paatero et al. 2002) and sometimes equivocal determination of the number of factors, source cross-contamination is inevitable in PMF solutions.

$$c_{ik} = \sum_{j=1}^{N} g_{jk} \cdot f_{ij} + e_{ik} \tag{1.5}$$

In PMF modeling, an object function, Q(E), normalized to measurement uncertainties is defined as follows.

$$Q(E) = \sum_{i=1}^{l} \sum_{k=1}^{m} \left[\frac{c_{ik} - \sum_{j=1}^{n} g_{jk} f_{ij}}{\sigma_{ik}} \right]^2 \tag{1.6}$$

where σ_{ik} is the measurement uncertainty of the i^{th} species in the k^{th} sample. The PMF model seeks solutions towards minimizing Q(E) by iterative calculations of the standard deviations of each data point, c_{ik}, according to Equation 1.7. That is, samples with large measurement uncertainties will be down-weighted in PMF solutions (U.S.EPA 2008).

$$\sigma_{ik} = c_1 + c_2 max\left(|c_{ik}|, \sum_{j=1}^{N} |g_{jk} f_{ij}|\right) \quad (1.7)$$

where c_1 is the uncertainty measured for each data point, and c_2 is the extra modeling uncertainty (i.e., set to 0.10 in my study), which encompasses various errors (e.g., possible variations in source profiles) not considered in measurement errors. In the EPA PMF program, down-weighting of the effect of species thought to be less valuable in their ability to resolve sources is allowed by designating them as "weak" species. That is, additional uncertainties (i.e., a larger c_2 value) can be attributed to these species in the modeling.

The UNMIX model treats ambient concentrations as a linear combination of source contributions as well (Equation 1.5) and non-negative constraints are also applied to the matrices of compositions and contributions. Neither uncertainty data nor a pre-defined number of sources is required in UNMIX modeling, as the model seeks the number of sources and fitting solutions through those so-called edge points at which the contributions from certain source(s) are negligible. In other words, UNMIX reduces the degree of freedom in the solutions by ignoring small crossing contributions in the samples and explores for constraints from inside the data themselves, rather than minimizing a residual function that is correlated with contributions and chemical compositions of sources. Hence UNMIX modeling shows a weak ability to resolve minor sources and a feasible modeling solution cannot be always guaranteed.

Air quality managers are concerned with several key issues including source identification and quantification of estimates of emission rates. In particular, correct source identification is a prerequisite to successful source apportionment. As many

sources can exist but not all of them are necessarily active during the study period, it is critical to narrow down the scope of potential sources using the relevant information (e.g., locations and emission profiles of sources with large emissions in past studies, meteorological conditions, etc.). In practice, back trajectory (Cohen et al. 2011), wind direction analysis (i.e., potential source contribution function (PSCF) analysis (Wang, Hopke and Turner 2011), Non-Parametric Regression (NPR) (Kim and Hopke 2004)), and regional transport models (Hartley and Prinn 1993) have been employed to provide convincing source determinations. Besides, source identification is often performed using the receptor modeling results. For instance, CMB modeling can include excess sources and identify which ones were actually active within an observation, based on its solution of source contributions. For PMF or UNMIX, matching those model-derived source profiles with known facts of possible sources is another convenient approach of post-modeling source identification efforts.

None of those above-mentioned receptor models can provide quantitative estimates of source emission rates, as the SCE term (S_{jk} or g matrix) is not further resolved by dispersion factors. In fact, none of these models relies on any physical constraint (e.g., terrain effect) other than dispersion factors and their solutions are based upon a pure mathematic formulation. As a consequence, challenges in interpretations of results or significant discrepancies between different model solutions are not unusual.

During the EPA supersite project, a multivariate pseudo-deterministic receptor model (PDRM) was proposed by Park and Ondov (Park, Pancras and Ondov 2005b), in which a Gaussian plume model (GPM) was implanted to estimate dispersion

factors based on meteorological inputs and emission rates of ambient pollutants were then obtained. The core expression of PDRM also follows Equation 1.1. The product of F_{ij} and Q_{jk}, which is denoted as ER_{ijk}, is the emission rate (g s^{-1}) of the i^{th} species in the emission from the j^{th} source during the k^{th} time period (Equation 1.8). T_{ijk} is set to unity as in other receptor models such as CMB. The dispersion factor is denoted as $(\frac{\chi}{Q})_{jk}$ (s m^{-3}) in PDRM.

$$ER_{ijk} = F_{ij} \cdot Q_{jk} \tag{1.8}$$

$$(\frac{\chi}{Q})_{ijk} = T_{ijk} \cdot D_{jk} \tag{1.9}$$

Hence the PDRM model can be expressed as follows.

$$c_{ik} = \sum_j ER_{ijk} \cdot (\frac{\chi}{Q})_{ijk} + e_{ik} \tag{1.10}$$

The calculation of GPM dispersion factors, χ/Qs, follows the simple Gaussian plume model:

$$(\chi/Q)_{jk}^{MET} = \frac{1}{2\pi\sigma_y\sigma_z u} e^{-\frac{y^2}{2\sigma_y^2}} \left[e^{-\frac{(z-H)^2}{2\sigma_z^2}} + e^{-\frac{(z+H)^2}{2\sigma_z^2}} \right] \tag{1.11}$$

where u is the mean transport speed (m s^{-1}) of the plume. Dispersion coefficients, σ_y and σ_z (m), are the standard deviations of the concentration distributions in lateral (y) and vertical (z) directions, respectively. H is the effective stack height (m) at which the plume centerline travels, y is off-plume-centerline distance (m) from the receptor site, and z is the elevation (m) of the receptor site (Seinfeld and Pandis 2006).

Note that the PDRM expression in Equation 1.10 is similar to those of source-based models rather than the three EPA receptor models. Nevertheless, an underlying

difference between PDRM and deterministic models is that the GPM-derived dispersion factors which are subject to large errors (Cooper 1982, Yamartino 1982) are only applied to seed the model and PDRM seeks a reconciled solution between constrained dispersion factors and ambient concentrations. Since the dispersion factors are used to constrain emissions, the possibility of over-estimating contributions from sources that are insufficiently aligned with wind directions is minimized.

In PDRM, a nonlinear least square curve fit function describing the residuals is defined as follows and the modeling aims at the minimization of this object function.

$$\text{FUN} = \sum_{i=1}^{l} \sum_{k=1}^{m} [\sum_{j=1}^{n} ER_{i,j,k} (\chi/Q)_{jk}^{PDRM} - C_{ik}]^2 \qquad (1.12)$$

Several assumptions are made in Park's PDRM model. First, all emitted species are conserved. Second, variations of source emissions are ignored within each modeling period. Third, calculations of dispersion factors were based on straight-line plume trajectories towards the receptor site. These assumptions were generally valid since past PDRM applications were mostly the analyses of short-term, high time resolution measurements.

Park's PDRM model was first applied in the Tampa Bay Regional Aerosol Chemistry Experiment (BRACE) (Park et al. 2005b) and later applied in the Pittsburgh Supersite project (Park et al. 2006b). In these studies, SO_2 was chosen as a tracer gas, as to evaluate the predictions by comparing with continuous emission monitor (CEM) data. χ/Qs were then allowed to be tuned linearly from the GPM-predicted values. That is, a scaling factor for each source during each sampling

interval, $a_{j,k}$, was introduced to account for the difference between the predicted dispersion factors by the meteorological model and those in PDRM (Equation 1.13), which was determined using the known SO_2 emissions. In Park's Tampa study, the predicted SO_2 emission rates of all the six sources were in good agreement with the CEM data (i.e., $|ER_{pred}\text{-}ER_{CEM}|/ER_{CEM} < 8\%$) and the predicted concentrations of most elemental constituents of $PM_{2.5}$ well fit ambient measurements as well.

$$(\chi/Q)_{jk}^{PDRM} = a_{jk}(\chi/Q)_{jk}^{MET} \tag{1.13}$$

where $0.1 \leq a_{jk} \leq 2.0$.

As the PDRM model was specifically designed for point sources and did not well treat area or regional sources, large modeling residuals were observed for some source non-specific elements such as Al, Cu, Fe, and Zn in Park's Tampa study. Besides, it was also found that the predicted maximum concentrations and the observed excursions were asynchronous for some key marker species, which was later attributed to the over-simplification of the plume trajectory.

Most recently Beachley (Beachley and Ondov 2012) supplemented the PDRM with forward trajectories and reanalyzed the Tampa data. Several crucial improvements were made in this second generation of PDRM model. First, curvilinear plume trajectories were computed at different aloft levels, to correct for the plume arrival times. Second, CMB terms were introduced (Equation 1.14) to better account for the non-point background sources (i.e., area soil and marines sources). Third, for sources with definitive key tracer species, temporal profiles of tracer concentrations were used to condition their χ/Q profiles and intermittent

emission rates were allowed. Hence both the widths and amplitudes of χ/Q "peaks" could be adjusted towards the observed excursions in Beachley's modified PDRM model, surpassing Park's model in which plume shape-tuning was done by parallel translation of χ/Q profiles. Moreover, improved model performance statistics and better agreement with published source profiles were achieved by Beachley's modeling of the Tampa data, compared with Park's results.

As implemented by Beachley,

$$c_{ik} = \sum_{j=1}^{m} ER_{ijk} \cdot \left(\frac{x}{Q}\right)_{ijk}^{PDRM} + \sum_{j=m+1}^{n} A_{ijk} \cdot [PM_{2.5}]_{ijk} + e_{ik} \qquad (1.14)$$

where, A_{ijk} is the abundances of species i in particles emitted from the j^{th} area source during the k^{th} sampling interval, $[PM_{2.5}]_{ijk}$ is the ambient concentration of $PM_{2.5}$ (g m^{-3}) at the receptor site by each area source j during the k^{th} sampling interval, and other terms are the same as those in Equation 1.10. In Beachley's study (Beachley and Ondov 2012), χ/Q profiles at three different elevations (i.e., 10, 100, and 500 m, respectively) were used as the model input for near ground sources, stacks with medium heights (i.e., 10 ~ 500 m), and stacks with large effective heights (i.e., > 500 m), respectively.

A cornerstone for both Park's and Beachley's PDRMs is that the plume widths are related to the observed widths of the Gaussian-shaped excursions in ambient pollutant concentrations which contain dispersion information. Ideally, narrow Gaussian peak shapes are observed only when plumes from point sources are swept across the receptor site as a result of slow rotation of the mean wind direction. However, a plume may sweep across the receptor site for multiple times within an observed

Gaussian peak, masked by the lower time resolution of sampling compared with meteorological measurements. Besides, Gaussian-shaped or near Gaussian-shaped peaks can also be observed when the plume approaches the receptor site but departs towards its original incoming direction before touching the receptor site. In the past PDRM applications, curvilinear trajectories using a low time resolution (i.e., 30-minute) average of wind data neglected those potential problems and could have resulted in underestimated plume transport distances and thus inaccurate dispersion factors.

1.2 Advanced Receptor Model Trends

Ideally a receptor model adopted for authentic exposure assessment can generate solutions that are in good comparability with those from others. For this reason, inter-comparison of receptor models have been performed in the US (Lane et al. 2007), Europe (Viana et al. 2008), and China (Song et al. 2006), and by using synthetic data (Miller et al. 2002). Undoubtedly, similar results from independent models can add confidence. In cases that the results do not agree, contemplation of physical facts in the study area is more fruitful than comparison of the quality of fits (Henry and Christensen 2010).

It is controversial to conclude which model is generally the most preferable, as each receptor model has its limitations as well as unique advantages. For example, CMB is unable to identify unknown sources (e.g., one can only perceive the missing sources from large modeling residuals), although it is the first choice for sources with known emission profiles. In contrast, UNMIX can predict the number of sources but it inherently tends to ignore sources with minor mass contributions. This can be

problematic in cases where minor or trace components of ambient mass carry the bulk of the toxic activity. PCA requires little quantitative knowledge of sources and provides an explicable solution based on the assumption that each source has a unique set of tracer species. However, tracer species are often source non-specific and the PCA-MLR analyses may even afford negative source contributions. PMF will always produce non-negative source contributions and profiles simultaneously but it cannot well separate covariant sources. In a sense of incorporating realistic constraints (i.e., plume dispersion) into consideration and extracting emission rates, the PDRM model can provide more information than other receptor models. However, aberrant PDRM solutions may be achieved without effective modeling constraints. In particular, as CEM data for some well measured ambient pollutant, which allow effective tuning of GPM-derived dispersion factors, are sometimes absent, PDRM has to heavily rely on plume trajectories and chemical signature data. The former suffer from the fact that meteorological data for use in this model (i.e., wind angle and speed, ambient temperature, humidity, solar radiation, and preferably friction velocity, convective velocity, Monin-Obukhov length, and mixed layer depth) are acquired at very few (i.e., often only a single) stations and wind-versus-altitude data are seldom available.

Combining the profitable features of complementary receptor models has been attempted in the past. For example, Wåhlin (Wåhlin 2003) proposed a Constrained Physical Receptor Model (COPREM) in which the features of CMB and non-negative factor analysis was combined. Henry (Willis 2000) proposed a strategy of combining PMF and UNMIX. That is, UNMIX is used first to estimate the number of major sources and generate their profiles which could be used as a starting for PMF

modeling, as the latter is good at finding minor sources. In general, those efforts of hybrid modeling were limited to the interaction of two complementary models of a similar nature (e.g., both PMF and UNMIX models explore exactly the same outputs and their differences lie in the solving procedure), and their significance is no more than mathematically facilitating a compromised, feasible solution.

As a matter of fact, Beachley's PDRM model was a first trial of combining two models in fundamentally different types. In Beachley's study, ambient concentrations were split into two parts (from point and non-point sources, respectively): the PDRM main program computed the contributions from stationary sources by coordinating source emission rates and plume dispersion factors, while the CMB components accounted for area sources by modeling source contributions and compositions of emissions. However, each of these two model moieties independently accomplished its own "task", resulting in a lack of interactive cooperation with each other.

In this work, I focused on the joint applications of two distinct models, PDRM and PMF, in resolving nearby industrial sources in Baltimore and St. Louis. As the most commonly used model when a detailed knowledge of sources is unavailable, PMF is a powerful tool to extract the profiles of major sources but, like CMB, it is vulnerable to the impact of source collinearity (Habre, Coull and Koutrakis 2011). PDRM, however, can even resolve sources in close proximity as far as the profiles of their plume dispersions differ. Highlights of this proposed approach include: 1) PMF modeling provided a rough apportionment by which the contributions from non-point sources can be removed from ambient concentrations; 2) PMF modeling also provided cursory source profiles with which source emission rates can be better

constrained; 3) algorithms from the EPA ISCST3 model (U.S.EPA 1995) were implanted which specifically considers plume dispersion from short-range (< 10 km) sources; 4) high time resolution (5-minute) trajectories at the effective plume heights allowed more reasonable trajectory-driven GPM outputs according to the actual plume arrival times; and 5) plume widths were adjustable by allowing the changes in source emission rates among various modeling sub-periods.

Chapter 2: A Case Study of a PMF-seeded PDRM Model to Resolve Two Neighboring Power Plants of Different Fuel Types in Baltimore

2.1 Background

One of the principle objectives of the EPA Supersite Program was to provide high quality data sets that could be used to evaluate advanced receptor models (Russell 2008). In the Baltimore Supersite Project (2000~2003), highly time (1h or less) resolved measurements of a wide variety of ambient pollutants were carried out. Receptor modeling was attempted to exploit the temporal information provided by the data (Ogulei et al. 2005, Ogulei et al. 2006). Owing to the high temporal resolution of measurements, better source identifications were achieved (i.e., both oil-fired power plant and coal-fired power plant were resolved with the multilinear engine (ME), as well as both gasoline-type and diesel-type vehicles), compared with past studies conducted in Baltimore (Suarez and Ondov 2002, Hopke et al. 2003, Larsen and Baker 2003).

As mentioned above, source cross contamination is often inevitable in the applications of factor analysis models such as ME, due to collinearity in source contributions or profiles (Habre et al. 2011). In the Lee et al. (Lee et al. 2002) study of Mid-Atlantic regional aerosol, a blending of the PMF-resolved oil combustion and coal combustion factors is indicated by the high abundance of Ni, a well-known source specific tracer of oil combustion (Osan et al. 2000, Li et al. 2004), in the coal

combustion source in summer (Figure 2.1). In a previous study in Baltimore (Ogulei et al. 2005), a low OC/TC ratio (< 0.01) was ascribed to an oil-fired power plant (OFPP), which contradicted the common findings in such facilities, i.e., where OC/TC = 0.25 ~ 0.50 (Hays et al. 2009). This is partially because the major utility generating facilities in Baltimore, an oil-fired power plant (OFPP) and a coal-fired one (CFPP), were located in close proximity (< 500 m; Figure 2.2) and the factor analysis was unable to properly separate these sources.

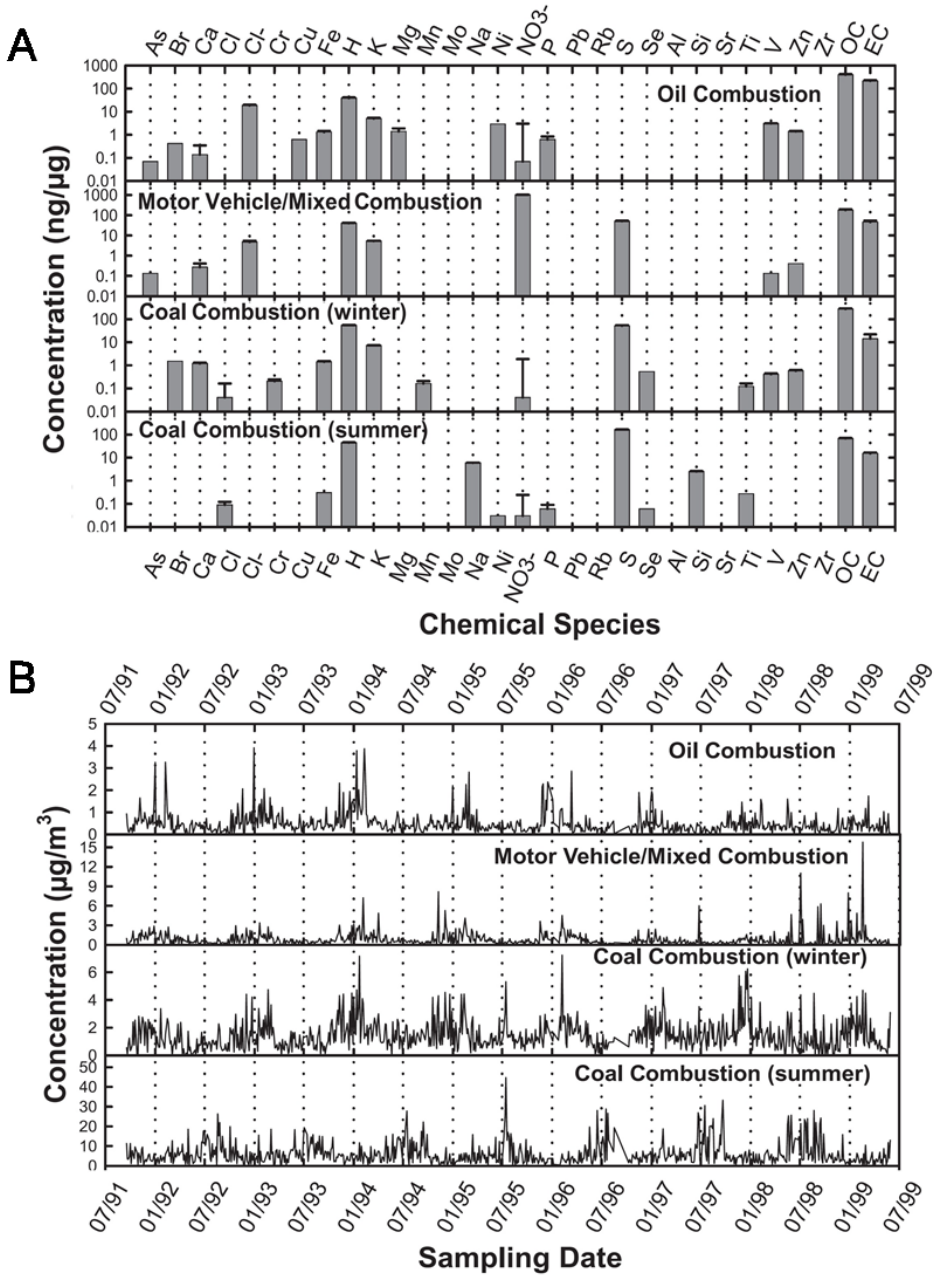

Figure 2.1 Several resolved (A) source profiles and (B) their contributions in the Mid-Atlantic regional aerosol study by PMF (adapted from Lee et al., 2002).

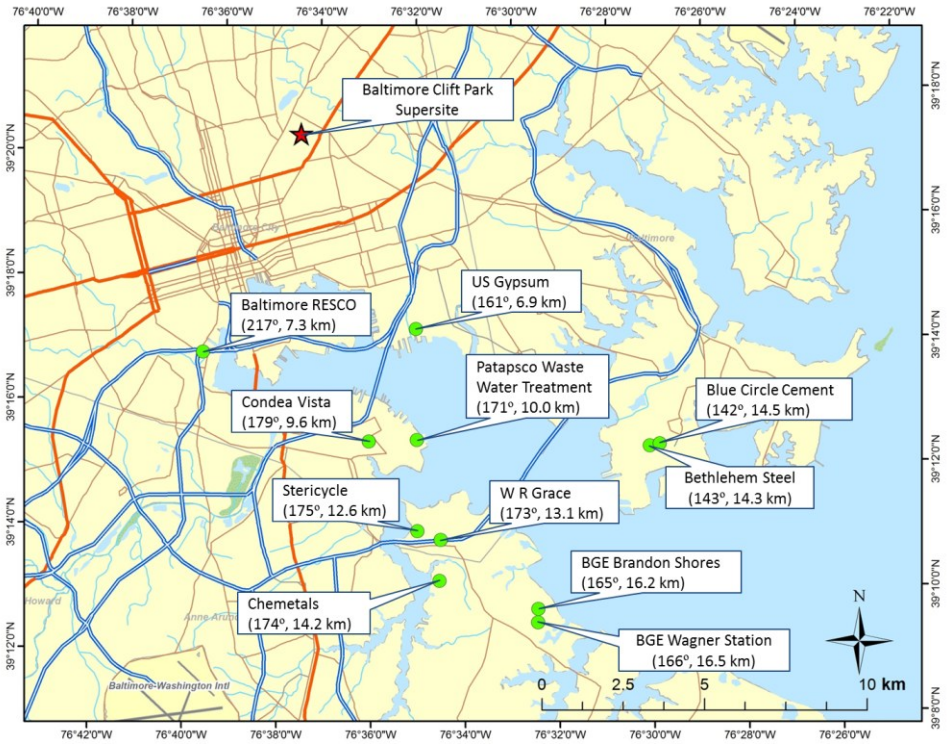

Figure 2.2 Map showing the Clifton Park supersite location and major PM sources within 20 km.

Sulfate, which is largely derived from the conversion of SO_2, was the largest single contributor to urban PM in the Baltimore area, and, in addition to regional sources, local utility power plants added a significant portion to atmospheric SO_2 and sulfate (Suarez and Ondov 2002, Ogulei et al. 2005). In the Tampa studies by Park and Beachley (Park et al. 2005b, Beachley and Ondov 2012), SO_2 was measured at both the receptor site and with CEMs at each of the four power plants, and was employed as a tracer gas to condition the dispersion factors and evaluate modeling performance. Two of these power plants were resolved despite having nearly the same source angle, as the PDRM model is especially good at handling sources with similar profiles based on their different plume widths at the receptor site. However, in

the Baltimore Supersite study, SO_2 was not measured at the receptor site and thus could not be used for these purposes.

NO_x is another criteria gas that is commonly present in primary emissions from industrial combustion sources. Unlike SO_2 which is an unique marker of coal combustion (e.g., > 95% of atmospheric SO_2 emissions were from fossil fuel combustion power plants (http://www.epa.gov/air/emissions/so2.htm) in Maryland in 2008), NO_x can also arise from other sources including motor vehicle emissions (Landis et al. 2001, Hopke et al. 2003, Larsen and Baker 2003, Ogulei et al. 2005), which are highly dispersed in urban areas. For this reason, NO_x had not been used in the past PDRM applications (Park et al. 2005b, Park et al. 2006b, Beachley and Ondov 2012). However, lacking ambient SO_2 data to define χ/Qs, the efficacy of using ambient NO_x with available CEM data was investigated in this study. In my preliminary study (refer to Section 2.4.1), factor analysis revealed that NO_x concentrations measured in the Baltimore supersite project were closely correlated with Se, which is a strong tracer of coal combustion (Gladney et al. 1976, Ondov et al. 1989, Morawska and Zhang 2002), Ni, which is a highly useful tracer of oil fuel combustion (Gordon and Zoller 1974, Osan et al. 2000), and also elemental carbon (EC) when occurring with large Se excursions, suggesting that utilizing NO_x as a tracer gas of fossil-fuel fired power plants might be useful.

In this part of my modeling study, I was particularly interested in resolving the two aforementioned neighboring power plants in Baltimore, i.e., the Wagner Station (WS) and Brandon Shores (BS), both operated by the Constellation Energy (formerly BGE), and extracting their emission profiles. A novel modeling approach of combining

PDRM, in which a trajectory-driven GPM was implanted, with PMF analysis was proposed.

2.2 Data Inputs

2.2.1 Description of Receptor Site and Sources

The Baltimore supersite at Clifton Park (latitude 39.32ºN, longitude 76.58ºW, ASL 45 m) was located in an urban residential area north-northwest of downtown Baltimore and nearly due north of the heavily industrial area (Figure 2.2) along the shores of the Patapsco River and Curtis Bay in South Baltimore. As shown in Figure 2.3, significant excursions in ambient concentrations of Se and Ni were observed at Clifton Park site during three consecutive afternoons of September 7th, 8th, and 9th, 2001, when atmospheric stability stayed from moderately unstable to slightly unstable, prevailing wind angles (with respect to true north) spanned 135 to 195º, and surface wind speeds ranged from 2 to 3.5 m s^{-1} (Figure 2.2). Accordingly, a total of 21-hourly periods (1200 - 1900 LT each afternoon) were selected for data analysis and modeling.

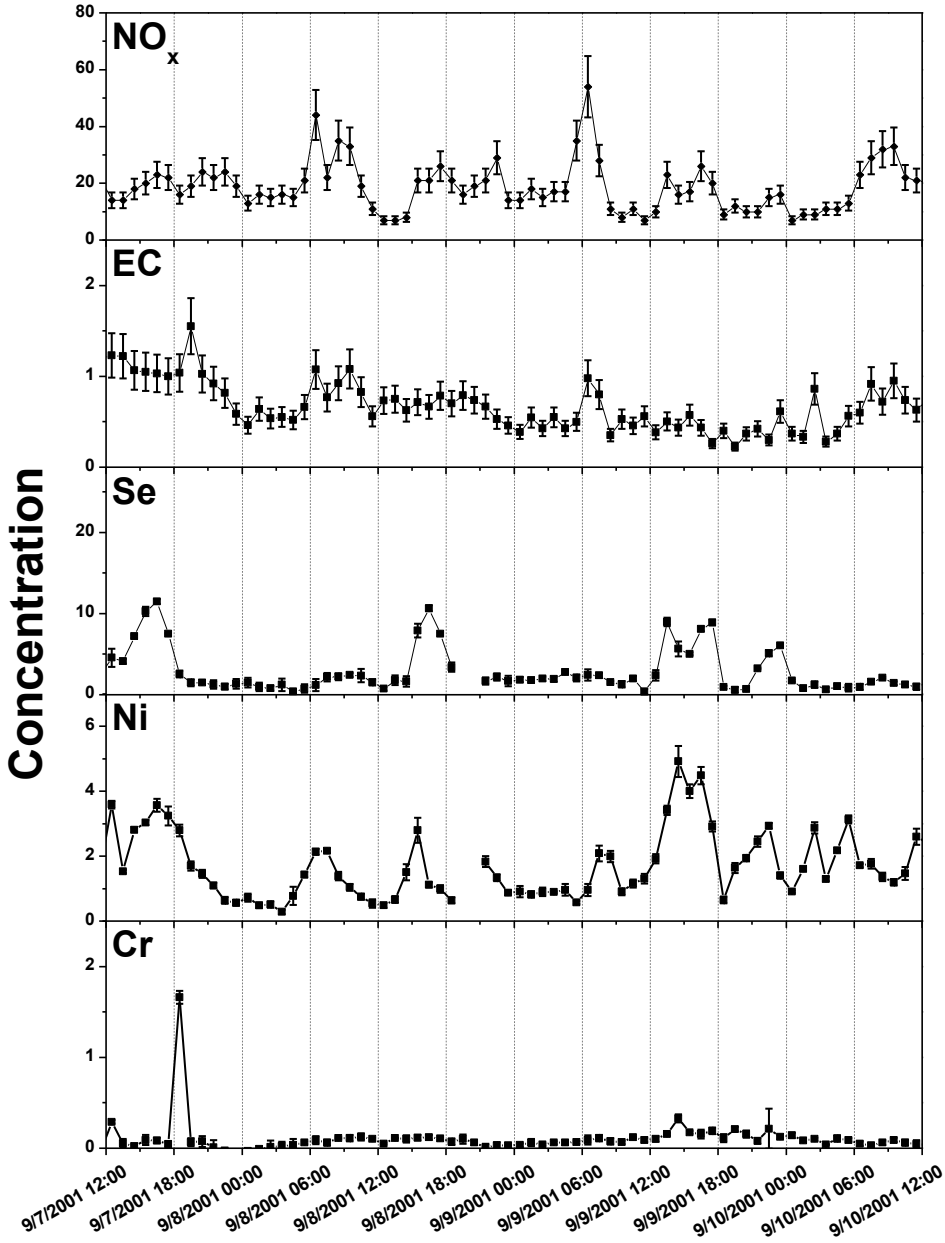

Figure 2.3 Time series of airborne concentrations of NO_x (ppb), EC (μg m^{-3}), Se (ng m^{-3}), Ni (ng m^{-3}), and Cr (ng m^{-3}) measured at the Clifton Park supersite on September 7th through 10th, 2001.

Sources located within this wind sector included the two power plants of interest (the Wagner Station and Brandon Shores), and a cluster of industrial sources (Stericycle, Chemetals, W.R. Grace, Condea Vista, and Patapsco Waste Water Treatment Plant) which lay within a radius of 2.5 km of one another along Curtis

Bay. The Wagner Station has four generating units: two burning coal only, and two burning either oil or natural gas (NG). The coal-fired units are equipped with electrostatic precipitators (ESP), and the oil/gas-fired units were equipped with multiple cyclones (MC). The Brandon Shores plant has two identical coal-burning units, each equipped with Selective Catalytic Reduction (SCR) devices for NO_x control and ESPs. Fuel type, nominal capacities, emissions data for particulate matter (PM) and NO_x, source-receptor distances, and station angles, of the two power plants are listed in Table 2.1. Stack parameters are listed in Table 2.2.

Table 2.1 Emission source information of the Brandon Shores and Wagner Station.

Plant	Unit ID	Fuel	Capacity, MW	Control technology[1]	Distance, km	Station angle, deg	PM, tpy[2]	NO_x emission, tpy[2]
Wagner Station	1	oil/NG	140	MC	16.5	166	3	113
	2	coal	130	ESP	16.5	166	77	2634
	3	coal	320	ESP	16.5	166	176	10335
	4	oil/NG	400	MC	16.5	166	37	641
Brandon Shores	1	coal	690	ESP, SCR	16.2	165	496	11383
	2	coal	690	ESP, SCR	16.2	165	428	11604

[1] Multiple cyclone (MC); electrostatic precipitator (ESP); and selective catalytic reduction (SCR) system.
[2] Metric tons per year in 2001.

Table 2.2 Stack information of the Brandon Shores and Wagner Station.

Plant	Unit ID	Stack height (m)	Temperature (K)	Diameter(m)	Exit velocity ($m\ s^{-1}$)	Flow rate [1] ($m^3\ s^{-1}$)
Wagner Station	1	87.48	409.80	3.10	22.86	172.26
	2	87.48	409.80	3.10	22.86	172.26
	3	105.46	418.70	4.21	28.65	399.27
	4	106.68	588.70	5.34	35.05	786.74

Brandon Shores	1	179.07	435.93	6.71	35.41	1225.63
	2	179.07	435.93	6.71	35.41	1225.63

[1] Flow rate at stack conditions.

Owing to their identical stack profiles (Table 2.2) and locations, the plume trajectories of two units at the Wagner Station (unit #1 and #2) are indistinguishable despite their different fuel categories. These two units were thus treated as one in the PDRM modeling. For the same reason, the Brandon Shores was considered as a single point source. Therefore, totally four individual stacks rather than six were considered: Wagner Station Unit #1 and #2 (WS Unit 1&2), Wagner Station Unit #3 (WS Unit 3), Wagner Station Unit #4 (WS Unit 4), and Brandon Shores Unit #1 and #2 (BS Unit 1&2).

2.2.2 Ambient Pollutants

Data used in this study were retrieved from the Baltimore Supersite Database (http://www2.chem.umd.edu/supersite/) and the project's archives. These included: 1) $PM_{2.5}$ metals (Al, As, Cd, Cr, Cu, Fe, Mn, Ni, Pb, Se, and Zn) determined at 30 minute intervals for samples collected with the University of Maryland Semi-continuous Element Aerosol Sampler (SEAS); 2) both particulate sulfate and nitrate measured at 10-min intervals with an R&P (Rupprecht and Patashnick, Albany, NY) 8400S ambient particulate sulfate monitor and an R&P 8400N ambient particulate nitrate monitor, respectively; 3) hourly OC and EC obtained with an R&P 2100 carbon analyzer (total carbon was determined as the sum of OC and EC); and 4) 30-min $PM_{2.5}$ mass concentrations measured with an R&P Tapered Element Oscillating Microbalance (TEOM, 1400a) ambient particulate monitor, equipped with a sharp-cut

$PM_{2.5}$ cyclone inlet. Hourly measurements of gaseous criteria pollutants (NO_x, CO, and O_3) at the supersite were carried out as well by Maryland Department of Environment (MDE). Additional data details are described in Ondov et al. (Ondov et al. 2006) Hourly NO_x emission rates from the Wagner Station and Brandon Shores were obtained for the modeling periods from the EPA Clean Air Markets Database (http://www.epa.gov/airmarkets/). Herein all of the pollutant data were synchronized and converted into hourly averages prior to the modeling.

2.2.3 Meteorological Data

On-site meteorological measurements included temperature, relative humidity (RH), wind speed and direction (Figure 2.4), pressure, precipitation, and solar radiation recorded at 10-minute intervals by sensors placed on a 10-m tower at the Clifton Park site. These data are available on the NARSTO Database (ftp://narsto.esd.ornl.gov/pub/EPA_Supersites/baltimore/JHU_MET/NARSTO_EPA_SS_BALTIMORE_JHU_MET_V1.html), as part of the Baltimore data set. Surface albedo and cloud cover measured at the nearby BWI airport were used which were retrieved from the National Solar Radiation Database (NSRDB). Other meteorological parameters describing the atmospheric boundary layer (ABL) were derived with the AEROMET algorithms (U.S.EPA 2004a) in MATLAB scripts (MathWorks, Inc., version 7.8) as described in Appendix B1, including: Pasquill atmospheric stability class, friction velocity, convective velocity, Monin-Obukhov length, and mixed layer depths (MLDs). The Johns Hopkins University elastic backscatter lidar system (JHU 2000) (Adam 2004) was used to experimentally determine the MLDs at 30-minute intervals on several days in August 2001, but the

instrument was offline during the selected SEAS measurement periods, owing to damage by lightning. However, the measured MLDs by JHU were used to tune the mixing height model calculations (Appendix B1). The 3D anemometer installed at the supersite was also off line after the lightning strike and those high quality micrometeorological data were unavailable for the modeling periods.

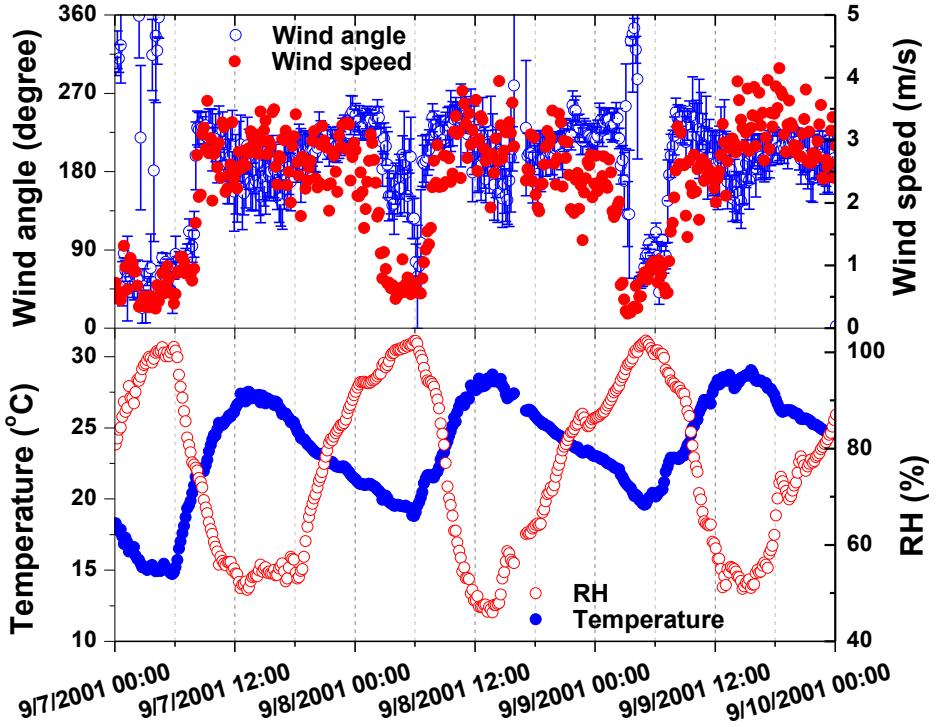

Figure 2.4 Time series of surface wind, temperature, and RH from September 7th through 10th, 2001.

It is noteworthy that the instrument maintenance log recorded an anemometer resetting at 1600 LT on September 8th 2001 and large uncertainties associated with the wind direction measurement ($\sigma > 40^{o}$) lasted for about two hours thereafter. In the modeling, we used the linearly interpolated wind directions as an alternate for this affected period.

2.3 Methods

2.3.1 Multiple Linear Regression

Multiple linear regression (MLR) analysis is a statistical technique for estimating the degree to which changes in independent variables will correlate with changes in a dependent variable (Kleinman et al. 1980). Herein, I used MLR to apportion contributions of the tracer gas from the two power plants and other non-interested sources. Thus, in this case the dependent variable was ambient NO_x concentration measured at the Clifton Park receptor site, and the independent variables were elemental (SEAS metals and EC) and molecular (sulfate, nitrate, and OC) aerosol particle constituents, and other measured criteria gases (CO and O_3). The dataset used was either for the entire 153 hours of data acquisition in early September, or for the 21 afternoon hours (1200 ~ 1900 LT) of interest from September 7th through 9th, 2001. Simple linear regression between NO_x and individual species was used to assist the selection of the best independent variables. The selection criterion was that the independent variables need be source specific. Statistical analysis was performed with a least-square multiple linear regression function available in the MATLAB software (MathWorks, Inc., version 7.8).

2.3.2 PMF

The EPA PMF v3.0 program was used and 22 species were selected for analysis, including $PM_{2.5}$ components (Al, As, Cd, Cr, Cu, Fe, Mn, Ni, Pb, Se, Zn, sulfate, nitrate, EC, OC, TC, and TEOM $PM_{2.5}$ mass) and gaseous criteria pollutants (NO, NO_2, NO_x, O_3, and CO). A few TEOM readings were negative and replaced with the

linearly interpolated values. Accordingly, TEOM $PM_{2.5}$ mass was then considered to be a "weak" species with additional uncertainties allowed in the modeling. CO and NO were also treated as "weak" species, as several measurements of these two species showed zero values.

Different numbers of factors (3 to 10) were tested in this study and an optimal fit yielding interpretable results was reached with a 6-factor model. When the factor number was ≤ 5, the predicted value of Q was greater than 1.1 times of the robust value of Q, indicating that fitting was non-robust, and the solutions did not adequately explain the observed mass. When the factor number was ≥ 7, there were no significant changes in the ratios of predicted and expected Q values. Also, the modeling consistently produced negative coefficients in the solutions, suggesting that too many factors were considered.

2.3.3 Trajectory Analysis

For each source, forward trajectories at the effective plume heights were calculated every 10 minutes, using 10-minute wind averages. Standard deviations of the 10-minute averages were used in error propagation to assess the uncertainty in the results predicted with the TGPM, as described below. The coordinates of all points on the trajectories were referenced from the receptor site (0, 0). Using the point of closest approach (Beachley and Ondov 2012), the horizontal off-plume centerline distance, the accumulated plume downwind distance to the receptor site, and the corresponding time of the plume transport were calculated for each trajectory. The point of closest approach, (x_c, y_c), for each wind vector segment (i.e., (x_i, y_i, x_f, y_f)) (Figure 2.5) was determined as:

$$x_c = -k \times b/(k^2+1) \quad (2.1)$$

$$y_c = b/(k^2+1) \quad (2.2)$$

where $k=(y_f-y_i)/(x_f-x_i)$, and $b=(x_f \times y_i - x_i \times y_f)/(x_f-x_i)$.

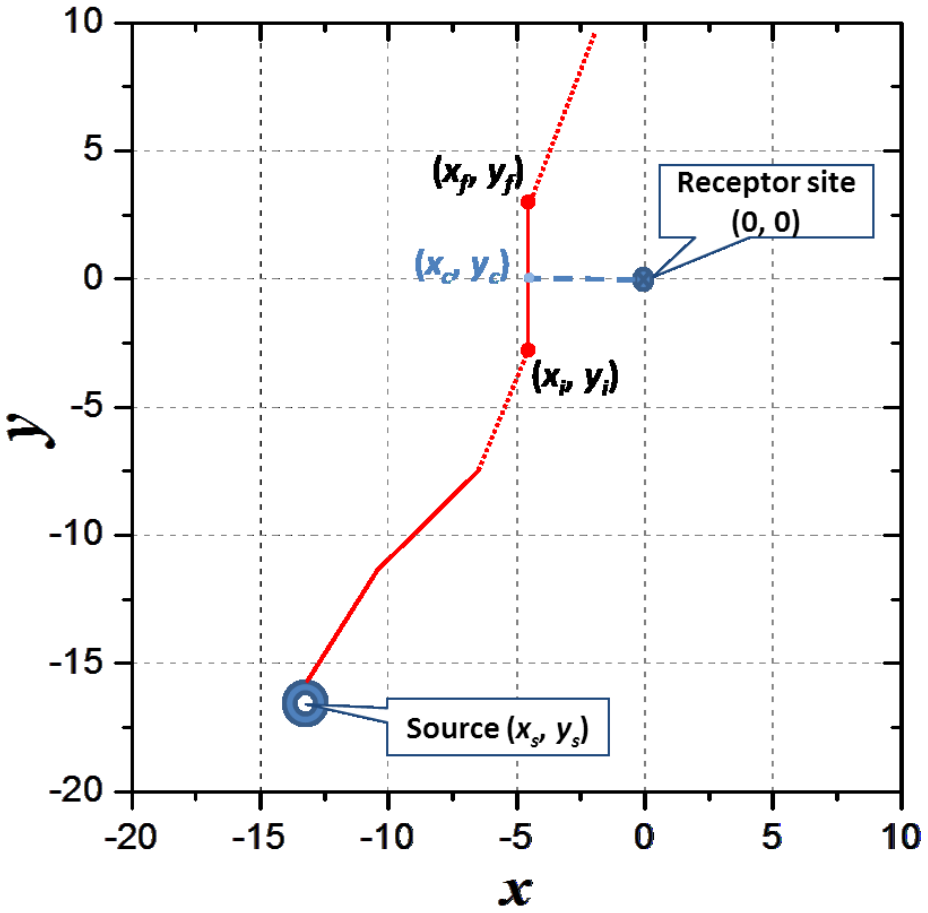

Figure 2.5 A curvilinear forward trajectory with respect to the receptor site (0, 0).

Accordingly, the off-axis distance (Y_i) between the selected trajectory segment and the receptor site was calculated as follows:

$$Y_i=\sqrt{(x_c^2+y_c^2)} \quad (2.3)$$

In case that the point of closest approach was on the line extension of the selected segment, its off-axis distance (Y_i) was considered to be the linear distance between the closer end of the segment and the receptor site.

$$Y_i=\min(\sqrt{(x_i^2+y_i^2)}, \sqrt{(x_f^2+y_f^2)}) \quad (2.4)$$

The off-plume centerline distance (Y) between the trajectory and the receptor was the minimum value of Y_is among all trajectory segments.

$$Y=\min(Y_i) \quad (2.5)$$

The point of closet approach for the trajectory was that corresponded to the determined Y. The plume transport distance, x, was the accumulated lengths of segments up to the point of closest approach for the overall trajectory, and the plume transport time was the sum of the quotient of the length of each trajectory segment and the segment average wind velocity. The mean transport velocity was the plume transport distance divided by the transport time. And the plume arrival time for each trajectory was its originating time plus the calculated plume transport time.

2.3.4 Trajectory-driven Gaussian Plume Model (TGPM)

Herein, the core expression of the TGPM is as follows:

$$\left(x/Q\right)_{j,k}^{TGPM} = \frac{1}{2\pi\sigma_y\sigma_z u} e^{-\frac{y^2}{2\sigma_y^2}} \left[e^{-\frac{(z-H)^2}{2\sigma_z^2}} + e^{-\frac{(z+H)^2}{2\sigma_z^2}} \right] \quad (2.6)$$

Equation 2.6 is identical to the simple GPM (Equation 1.11) discussed earlier and detailed descriptions of the solving procedure can be found elsewhere (Park et al. 2005b, Beachley 2009). In the equation, the pre-exponential term (s m^{-3}) describes the

plume volume dilution, the first exponential factor accounts for the lateral decay of the plume, and the terms in the bracket account for the vertical decay of the plume. In both Park's and Beachley's studies, Briggs' equations (Briggs 1969, Briggs 1971, Briggs 1972, Briggs 1974, Briggs 1975, Seinfeld and Pandis 2006) were used to compute buoyancy flux and momentum flux parameters and thus the effective plume height, H. Aloft wind velocity, *u*, was calculated from the power law wind profile (Panofsky, Blackadar and McVehil 1960). Equations from Draxler (Draxler 1976), Irwin (Irwin 1979), and Binkowki (Binkowski 1979) were used to calculate σ_y and σ_z.

In my study, several updates in the algorithms for plume dispersion calculations were made. First, the power law was replaced by the log-law wind profile (Cinoco 1965, Oke 1987), because the latter contains the surface roughness as an input (Huang 1979, Oke 1987), which could be a critical factor for complex urban cases such as in Baltimore. According to the log-law algorithms, the wind speed (U) at an aloft height, z (m), is equal to:

$$U(z) = (u^*/k_f) \times \ln((z - D)/z_0) \tag{2.7}$$

where u^* is the friction velocity, k_f is von Karman constant, which is equal to 0.4, z_0 is the surface roughness, which was set to 0.25 m in this scenario due to the heterogeneous terrain (i.e., mixed urban/industrial land use with about one third of water cover) as suggested by Nicholas and Lewis (Nicholas and Lewis 1980), and D is the zero-plane displacement height, which is approximately equal to seven times the surface roughness.

Given the wind speed, $U(z')$, at an altitude of 10 m (z' = 10 m), the wind speed at height, z, can be obtained as:

$$U(z) = [\ln(z - D)/z_0)/\ln(z' - D)/z_0)] \times U(z') \quad (2.8)$$

Plume trajectories at different originating times were simulated for each source in MATLAB, using the calculated aloft wind speeds at the corresponding effective plume height.

Second, the EPA Industrial Source Complex Short Term plume model 3, ISCST3 (U.S.EPA 1995), was applied to compute σ_y and σ_z. In ISCST3, these calculations are based upon the Pasquill-Gifford dispersion curves (Pasquill 1979) that were obtained from trustworthy surface release experiments under six discrete stability classes, as follows:

$$\sigma_z = ax^b \quad (2.9)$$

$$\sigma_y = 465.11628 \times x \times \tan(TH) \quad (2.10)$$

where $TH = 0.017453293 \times [c - d \times \ln(x)]$

In the above equations, x is the plume downwind distance in kilometers based on the curvilinear trajectories. *a*, *b*, *c* and *d* are coefficients (Table 2.3) regarding x and the Pasquill-Gifford atmospheric stability class (Gifford 1961) which were estimated from the solar radiation and the surface wind speed as shown in Table 2.4. This stability classification approach is part of the EPA regulatory model of Gaussian plume dispersion and suited to cases where sophisticated micrometeorological data are unavailable, despite the fact that it insufficiently captures the continuously

varying nature of atmospheric conditions. Nevertheless, this approach is deemed adequate for short plume transport periods, such as the case here.

Table 2.3 Parameters used to calculate Pasquill-Gifford σ_y and σ_z (Gifford 1961).

Atmospheric stability class [1]	x (km)	a	b	c	d
B	< 0.2	90.673	0.93198	18.3330	1.8096
B	0.21 - 0.40	98.483	0.98332	18.3330	1.8096
B	> 0.4	109.3	1.0971	18.3330	1.8096
C	All	61.141	0.91465	12.5000	1.0857

[1] B: moderately unstable; and C: slightly unstable.

Table 2.4 Daytime atmospheric stability classification [1].

Surface wind speed ($m\ s^{-1}$)	Strong (> 700 $W\ m^{-2}$)	Moderate (350 - 700 $W\ m^{-2}$)	Slight (< 350 $W\ m^{-2}$)
2 – 3	A – B	B	C
3 – 5	B	B – C	C

[1] A: extremely unstable; B: moderately unstable; and C: slightly unstable.

Another feature of the ISCST3 model was employed for the modeling. That is, a zero vertical dispersion factor is assumed if the effective plume centerline is above the mixed layer under convective conditions. Details about these updates are given in Appendices B1 and B2.

The plume dispersion factors, χ/Qs, were then calculated individually for each successive trajectory. These high time resolution trajectories were sorted by the actual plume arrival times rather than their originating times, and the dispersion factors for

those within the same hourly period were combined into hourly averages, to coincide with the ambient pollutant sampling interval.

2.3.5 PMF-seeded PDRM (PDRM III)

Background correction is especially crucial in this study, as the tracer gas, NO_x, is source non-specific. Nevertheless, due to lack of apparent source-specific tracer sets and detailed background information (i.e., the types of background sources that were effective during the study period and their validated emission profiles), neither linear regression nor Beachley's CMB approach could be applied. Alternatively, PMF was used to remove background sources for PDRM-III, as follows.

$$c_{ik} = \sum_{j=1}^{m} ER_{ijk} \cdot \left(\frac{x}{Q}\right)_{jk}^{PDRM} + \sum_{j=m+1}^{n} g_{jk} \cdot f_{ij} + e_{ik} \qquad (2.11)$$

where the terms are the same as those in Equations 1.5 and 1.10. As shown in Equation 2.11, ambient pollutant concentrations, c_{ik}, are expressed as the sum of the contributions from the m point sources of interest (the first summation term) and other n-m area sources (the second summation term). PMF analysis was incorporated in the PDRM-III for the contribution estimates of area sources but done independently prior to PDRM.

The NO_x emission ratio (r) of coal-fired to oil-fired units at the Wagner Station was calculated using the in-stack CEM data (Equation 2.12). This allowed further resolving of the emission profiles from different stacks at the Wagner Station while allowing the assumption to be made that the coal-burning units in the Brandon Shores and Wagner Station had the collinear profiles (Equations 2.13 to 2.14):

$$r = \overline{ER}_{NOx,coal} \Big/ \overline{ER}_{NOx,oil} \tag{2.12}$$

$$f_{i,WS,coal} = \frac{f_{NOx,WS}}{f_{NOx,BS}} \cdot f_{i,BS} \tag{2.13}$$

$$f_{i,WS,oil} = (1 + r) \cdot f_{i,WS} - r \cdot f_{i,WS,coal} \tag{2.14}$$

where $\overline{ER}_{NOx,coal}$ and $\overline{ER}_{NOx,oil}$ are the average NO_x emission rates due to the coal and oil/NG burning at the Wagner Station, respectively. $f_{NOx,BS}$ and $f_{NOx,WS}$ are the NO_x abundances in the PMF-derived source profiles for BS and WS, respectively. $f_{i,BS}$ and $f_{i,WS}$ correspond to the abundances of the i^{th} species in the PMF-derived source profiles for the coal- and oil-fired power plants, respectively. $f_{i,WS,coal}$ and $f_{i,WS,oil}$ are the abundances of the i^{th} species in the desired source profiles for the coal-burning only unit (WS Unit 3) and oil-burning only unit (WS Unit 4) at the Wager Station, respectively. The PMF-derived profile of the oil-fired power plant represented the aggregate of units 1 and 2 at the Wagner Station (WS Unit 1&2).

In our initial PDRM trials, initial ERs were roughly estimated and ER solutions were loosely bound (i.e., LB: 10^{-4} g s^{-1}; UB: 5×10^{4} g s^{-1}) for all species as done by Park (Park et al. 2006b), unless CEM or other external sources (i.e., EPA national emission inventory, NEI; or toxics release inventory, TRI) could provide the information. For a multivariate receptor model such as PDRM, it is critical to set near realistic initial inputs with proper constraints to avoid aberrant solutions. Although source cross contamination was realized in our PMF results, the PMF generated emission profiles were good values to serve as the initial guesses for PDRM and

assured a rapid convergence to interpretable solutions. Therefore, the PDRM model was upgraded by applying PMF constraints as described below.

The initial guess of emission rates of ambient pollutants from a given source was normalized to its NO_x emission rate:

$$ER_{i,j} = ER_{NOx,j} \cdot f_{i,j}/f_{NOx,j} \quad (2.15)$$

where $ER_{i,j}$ is the initial emission rate (g s^{-1}) of species *i* from source *j* during the modeling period. $ER_{NOx,j}$ is the initial emission rate of NO_x (g s^{-1}) from source *j* during the modeling period, as determined from CEM data. $f_{i,j}$ and $f_{NOx,j}$ are the abundances of species *i* and NO_x from source *j*, respectively, obtained from the PMF analysis. ERs of ambient species were then more tightly constrained as follows:

$$\text{LB}(ER_{i,j}) \leq ER_{ij} \leq \text{UB}(ER_{i,j}) \quad (2.16)$$

where LB and UB are the lower and upper bounds which were set as 0.1 and 10 times the initial value, respectively.

Two PDRM runs were performed for each day of study, using a MATLAB script in which the solution for Equation 2.11 is obtained by minimizing the object function defined as follows:

$$\text{FUN} = \sum_{i=1}^{l}\sum_{k=1}^{p}[\sum_{j=1}^{m} ER_{ijk} \cdot \left(\frac{\chi}{Q}\right)_{jk}^{PDRM} + \sum_{j=m+1}^{n} g_{jk} \cdot f_{ij} - C_{ik}]^2 \quad (2.17)$$

The first run used NO_x only, to tune χ/Q profiles ($(\chi/Q)^{PDRM}$) for the three or four sources (WS Units 1 and 2 were inactive on September 8th and 9th) using the NO_x emission rates from CEM. In the second run, all species were added. Note that the

seed values of emission rates of all species other than NO_x from different stack units were obtained using those ERs of NO_x solved in the first PDRM run and the PMF-derived source profiles, as described in Equation 2.15. Finally, all PDRM-derived ERs of various species from those different stacks were normalized with respect to the corresponding ER of $PM_{2.5}$, to generate the PDRM-derived source profiles.

2.4 Results and Discussion

2.4.1 Linear Regression

When the entire 153-hour sampling periods in early September were included, the three species best correlating with NO_x were EC ($r^2 = 0.895$, $p < 0.001$), Se ($r^2 = 0.636$, $p < 0.001$), and Ni ($r^2 = 0.443$, $p < 0.001$). However, if only considering the 21 afternoon hours when plume influences were observed as evidenced by Se and Ni, the best correlations with NO_x were found for Se ($r^2 = 0.696$, $p < 0.001$), Ni ($r^2 = 0.203$, $p = 0.04$), and As ($r^2 = 0.125$, $p = 0.12$). As a matter of fact, the most prominent peaks of NO_x occurred in the mornings (Figure 2.3), coinciding with the largest EC excursions and traffic rush hours, which together pointed to motor vehicle exhaust. In contrast, weaker NO_x occurrences in the afternoons were accompanied with large excursions of Se and Ni. Selenium, nickel, and EC were thus selected as the tracers of coal combustion, oil combustion, and motor vehicle emissions, respectively, for the MLR analysis of the 21-hour period. Solving for the coefficients with multiple regression analysis, we obtained the following relationship:

$$[NO_x] = 1.46 \times [Se] + 0.23 \times [Ni] - 0.54 \times [EC] + 8.51 \qquad (2.18)$$

where concentrations of Se and Ni are in ng m^{-3}, NO_x in ppb, and EC in μg m^{-3}. The regression equation had a correlation coefficient of 0.699 ($p < 0.001$) and the standard deviation of the residuals was ± 2.96 ppb.

From Equation 2.18, we found that a residual of about 9 ppb of NO_x was not related to emissions from the three modeled sources. This was significant considering the average NO_x concentration during the study period was only 17 ppb. This residual was probably due to the contributions from industrial emissions other than the coal- and oil-fired power plants that were not considered. The remaining 8 ppb of NO_x was split as follows: 98.0 ± 19.6 % from Se source (i.e., CFPP) and 6.6 ± 20.4 % from Ni source (i.e., OFPP). These rough estimates by MLR provided a useful and important constraint to χ/Q predictions made with the TGPM-driven PDRM-III.

2.4.2 PMF Source Apportionment

Herein the data were best fit with a six-factor PMF solution, identified as follows: coal-fired power plant, oil-fired power plant, traffic, area comprehensive industrial, road dust, and an unknown Fe factor. Their emission abundance profiles and time-series contributions to $PM_{2.5}$ are shown in Figure 2.6 and 2.7, respectively. The assignments of sources to the six factors are described immediately below.

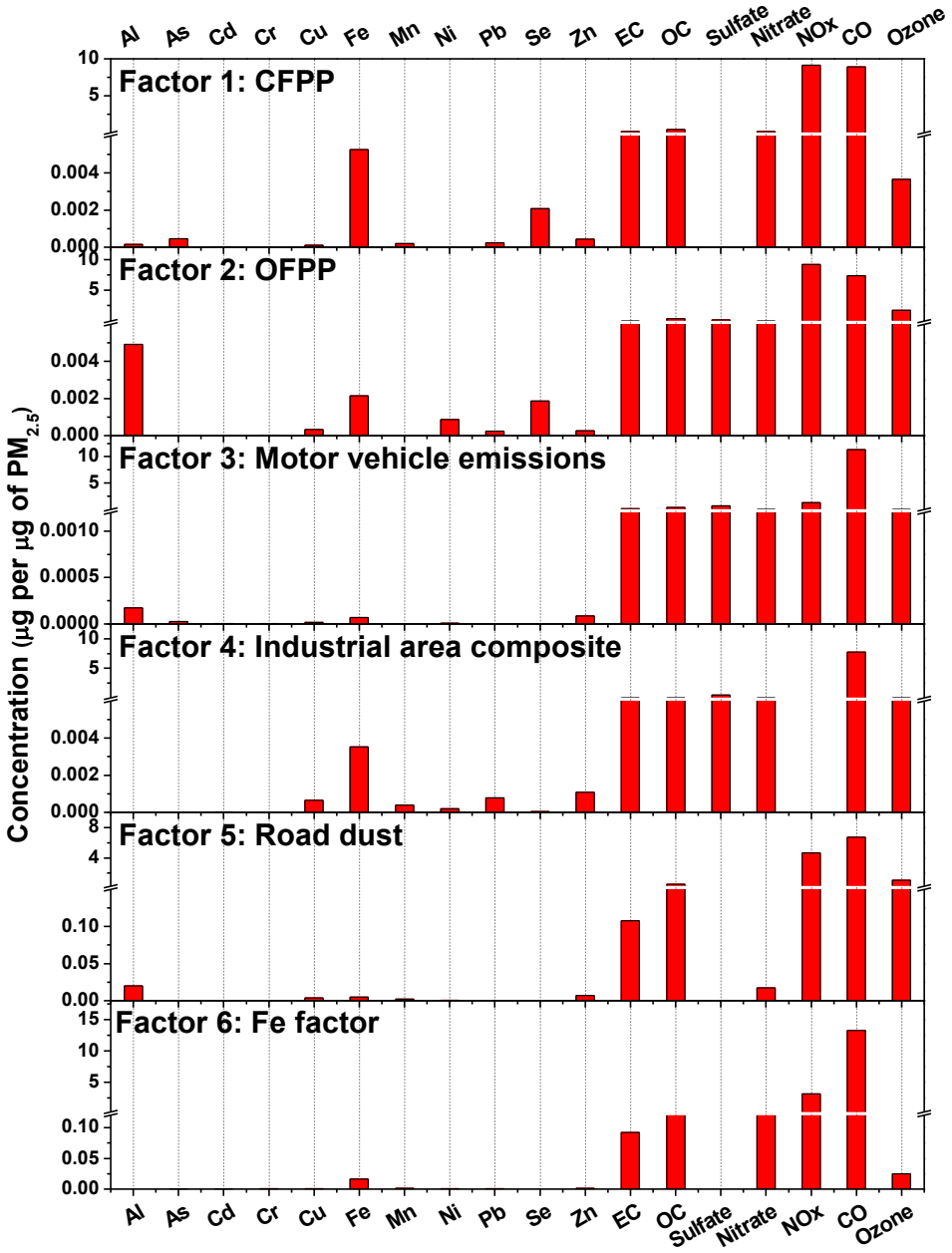

Figure 2.6 PMF resolved factor profiles.

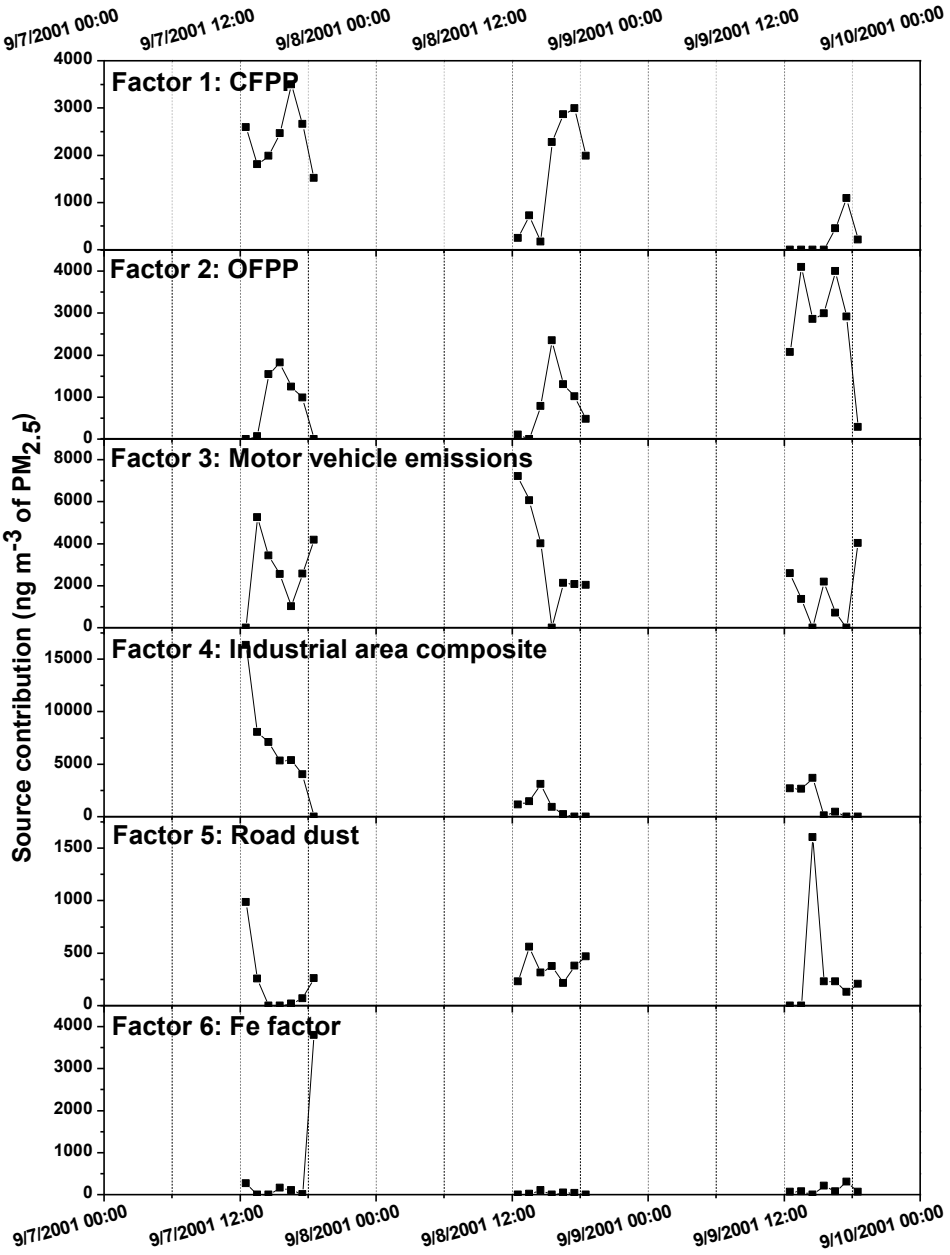

Figure 2.7 Time series of source contributions.

Factor 1 was attributed to coal-fired boilers. As noted above, Se and As have been widely used as tracers for coal burning (Ragaini and Ondov 1977, Ondov, Ragaini and Biermann 1979, Suarez and Ondov 2002). The coal-fired power plant was identified by its high abundances of Se, As, EC and NO_x, and low abundance of Ni. The abundances of Se and As for this factor are 0.21 % and 0.046 %, respectively,

and that of Ni was less than 0.01 %. The Se abundance is comparable with the composite CFPP profile (i.e., 0.24 ± 0.18 %) by Watson (Watson, Chow and Houck 2001) but much larger than that of 21 coal boilers (i.e., 0.0024 ± 0.0017 %) in Sheffield and Gordon's study (Sheffield and Gordon 1986). The As abundance falls into the range of 0.004 ~ 0.05 % for Sheffield and Gordon (Sheffield and Gordon 1986). The OC/TC ratio is 0.72, compared to 0.56-0.89 from Watson (Watson et al. 2001). Sulfate was often attributed to coal combustion sources as a result of gradual transformation from SO_2. However, very low sulfate concentrations (i.e., $SO_4^{2-}/Se <$ 100) were attributed to this coal-combustion factor, probably because the distance between the Brandon Shores and the receptor site was only 16 km and the emissions from the former were still fresh without sufficient aging at plume arrivals (Tuncel et al. 1985, Tuncel et al. 1987) as wind blew directly towards the supersite.

Factor 2 was recognized as the oil-fired power plant by the presence of both Ni and Se. In the absence of refineries and smelters, Ni is a unique tracer for oil combustion (Osan et al. 2000, Suarez and Ondov 2002) and the concurrent observation of Se in this factor is consistent with the mixed fuel types (oil, NG, and coal) at the Wagner Station. Moreover, the coal- and oil-fired power plants accounted for 98 % of the total emission of selenium, which is consistent with previous findings that the Brandon Shores and Wagner Station complex was the major source of atmospheric selenium in the Baltimore area (Suarez and Ondov 2002). And the OC/TC ratio is 0.87 for this factor, slightly higher than that of the CFPP factor.

The third factor was marked by high abundances of EC and NO_x and attributed to motor vehicle emissions. The presence of traffic-related metallic tracers in this factor

including Zn, which is used in motor oil additives (Ondov, Zoller and Gordon 1982b), Fe, Al, and Cu, which could be attributed to brake linings and cylinder wear (Oliveira et al. 2010), supported the assignment. This factor was the largest $PM_{2.5}$ contributor ($\geq$ 40 % of the total $PM_{2.5}$) in this case, which is not a surprise as the supersite was located adjacent to heavily trafficed downtown area and only 6 km away from the toll booths of the I-95 and I-895 traffic tunnels. The OC/TC ratio of 0.78 for this factor is on the high end of those reported by Watson (Watson et al. 2001) for vehicle exhaust samples (OC/TC = 0.58 ± 0.15), However, this OC/TC ratio is in excellent agreement with that (OC/TC = 0.77 ± 0.21) of the motor vehicle profile obtained from another study in November 2002 in Baltimore (refer to Section 4.4.3 in Chapter 4).

The fourth factor showed a high abundance of sulfate (i.e., 48 % of the $PM_{2.5}$ mass), suggesting a role of secondary aerosol. Meanwhile, this factor also showed high percentages of transition metals (i.e., Fe: 0.35 %; Zn: 0.11 %; Pb: 0.8 %; Cu: 0.6 %; Mn: 0.4 %; and Ni: 0.2 %), suggesting an industrial nature for this factor. By further examining the time series source contributions (Figure 2.7), it was revealed that its contribution on September 7th was by far greater (> 5 fold) than those on the other two days. This pattern is probably due to the fact that September 8th and 9th were weekend days when many industries were under maintenance mode. During the study periods, the industrial area along Curtis Bay was aligned with the prevailing wind direction, so that emissions from Stericycle, Chemetals, W.R. Grace, Condea Vista, and/or the Patapsco Waste Water Treatment Plant could be observed. In particular, Stericycle Inc., the largest medical waste treatment company in the United States, is capable of incinerating over 300,000 tons of waste annually. This primary

consideration agreed with the large abundances of Pb and Zn (Singh and Prakash 2007) but could not explain the high concentrations of Fe and Mn. Hence it is likely that this industrial area factor contained contributions from other nearby facilities (e.g., Mn and Fe from Chemetals Inc., and Zn from W. R. Grace Co.) and this factor was eventually named as an industrial area composite. The OC/TC ratio for this factor is 0.62, which is the smallest among all factors.

Factor 5 contained substantial quantities of Al (2.0 %), Zn (0.7 %), Fe (0.5 %), Cu (0.36 %), and Mn (0.21 %), indicative of road dust emissions as city road dust profiles were often characterized by high levels (i.e., 0.1 to 10 %) of Fe, Cu, Zn and Mn (Adachi and Tainosho 2004, Lough et al. 2005, Ning et al. 2008). Cu and Zn are well known tracers for braking activities (e.g., wearing of brake pads or tires), and Al_2O_3, K, and Mn are representatives of road pavement erosion and re-suspension (Amato et al. 2009). In addition, high OC/TC fractions (> 0.8) were often observed for urban road dust (Watson and Chow 2001), as found in the profile of this factor (OC/TC = 0.88).

As shown in Figure 2.7, factor 6 consisted of a sudden outburst of Fe, Cr, and Mn without an elevated $PM_{2.5}$ level during the short period from 1800 to 1900 LT on September 7th, 2001. This unknown Cr-containing Fe factor could be due to a certain fugitive event nearby the receptor site, or possibly because of contamination by stainless steel during the sample analysis. The latter was suspected as such excursions of Fe, Cr, and Mn due to contamination had been observed before during the Supersite project (Park et al. 2005b, Beachley 2009) and the fingerprint compositions (i.e., Cr/Fe = 0.025, and Mn/Fe = 0.092) are consistent with those average

compositions (i.e., Cr/Fe = 0.028, and Mn/Fe = 0.074) reported for stainless steel (MatWeb 2012).

It is noteworthy that there was no separate secondary aerosol factor resolved in this PMF analysis. Besides, high contents of CO, ozone, and EC were found in all factors. These suggested that secondary aerosol and probably motor vehicle emissions as well were intermingled with all the factors.

As shown in Figure 2.8, the reconstructed $PM_{2.5}$ concentrations were well correlated ($r^2 = 0.974$) with the measured concentrations. In contrast, PMF-predicted NO_x concentrations were fairly well correlated ($r^2 = 0.858$) with those observed and the relative errors in the NO_x predictions ranged from -15.1 ~ +34.4 % with a mean absolute value of 9.6 %. The predicted mass of other species generally fit well with the measured values: eight of the 11 SEAS metals (As, Cr, Cu, Fe, Mn, Pb, Se, and Zn) showed $r^2 > 0.90$ as well as EC and sulfate. Poorer predictions were found for Cd ($r^2 = 0.789$), OC ($r^2 = 0.732$), and nitrate ($r^2 = 0.513$).

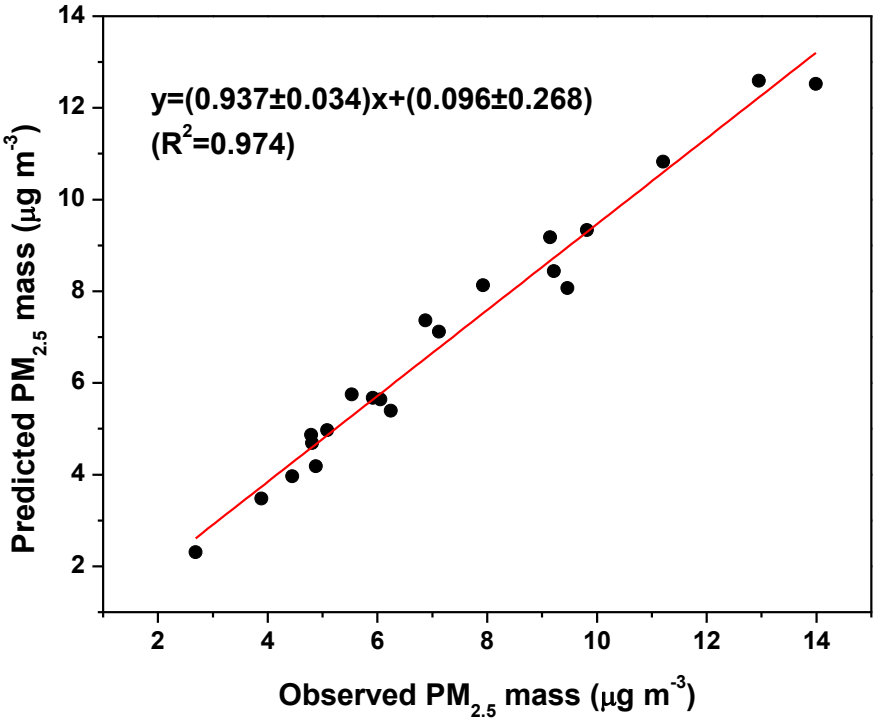

Figure 2.8 Comparison of PMF predicted and observed $PM_{2.5}$ concentrations.

As shown in Figure 2.9, motor vehicle emissions and industrial area composite were two largest contributors to ambient $PM_{2.5}$ mass (40.3 % and 27.1 %, respectively), followed by OFPP and CFPP sources which together contributed 28.1 % of the $PM_{2.5}$ mass. In contrast, OFPP and CFPP contributed 42.5 % and 40.2 %, respectively, to ambient NO_x, which were four times greater than that from the third largest contributor of NO_x, motor vehicle emission (10.3 %). The summed NO_x contribution from OFPP and CFPP sources by the PMF modeling was nearly twice as much as that predicted by MLR (i.e., ~ 50 % of NO_x was from the power plants during the study period according to MLR). Moreover, unlike the MLR results in which NO_x contributions from CFPP were 3~15 times greater than that from OFPP, the PMF results showed nearly equal contributions of NO_x from these two different types of power plants. This difference could be partially due to the reason that the

CFPP and OFPP units (i.e., BS and WS) were too close to each other and PMF did not well resolve these covariant emissions. However, the PMF allocation of NO_x was still adopted in the PDRM modeling for two considerations. First, PDRM would re-allocate NO_x contributions based on the different plume dispersion factors of emission sources, which could remedy possible cross-contamination of source contributions. Second, a large average residual of NO_x was left unexplained in the MLR results.

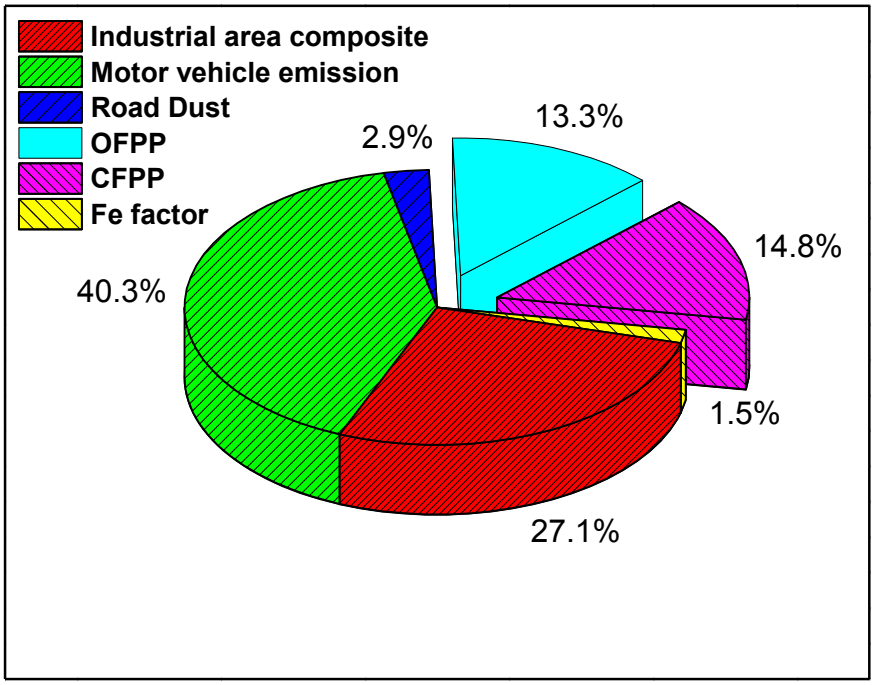

Figure 2.9 $PM_{2.5}$ mass allocation by PMF resolved sources.

The profiles of OFPP and CFPP resolved by PMF exhibited unexpected similarity in Pb, Se, Zn, TC, and NO_x, except for the remarkable disparity between them in Ni (Figure 2.6). As CEM data showed that only one third of NO_x emissions at the Wagner Station were from coal-fuel stacks during the study period, there was no other plausible interpretation for this finding but that those factors were compromised

by cross contamination. Ratios between gaseous emissions (i.e., NO_x and CO) and particle emissions (i.e., $PM_{2.5}$) were often variable in the presence of multiple effective sources (Morawska and Zhang 2002). However, an excellent correlation (r^2 = 0.936) between NO_x and $PM_{2.5}$ was revealed using the summed contributions from OFPP and CFPP factors apportioned by PMF, as shown in Figure 2.10. This consistency suggested that the total contributions from these two sources were accurately extracted by PMF, and provided confidence that these PMF results could well seed the PDRM solution. Simple linear regression of the combined contributions of NO_x from OFPP and CFPP sources with those of individual species found that the combined NO_x were highly correlated with Se (r^2 = 0.992, $p < 0.001$), and the regression intercept (i.e., 2.51 ppb of NO_x) were insignificant with respect to ambient concentrations (i.e., an average of 14.19 ppb of NO_x), indicating that there was little influence from sources other than these power plants. Meanwhile, although poor correlations between NO_x and As (coal combustion tracer) or Ni (oil combustion tracer) were found (i.e., r^2 = 0.264 for As, and r^2 = 0.402 for Ni), an MLR analysis of $PM_{2.5}$ against Ni and As showed a remarkable correlation (r^2 = 0.999, $p < 0.001$; the ratio of fitting slopes Ni/As = 0.45). This also indicated a non-collinearity in the emission profiles of the two power plants. With known NO_x emission rates attributed to coal and oil combustion from CEM, a linear regression as described above (Equation 2.12 to 2.14) was used to separate the profiles for different coal- and oil-combustion units in the Wagner Station which were then used to seed the PDRM modeling. The resolved profiles of individual units are shown in Figure 2.11.

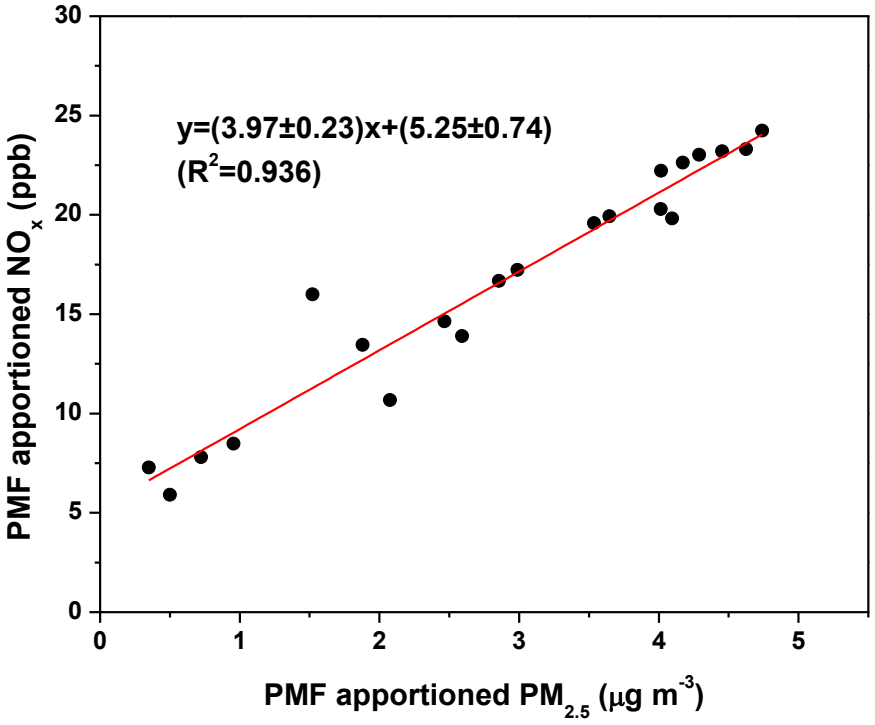

Figure 2.10 NO_x concentrations versus $PM_{2.5}$ concentrations from the total contributions of CFPP and OFPP apportioned by PMF.

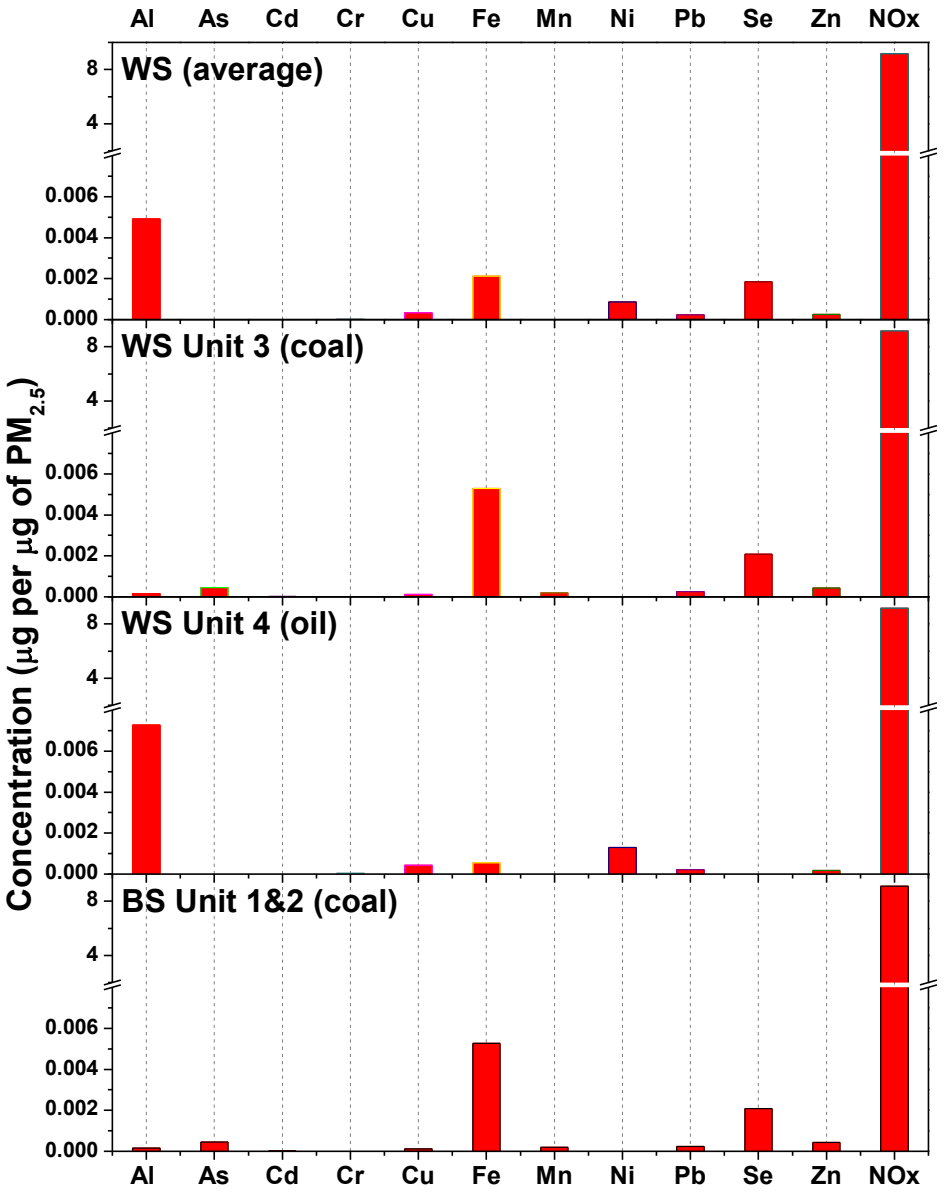

Figure 2.11 Stack emission profiles resolved by linear regression.

2.4.3 Trajectory Simulations

The plume forward trajectories from the different stacks in the power plants at 10-minute resolution are shown in Figure 2.12. Temporal profiles of the TGPM-derived dispersion factor, $(\chi/Q)^{TGPM}$s calculated as described in Section 2.3.4 are shown in Figure 2.13.

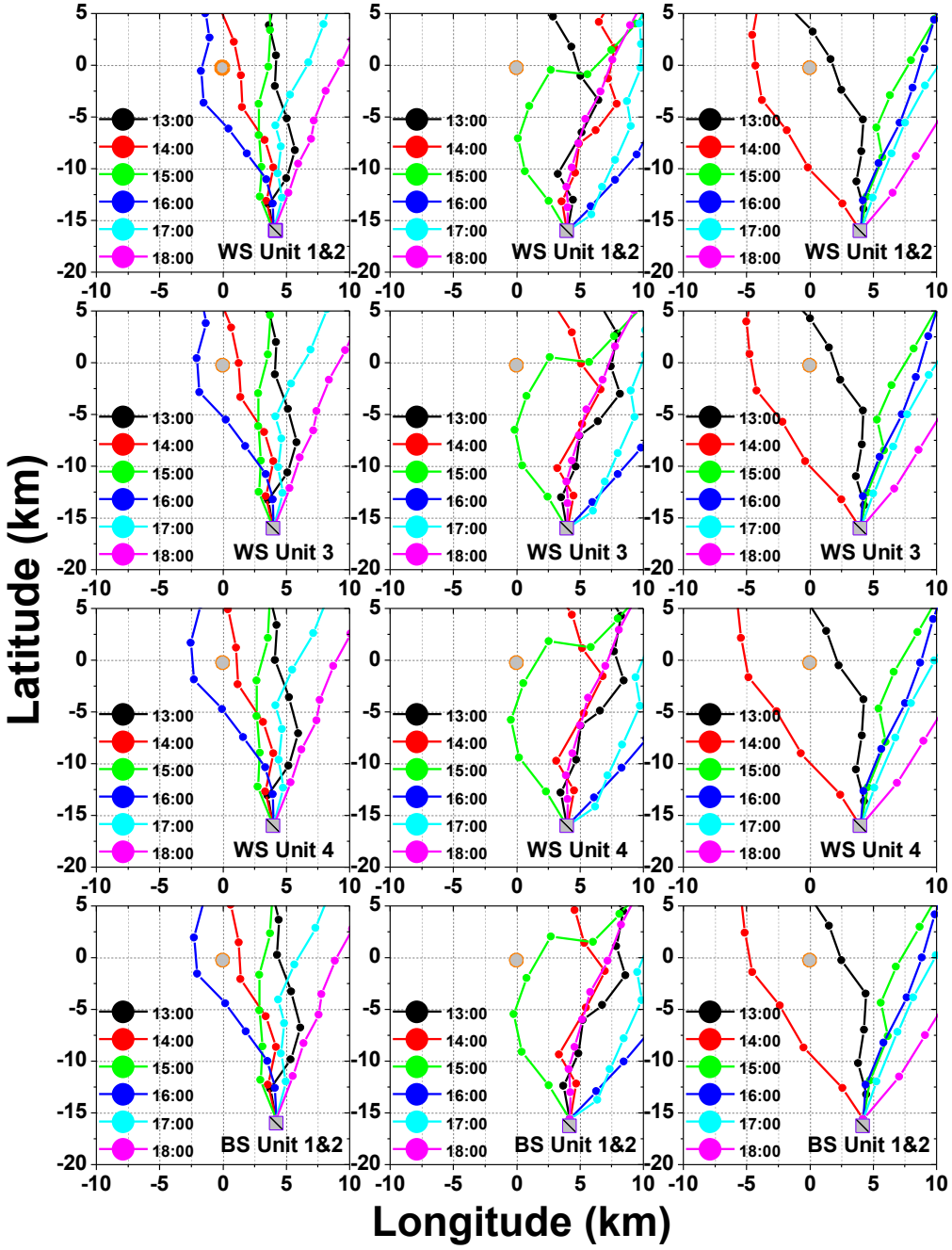

Figure 2.12 Plume forward trajectories from 1300 LT to 1800 LT on September 7th (left panels), 8th (central panels), and 9th (right panels), 2001 (the grey squares represent the plume sources and the grey cycles at the origins represent the Clifton Park supersite).

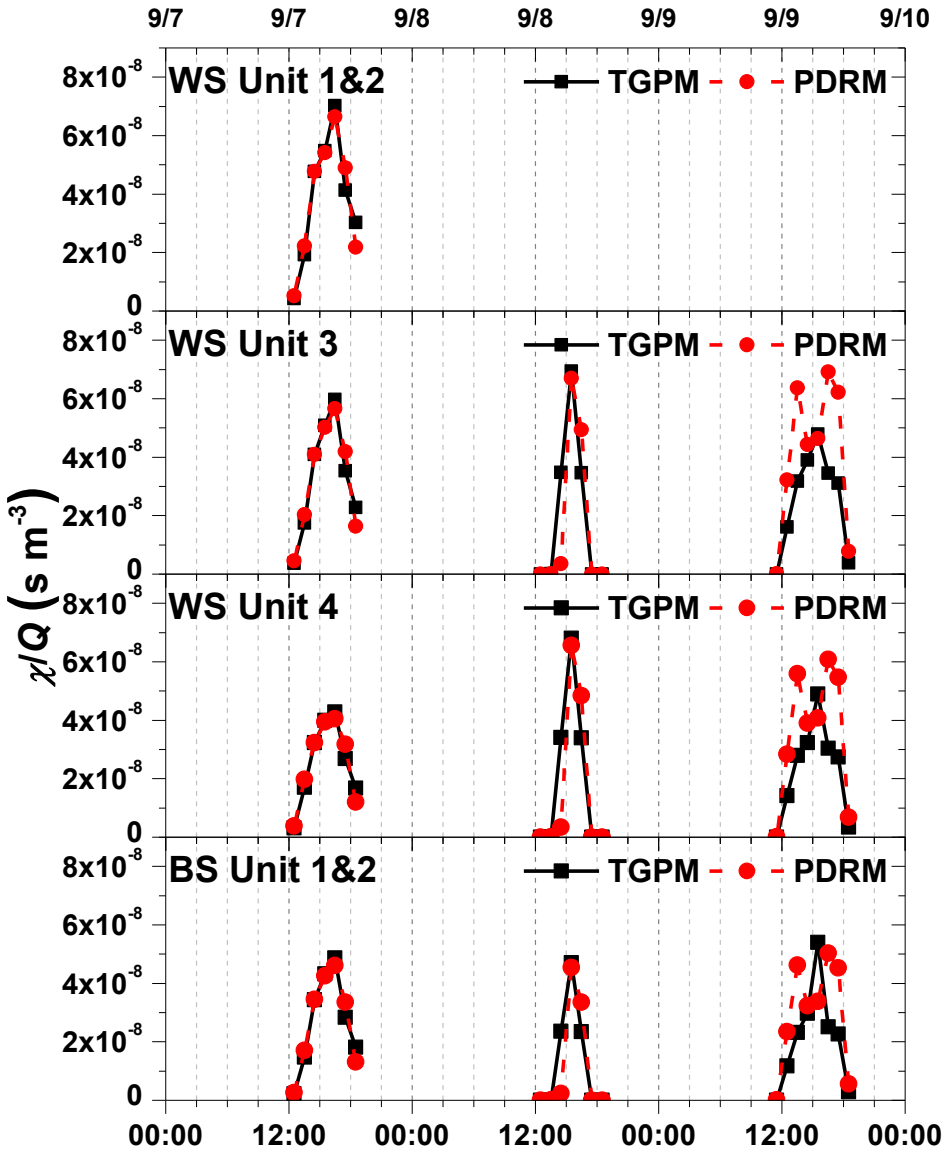

Figure 2.13 TGPM (solid black lines) and PDRM-derived (dashed red lines) dispersion factors (χ/Q) for the four different generating units in the Wagner Station and Brandon Shores power plants from September 7th through 9th, 2001.

In the afternoon of September 7th, the plume trajectories originating from the units in the power plant complex began approaching the receptor site from the easterly direction after 1300 LT. The plumes then departed towards the east after nearly crossing the receptor site at around 1500 LT, and then turned back to approach the receptor site again after 1530 LT. The plumes swept across the receptor site at around

1640 LT but their trajectories immediately altered direction and swept across the receptor site again. At 1800 LT, the plumes almost retreated to their initial trajectory positions at 1400 LT. And the plume trajectories were completely off the receptor site after 1900 LT. As a result, the TGPM predicted hourly χ/Qs of the stack units peaked at 1630 LT with a shoulder at 1530 LT (Figure 2.13). Note that WS Unit 4 showed the smallest value of maximum χ/Q among all WS units because of its largest effective stack height.

In the afternoon of September 8th, the plume centerlines again swung back and forth but were substantially farther (> 4 km) from the receptor site except during the period from 1500 to 1600 LT when they suddenly approached the receptor site before quickly moving away. Hence the TGPM-predicted temporal profile of χ/Qs showed a narrower peak width compared with that in the previous afternoon. It is noteworthy that the centerline of plume trajectories never crossed the receptor site in that afternoon, although a Gaussian-shape χ/Q profile was predicted. As a result, the excursions of Se and Ni in this afternoon should have been and were, indeed, less significant than those in the other two afternoons.

The evolution of plume trajectories on September 9th was to some extent similar to that on September 7th. The plume trajectories swept across the receptor site at around 1400 LT but swept back again at around 1500 LT. Note that the trajectories shown in Figure 2.12 only represent those originated at whole hours and that the 10-minute trajectories actually swept back and forth multiple times in the afternoon of September 9th due to the large wind variations during that period. However, this fine structure could not be detected in the ambient concentrations. As a result, the PDRM

tuned χ/Q profiles for September 9th contained a bimodal distribution rather than the TGPM-predicted shoulders on a single central peak as shown in Figure 2.13.

Given their close proximity as well as similar stack heights, gas temperature, and velocities, it is not a surprise that those coal-fired and oil-fired units at the two power plants showed similar dispersion profiles (i.e., the maximum χ/Q values for these units were all within the range of 4~7 × 10^{-8} s m^{-3}), as shown in Figure 2.13. The TGPM-predicted χ/Q values generally remained at a quite similar level (i.e., ~10^{-8} s m^{-3}) on these different days. The maximum plume dispersion factor (χ/Q^{PDRM} = 7.0×10^{-8} s m^{-3}) corresponded to the maximum NO_x of 23 ppb which occurred at 1600 LT on September 7th 2001. Excellent agreement between χ/Q^{TGPM}s and χ/Q^{PDRM}s was found for all the units except on September 9th, when the temporal profile of χ/Q^{PDRM}s resembled the time series ambient NO_x concentrations by showing a similar bimodal pattern but that of χ/Q^{TGPM}s did not.

2.4.4 PDRM Results

In our initial PDRM trial, the PMF source profiles were not applied as constraints and loose bound conditions of metal emission rates (i.e., LB: 10^{-4}; UB: 5×10^{4} g/s) were applied as done in Park's study. The resulted emission rates and source contributions are listed in Tables 2.5 and 2.6, respectively. Later PMF constraints were applied and emission rates of metals and source contributions were recalculated, (Tables 2.7 and 2.8). In the PMF-seeded PDRM solution, the predicted NO_x contributions of individual sources (Table 2.8) differed insignificantly (within 5 %) from those corresponding contributions without PMF constraining (Table 2.6).

However, apportionment of metals was quite different between the constrained and unconstrained solutions.

Note that the PDRM-predicted emission rates of NO_x were nearly identical with or without applying the PMF constraints, as those constraints had little influence on the tracer gas. Moreover, the PDRM-predicted emission rates of NO_x were in excellent agreement with the CEM data (i.e., the average difference was < 8 %), as shown in Tables 2.5 and 2.7, greatly adding our confidence in the modeling performance.

The PDRM predictions without PMF constraining turned out to be a blend of source emissions, because the Levenberg-Marquardt algorithm (LMA) used by the nonlinear least squares solver in PDRM only seeks a local minimum of the FUN function which relies on the constrained range of emission rates. As is evident in Table 2.5, substantial collinearity in predicted emission profiles was evident for different stacks (i.e., the Ni/Se ratios were found between 0.2 and 0.5 for all units at these plants), in contradiction with their different fuel types. Consequently, inexplicable contributions (e.g., apparently over-estimated Ni contributions from the two coal-fired units, the WS Unit 3 and the BS Unit 1&2) were predicted (see Table 2.6). In contrast, these signature tracers (Ni and Se) were well attributed in the PMF-seeded PDRM solution (Table 2.8). For example, the WS oil-fired unit (Unit 4) accounted for 28 ~ 46 % of Ni contributions in the unconstrained solution (Table 2.6) while it was 94 ~ 100 % of Ni contributions in the constrained solution (Table 2.8). The predicted Se contributions were from 28 to 42 % for the WS Unit 3, and 11 to 28 % for the BS units without PMF constraining. In contrast, the WS Unit 3 (coal-fired unit) was the major Se contributor (93 %) on September 7th while the BS units

were dominantly responsible (81 ~ 94 %) on the other two days, according to the PMF-seeded solution. Overall, these comparisons suggested that the PMF-seeded PDRM approach could better explain the observations as it considers the difference of sources in both dispersion factors (χ/Q) and abundance profiles simultaneously.

Table 2.5 Predicted emission rates of NO_x and metal species without PMF constraints.[1]

Species [2]	WS Unit 1&2	WS Unit 3	WS Unit 4	BS Unit 1&2
NO_x (observed) [3]	86.7	126 ± 1	218 ± 10	428 ± 112
NO_x (predicted) [4]	124	116 ± 25	224 ± 41	424 ± 57
Al	7.1	55 ± 51	70 ± 29	73 ± 42
As	7. 9	3.5 ± 2.1	5.6 ± 4.4	6.1 ± 4.6
Cd	1.1	0.5 ± 0.5	0.5 ± 0.6	3.5 ± 3.8
Cr	1.1	0.6 ± 0.4	0.7 ± 0.5	3.7 ± 3.7
Cu	3.1	4.8 ± 1.8	5.4 ± 1.6	7.6 ± 2.2
Fe	111	42 ± 29	123 ± 81	36 ± 12
Mn	2.6	1.5 ± 1.1	2.1 ± 1.5	4.8 ± 3.8
Ni	1.0	9.9 ± 7.7	12 ± 5	12 ± 4
Pb	4.2	5.1 ± 0.2	6.7 ± 1.0	7.5 ± 2.0
Se	13.6	43 ± 8	60 ± 27	29 ± 10
Zn	7.0	6.7 ± 1.1	8.3 ± 2.4	7.7 ± 2.4

[1] Units are in g s^{-1} for NO_x and mg s^{-1} for SEAS metals.

[2] Modeling period from 1200 to 1900 LT.

[3] Average continuous emission monitor data from the stacks (1200~1900 LT).

[4] Predicted NO_x emission rates when all four sources identically constrained to range 0.5~2.0.

Table 2.6 Predicted contribution averages (% of contribution) attributed to individual generating units without PMF constraints.[1]

	09/07/2001				09/09/2001			09/09/2001		
	WS Unit 1&2	WS Unit 3	WS Unit 4	BS Unit 1&2	WS Unit 3	WS Unit 4	BS Unit 1&2	WS Unit 3	WS Unit 4	BS Unit 1&2
NO_x	20.1 ± 6.1	20.3 ± 2.0	28.6 ± 1.9	31.1 ± 3.7	17.3 ± 0.4	36.8 ± 3.9	45.9 ± 1.3	13.1 ± 3.1	20.6 ± 2.6	66.3 ± 6.4
Al	6.9 ± 2.1	0.7 ± 0.1	39.3 ± 2.6	53.2 ± 6.2	41.9 ± 1.0	45.1 ± 4.8	12.9 ± 0.4	42.2 ± 10	30.1 ± 3.9	27.7 ± 2.7
As	36.5 ± 11	24.0 ± 2.4	39.5 ± 2.6	0.1 ± 0.0	22.8 ± 0.5	24.5 ± 2.6	52.7 ± 1.5	24.7 ± 5.9	28.3 ± 3.6	47.1 ± 4.5
Cd	28.6 ± 8.7	27.2 ± 2.7	26.9 ± 1.7	17.3 ± 2.0	1.7 ± 0.0	1.8 ± 0.2	96.5 ± 2.8	15.1 ± 3.6	23.9 ± 3.1	60.9 ± 5.9
Cr	28.7 ± 8.7	27.3 ± 2.8	26.8 ± 1.7	17.2 ± 2.0	2.1 ± 0.1	2.4 ± 0.3	95.5 ± 2.8	21.5 ± 5.1	27.3 ± 3.5	51.2 ± 4.9
Cu	25.1 ± 7.6	26.1 ± 2.6	29.7 ± 1.9	19.1 ± 2.2	22.1 ± 0.5	23.1 ± 2.5	54.8 ± 1.6	36.4 ± 8.7	30.0 ± 3.8	33.6 ± 3.2
Fe	36.7 ± 11	0.3 ± 0.0	57.6 ± 3.7	5.4 ± 0.6	39.8 ± 1.0	47.4 ± 5.0	12.8 ± 0.4	42.1 ± 10	30.1 ± 3.9	27.8 ± 2.7
Mn	26.3 ± 8.0	25.4 ± 2.6	29.6 ± 1.9	18.7 ± 2.2	13.1 ± 0.3	15.5 ± 1.6	71.4 ± 2.1	20.3 ± 4.9	26.8 ± 3.4	52.9 ± 5.1
Ni	22.9 ± 7.0	27.3 ± 2.8	28.3 ± 1.8	21.5 ± 2.5	15.4 ± 0.4	45.5 ± 4.8	39.1 ± 1.1	40.4 ± 9.7	30.1 ± 3.9	29.5 ± 2.8
Pb	26.2 ± 8.0	26.8 ± 2.7	28.6 ± 1.9	18.4 ± 2.2	0.1 ± 0.0	47.3 ± 5.0	52.6 ± 1.5	34.8 ± 8.3	29.8 ± 3.8	35.4 ± 3.4
Se	9.7 ± 3.0	28.9 ± 2.9	50.9 ± 3.3	10.6 ± 1.2	39.3 ± 0.9	43.6 ± 4.6	17.2 ± 0.5	41.9 ± 10	30.1 ± 3.9	28.0 ± 2.7
Zn	27.7 ± 8.4	28.5 ± 2.9	34.2 ± 2.2	9.7 ± 1.1	26.4 ± 0.6	30.0 ± 3.2	43.6 ± 1.3	35.8 ± 8.6	29.9 ± 3.8	34.3 ± 3.3

[1] Modeling period from 1200 to 1900 LT on each day.

Table 2.7 Predicted emission rates of NO_x and metal species with PMF constraints.[1]

Species [2]	WS Unit 1&2	WS Unit 3	WS Unit 4	BS Unit 1&2
NO_x (observed) [3]	86.7	126 ± 1	218 ± 10	428 ± 112
NO_x (predicted) [4]	124	116 ± 25	224 ± 41	424 ± 57
Al	6.5	1.3 ± 1.5	165 ± 102	49 ± 21
As	*	8.8 ± 9.2	*	41 ± 55
Cd	0.4	0.1 ± 0.1	*	0.3 ± 0.2
Cr	*	*	1.0 ± 0.5	*
Cu	0.4	0.7 ± 0.7	13 ± 5	7.0 ± 4.7
Fe	108	35 ± 29	66 ± 57	795 ± 988
Mn	*	4.0 ± 3.9	*	12 ± 15
Ni	1.2	*	34 ± 18	*
Pb	0.3	1.0 ± 0.8	12 ± 9	16 ± 14
Se	2.5	67 ± 51	*	335 ± 376
Zn	2.5	1.3 ± 1.0	15 ± 14	37 ± 39

[1] Units are in g s^{-1} for NO_x and mg s^{-1} for SEAS metals.

[2] Modeling period from 1200 to 1900 LT.

[3] Average continuous emission monitor data from the stacks (1200 ~ 1900 LT).

[4] Predicted NO_x emission rates when all four sources identically constrained to range 0.5 ~ 2.0.

* < 0.1 mg s^{-1}.

Table 2.8 Predicted contribution averages (% of contribution) attributed to individual generating units with PMF constraints.[1]

	09/07/2001				09/09/2001			09/09/2001		
	WS Unit 1&2	WS Unit 3	WS Unit 4	BS Unit 1&2	WS Unit 3	WS Unit 4	BS Unit 1&2	WS Unit 3	WS Unit 4	BS Unit 1&2
NO_x	18.2 ± 5.5	18.2 ± 1.8	23.7 ± 1.5	39.9 ± 4.7	18.9 ± 0.5	40.5 ± 4.3	40.6 ± 1.2	14.0 ± 3.3	24.6 ± 3.2	61.3 ± 5.9
Al	5.3 ± 1.6	0.2 ± 0.0	56.5 ± 3.7	38.0 ± 4.5	0.2 ± 0.0	66.0 ± 7.0	33.9 ± 1.0	1.2 ± 0.3	94 ± 12	4.8 ± 0.5
As	0.0 ± 0.0	93.3 ± 9.4	0.0 ± 0.0	6.7 ± 0.8	5.1 ± 0.1	0.0 ± 0.0	94.9 ± 2.8	18.6 ± 4.4	0.0 ± 0.0	81.4 ± 7.8
Cd	71.1 ± 22	22.0 ± 2.2	0.3 ± 0.0	6.6 ± 0.8	36.4 ± 0.9	0.1 ± 0.0	63.5 ± 1.9	13.5 ± 3.2	0.0 ± 0.0	86.5 ± 8.3
Cr	5.7 ± 1.7	0.0 ± 0.0	93.9 ± 6.1	0.5 ± 0.1	0.1 ± 0.0	100 ± 11	0.0 ± 0.0	0.0 ± 0.0	100 ± 13	0.1 ± 0.0
Cu	3.2 ± 1.0	1.1 ± 0.1	93.2 ± 6.1	2.4 ± 0.3	1.1 ± 0.0	46.8 ± 5.0	52.1 ± 1.5	8.7 ± 2.1	57.4 ± 7.4	33.9 ± 3.3
Fe	38.1 ± 12	22.6 ± 2.3	33.8 ± 2.2	5.5 ± 0.6	0.4 ± 0.0	3.2 ± 0.3	96.3 ± 2.8	15.3 ± 3.7	3.1 ± 0.4	81.6 ± 7.9
Mn	0.0 ± 0.0	93.2 ± 9.4	0.0 ± 0.0	6.7 ± 0.8	9.8 ± 0.2	0.0 ± 0.0	90.1 ± 2.6	16.8 ± 4.0	0.0 ± 0.0	83.2 ± 8.0
Ni	5.7 ± 1.7	0.0 ± 0.0	94.3 ± 6.1	0.0 ± 0.0	0.0 ± 0.0	100 ± 11	0.0 ± 0.0	0.0 ± 0.0	100 ± 13	0.0 ± 0.0
Pb	1.7 ± 0.5	1.8 ± 0.2	92.4 ± 6.0	4.0 ± 0.5	1.1 ± 0.0	22.5 ± 2.4	76.4 ± 2.2	14.2 ± 3.4	22.8 ± 2.9	63.0 ± 6.1
Se	1.9 ± 0.6	93.3 ± 9.4	0.0 ± 0.0	4.8 ± 0.6	6.2 ± 0.1	0.0 ± 0.0	93.8 ± 2.7	19.4 ± 4.6	0.0 ± 0.0	80.6 ± 7.8
Zn	9.0 ± 2.7	2.1 ± 0.2	84.3 ± 5.5	4.6 ± 0.5	0.8 ± 0.0	12.0 ± 1.3	87.3 ± 2.6	15.4 ± 3.7	11.6 ± 1.5	73.0 ± 7.0

[1] Modeling period from 1200 to 1900 LT on each day.

The emission profiles obtained by PMF and PMF-seeded PDRM are compared in Figure 2.14. The PDRM-derived profiles of the coal-fired units in both plants generally agreed (e.g., comparable abundances of Se) with the CFPP profile determined by PMF, except that PDRM attributed greater Al and Cu contributions to the BS plant than to the coal-fired units in the WS plant. In contrast, the PDRM-derived profile of the oil-fired units in the WS plant (i.e., WS Unit 3) exhibited a much lower presence of Se, compared with the OFPP profile determined by PMF. That is, oil-fired units were distinguished from coal-fired ones by their large Ni/Se ratios.

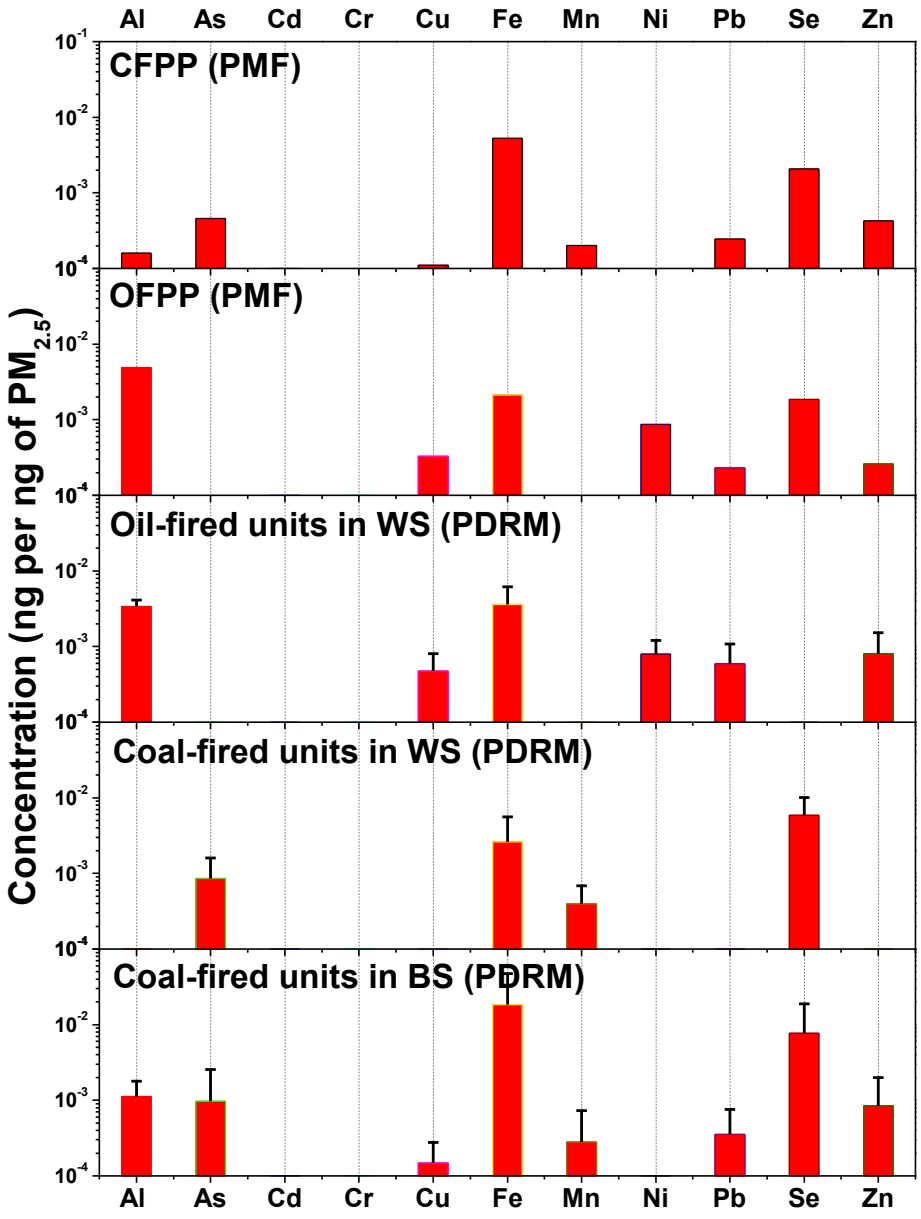

Figure 2.14 Comparison of resolved source profiles of the utility plants by PMF and PMF-seeded PDRM.

The emission rates of NO_x and metal species predicted for the different units were summed (Table 2.9) for comparisons with the total CEM-derived and total annual emissions according to the NEI or TRI, in which the two plants were treated as one. Despite the excellent agreement with the CEM data (751 ± 21 g s^{-1}), the total

emission rates of NO_x (806 ± 61 g s^{-1}) predicted by PMF-constrained PDRM was 27 % below the annual average (1100 g s^{-1}) of this plant complex reported by NEI. This is because the study period was during the weekend when the facilities were not in full operation (e.g., WS Units 1&2 were in hibernation on September 8th and 9th). TRI data for Al, Cd, and Fe were not available and thus no comparison was made for these species. Six of the other eight metals (As, Cu, Mn, Pb, Se, and Zn) agreed well with the expected emission rates (e.g., within a factor of 2 (Fa2) with respect to the corresponding TRI annual average: $0.5ER^{TRI} < ER^{PDRM} < 2ER^{TRI}$) in the PMF-constrained PDRM solution. Two oil-combustion tracers, Ni and Cr, were the species with predicted emission rate far below the TRI annual average (< 20 %). This again could be partially attributed to the fact that the WS Unit 1 (oil-fired) was not in operation during two of the three days of study.

Table 2.9 Predicted total emission rates (unit: g s^{-1} for NO_x, and mg s^{-1} for metals) of NO_x and metal species for the Wagner Station and Brandon Shores complex.[1]

	NO_x	Al	As	Cd	Cr	Cu	Fe	Mn	Ni	Pb	Se	Zn
NEI/TRI average[2]	1100	n.a.	11	n.a.	16	14	n.a.	20	274	17	245	33
Non-PMF constrained (ave ± σ)	806 ± 61 (751 ± 21)[3]	200 ± 96	16 ± 9	5 ± 4	5 ± 3	19 ± 3	237 ± 103	9 ± 6	36 ± 16	19 ± 2	136 ± 42	25 ± 5
PMF-constrained: (ave ± σ)	806 ± 61 (751 ± 21)[3]	217 ± 82	13 ± 8	1 ± 1	1 ± 1	21 ± 2	930 ± 928	16 ± 15	34 ± 18	29 ± 9	403 ± 352	54 ± 33

[1] Modeling period from 1200 to 1900 LT on the days of study.

[2] Annual average emissions based National Emission Inventory (NEI) for NO_x or Toxics Release Inventory (TRI) for metals in 2001.

[3] Number given in parentheses is total emission rate of all stacks by CEM (1200~1900 LT).

The model performance was evaluated in various statistical measures (Table 2.10), including the ratios of predicted and observed values, mean bias (MB), mean normalized bias (MNB), mean fraction bias (MFB), mean absolute gross error (MAGE), mean normalized gross error (MNGE), root mean square error (RMSE), normalized mean square error (NMSE), the fraction of predicted concentrations lying within a factor of 2 of the measured ambient concentrations (Fa2), and the Pearson's correlation coefficients (*r*). According to *Kumar et al.* (Kumar, Luo and Bennett 1993), model performance is deemed acceptable if NMSE ≤ 0.5, $-0.5 \leq$ MFB ≤ 0.5, and Fa2 ≥ 0.8.

Table 2.10 Performance statistics between the observed and predicted concentrations for NO_x and SEAS metals.

	Unit	NO_x[1]	Al	As	Cd	Cr	Cu	Fe	Mn	Ni	Pb	Se	Zn
Observed	ng m^{-3}	25.3	7.80	0.54	0.02	0.04	0.65	9.50	0.23	1.35	0.65	5.32	0.91
Predicted	ng m^{-3}	26.5	7.90	0.49	0.02	0.04	0.64	9.02	0.21	1.37	0.63	5.14	0.88
P/O (avg ± σ)	-	1.02 ± 0.08	0.92 ± 0.06	0.82 ± 0.12	0.63 ± 0.15	0.88 ± 0.07	0.97 ± 0.07	0.87 ± 0.12	0.82 ± 0.12	0.91 ± 0.06	0.93 ± 0.10	0.94 ± 0.10	0.90 ± 0.11
r^2	-	0.91	0.94	0.74	0.52	0.92	0.92	0.78	0.74	0.94	0.86	0.85	0.81
MB[2]	ng m^{-3}	-0.78	-0.15	0.03	0.00	0.00	0.01	0.23	0.01	-0.03	0.00	0.07	0.01
MNB[3]	%	-1	-113	-2848	-202	-237	-7	-10	-1254	-3646	-7	-5	-7
MFB[4]	%	1.4	-25.4	-30.1	-18.3	-35.2	0.4	1.2	-29.9	-33.2	-2.0	0.2	-0.1
MAGE[5]	ng m^{-3}	2.30	1.43	0.21	0.01	0.01	0.10	1.95	0.09	0.25	0.07	0.67	0.14
MNGE[6]	%	11	126	2888	236	250	27	31	1293	3658	16	18	23
RMSE[7]	ng m^{-3}	4.62	1.69	0.28	0.01	0.01	0.12	3.01	0.12	0.30	0.14	1.23	0.24

NMSE[8]	%	2.2	2.5	14.1	25.9	3.6	2.4	6.9	14.0	2.7	3.4	3.8	5.0
Fa2[9]	%	100	82	**53**	**65**	**76**	94	94	**53**	82	94	94	94
r [10]	-	0.96	0.96	0.86	0.67	0.96	0.95	0.86	0.86	0.96	0.91	0.90	0.88

[1] NO_x concentration variables are given in μg m^{-3}.

[2] MB: mean bias ($= \left(\frac{1}{N}\right)\sum_{i=1}^{N}(O_i - P_i)$).

[3] MNB: mean normalized bias ($= \left(\frac{1}{N}\right)\sum_{i=1}^{N}[(O_i - P_i)/O_i]$).

[4] MFB: mean fractional bias ($= \left(\frac{2}{N}\right)\sum_{i=1}^{N}[(O_i - P_i)/(O_i + P_i)]$).

[5] MAGE: mean absolute gross error ($= \left(\frac{1}{N}\right)\sum_{i=1}^{N}|O_i - P_i|$).

[6] MNGE: mean normalized gross error ($= \left(\frac{1}{N}\right)\sum_{i=1}^{N}[|O_i - P_i|/O_i]$).

[7] RMSE: root mean square error ($= \left[\left(\frac{1}{N}\right)\sum_{i=1}^{N}(O_i - P_i)^2\right]^{1/2}$).

[8] NMSE: normalized mean square error ($= \left[\left(\frac{1}{N}\right)\sum_{i=1}^{N}(O_i - P_i)^2\right] / \left[\left(\frac{1}{N}\right)\sum_{i=1}^{N}(O_i \times P_i)\right]$).

[9] Fa2: fractions of the predictions within a factor of 2 of the observed values.

[10] r: Pearson's coefficient of correlation (r).

The ratio of the predicted and observed NO_x concentrations on average was 1.02 ± 0.08. The temporal profile of the predicted NO_x concentrations agreed well with those observed except the period between 1700 and 1900 LT on September 8th. As discussed earlier, interpolated wind data were used for the trajectory simulations during this 2-hour period, which could have resulted inaccurate estimates of $(\chi/Q)^{TGPM}$.

Excellent agreement between the observations and the predictions was achieved for those metals showing temporal concentration profiles similar to that of NO_x (i.e., Al, Cr, Cu, Ni, Pb, Se, and Zn). The average prediction-to-observation ratio was 0.92 ± 0.06 for Al, 0.88 ± 0.07 for Cr, 0.97 ± 0.07 for Cu, 0.87 ± 0.12 for Fe, 0.91 ± 0.06 for Ni, 0.93 ± 0.10 for Pb, 0.94 ± 0.10 for Se, and 0.90 ± 0.11 for Zn, respectively.

Largest deviations were mostly observed during the periods when these species remained near background levels (e.g., at 1200 or 1800 LT). As is listed in Table 2.10, all species except As, Cd, Cr, and Mn showed performance within the acceptable range of *Kumar's* criteria in the PMF-seeded PDRM solution. The concentrations of these "poorly" predicted metals were below the detection limits during at least a fourth of the measuring period and thus showed unsatisfactory Fa2 statistics. Besides, the ratios of their MNB and MNGE statistics are close to -1, indicating consistent over-predictions of these species by PDRM.

In the PDRM modeling, the errors in the ER predictions were subject to the propagated uncertainties in both TGPM-derived χ/Q estimates and measurements of ambient concentrations at the receptor site. The uncertainties of χ/Q^{TGPM}s for individual stack units (Table 2.11) were estimated from the standard deviations of wind speeds and directions using trajectory perturbation algorithms described in Appendix B3. The measurement uncertainties varied on both sample- and species-basis but these were generally less than 10 %. Therefore, about 120 % relative errors were expected for the overall predictions of emission rates of ambient pollutants from these sources of interest. These errors appeared large at the first glance but were deemed acceptable considering that the uncertainty for Gaussian plume dispersion models is generally considered to be a factor of 2 (Bevington 1969, Claiborn et al. 1995).

Table 2.11 Estimated average uncertainties (relative, in %) of the dispersion parameters based on the TGPM modeling at the Clifton Park supersite.

	σ_y	σ_z	u	$exp(y)$ [1]	$exp(z)$ [2]	χ/Q [3]
WS Unit 1&2	35	53	12	58	75	114
WS Unit 3	35	53	12	58	75	114
WS Unit 4	35	53	12	58	75	114
WS Unit 1&2	36	54	12	58	76	116

[1] $exp(y) = e^{-\frac{y^2}{2\sigma_y^2}}$

[2] $exp(z) = e^{-\frac{H^2}{2\sigma_z^2}}$

[3] Corresponding relative uncertainties in the off axis distance, *y*, were 107 % for WS units and 108 % for BS units.

2.5 Concluding Remarks

A case study of high frequency measurements at the Baltimore supersite by PMF-seeded PDRM was performed to resolve two neighboring power stations located 16 km from our measurement site. With the PMF modeling, area background contributions were obtained and the afforded abundance profiles of point sources (i.e., two BGE utility power plants) were applied to constrain PDRM solutions. With or without PMF-constraining, the PDRM modeling predicted similar NO_x emissions but quite different emissions of other species. The manual examination of the signature tracers (i.e., Ni and Se) in the composition profiles of the different utility units revealed that the PMF-seeded PDRM solution is at least qualitatively accurate. Our model predictions well fit the observations made at the receptor site, according to

Kumar's criteria. Besides, the predicted emission rates of NO_x at those stacks well agreed with the CEM-derived data. Thus this combinative application of the PMF and PDRM models could provide a novel approach to remotely monitor emission rates of both NO_x (or other criteria gas such as SO_2) and non-criteria air pollutants within acceptable limits.

Chapter 3: Application of the PMF-seeded PDRM Model to Resolve Contributions from Nearby Industrial Sources during Two Metal Pollution Episodes in St. Louis

3.1 Background

Metals in airborne particles can be sensitive indicators of air quality deterioration, despite the fact that they represent only a small fraction of PM mass. Although maintaining a certain level of essential metallic elements such as copper, zinc, and iron is beneficial to human health, excess inhalation of metal-containing particles can result in severe outcomes (Valavanidis, Fiotakis and Vlachogianni 2008, Chen and Lippmann 2009). For instance, high exposures to copper and zinc have been proven to cause neuron dysfunction and enhanced risk of Parkinson's disease (Kang and Kim 2003, Kumar et al. 2012). Inhaled particle-borne zinc can also result in lung injury and inflammation because of its catalytic release of proinflammatory cytokines (Sayes, Reed and Warheit 2007) and pediatric asthma morbidity has been directly associated with ambient $PM_{2.5}$ zinc levels (Hirshon et al. 2008).

Air quality in the St. Louis area is known to be severely influenced by several large local metal production industries (Figure 3.1), including a zinc refinery, a copper production plant, and a steel foundry (Lee and Hopke 2006, Turner 2007, Wang et al. 2011, Amato and Hopke 2012). From 1999 to 2005, the US EPA sponsored the St. Louis Midwest "Supersite" project (Turner 2007) during which a large number of research grade air pollutant measurements were made in East-St. Louis. These included hourly measurements made with the UMCP Semi-continuous

Element Aerosol Sampler (SEAS) for 11 metals (Ondov et al. 2003), including Zn, Cu, Pb, and Cd, i.e., excellent markers of these facilities. Between 2001 and 2002, surface winds at St. Louis were predominantly from southerly directions (Turner 2007) (Figure 3.2), which allowed numerous opportunities to observe the influences of these facilities on air quality in East-St. Louis. In this chapter, two large excursions of metal pollution in East St. Louis that were identified in the SEAS metal data sets, one in November 2001 and the other in March 2002, herein episodes A and B, were analyzed to determine metal emission rates from individual stacks at those facilities. In particular, we aimed to provide a new strategic paradigm for remote emission rate measurements of underrepresented pollutants (e.g., transition metals) by highly-time resolved receptor sampling/analysis combined with the newly proposed modeling approach.

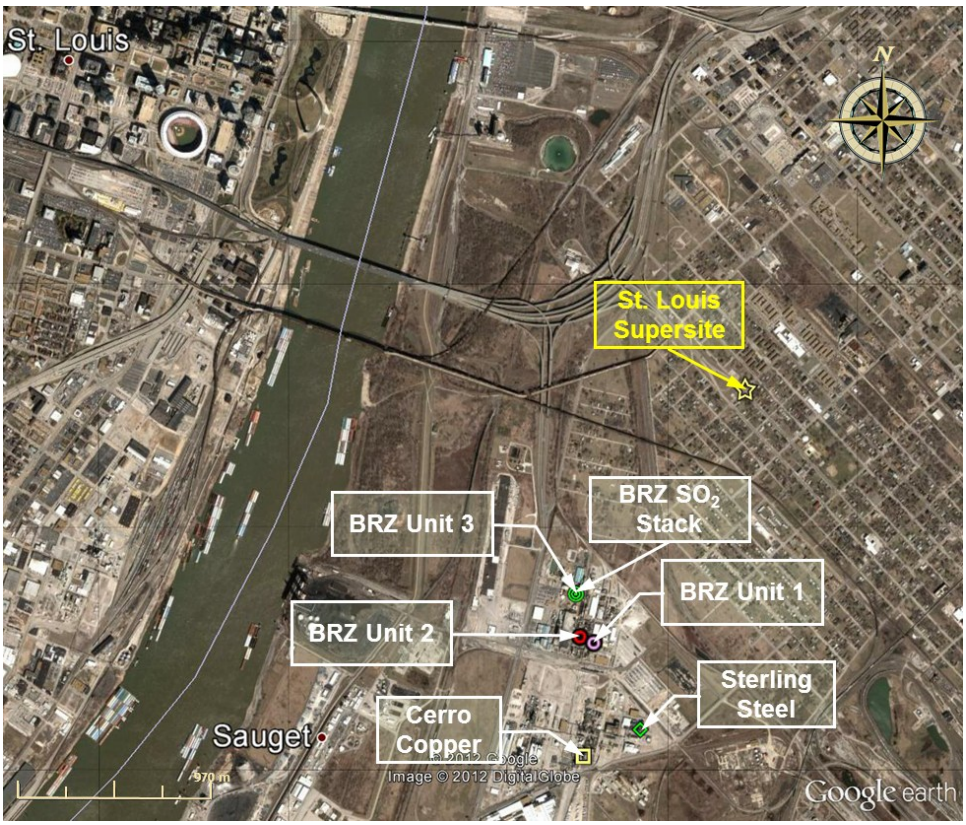

Figure 3.1 Map of the St. Louis supersite and nearby industrial sources, including Big River Zinc (BRZ), Cerro Copper, and Sterling Steel (provided by *Google* Map).

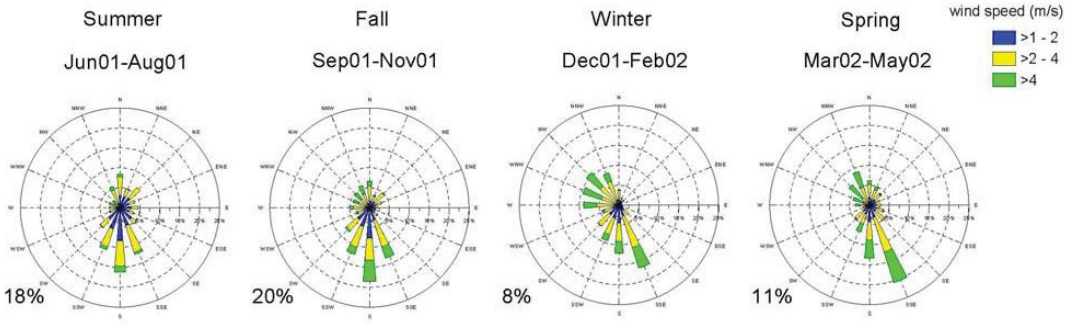

Figure 3.2 Hourly wind roses by season for the St. Louis supersite. Percentage calms (wind speed < 1 m s^{-1}) of total hours listed in the lower-left of each plot (adapted from Turner, 2007).

3.2 Data Inputs

3.2.1 Description of Receptor Site and Sources

Topographically, St. Louis lies on a plateau with little water coverage (3 % of the area) which is ideal for studies of the transport of ambient particles (McElroy and Pooler 1968, Hjelmfelt 1982). The St. Louis–Midwest supersite was strategically located within a residential neighborhood in East St. Louis and on the north bound of the Sauget industrial area, which is home to one of the largest domestic zinc producers, Big River Zinc Corporation (BRZ), and one of the largest domestic manufacturers of copper tubes, Cerro Copper Production Company (Cerro Copper) (Figure 3.1).

The BRZ facility contains 20 separate metal processing units as reported by EPA (http://www.epa.gov/ttn/naaqs/ozone/areas/plant/il/pl24099x.htm), including 10 primary Zn smelters, 6 secondary Zn slab production units, and 4 primary cadmium smelters, each with fugitive and stack emissions. As shown in Figure 3.1, the BRZ

plant is < 1.5 km from the receptor site (38.6120ºN, 90.1605ºW, ASL 0 m) and the station angles of its twenty units span a range from 215º to 220º as measured from due north of the receptor site location. The ten primary metal refining and six secondary metal production units were located in the southern part of the plant in a tight cluster, and the four cadmium smelters were clustered in close proximity to one another near the north boundary of the plant. Detailed stack parameters for each of the 20 units are listed in Appendix C1. Primary Zn smelters all had stack heights between 20 and 25 m, similar exit gas velocities, and were clustered within a radius of 100 m. Moreover, 65 % of the $PM_{2.5}$ emissions (7.8 tonne yr^{-1}) from the primary Zn units were emitted from four identical units according to the 2002 National Emission Inventory (NEI). Thus for modeling purposes, the 10 primary units were represented by a single unit (BRZ unit 2) with stack parameters listed in Table 3.1. The 6 secondary units were likewise clustered and represented by a single unit (BRZ unit 1), with annual $PM_{2.5}$ emissions estimated to be 14.1 tonne yr^{-1}. The four cadmium smelters had identical stack parameters and were represented by BRZ unit 3, with total $PM_{2.5}$ emissions of 2.6 tonne yr^{-1}.

According to Jones et al. (Jones, Lapp and Wallce 1993), Zn is extracted from zinc-rich (2 to 11 % by mass) sulfide ores that also contain substantial amounts of Pb (1.0 to 5.0 %), Cu (0.1 to 2.0 %), and Cd (0.1 to 0.8 %). At BRZ, Zn is produced in the primary Zn smelters in a four-step process involving roasting, leaching, purification, and electrolysis (Jones et al. 1993). The Zn roaster produces a Cd-rich calcine that is treated with sulfuric acid and electromotively reduced by the addition of Zn dust in the Cd “smelter” units yielding Cd metal, which is melted in furnaces to

produce cadmium metal products. Subsequently, cadmium oxide is produced in the secondary cadmium units. Note that during zinc-ore roasting, both Zn and Cd are emitted, but as a lower boiling constituent (Jones et al. 1993), peak Cd emissions probably precede those of Zn.

Sulfur dioxide produced by the smelting units is captured and processed to make sulfuric acid in contact process units. According to the 2002 NEI, sulfur dioxide emissions from BRZ were 1,379 tonne yr^{-1}. 99.9% of these emissions were discharged from the stack of the sulfuric acid manufacturing unit shown in Figure 3.1.

The Cerro Copper plant contains 18 units lying closely within a narrow vector of 203 ± 0.5º with respect to the receptor site which is 2 km away, and thus is separated from the BRZ units by from 10^{o} to 15^{o} (i.e., 0.5 to 0.8 km). Two of these units had identical stacks and accounted for more than 80 % of the annual $PM_{2.5}$ emissions at this plant and were located in such close proximity that these could also be treated as a single source.

The highly-definitive marker species (i.e., Cu, Zn, Pb, and Cd) showed concentration maxima at least 20 times their background levels (Figure 3.3), which could be identified for each source of interest (Table 3.1). Note that Pb was used as the tracer for the Cd smelter source instead of Cd in the modeling because its peak concentration at the receptor site exceeded that of Cd by more than a factor of 10. Given the close proximity of the sources, their distinct chemical abundance profiles, and enormous concentrations induced at the receptor site due to the favorable prevailing wind directions, there should be no doubt that these three sources were

indeed and by far the major sources of these marker elements in the episodes modeled herein.

Table 3.1 Representative stack information (NEI 2002).

Plant	Unit ID	Stack height (m)	Exit gas temperature (K)	Inner diameter (m)	Exit gas velocity ($m\ s^{-1}$)	Flow rate ($m^3\ s^{-1}$)	Control technology	Distance (km)	Station angle (°)	Tracer element
Big River Zinc (secondary)	1	10.06	293.71	0.10	0.11	0.10	FF [1]	1.46	215	Zn
Big River Zinc (primary)	2	20.73	310.37	1.25	11.27	13.83	ME [2]	1.46	215	Zn
Big River Zinc (Cd)	3	9.14	330.37	0.52	17.01	3.59	CC [3], FF	1.22	220	Pb, Cd
Cerro Copper	4	28.96	487.04	1.68	6.39	14.11	WS [4]	1.99	203	Cu

[1] Fabric filter (FF); [2] Mist eliminator (ME); [3] Centrifugal collector (CC); [4] Wet scrubber (WS).

3.2.2 Ambient Pollutants

Highly time-resolved particle measurements made during the St. Louis - Midwest Supersite project (2001-2005) included hourly $PM_{2.5}$ mass measured with an Andersen Continuous Ambient Mass Monitoring System (CAMMS), hourly $PM_{2.5}$-borne elemental and organic carbon (EC and OC) by semi-continuous thermo-optical analysis, and hourly $PM_{2.5}$ concentrations of eleven metals (Al, As, Cd, Cr, Cu, Fe, Mn, Ni, Pb, Se, and Zn) from the samples collected with the UMCP SEAS. All these data are available online from the NARSTO database (http://eosweb.larc.nasa.gov/GUIDE/dataset_documents/narsto_epa_ss_st_louis_air_chem_pm_met_data.html). In addition, hourly measurements of six criteria gases (SO_2, CO, NO, NO_2, NO_x, and O_3) were made by the Illinois EPA during the study period. Hourly $PM_{2.5}$ sulfate and nitrate measurements were made with the particle-into-liquid sampler-ion chromatography (PILS-IC) instrument (Orsini et al. 2003) but, unfortunately, these data were unavailable for the days selected for our modeling.

3.2.3 Meteorological Data

5-minute on-site meteorological data including wind (i.e., speed and direction), temperature (@ 2 m and 10 m, respectively), relative humidity (RH), solar radiation, barometric pressure, and precipitation were also retrieved from the NARSTO database. Additional meteorological inputs required for the modeling (i.e., friction velocity, convective velocity, Monin-Obukhov length, mixed layer depth (MLD), and Pasquill stability class) were computed with a meteorological preprocessor incorporated in the PDRM model as described in Appendix B2.

3.3 Methods

3.3.1 PMF

In this study, PMF was again used to seed and constrain the PDRM. Sixteen species were selected for these analyses, including the two gaseous criteria pollutants (NO_x and SO_2), PM metals (Al, As, Cd, Cr, Cu, Fe, Mn, Ni, Pb, Se, and Zn), carbonaceous species (EC and OC), and total $PM_{2.5}$ mass. As reported by Pancras et al. (Pancras, Ondov and Zeisler 2005), the SEAS typically collects about 10 mL of slurry during a 30-min collection period, and about ~ 0.2 mL is left in the sampler for each sample collection. Left uncorrected, peaks in the time-series are artificially broadened. Accordingly, the SEAS data were processed with a MATLAB script (Appendix C2) to minimize this artifact prior to modeling.

PMF was run with from 3 to 10 factors to determine the optimal number using the scaled residuals (i.e., < 2 if the species is well-modeled) as a criterion of fitting quality (U.S.EPA 2008). Using this criterion, the optimum number of factors were 7 for episode A, and 6 for episode B. In addition, values of the rotational parameter, FPEAK, ranging from -0.2 to +0.2 were tested for this data set (Paatero et al. 2005) and solutions were determined without applying rotational forcing (FPEAK = 0) for both episodes.

3.3.2 Trajectory Analysis and TGPM

Forward plume trajectories originating from the sources of interest (Table 3.1) were simulated every 5 minutes. Those trajectories were all at the effective plume heights (*H*), which were calculated by the *Briggs'* plume rise model (Briggs 1969,

Briggs 1971) as described elsewhere (Park et al. 2005b). A surface roughness of 0.2 m, as determined for this particular area by Hjelmfelt (Hjelmfelt 1982), was used in this study. Five-minute aloft wind velocities at the effective plume heights were derived from the corresponding ground-level measurements at the receptor site using the log-law wind speed model (Cinoco 1965). In this trajectory-driven Gaussian plume model (TGPM), the effective plume heights were further tuned between stack physical heights at the lower bound and mixing heights at the upper bound, until the plume arrival time agreed with the observed peak concentration of the most abundant marker species of each representative source. Plume arrivals usually required from 5 to 20 minutes (i.e., 1 to 4 time steps). The largest plume height required to fit the data was 74 m, i.e., only 45 m above the stack, far below the mixed layer depths and well within the accuracy of prediction by the *Briggs'* plume rise model.

The point of the closest approach to the receptor site on each plume trajectory centerline was identified (Beachley and Ondov 2012), and the off-axis distance (*y)* from the centerline was calculated as the horizontal distance between the point of the closest approach and the receptor site. The uncertainty (*dy*) in y was calculated from the standard deviation of the wind angle (Appendix B3). The plume transport distance, *x*, was the sum of the lengths of those wind vector segments up to the point of the closest approach, and the plume transport time was determined as the sum of the quotients of each segment length and the corresponding aloft wind speed.

Herein, the EPA's Industrial Source Complex Short Term plume model 3, ISCST3 (U.S.EPA 1995), designed specifically for cases with known meteorological conditions and plume travel distances, was applied to compute the lateral and vertical

Gaussian dispersion coefficients (σ_y and σ_z) at plume arrival for each trajectory. The values of the plume dispersion factor, χ/Qs, were calculated for each successive trajectory at 5-minute resolution, and then combined into 1-hour averages to coincide with the hourly sampling periods.

3.3.3 PMF-seeded PDRM Modeling with a Tracer Approach

By and large, the PMF-seeded PDRM modeling in this study was similar to that employed in resolving the power plants in Baltimore described in Chapter 2 (see Appendix C3 for the flow chart representation of modeling processes). PMF terms were implanted in the modeling to account for the contributions from non-point background sources which were not of interest, and the solutions were obtained by minimizing the object function defined in Equation 2.17. However, as CEM data were unavailable at the metal production facilities, it was not possible to utilize any criteria gas (i.e., SO_2 or NO_x) to effectively constrain the TGPM derived χ/Qs. Instead, the marker species of the sources were used for this purpose as described below.

A fundamental assumption of PDRM is that source emissions are constant during the modeling period. This is often true for utility-generating plants (Park et al. 2006b, Beachley and Ondov 2012). However, large variations in production rates within a day are not unusual for many industries such as metal smelting and casting, e.g., due to the timing of different batch processes. To minimize the effects of changing emission rates from the facilities, the PDRM modeling was carried out for a short time frame of 4 hours, instead of using the whole 12-hours worth of data in a single model run. Even shorter timeframes would have allowed better tracking of possible temporal variations in the ERs of those industrial sources more precisely. But this was

not possible in this study because the number of measurements was not adequate to permit solutions to be determined for the four sources used in the model with fewer than 4-hours worth of measurement input.

The PDRM solutions for the plume dispersion factors, $(\chi/Q)_{j,k}^{PDRM}$, were constrained to the TGPM-estimated values as follows.

$$(\chi/Q)_{j,k}^{PDRM} = a_{j,k}(\chi/Q)_{j,k}^{TGPM} \quad (3.1)$$

where $0.1 \leq a_{j,k} \leq 2.0$ as proposed by Park et al. (Park et al. 2005b).

Specifically, three individual PDRM runs of 4-hour sub-periods were performed using the marker species alone. The scaling factor for each source during each sampling interval, $a_{j,k}$, was iteratively sought until the shape of χ/Q temporal profile converged to the temporal profiles of the marker species. In a second round of PDRM runs, all other species were added and ERs of individual species from specific sources were solved, again, at 4-hour intervals, using the conditioned χ/Qs obtained from the previous round.

The tracer approach was crucial to constraining the initial guess of emission rates by exploiting the PMF outputs. The initial emission rate of each marker element from its corresponding source was estimated by the TGPM-derived χ/Qs and the PMF apportioned contributions (Equation 3.2). The upper bound (UB) of the ER was based on the observed concentrations of the tracer element as shown in Equation 3.3 and the lower bound (LB) was set to a half of the initial guess, consistent with the upper bound of the χ/Q scaling factor. The initial guess of ERs for other species was based on the PMF-derived abundance profiles, and their bounds were set broader (i.e. to

LB(ER) = 0.05ER_{ini}, and UB(ER) = 10ER_{ini}), than those for the key marker element, allowing greater modeling flexibility, given the greater uncertainty in the allocations of these species.

For the key marker species,

$$ER_{tra,j}^{ini} = \sum_{k=1}^{n}(g_{j,k} \cdot f_{tra,j}) \Big/ \sum_{k=1}^{n}\left(\frac{\chi}{Q}\right)_{j,k}^{TGPM} \quad (3.2)$$

$$\mathrm{UB}(ER_{tra,j}) = \sum_{k=1}^{n} C_{tra,k} \Big/ \sum_{k=1}^{n}\left(\frac{\chi}{Q}\right)_{j,k}^{TGPM} \quad (3.3)$$

In Equation 3.2, $ER_{tra,j}^{ini}$ is the initial guess of emission rate (g s^{-1}) of the key marker element (*tra*) from the j^{th} source, $g_{j,k}$ is the particulate mass concentration from the j^{th} source contributing to the k^{th} sample, $f_{tra,j}$ is the mass fraction of the tracer species in the j^{th} source, and $\left(\frac{\chi}{Q}\right)_{j,k}^{TGPM}$ is the calculated meteorological dispersion factor of the j^{th} source at the k^{th} observation. In Equation 3.3, $\mathrm{UB}(ER_{tra,j})$ is the upper bound of the tracer emission rate for source j, and $C_{i,tra}$ is the observed concentration of the tracer at the k^{th} observation.

The initial guesses of emission rates of ambient pollutants (non-tracer species) from a given source were normalized to the emission rate of the corresponding tracer:

$$ER_{i,j} = ER_{tra,j} \cdot f_{i,j}/f_{tra,j} \quad (3.4)$$

where $ER_{i,j}$ is the initial emission rate (g s^{-1}) of species i from source j during the modeling period. $f_{i,j}$ and $f_{tra,j}$ are the abundances of species i and the tracer from

source *j*, respectively, obtained from the PMF analysis. ERs of ambient species were then tightly constrained as follows.

$$\text{LB}(ER_{i,j}) \leq ER_{ij} \leq \text{UB}(ER_{i,j}) \quad (3.5)$$

where LB and UB are the lower and upper bounds which were set as 0.1 and 10 times the initial value, respectively.

3.4 Results and Discussion

3.4.1 Correlation of Ambient Pollutants and Meteorological Observations

As shown in Figure 3.3, episodes in which high levels of metal-containing airborne particles were observed occurred during the mornings of 8 November 2001 (episode A) and 23 March 2002 (episode B) under mild (i.e., surface wind speed < 2 m s^{-1}) southwesterly (i.e., wind angle between 180 and 220 degrees with respect to true north) winds (Figure 3.4). During episode A, the concentration of Zn at the receptor site reached 1.08 μg m^{-3} at 0030 LT. In contrast, the maximum Cu concentration was only 0.33 μg m^{-3}, indicating that BRZ emissions dominated this event, with relatively little influence from Cerro Copper. During episode B, copper concentrations peaked at 1.65 μg m^{-3} at 0730 LT, while the maximum Zn concentration at this time was only 0.15 μg m^{-3}. Thus, episode B was clearly dominated by influence from copper smelters at the Cerro Copper plant.

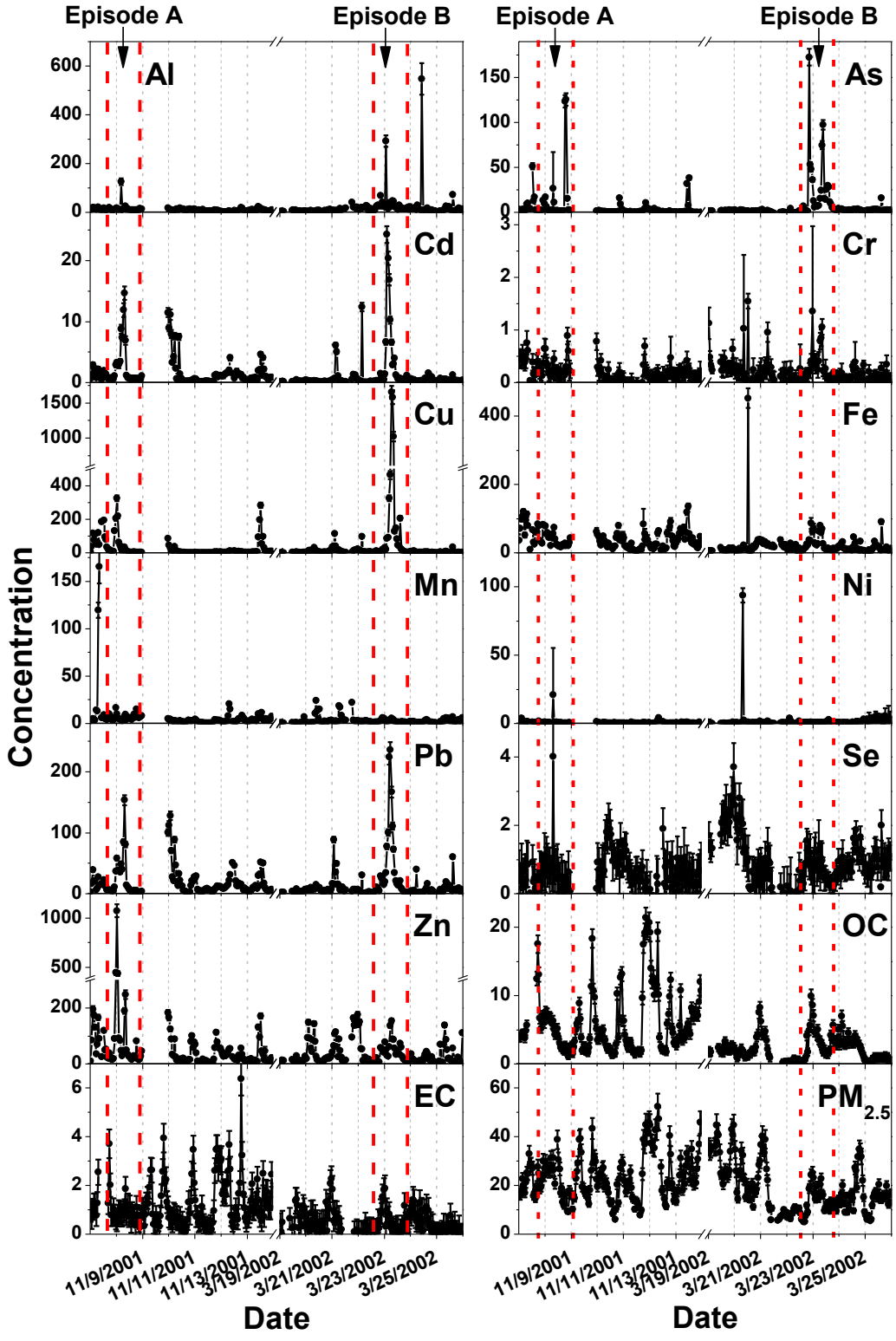

Figure 3.3 Ambient pollutant concentrations (μg m^{-3} for OC, EC, and $PM_{2.5}$; ng m^{-3} for SEAS metals) observed at the St. Louis supersite during the two episodes.

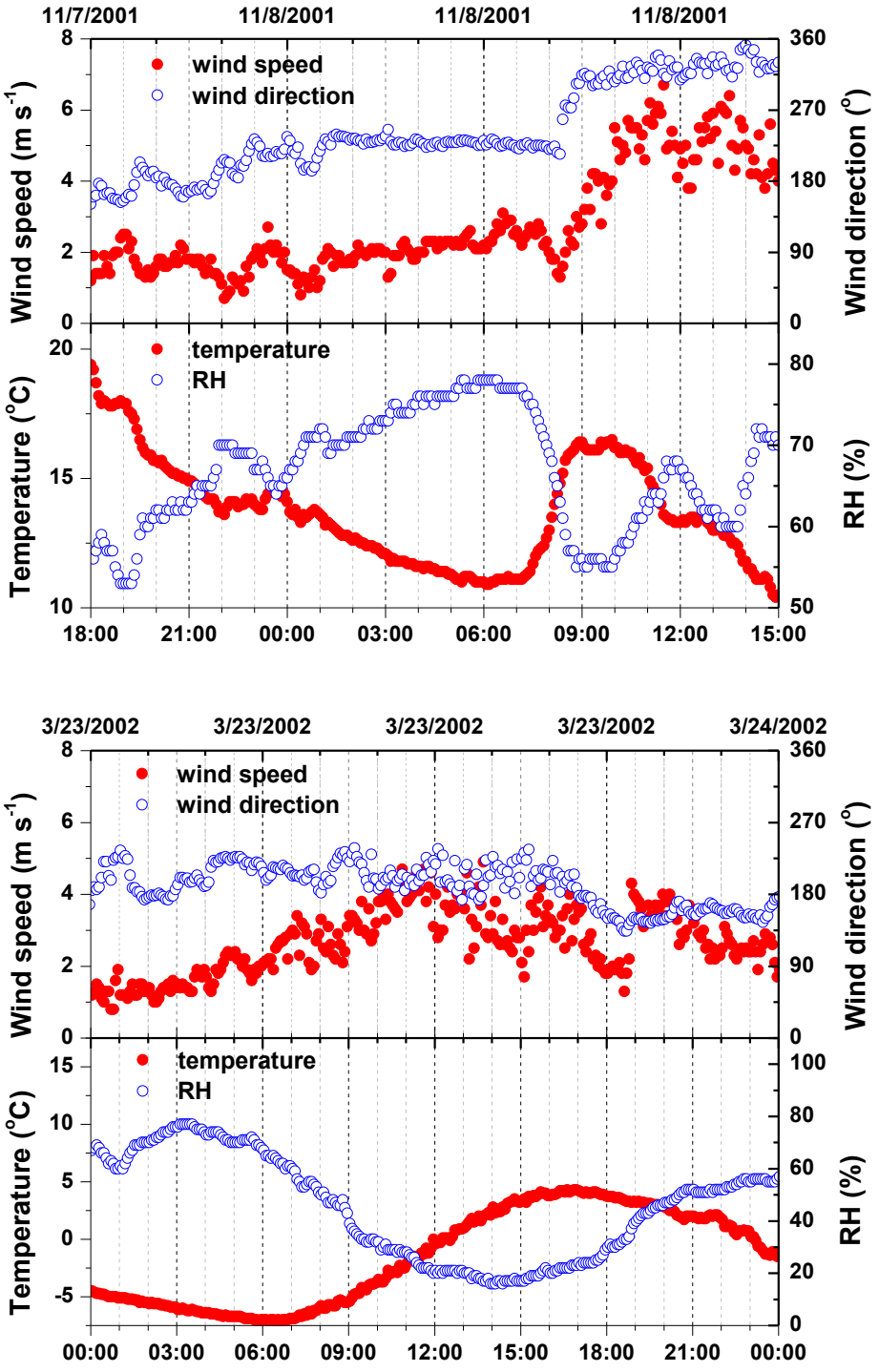

Figure 3.4 Temporal profiles of wind speed, wind direction, ambient temperature, and relative humidity in episodes A (top panel) and B (bottom panel).

These maxima corresponded to extraordinarily high fractions of zinc (i.e., ~ 4 % of $PM_{2.5}$) in episode A, and copper (i.e., ~ 8 % of $PM_{2.5}$ mass) in episode B, despite the fact that the $PM_{2.5}$ concentrations (29.6 and 22.7 μg m^{-3} for episode A and B, respectively) were below the 24-hr National Ambient Air Quality Standard (NAAQS) which was at that time 65 μg m^{-3} (U.S.EPA 2004b) and now 35 μg m^{-3} (U.S.EPA 2005).

Simple linear regressions were performed by regressing ambient SO_2 or NO_x concentrations against metal tracers, for episodes A and B, respectively. In episode A, SO_2 was well correlated with Zn (r^2 = 0.791, p < 0.001) and Cu (r^2 = 0.565, p = 0.005) but poorly so with Cd (r^2 = 0.001, p = 0.907). And NO_x was poorly correlated with SO_2 (r^2 = 0.043, p = 0.519).

Multilinear regressions (MLR) were also performed to apportion SO_2 to the sources using Cu, Zn, and Cd as markers of the three types of sources. The MLR analysis for episode A using ambient SO_2 as the dependent variable resulted in the following relationship:

$$[SO_2] = (0.03 \pm 0.13) \times [Cu] + (0.09 \pm 0.04) \times [Zn] + (1.89 \pm 1.43) \times [Cd] + (5.65 \pm 12.41) \quad (3.6)$$

where concentrations of Cu, Zn, and Cd are in ng m^{-3}, and SO_2 in ppb. The regression equation showed a good correlation coefficient of 0.846 (p = 0.001).

In episode B, the marker species best correlated to SO_2 was Cu (r^2 = 0.409, p = 0.025), followed by Zn (r^2 = 0.288, p = 0.072) and Cd (r^2 = 0.002, p = 0.888). In contrast to episode A, their correlations with NO_x were in generally better (i.e., r^2 = 0.526 and p = 0.008 for Zn, and r^2 = 0.741 and p < 0.001 for Cd) except Cu (r^2 =

0.342, p = 0.046) in this scenario. And NO_x was better correlated with SO_2 (r^2 = 0.138, p = 0.234) as well.

The MLR analysis for episode B using ambient NO_x as the dependent variable and Cu, Zn, and Cd as the independent variables set resulted in the following relationship:

$$[NO_x] = (0.008 \pm 0.004) \times [Cu] + (0.09 \pm 0.07) \times [Zn] + (2.43 \pm 0.41) \times [Cd] + (3.58 \pm 4.08) \quad (3.7)$$

where concentrations of Cu, Zn, and Cd are in ng m^{-3}, and NO_x in ppb. The regression equation showed an excellent correlation coefficient of 0.933 ($p < 0.001$).

In either case, the relative small residuals obtained for the MLR analysis (i.e., an average SO_2 residual of 5.65 ppb compared with the average SO_2 concentration of 39.8 ppb in the former, or an average NO_x residual of 3.58 ppb compared with the average NO_x concentration of 23.9 ppb in the latter) implied that the corresponding sources (i.e., Cu production, Zn smelters, and Cd smelters) were the major contributors to the criteria gas (SO_2 or NO_x).

The lack of CEM data at those sources of interest restricted the further application of these tracer gases for the PDRM modeling as did in the previous study (Beachley and Ondov 2012). Nevertheless, the MLR results added confidence to apply these metallic marker species in tuning the TGPM-derived profiles of χ/Qs.

3.4.2 PMF Source Apportionment

Herein, episode B is discussed first, because it contains a large excursion for only one element (Cu) and therefore its analysis is less complicated. A six-factor solution for this episode was obtained and the PMF profiles are plotted in Figure 3.5, wherein the species are normalized to the corresponding values of PMF-apportioned $PM_{2.5}$

contributions. The temporal profiles of source strengths (*g* matrix of predicted ambient concentrations) are shown in Figure 3.6.

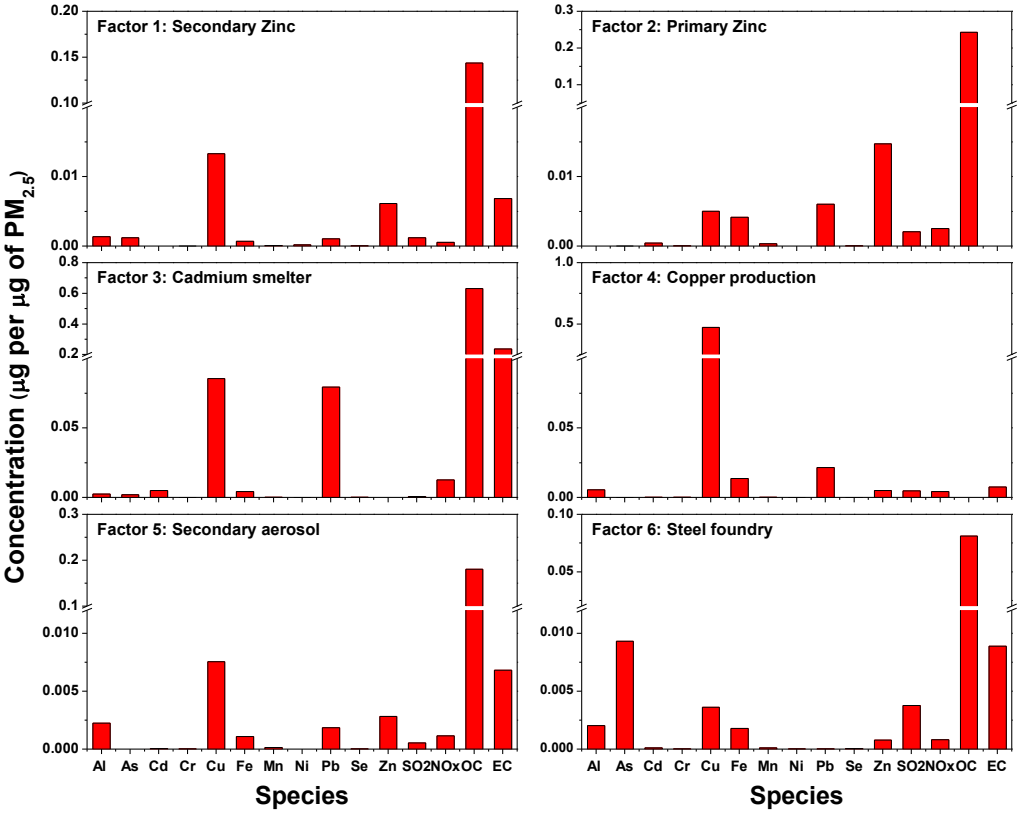

Figure 3.5 PMF-resolved source profiles in the copper episode (episode B).

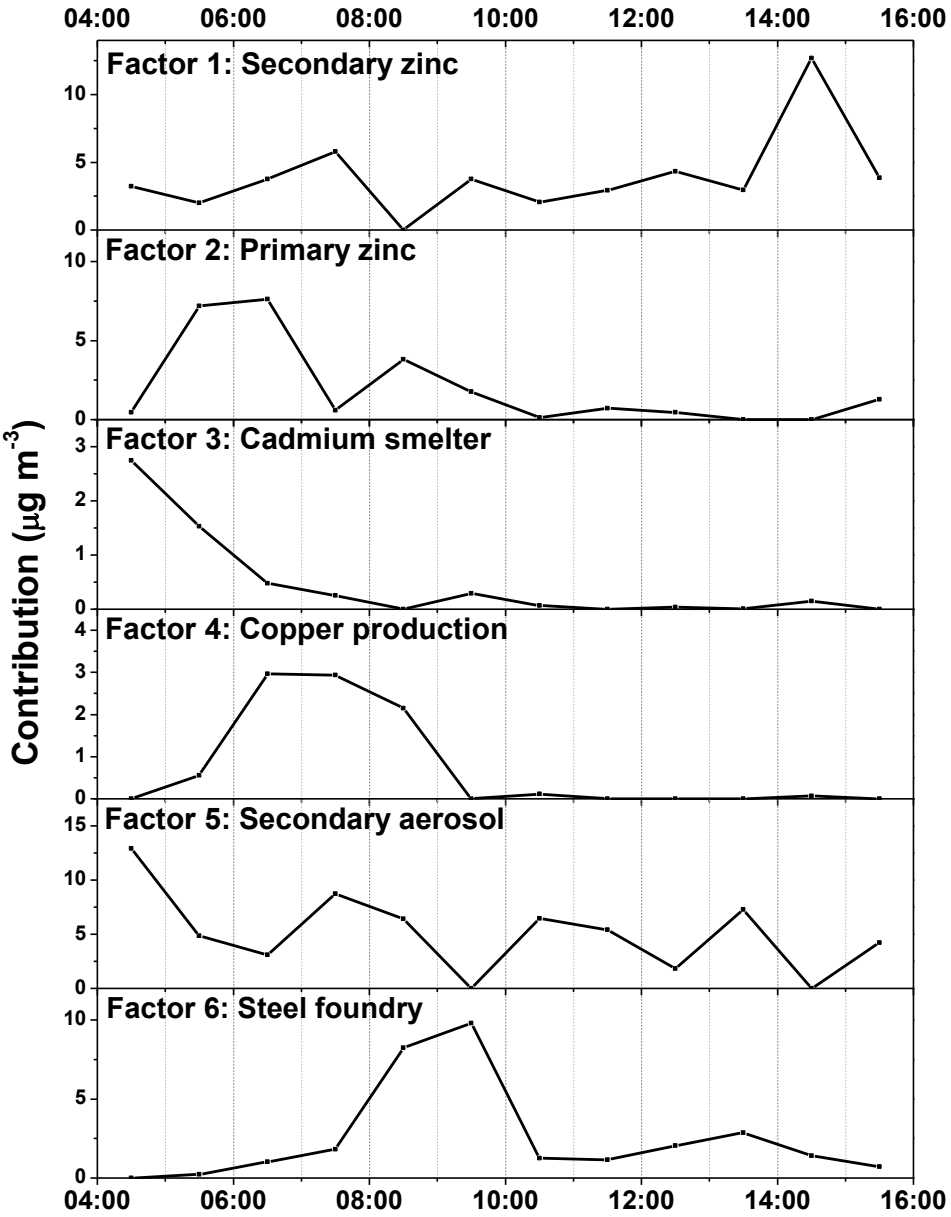

Figure 3.6 Time series source contributions in episode B predicted by PMF.

Two zinc factors (factor 1 and 2) were identified, both characterized by high abundances of Zn. A distinction between these two factors was that Cd was present in factor 2 but absent in factor 1. According to the TRI (TRI 1990), BRZ's cadmium emissions were from primary zinc refining and cadmium smelting, whereas secondary zinc production contributed nearly none to the cadmium emission. Hence

factor 1 was identified as primary zinc refining, and factor 2 was attributed to secondary zinc production, respectively.

Factor 3 was recognized as the cadmium smelter because its Cd abundance (0.51% of $PM_{2.5}$ mass) was more than 10-fold greater than that of the other Cd-containing factors. This factor also contained large abundances of Pb, Cu, and EC, and very little Zn and SO_2. Cadmium ores typically contain too little Cd to be extracted as a stand-alone operation and cadmium is, therefore, generally produced as a byproduct of Zn, Pb, or Cu refining (Jones et al. 1993). At BRZ cadmium is a byproduct obtained from zinc sulfate concentrates produced after the ore is calcined and dissolved in sulfuric acid. As noted above, the BRZ plant uses the electromotive process for cadmium refining (Jones et al. 1993), in which zinc dust is consumed to displace cadmium metal out from the stream of cadmium-rich sulfate solution. As a result, low zinc emissions were expected while cadmium and lead emissions were high at the cadmium refinery. A substantial amount of SO_2 was generated from the roasting of zinc sulfide ore but its emission was low because SO_2 was captured and converted to sulfuric acid in a separate unit.

According to the 1990 TRI, BRZ's cadmium smelting operations emitted ~760 kg (i.e., 88 %) of cadmium, while primary zinc refining contributed ~100 kg (i.e., 12 %) of Cd, out of 860 kg of its annual cadmium emission. For this measurement period, however, PMF attributed 58 % of the total cadmium to this factor and 23 % to primary zinc refining. As shown in Figure 3.3, Cd concentrations peaked 2 hours before the start of the PMF modeling period. Note that the maximum contribution from the cadmium smelter was about four hours earlier than the maximum from the

primary zinc refinery, which suggests that a Zn episode probably preceded the Cd episode. This could not have been detected at the receptor site because winds were more westerly (220^{o} to 270^{o}) and thus unfavorable. A small Cd excursion occurred at 0930 LT, following the Zn maximum at 0630 LT. As discussed below, this Cd excursion was small because the plume centerline was substantially farther from the receptor site at this time.

Factor 4 was unambiguously identified as resulting from copper production at Cerro Copper, owing to its huge maximum concentration, favorable plume trajectories, and the lack of other credible Cu sources in the region. Indeed, among all possible sources, only the Cerro Copper plant's excursion profile could be fit by the temporal profile of the TGPM-derived plume dispersion parameter, χ/Q (Figure 3.6). Clearly this factor contained the greatest Cu abundance (47 % by mass at peak concentration) of all the factors. The PMF analysis attributed more than 70 % of the total Cu, 20 % of the total Pb, and 5 % of the total Zn to this factor (Figure 3.7).

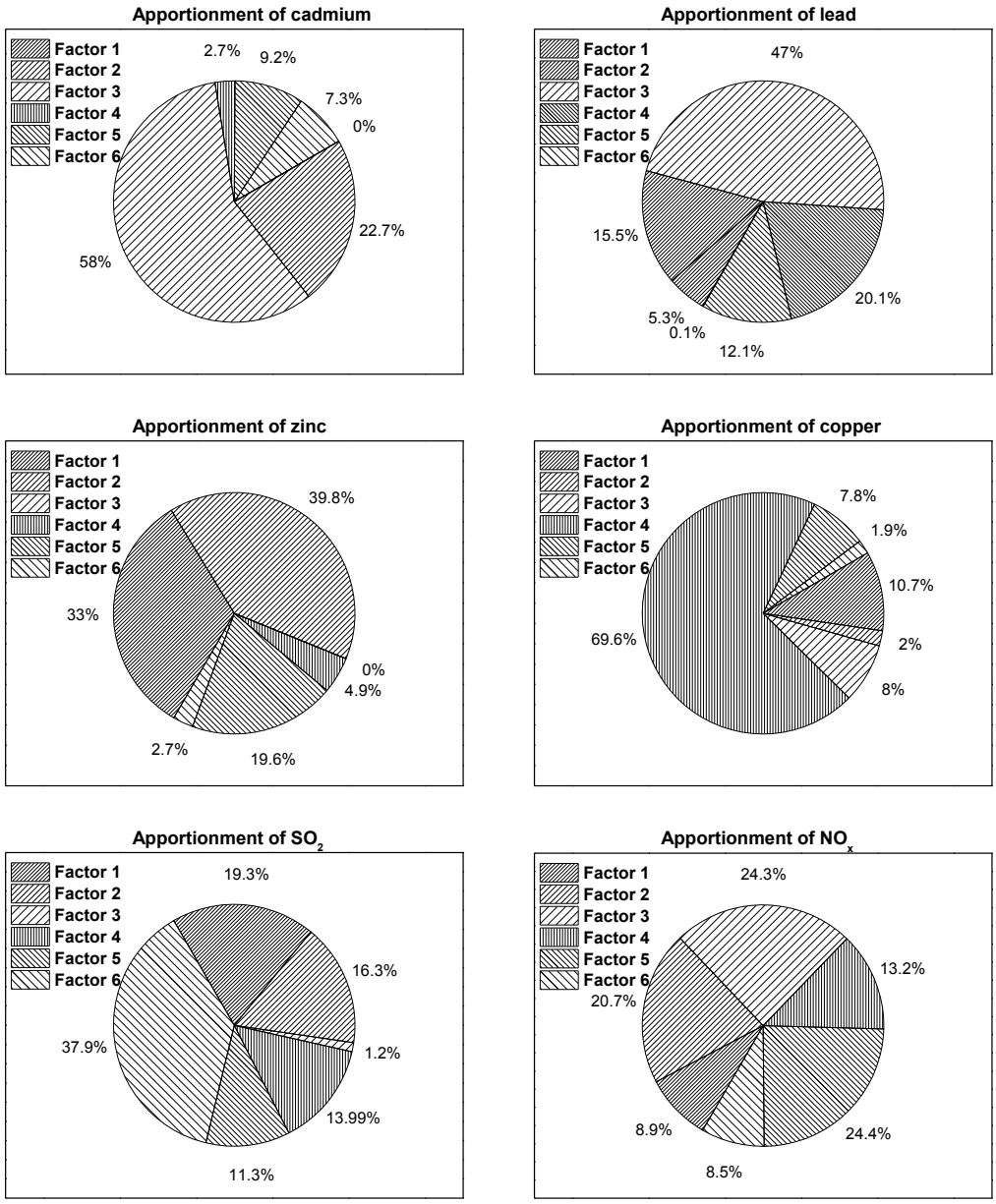

Figure 3.7 PMF source apportionments of Cd, Pb, Zn, Cu, SO_2, and NO_x in episode B.

Factor 5 was initially tentatively assigned to regional secondary aerosol, as it showed less fluctuated contributions with the wind direction variations. Unfortunately, secondary species data for sulfate and nitrate were not available for reasons mentioned above, so this assignment is highly speculative. The most striking feature

of this factor was its high OC/TC ratio (0.96), i.e., comparable to the OC/TC fractions (0.93 ± 0.05) observed for ambient concentrations measured throughout the episode. Moreover, considering the high abundances of Cu (0.8 %), Zn (0.3 %), and Pb (0.2 %) which are unusual for secondary aerosol, this factor could be a mixed residual factor made up of contributions from the various other sources. OC/TC ratios for primary and secondary Zn sources resolved by PMF were 0.99 and 0.95, respectively, suggesting that these sources contributed to factor 5. Likewise, Cu at 0.8 % of $PM_{2.5}$ in this factor appears to include a contribution from Cerro Copper. Overall, this factor accounted for 35 % of $PM_{2.5}$ mass, 17 % of EC, 37 % of OC, 19 % of Zn, 8 % of Cu, 12 % of Pb, and 9 % of Cd during this episode.

Factor 6 was assigned to the Sterling Steel plant (station angle 195°) 2 km away, which was identified by its high abundances of Fe (0.2 % of $PM_{2.5}$) and SO_2 (300 ppb m^3 per μg of $PM_{2.5}$). The low Fe/SO_2 ratio could be expected for Sterling Steel, as its centrifugal collector is inefficient for gaseous pollutants but moderately efficient for particles. In Lee and Hopke's source apportionment for St. Louis (Lee and Hopke 2006), they suggested that a significant contribution of local fossil fuel combustion was attributed to steel processing. This might be true of our PMF steel foundry factor as 38 % of SO_2 and 11 % of EC were attributed to it.

It is noteworthy that a high abundance of copper was present in all the PMF-derived source profiles. For instance, copper was the most abundant metallic component of emissions from the cadmium smelter, secondary zinc production, and secondary aerosol; second richest for the steel foundry; and third richest for the primary zinc refinery. It is known that the PMF model emphasizes the uncertainties of

measurements and that samples with high uncertainties will be down-weighted in the solution (U.S.EPA 2008), as indicated in Equation 1.6. Given the enormous excursion of copper in this episode, its absolute uncertainty by which χ^2 was weighted forced the copper abundance of the major copper factor (the Cerro Copper plant) to be underestimated. Meanwhile, additional copper contributions from other minor sources of copper were driven by the model to offset the residuals during the off-peak period. Stated in another way, the actual copper abundances of the sources other than the Cerro copper plant are surely severely overestimated. This is not surprising given the relative small number of measurements available for PMF.

The PMF-derived emission profiles of the BRZ and Cerro Copper plants are listed in Table 3.2 along with those reported in past studies (Lee and Hopke 2006, Lee, Hopke and Turner 2006, Amato and Hopke 2012). The abundance profile of the Cerro copper emissions determined by PMF agreed well with Amato's recent study (Amato and Hopke 2012). However, all the three types of BRZ units in our PMF study showed tremendous abundances of Cu, Pb, and OC, compared to the other studies listed, suggesting over-predictions for these sources. Still, more than 91 % of Cu, 78 % of Zn, and 84 % of Cd were attributed to the copper and zinc sources, thus these were deemed be good initial inputs for the PDRM modeling. Over-predictions believed to have resulted for factor 5 and 6 had little effect on PDRM modeling of the major sources (i.e., Zn, Cd, and Cu smelters) as just noted, but permitted removal of background from the data set as noted above.

Table 3.2 PMF-derived emission profiles of the BRZ and Cerro Copper plants in St. Louis.

Species	Zinc/cadmium smelter						Copper production			
	BRZ Unit1[1]	BRZ Unit2[1]	BRZ Unit3[2]	Lee's study 1[3]	Lee's study 2[4]	Amato's study[5]	Cerro Copper[6]	Lee's study 1[3]	Lee's study 2[4]	Amato's study[5]
Al	0.220	0	0.514	0.015	0.049	<0.001	0.012	0.011	0.057	0.013
As	0.198	<0.001	0.392	<0.001	<0.001	<0.01	<0.001	0.005	<0.001	<0.01
Cd	<0.001	0.031	1.00	n. a.	n. a.	n. a.	<0.001	n. a.	n. a.	n. a.
Cr	<0.001	0.002	0.002	<0.001	<0.001	<0.01	<0.001	<0.001	<0.001	<0.01
Cu	2.16	0.340	16.79	<0.001	<0.001	<0.01	1.00	1.00	1.00	1.00
Fe	0.116	0.284	0.863	1.01	0.910	<0.01	0.029	0.008	0.238	0.023
Mn	0.017	0.023	0.051	0.011	<0.001	<0.01	<0.001	0.007	<0.001	<0.01
Ni	0.032	<0.001	0.009	0.008	<0.001	<0.01	<0.001	<0.001	<0.001	<0.01
Pb	0.170	0.411	15.55	<0.001	<0.001	<0.01	0.046	0.003	<0.001	0.033
Se	0.005	0.002	0.037	<0.001	<0.001	<0.01	<0.001	<0.001	<0.001	<0.01
Zn	1.00	1.00	<0.001	1.00	1.00	1.00	0.011	<0.001	0.143	0.047
OC	23.30	16.48	123.46	0.067	0.307	2.17	<0.001	0.968	0.143	4.67
EC	1.11	<0.001	46.39	1.10	5.38	<0.01	0.016	0.419	2.29	1.33

[1] Normalized by Zn.

[2] Normalized by Cd.

[3] Lee's analysis of data from the EPA St. Louis supersite (Lee and Hopke 2006), normalized by Zn.

[4] Lee's analysis of data from the Blair site in St. Louis (Lee et al. 2006) , normalized by Zn.

[5] Amato's re-analysis of the EPA St. Louis supersite data (Amato and Hopke 2012), normalized by Cu.

[6] Normalized by Cu.

A seven factor solution was obtained similarly using the data set for episode A, with factors identified as follows: a cadmium emission source, two zinc smelters, a

copper plant, a steel foundry, secondary (mixed source) aerosol, and motor vehicle emissions. The additional factor revealed in episode A was assigned to motor vehicle emissions because the time for its major contributions corresponds to the morning traffic rush hours (0730 to 0930 LT) and its strengths were weak at other times (Appendix C4). This factor contributed 5 % of $PM_{2.5}$, 11 % of NO_x, and 16 % of EC measured during episode A. Considering that episode A was a weekday (Thursday) morning while episode B was a Saturday morning, it is not a surprise that the vehicular emission factor was absent in the latter.

The source profiles (normalized to the corresponding marker species) of the facilities at the BRZ and Cerro plants during the two episodes are compared in Figure 3.8. On one hand, the copper abundances of the BRZ units were significantly reduced as compared with episode B, which indicated a lesser extent of copper cross contamination. On the other hand, the greater abundances of Zn, As, and Cd of the copper production factor in episode A (Zn-type), again, suggests zinc cross contamination due to underweighting of the large zinc excursion in this episode. Overall, it suggested that PMF was unable to well resolve these sources, but nevertheless provided useful seed values for the PDRM solutions and background source removal.

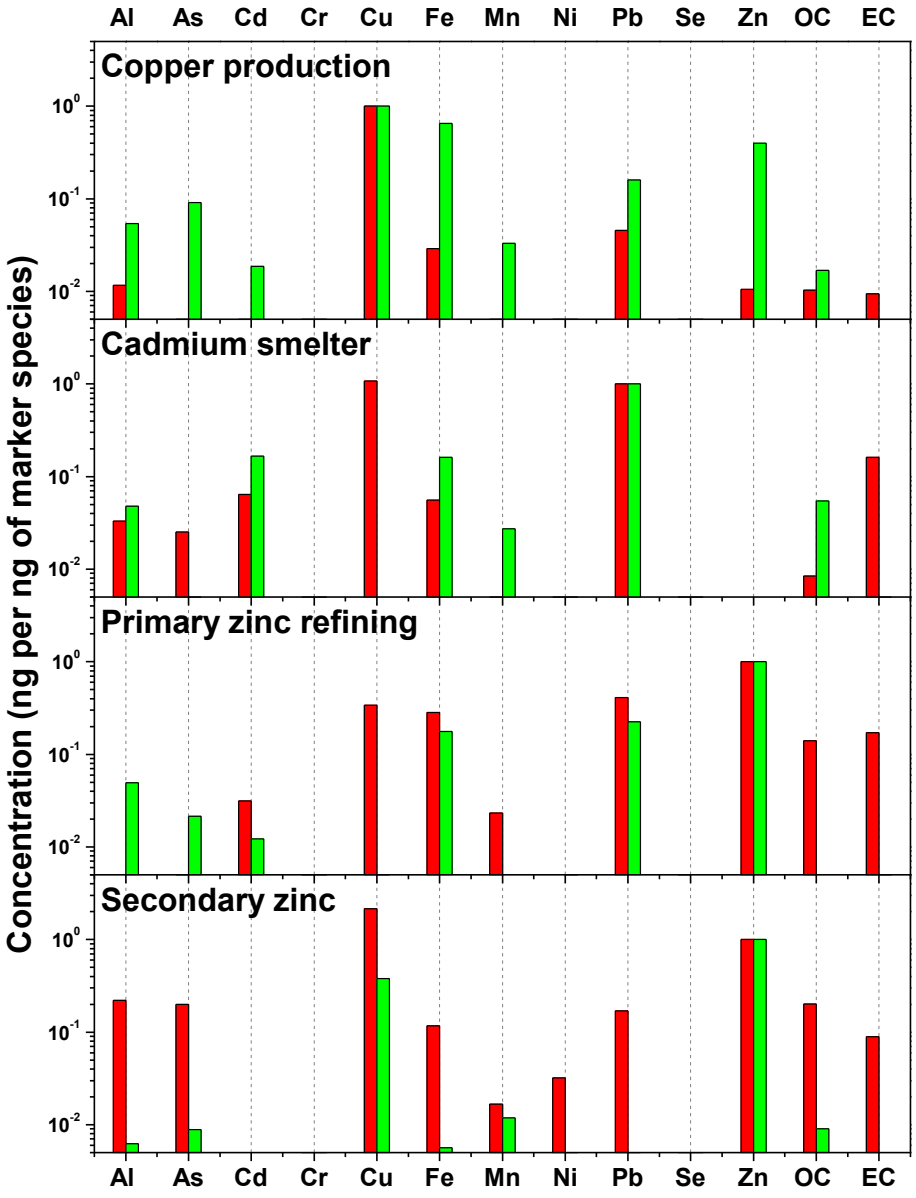

Figure 3.8 Comparison of source profiles of the BRZ and Cerro Copper facilities determined by PMF during the two episodes (episode A in green and episode B in red, respectively).

3.4.3 TGPM Analysis

Plume forward trajectories from the representative stacks in the BRZ and Cerro Copper plants for the two episodes are shown in Figure 3.9. Time series profiles of TGPM-derived dispersion factors, $(\chi/Q)^{TGPM}$s, used to seed PDRM are shown in

Figure 3.10, using the algorithms described in the previous chapter. Relative errors in the χ/Q estimates from the TGPM were calculated by propagation of standard deviations of the 5-minute averages of wind directions and speeds, and are listed in Table 3.3.

Table 3.3 Estimated average uncertainties (relative, in %) of the dispersion parameters based on the TGPM model during the plume periods: A) 2200-0300 LT on 7 ~ 8 November 2001; and B) 0400-0900 LT on 23 March 2002, respectively, at the St. Louis supersite.

	σ_y		σ_z		u		$exp(y)$ [1]		$exp(z)$ [2]		χ/Q [3]	
	A	B	A	B	A	B	A	B	A	B	A	B
BRZ Unit 1	5.7	4.2	16.3	8.8	25.1	20.9	83.7	53.3	23.0	12.4	92.0	59.3
BRZ Unit 2	5.7	4.2	16.3	8.8	26.5	20.9	83.7	53.3	23.0	12.4	92.4	59.3
BRZ Unit 3	5.8	5.2	16.3	9.4	24.7	20.9	69.4	55.7	23.0	13.4	79.1	61.9
Cerro Copper	7.7	4.9	19.1	10.7	26.8	20.9	61.2	56.8	27.1	15.1	74.9	63.4

[1] $exp(y) = e^{-\frac{y^2}{2\sigma_y^2}}$

[2] $exp(z) = e^{-\frac{H^2}{2\sigma_z^2}}$

[3] Corresponding uncertainties in the off axis distance, y, were 25.8% (BRZ units), 26.5% (Copper unit); and 24.5% (BRZ units), 24.7% (Copper unit) in episode A, and episode B, respectively.

Figure 3.9 Forward plume trajectories from the stacks at the BRZ and Cerro Copper plants: bottom panels for episode A and top panels for episode B (the yellow solid cycles at the origins represent the St. Louis supersite).

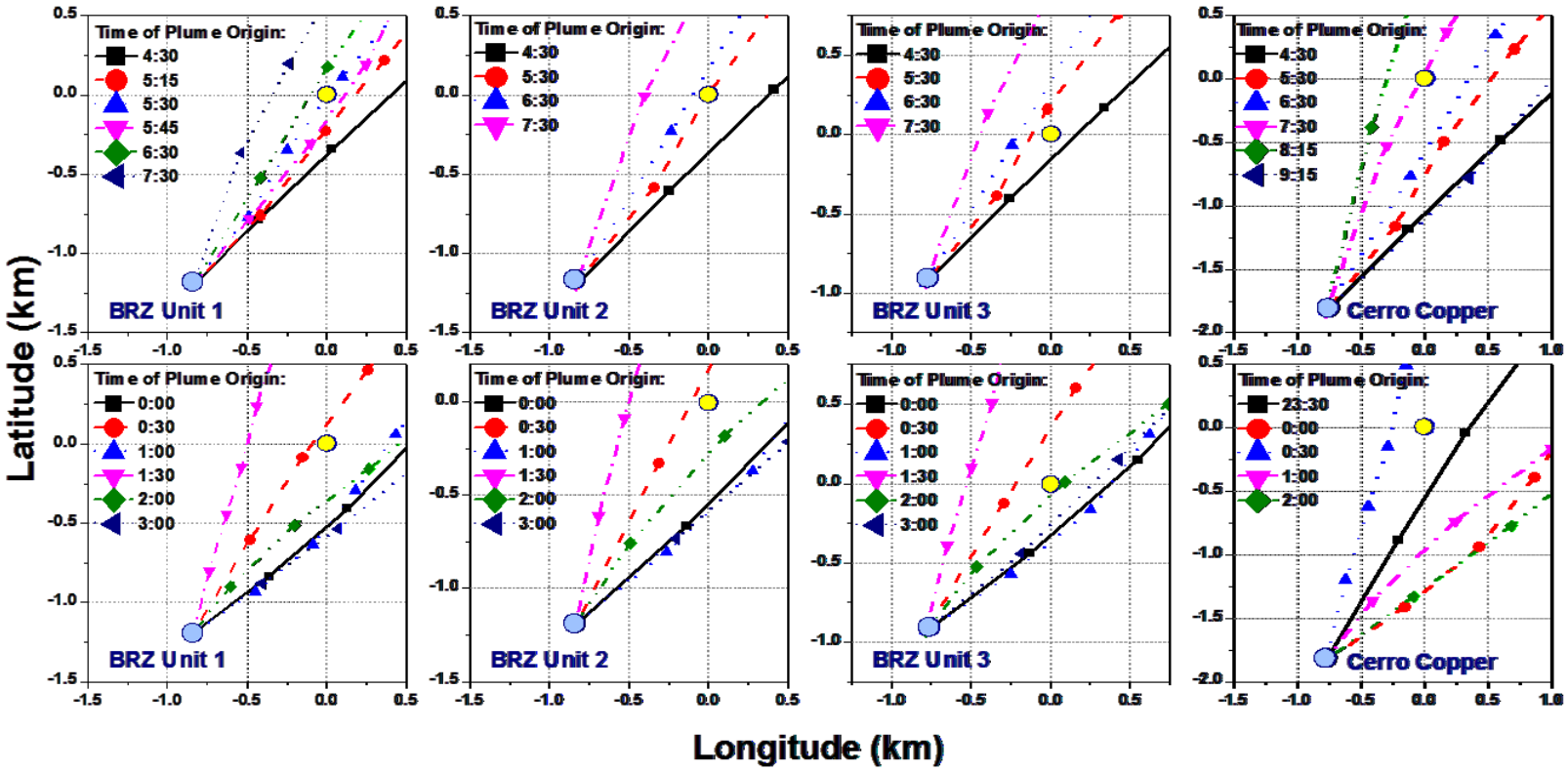

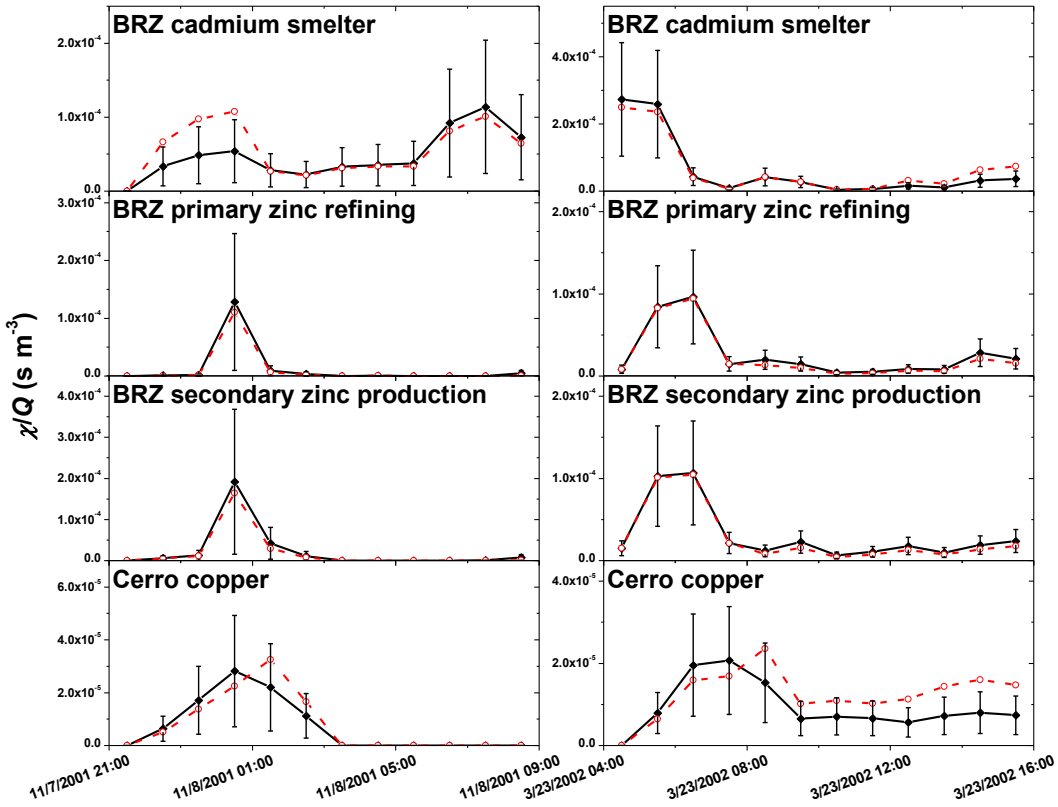

Figure 3.10 The time series profiles of TGPM-derived dispersion factors (black solid line) and PDRM-tuned dispersion factors (red dash line) in episode A (left panels) and episode B (right panels), respectively.

As shown in Table 3.3, our calculations attributed larger relative uncertainties to vertical dispersion factors (σ_z) than lateral ones (σ_y). However, the overall uncertainty in the χ/Qs was to a great extent dependent on the lateral exponent as the uncertainties in off-axis distances dominated the errors in the other terms. And because of the greater variability of 5-minute averages of wind directions and speeds in episode A than in episode B, larger uncertainties in χ/Qs were obtained in the former.

The 5-minute resolution horizontal trajectory simulations at the effective stack heights, based on which the plume arrival time from each source was determined, showed a typical plume transport time of 10 to 20 minutes from those BRZ and Cerro

Copper units (Figure 3.9). The plumes that originated simultaneously from the BRZ primary zinc and secondary zinc units showed very similar trajectories due to their nearly identical locations.

In episode A, the plumes originated from the BRZ zinc units began approaching the receptor site from easterly after midnight and swept across the receptor site at around 0040 LT. Thereafter, their plume centerlines swept back and forth across the receptor site and finally departed from the receptor site after 0200 LT. The plumes originating from the BRZ cadmium unit and the Cerro Copper unit showed a similar evolution pattern. However, as their station angles coincided with the 5-minute wind direction more frequently until 0400 LT, their temporal χ/Q profiles appeared broad and irregular in shape, compared with those of the BRZ zinc units.

In episode B, the plume trajectories that originated from the BRZ and Cerro Copper units also swept across the receptor site multiple times. As shown in Figure 3.9, the arrival times of the plumes for which the trajectory centerlines were through the receptor site were different for those units, i.e., 0545 LT for the BRZ Zn units, 0500 LT for the BRZ Cd unit, and 0740 LT the Cerro Copper unit, respectively. And these predictions were generally synchronous with the maximum concentrations of the corresponding tracers measured at the receptor site, i.e., 0530 ~ 0630 LT for Zn, 0430 ~ 0530 LT for both Cd and Pb, and 0630 ~ 0730 LT for Cu. Again, this agreement indicated that the BRZ and Cerro Copper plants were indeed the major emission sources during the episode and thus the TGPM-derived χ/Qs shown in Figure 3.10 were likely to be good seed values for the PDRM. In addition, the temporal profiles of TGPM-derived χ/Qs (Figure 3.10) resembled those of the

corresponding source strengths predicted by PMF (Figure 3.6), suggesting a good compatibility between TGPM and PMF.

3.4.4 PMF-seeded PDRM Analysis

As shown in Figure 3.11, the predictions for the marker species (Cd, Cu, Pb, and Zn) for the first 4-hour run (i.e., 0400 ~ 0800 LT) were similar to those for the 12-hour model run. However, the 4-hour solution for the next two 4-hour runs (i.e., 0800 ~ 1600 LT) generally better fit the observed concentrations than did the 12-hour solution. The improved predictions by the 4-hour approach suggest that emission rates at those facilities were probably varying and thus individual predictions of ERs for multiple time blocks were more accurate than a single-period average estimate. As for the cadmium smelters in the BRZ plant, their maximum emission rate (i.e., indicated by the cadmium ERs) in the early morning (0400 ~ 0800 LT) was consistent with the concurrent large excursion of cadmium observed at the receptor site. The largest ER of copper from the Cerro copper plant was also found in the early morning (0400 ~ 0800 LT). In contrast, the largest Zn emission rate of the primary zinc refining was predicted to occur in the late morning (0800 ~ 1200 LT). However, as a result of its greater χ/Qs in the early morning, the maximum contribution from the BRZ primary zinc unit as well as the maximum Zn concentration measured at receptor site was actually observed at around 0630 LT.

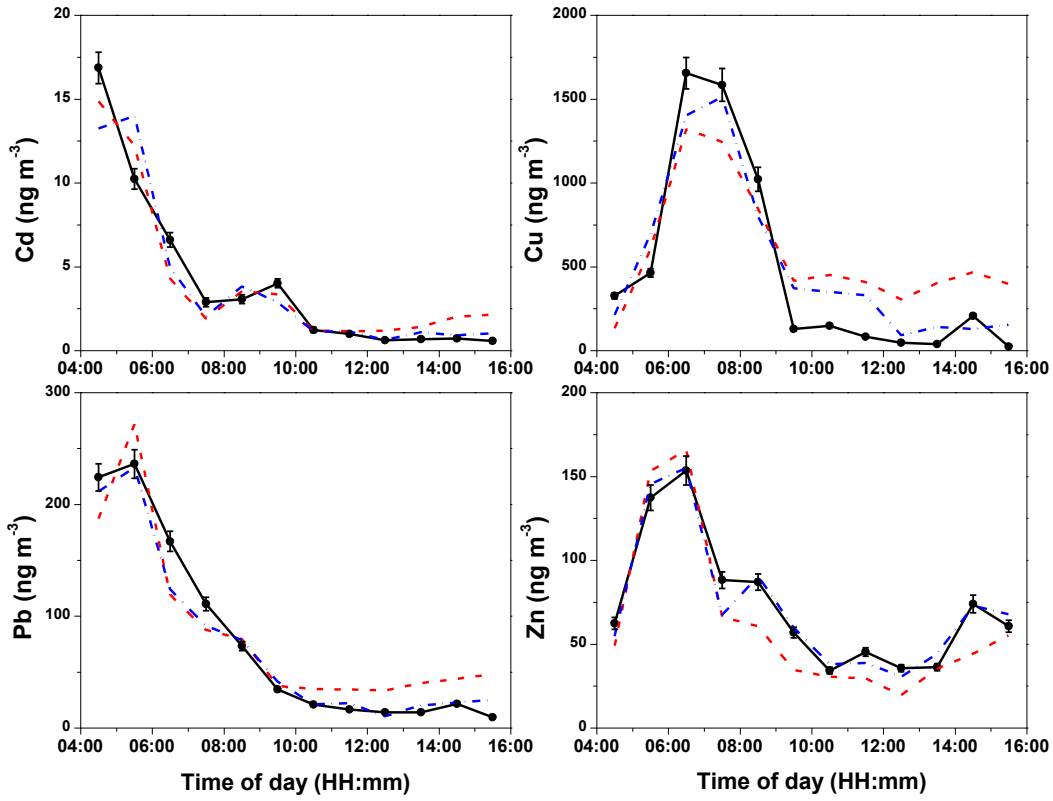

Figure 3.11 PDRM-predicted (blue dash-dot line for the three 4-hour model runs and red dash line for the single 12-hour solution, respectively) and observed concentrations (black solid line) of the key marker species in episode B.

In Figure 3.12 the source profiles (normalized with respect to the corresponding marker species) of the BRZ facilities are compared between the two episodes. The composite emission profiles of the BRZ plant (Figure 3.12d) did not show significant variations, except possibly for Pb and Cd which may be attributed to different production rates of primary zinc refining and cadmium smelting in the two episodes. However, as shown in panels a, b, and c of Figure 3.12, variations in the abundance profiles of Cu, Fe, and Mn were large for individual units. Compared with those corresponding profiles determined with PMF (Figure 3.5) in which copper levels were apparently overestimated, copper abundances in the BRZ profiles were effectively constrained by PDRM.

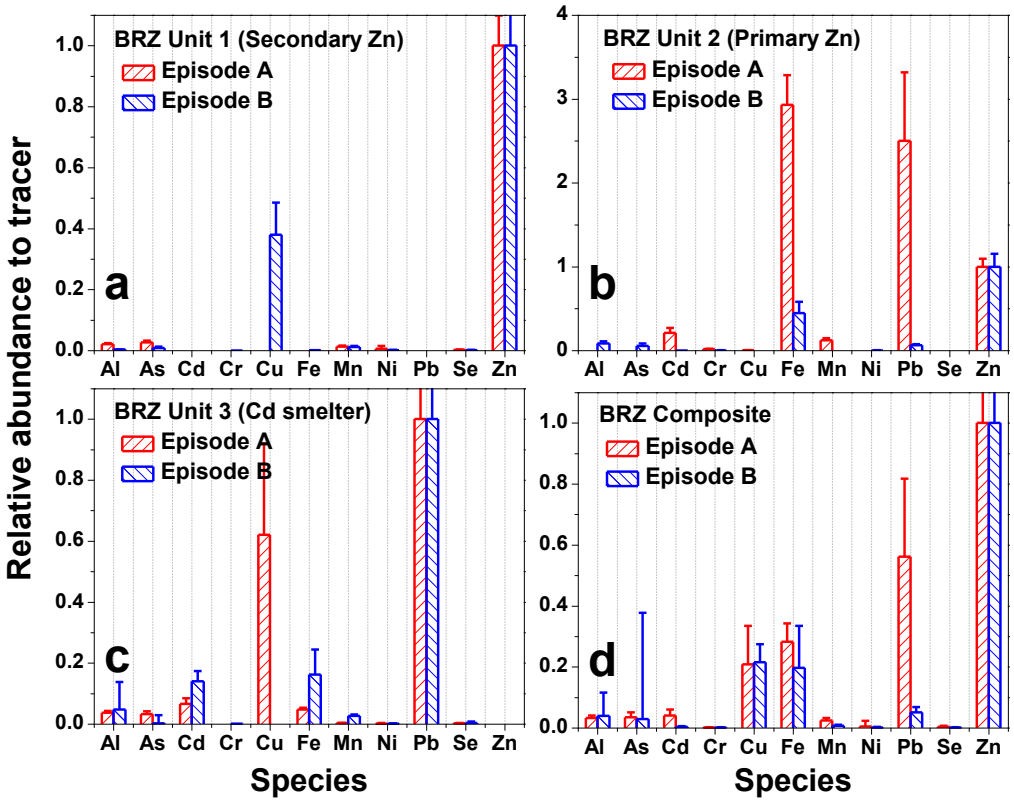

Figure 3.12 Comparison of the profiles of the BRZ units during the two episodes.

PDRM and PMF solutions for SEAS metals, $PM_{2.5}$, OC, EC, SO_2, and NO_x in episode B are shown in Figure 3.13. The PDRM-predicted pollutant concentrations in general were in good agreement with the ambient observations, although PDRM fits were slightly worse than those achieved with the PMF.

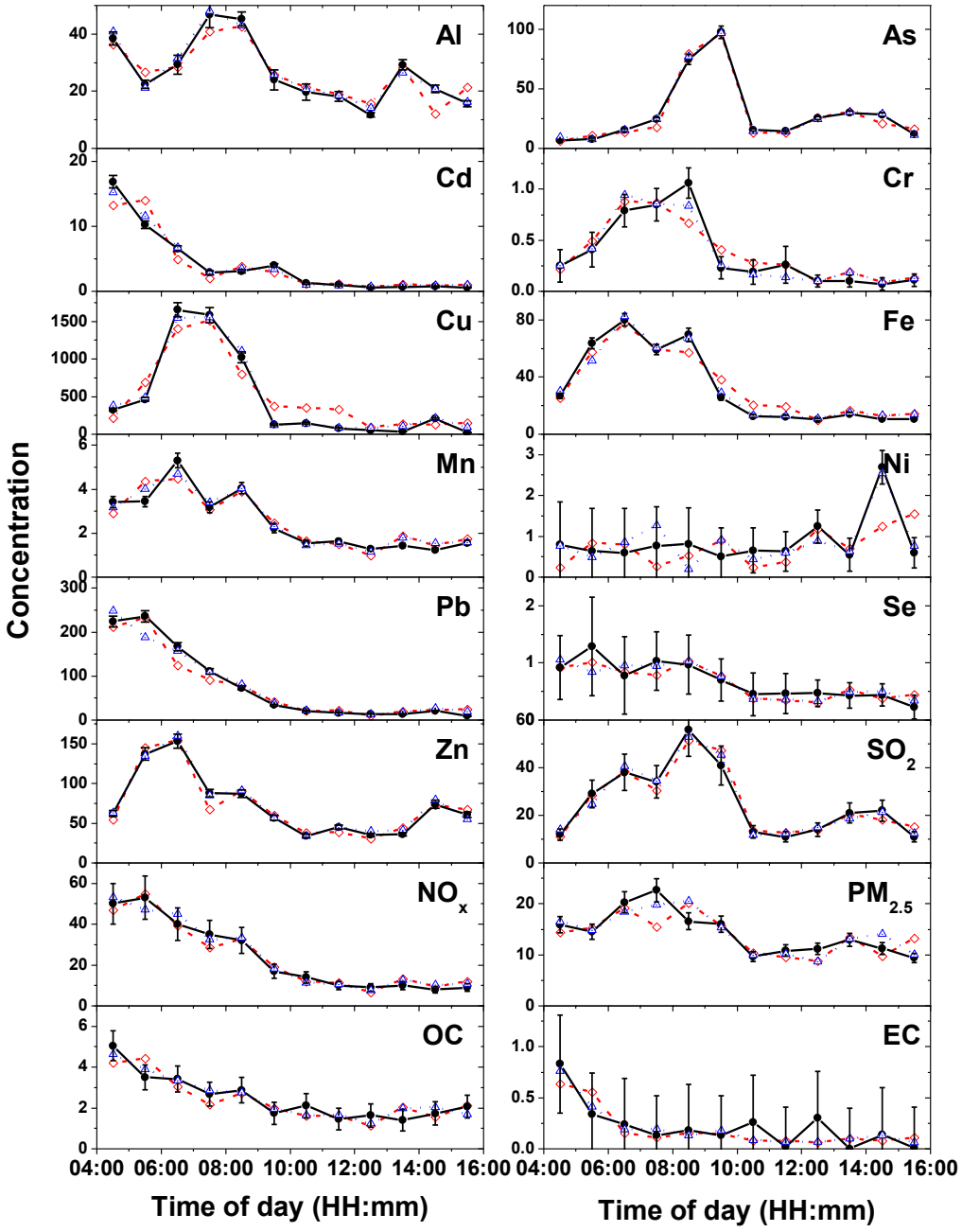

Figure 3.13 The observed (■), PMF-estimated (△), and PDRM-estimated (◆) concentrations of ambient pollutants at the St. Louis supersite in episode B (units: ng m^{-3} for metals; µg m^{-3} for $PM_{2.5}$, OC, and EC; and ppb for NO_x and SO_2).

The emission profiles of the BRZ units determined with PDRM are listed Table 3.4, wherein, each is normalized to the selected tracer species (i.e., whose normalized

value, 1.000, appears in bold type). ERs, in mg s^{-1}, relisted for each tracer species so that ER estimates for all species can be easily calculated. In episode B, the emission rate of Zn from the BRZ plant was only 4.9 mg s^{-1} predicted by PDRM (Appendix C5), far below its annual average ER of Zn (214 mg s^{-1}) according to TRI 2002. Meanwhile, a large ER of copper from the Cerro Copper plant was predicted to be 85 mg s^{-1}, although it was still less than the annual average ER of 135 mg s^{-1} from Cerro Copper according to TRI 2002. These predictions indicated that the BRZ plant was not in full operation during episode B. In contrast, the predicted ER of Zn from the BRZ plant was 174 mg s^{-1} in episode A and, meanwhile, the ER of Cu from the Cerro Copper plant was 13 mg s^{-1}, which suggested that the Cerro Copper plant was not in full operation during episode A.

Table 3.4 PDRM predicted profiles of the Zn and Cd units in the BRZ plant in episode B.

Species	BRZ Unit 1 [1]	BRZ Unit 2 [2]	BRZ Unit 3 [3]	BRZ composite [4]	Profile ratio of episode A to episode B [5]
Al	0.021 ± 0.003	$< 10^{-4} \pm < 10^{-4}$	0.037 ± 0.006	0.032 ± 0.009	1.22 ± 0.08
As	0.027 ± 0.006	$< 10^{-4} \pm < 10^{-4}$	0.033 ± 0.009	0.035 ± 0.016	0.83 ± 0.35
Cd	$< 10^{-4} \pm < 10^{-4}$	0.210 ± 0.061	0.066 ± 0.018	0.041 ± 0.019	0.10 ± 0.02
Cr	$< 10^{-4} \pm < 10^{-4}$	0.016 ± 0.005	$< 10^{-4} \pm < 10^{-4}$	0.001 ± 0.001	1.00 ± 0.001
Cu	$< 10^{-4} \pm < 10^{-4}$	0.003 ± 0.001	0.621 ± 0.300	0.209 ± 0.126	1.03 ± 0.14
Fe	$< 10^{-4} \pm < 10^{-4}$	2.932 ± 0.354	0.047 ± 0.006	0.282 ± 0.061	0.70 ± 0.15
Mn	0.013 ± 0.003	0.122 ± 0.026	0.003 ± 0.001	0.024 ± 0.009	0.29 ± 0.01
Ni	0.006 ± 0.009	0.000 ± 0.000	0.001 ± 0.002	0.005 ± 0.018	0.20 ± 0.02
Pb	$< 10^{-4} \pm < 10^{-4}$	2.503 ± 0.813	**1.000 ± 0.11**	0.562 ± 0.255	0.09 ± 0.26
Se	0.002 ± 0.002	$< 10^{-4} \pm < 10^{-4}$	0.002 ± 0.002	0.003 ± 0.004	0.33 ± 0.004

Zn	**1.000 ± 0.099**	**1.000 ± 0.096**	$< 10^{-4} \pm < 10^{-4}$	**1.000 ± 0.204**	1.00 ± 0.46
OC	17.75 ± 4.15	0.165 ± 0.039	8.46 ± 2.30	18.98 ± 8.24	0.28 ± 8.53
EC	$< 10^{-4} \pm < 10^{-4}$	$< 10^{-4} \pm < 10^{-4}$	2.95 ± 3.40	0.99 ± 2.06	0.09 ± 2.06
Tracer	Zn	Zn	Pb	Zn	
ER of tracer, mg s^{-1}	1.15	3.75	0.74	4.90	

[1] Secondary Zn smelter; profile normalized to Zn.

[2] Primary Zn smelter; profile normalized to Zn.

[3] Cd smelter; profile normalized to Pb.

[4] Composite of all BRZ units; normalized to Zn.

[5] The ratio of profiles obtained in episode A versus in episode B; normalized to Zn.

As shown in Table 3.5, the emission profile of the Cerro Copper plant determined by PDRM was compared with past reports (Chang et al. 1988, Amato and Hopke 2012) as well as with the SPECIATE profiles for secondary copper production (U.S.EPA 2006). The Zn/Cu and Pb/Cu ratios in the PDRM profiles are much smaller than those in Chang's study (Chang et al. 1988) and the SPECIATE profiles, but fall into the same magnitude compared with those in Amato and Hopke's study (Amato and Hopke 2012).

Table 3.5 Comparison of the PDRM-derived source profiles of the Cerro Copper plant with published profiles of copper production.

Species	PDRM-predicted		Amato and Hopke, 2012	SPECIATE (U.S.EPA 2006)		Chang et al., 1988
	Episode A	Episode B		Secondary Copper [1]	Secondary Copper [2]	
Al	0.0204 ± 0.0053	0.0116 ± 0.0023	0.0149	n.a.	n.a.	0.2
As	0.0288 ± 0.0166	$< 10^{-4} \pm < 10^{-4}$	0.0005	0.001 [3]	0.0072 [3]	n.a.
Cd	0.0002 ± 0.0001	0.0003 ± 0.0001	n.a.	n.a.	n.a.	n.a.
Cr	0.0007 ± 0.0004	0.0005 ± 0.0002	0.0005	n.a.	n.a.	n.a.

Cu	**1.0000 ± 0.3074**	**1.0000 ± 0.2041**	**1.0000**	**1** [3]	**1** [3]	**1.00**
Fe	0.0277 ± 0.0086	0.0291 ± 0.0047	0.0238	0.0114 [3]	0.0166 [3]	0.08
Mn	0.0117 ± 0.0030	0.0007 ± 0.0001	0.0019	0.0005 [3]	n.a.	0.012
Ni	0.0009 ± 0.0014	0.0001 ± 0.0001	0.0003	n.a.	0.0050 [3]	0.019
Pb	0.0009 ± 0.0002	0.0456 ± 0.0145	0.0415	0.1633 [3]	0.3817 [3]	0.87
Se	0.0000 ± 0.0000	0.0002 ± 0.0002	0.0004	n.a.	0.0084 [3]	0.007
Zn	0.0020 ± 0.0017	0.0106 ± 0.0031	0.0614	0.1083 [3]	0.1464 [3]	0.75
OC	0.1609 ± 0.0428	0.0003 ± 0.0001	3.7030	n.a.	n.a.	n.a.
EC	0.0093 ± 0.0052	0.0162 ± 0.0195	1.2457	n.a.	n.a.	n.a.

[1] Pyrometal - cathode charge.

[2] Pyrometal - regular charge.

[3] Uncertainty reported as zero.

3.4.5 Model Performance Evaluation

The overall modeling performance was evaluated for the observed and predicted concentrations (Table 3.6) using several statistical measures including mean fraction bias (MFB), normalized mean square error (NMSE), the fraction of predicted concentrations lying within a factor of 2 (Fa2) of the measured ambient concentrations, and Pearson's coefficient of correlation (*r*). The criteria for acceptable performance are: $-0.5 \leq MFB \leq 0.5$, $NMSE \leq 0.5$ and $Fa2 \geq 0.8$(Kumar et al. 1993). In addition, the correlation between predictions and observations is deemed excellent if $r \geq 0.9$ and poor if $r \leq 0.6$. The PDRM solution showed acceptable predictions of the marker species (Zn, Cd, Pb, and Cu) as well as other species except for Ni and EC. Despite their unacceptable performance evaluation, a good recovery (≥ 80%) of the total mass of Ni and EC was achieved and, as shown in Figure 3.13, the PDRM-

predicted concentrations of these two species were generally within their (large) measurement uncertainties.

Table 3.6 Performance statistics [1] between the observed and predicted concentrations by PDRM.

Species	Observed [2]	Predicted [2]	MFB [3]	NMSE [4]	Fa2 [5]	r [6]
Al	26.78	26.54	-0.01	0.02	1.00	0.933
As	29.28	28.82	0.01	0.01	1.00	0.991
Cd	4.02	3.90	-0.06	0.08	1.00	0.938
Cr	0.37	0.38	-0.14	0.08	1.00	0.912
Cu	476.13	515.13	-0.45	0.06	0.84	0.964
Fe	32.97	34.09	-0.13	0.03	1.00	0.976
Mn	2.52	2.53	-0.02	0.02	1.00	0.941
Ni	0.87	0.74	0.20	0.49	**0.58**	**0.363**
Pb	78.37	75.12	-0.09	0.02	0.92	0.987
Se	0.68	0.65	0.04	0.04	1.00	0.890
Zn	72.59	72.10	0.01	0.01	1.00	0.979
SO_2	25.17	25.06	-0.01	0.01	1.00	0.976
NO_x	23.92	23.87	-0.03	0.01	1.00	0.986
$PM_{2.5}$	14.27	13.83	0.03	0.04	1.00	0.724
OC	2.47	2.39	0.03	0.04	1.00	0.883
EC	0.22	0.19	-0.13	0.25	**0.58**	0.791

[1] Boldfaced type indicates unacceptable performance.

[2] Average concentrations; variables are given in ng m^{-3} for metals, ppb for SO_2 and NO_x, and µg m^{-3} for others.

[3] MFB: mean fractional bias ($= \left(\frac{2}{N}\right) \sum_{i=1}^{N} [(O_i - P_i)/(O_i + P_i)]$).

[4] NMSE: normalized mean square error ($= \left[\left(\frac{1}{N}\right)\sum_{i=1}^{N}(O_i - P_i)^2\right] / \left[\left(\frac{1}{N}\right)\sum_{i=1}^{N}(O_i \times P_i)\right]$).

[5] Fa2: fractions of the predictions within a factor of 2 of the observed values ($0.5 \leq C_{pred}/C_{obs} \leq 2.0$).

[6] *r*: Pearson's coefficient of correlation.

3.5 Concluding Remarks

Compared with PMF, the PDRM model has shown a strong capability of resolving contributions from nearby point sources based on the differences in their plume dispersion factors, but *a priori* knowledge of source emissions (i.e., approximate scale of emission rates) and detailed meteorological conditions (i.e., wind profiles, atmospheric stability classes) are essential to ensure meaningful results. Although source cross contamination in the PMF solution has been realized, the PMF analyses appear to well serve as the initial guess of emission rates and the estimates of non-point source contributions in the PDRM modeling. Instead of a source non-specific tracer gas (i.e., SO_2 or NO_x), a group of marker species (one specified for each source but they may be in common for different sources) were used to tune the TGPM-derived plume dispersion profiles of individual sources. In addition, the advantage of multiple PDRM runs for short modeling timeframes was revealed as it better tuned the shape of the plume dispersion profiles for industrial sources with possible temporal variations. The comparison with the PMF results showed that the possibly overestimated copper contributions from the BRZ plant by PMF were effectively restrained in the PMF-seeded PDRM approach. The comparison with past studies and the performance evaluation showed that, at least, qualitatively-accurate source profiles and emission rates could be obtained with this new approach. In the past, estimates of cadmium emissions at the BRZ plant were based on emission factor data

from the SPECIATE database. As the validity of the general emission profile could not be verified, the determined metal emissions in exhaust gases were presumably associated with large errors by that method. In contrast, our error analysis indicated that the TGPM-derived χ/Qs are subject to a maximum relative uncertainty of 59 to 92 %, which are almost within the bound conditions of PDRM tuning (i.e, $a_{j,k}$ = 0.1 ~ 2.0 in Equation 3.1). Thus the predicted ERs with the TGPM-driven PDRM are expected to be more accurate than those based on the SPECIATE data. In summary, this PMF-seeded PDRM approach coupled with highly time-resolved ambient measurements could provide a useful new tool for remote monitoring of ERs of those pollutants, such as heavy metals, not measured by continuous emission monitors.

Chapter 4: The Study of a Typical Traffic Episode in Baltimore

4.1 Background

Effects of short-term exposures to vehicular traffic emissions have been emphasized in the past years (Finkelstein, Jerrett and Sears 2004, Schwartz 2005, Lipfert et al. 2006, Kaur, Nieuwenhuijsen and Colvile 2007, Park, Akinbami and Woodruff 2009, Jacobs et al. 2010, Nawrot et al. 2011). For instance, it was found that a significant number of cardiac victims in Germany had been exposed to high traffic density in hours prior to their heart attacks (Peters et al. 2004). Rapidly elevated concentrations of airborne fine particles were often observed during traffic rush hours in US and Europe cities, which resulted in acute problems such as cardiovascular mortality (Chuang et al. 2007, O'Connor et al. 2008) and respiratory infections (Brauer 2002, Karr et al. 2009).

Routine monitoring of PM has been limited to mass concentrations in the United States, as current regulations are based upon total mass within a specified range of particle size. Recently, increasing attention has been attracted to number concentrations of fine PM, which are considered by some to be more directly associated with their health outcomes (Strak et al. 2009, Song et al. 2011). In particular, ultrafine particles (UFP, $d_p < 100$ nm) were usually predominant in number in areas affected by primary motor vehicle emissions (Morawska et al. 2008) and, despite their small contributions to the total $PM_{2.5}$ mass, they exhibited stronger adverse effects than larger ones (Knibbs, Cole-Hunter and Morawska 2011).

Positive matrix factorization (PMF) (Paatero and Tapper 1994, Paatero 1997, U.S.EPA 2008) and UNMIX (Henry 2000, U.S.EPA 2007) have been widely used in PM source apportionment (Ogulei et al. 2006, Pancras et al. 2011). However, very few applications of these complementary models have been made with regard to particle size distributions (Kim et al. 2004, Ogulei et al. 2007, Yue et al. 2008, Costabile et al. 2009, Ban-Weiss et al. 2010, Gu et al. 2011) and effective resolving of source profiles of size distributions was rarely achieved. This is to a great extent due to the fact that the signature size distribution of a particular aerosol emission, unlike its chemical composition, is not necessarily stable owing to coagulation and depositional growth processes and, therefore, is sensitive to changes in ambient environmental conditions such as wind speed (Knibbs and de Dear 2010), temperature (Thai, McKendry and Brauer 2008), relative humidity (Kaur and Nieuwenhuijsen 2009), and mixed layer depth (Weichenthal et al. 2008). Besides, lack of speciation information of size-specific particles was often another hindrance to confident source identification (Kim et al. 2004).

Past air quality studies in Baltimore (Suarez and Ondov 2002, Larsen and Baker 2003, Ogulei et al. 2005, Ogulei et al. 2006, Ondov et al. 2006, Park et al. 2006a) revealed that motor vehicle exhaust is an important primary source of air pollution because the city is both a populous urban area and a major Mid-Atlantic transport corridor. For example, gasoline and diesel vehicles accounted for 26 % and 1 % of the annual $PM_{2.5}$ in Baltimore, respectively, according to Ogulei et al. (Ogulei et al. 2005).

Assessments of the influence of motor vehicle emissions on air quality in urban areas heavily rely on the availability of relevant and detailed abundance profiles (Nielsen 1996, Glaser et al. 2005, Oliveira et al. 2010). Several motor-vehicle profiles are available in the EPA's SPECIATE database, but most were derived from dynamometer tests of a limited number of vehicles using a relatively small number of operating conditions. Moreover, very few of these profiles include much beyond abundances of EC, OC, several metals, and relatively few semi-volatile organic compounds known to be markers of various classes of motor vehicle emission scenarios (Watson 1979, Rogge et al. 1993b, Khalili, Scheff and Holsen 1995, Rönkkö et al. 2006, Landis et al. 2007). Motor vehicle source profiles of organic compounds were extensively investigated by Rogge (Rogge et al. 1993b, Rogge et al. 1996) and Schauer (Schauer et al. 1996, Schauer and Cass 2000) by measuring diluted tailpipe exhaust from several (< 20) vehicles with GC-MS. These early 1990's studies were generally carried out in California with different emission standards and environmental factors (e.g., temperature, humidity, altitude, engine inspection frequency) from urban areas in the Mid-Atlantic states, and are probably outdated because gasoline composition and engine and emission control technologies have changed substantially since then (e.g., the Clean Air Act completely banned the sale of leaded fuel since 1996 and gasoline typically contains up to 10 % ethanol nowadays). Lastly, there are few, if any, profiles containing a large number of semi-volatile organic compounds (SVOCs), in addition to EC, OC, nitrate, sulfate, metal, and VOCs, along with primary gas emissions of NO, NO_2, and CO. Fewer still were collected in urban areas or traffic tunnels such that emissions from large numbers of

vehicles could be examined during real-world driving conditions. And fewer still of these were collected at high time resolution, i.e., such that motor vehicle emissions could be better isolated from interfering sources.

In this present work, a short-term PM excursion due to motor vehicle emissions observed during the EPA Baltimore supersite project was investigated. In specific, we aimed to extract a comprehensive profile of motor vehicle emissions containing both particle size distributions and abundances of SVOCs in addition to routine species using highly-time resolved data collected during a cool-weather $PM_{2.5}$ episode in November 2002, described by Park et al. (Park et al. 2006a).

4.2 Data Inputs

4.2.1 Site and Episode Description

The Baltimore Ponca street supersite (Figure 4.1) was in close proximity to two major highways, I-895 and I-95, and about 1 kilometer north of the two tunnel toll facilities (i.e., Fort McHenry and Baltimore Harbor tunnels), through which more than 180,000 motor vehicles passed daily in total. In specific, I-895 curves from northbound to north eastbound near the supersite which was only 50 m away from the roadway and about 5 m lower than the road surface. Thus when the movement of motor vehicles was slow and drainage flows traveled along the I-895 corridor to the receptor site under windless or mild wind conditions, high concentrations of traffic emitted pollutants were observed at this site. This strategically-selected location renders it ideally suited to assess the traffic impact on urban air quality. Nevertheless, past studies (Ogulei et al. 2005, Park et al. 2005a, Ondov et al. 2006, Park et al. 2006a)

have revealed that air quality at this site was also influenced by local industrial sources, which mostly came from the southeastern Dundalk and southwestern Curtis Bay industrial areas. Thus, in this study, I sought to resolve motor vehicle emissions correlating with the traffic flux during the episode from possible contributions from industrial and residential sources of PM along the I-895 corridor.

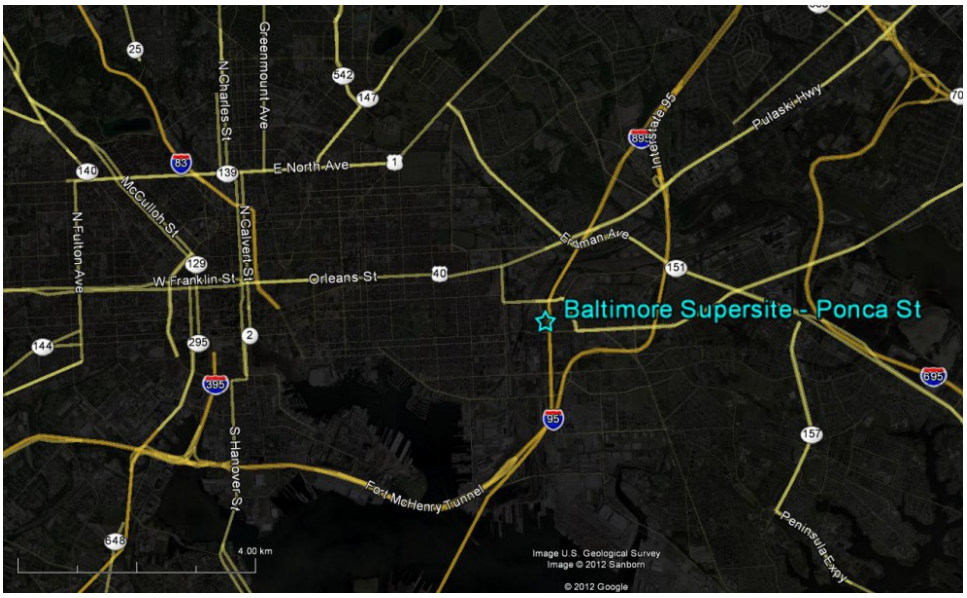

Figure 4.1 The Road map around the Baltimore supersite at Ponce street (provided by Google Map).

The three-day episode selected for this work lasted from November 19th through 21st, 2002, and corresponds to episode F in Park's study of a series $PM_{2.5}$ episodes at the Ponca street supersite (Park et al. 2006a). During this period, the time series of $PM_{2.5}$ concentrations were generally in a synchronous pattern with those of traffic-related gaseous pollutants (i.e., NO_x and CO), especially in the mornings, as shown in Figure 4.2. Nevertheless, close inspection revealed that NO_x/CO ratios were different during some $PM_{2.5}$ excursions. For example, NO_x/CO was small at ~ 1500 LT on the 20th, and might have been partially due to NO_x reaction with hydroxyl radicals in the

early afternoon, in contrast to that observed in the morning $PM_{2.5}$ excursion. However, the narrow peak width of that NO_x excursion and the prevailing southeasterly winds (> 2 m s^{-1}) during this period suggested an attribution to an industrial source (i.e., residual oil combustion). Northerly to northeasterly winds with low speeds (< 2 m s^{-1}) were prevailing in the whole episode except for the above-mentioned afternoon and the noon of the 19th when NO_x concentrations were low. In particular, the wind was nearly stagnant (< 1 m s^{-1}) in the morning of the 20th, which facilitated the rapid built-up of pollutants. As a result, a large $PM_{2.5}$ excursion exceeding the 24-hr National Ambient Air Quality Standard (NAAQS) of 65 μg m^{-3} at the time (U.S.EPA 2004b) was observed between 0500 and 0800 LT.

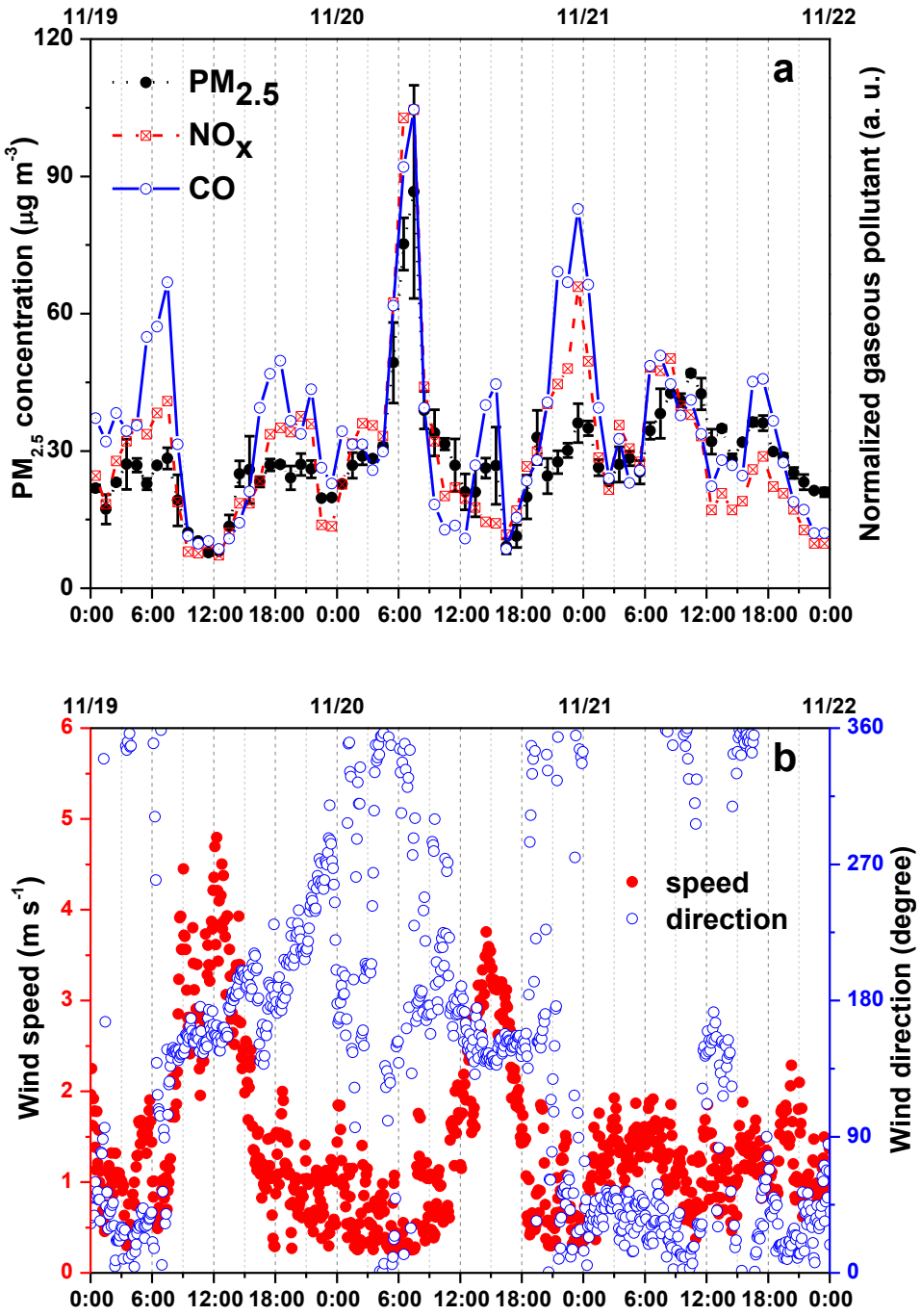

Figure 4.2 Time series of a) concentrations of $PM_{2.5}$, NO_x, and CO (concentrations of NO_x and CO were normalized to the maximum concentration of $PM_{2.5}$); and b) wind profile from November 19th through 22nd, 2002 at the Ponca street supersite.

The evolution of ambient temperature and relative humidity (RH) during this episode (Figure 4.3) was typical of the cold, late-fall season. That is, the highest RH

and lowest ambient temperature of the day was observed at around 0600 LT before sunrise. The low temperature was consistent with low mixing height, which trapped primary vehicular emissions and favored condensation/absorption of semi-volatile and nonvolatile species onto particles (Rönkkö et al. 2006). The episode ended in the morning of the 22nd due to precipitation.

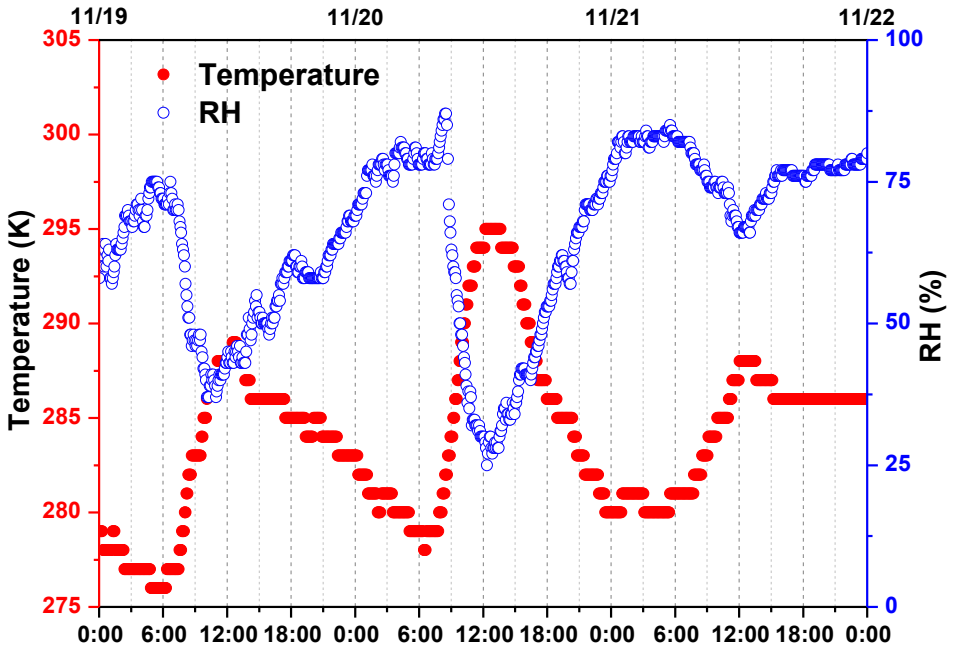

Figure 4.3 Temporal profiles of ambient temperature and relative humidity (RH) from November 19th through 22nd, 2002 at the Ponca street supersite.

4.2.2 Data Description

Ambient data were retrieved from the Baltimore Supersite database and the project's archives (http://www2.chem.umd.edu/supersite/), including 10-minute concentrations of principle PM constituents (EC, OC, sulfate and nitrate), 30-minute SEAS metal (Al, As, Cd, Cr, Cu, Fe, Mn, Ni, Pb, Se, and Zn) concentrations, 10-minute concentrations of NO_x and CO (provided by the Maryland Department of Environment), 5-minute number concentrations of airborne particles measured with

the Scanning Mobility Particle Sizer (SMPS) and the Aerodynamic Particle Sizer (APS), 5-minute meteorological records (wind speed and direction, ambient temperature, and humidity), and hourly tunnel (i.e., the I-895 tunnel and the Fort McHenry tunnel) traffic statistics for various vehicle types. In addition, measurements of 117 SVOC species in 19 categories (Rogge et al. 2011) were available at 3-hour intervals during the episode.

The SMPS and APS measurements encompassed 53 particle size channels ranging from 10 to 450 nm, and 22 channels ranging from 0.5 to 2.5 μm, respectively. In this study, those particle size distributions were combined to yield a composite dataset, following a standard preprocessing step which was taken to minimize the possible negative impact on the volume distribution caused by the combination (Peters et al. 1993). In specific, the data in the last channel (aerodynamic particle diameter, d_p, > 400 nm) of the SMPS distribution and the first five channels (d_p < 0.73 μm) of the APS distribution were eliminated to avoid the artificial wrinkles in the combining region by direct combination of SMPS and APS data for the same sample.

4.3 Methods

In this study, the abundance profiles of motor vehicle exhaust were extracted using the following four methods: 1) direct analysis of pollutant peaks occurring during the morning rush hour; 2) linear regression based on a windless model analysis (WMA); 3) positive matrix factorization analysis; and 4) UNMIX modeling.

It is convenient to retrieve the profile of motor vehicle emissions by direct peak observation (DPO), as the large excursion of $PM_{2.5}$ (i.e., about 5 fold background level with a full width at half maximum (FWHM) of only 2.5 hours) in the morning

of November 20th was highly correlated with that of the rush-hour traffic. Nevertheless, an inherent flaw of the DPO approach is that variations of background sources were insufficiently considered, although the peak observation was corrected to some extent by using the peak onset as the background. In this calm morning (i.e., wind speed < 1 m s^{-1} from 0100 to 0800 LT), a windless dispersion model is applicable, as described below, based on the assumption that motor vehicle contributions to ambient concentrations at the near-road receptor site were proportional to the road traffic density. Hence linear regressions of ambient concentrations against the traffic fluxes provided a way of excluding contributions from sources other than motor vehicles which were determined as the residuals of these regressions.

As described in the previous chapters, UNMIX and PMF are complementary methods that could provide alternative ways of background removal; both are able to generate matrices of abundance profiles and source contributions with non-negative constraints applied; neither requires *aprior* knowledge of those sources; and both have been simultaneously employed in many air quality studies (Kim et al. 2004, Pekney et al. 2006, Watson et al. 2008, Henry and Christensen 2010). Unlike the WMA-based linear regression, these receptor models rely on the covariance of contributions from all sources, rather than a single variable (i.e., traffic flux) that presumably well represents vehicular emissions.

4.3.1 Direct Peak Observation

The direct peak observation (DPO) was applied to the period between 0700 and 0800 LT on November 20th, when the largest concentrations of $PM_{2.5}$, EC and OC of

the day were observed. The hourly observation from 0100 to 0200 LT was considered as the background because it preceded the onset of the $PM_{2.5}$ excursion and the lightest traffic density of the day was observed during that period (Figure 4.5). The background-corrected peak concentrations of ambient pollutants including NO, NO_2, NO_x, CO, EC, OC, sulfate, nitrate, SEAS metals, and 117 SVOC species in 19 categories were then normalized with respect to that of $PM_{2.5}$ to obtain the corresponding abundances (µg per µg of $PM_{2.5}$) of those species, as follows:

$$F_j = \frac{c_{p,j} - c_{bkg,j}}{c_{p,PM} - c_{bkg,PM}} \quad (4.1)$$

where F_j is the abundance (µg per µg of $PM_{2.5}$) of ambient species j; $c_{p,j}$ and $c_{bkg,j}$ are the measured concentrations (µg m^{-3}) of species j in the peak observation and the background observation, respectively; and $c_{p,PM}$ and $c_{bkg,PM}$ are the measured concentrations (µg m^{-3}) of $PM_{2.5}$ in the peak observation and the background observation, respectively.

Note that for the SVOC data, the concentrations measured at 3-hour time resolution were reallocated into hourly intervals so that they could be treated with the hourly averaged species. This was done using the hourly traffic fluxes measured in the I-895 tunnel (refer to Appendix D1 for detailed process), as follows.

$$c_{1h,i} = \frac{v_{1h,i} \cdot c_{3h}}{v_{3h}/3} \quad (4.2)$$

where $c_{1h,i}$ is the 1-hour concentration (µg m^{-3}) of ambient SVOC species in the i^{th} hour of the 3-hour time block, c_{3h} is the background-corrected measured concentration (µg m^{-3}) of this SVOC species in the corresponding 3-hour time block,

$v_{1h,i}$ is the 1-hour vehicle counts (number of vehicles) in the i^{th} hour of the 3-hour time block, and v_{3h} is the total vehicle counts (number of vehicles) in the corresponding 3-hour time block. Note that each 3-hour set of all SVOCs was processed separately to ensure that data in different 3-hourly periods were not blended and that the temporal information in the raw data was retained.

The uncertainty associated with the resulted abundance of ambient species j, σ_{Fj}, was from the deviation propagation of measurement uncertainties, as follows.

$$\sigma_{Fj} = F_j \sqrt{\left(\frac{\sigma_{p,j}}{c_{p,j}}\right)^2 + \left(\frac{\sigma_{bkg,j}}{c_{bkg,j}}\right)^2} \quad (4.3)$$

where $\sigma_{p,j}$ and $\sigma_{bkg,j}$ are the measurement uncertainties (μg m^{-3}) of species j in the peak observation and the background observation, respectively.

By considering each size channel as an individual species, hourly-average particle number concentrations from the integrated SMPS-APS size distributions in 69 size channels (i.e., from 9.65 nm to 2.5 μm) were processed in the same way to generate the characteristic particle number size distribution of motor vehicle particle emissions.

4.3.2 Windless Model Analysis

The windless model analysis was performed for the period from 0100 to 0800 LT on November 20th, when calm winds (i.e., wind speed < 1 m s^{-1}) were observed. This windless condition allowed the application of a windless dispersion model (Jin and Fu 2005), in which traffic emissions affecting the receptor site are considered as being dispersed from a line source (i.e., I-895 in this study), as follows.

$$c_j = \frac{2s\sum k_i e_{ij}}{(2\pi)^{3/2}} \int \frac{1}{\beta r^2} dl \tag{4.4}$$

where c_j is the concentration (μg m^{-3}) of ambient pollutant species j in the windless period; s is the total traffic flux (vehicle s^{-1}); k_i is the fraction of vehicle type i; e_{ij} is the emission factor of species j (g m^{-1} $vehicle^{-1}$) from a single vehicle of type i at a given speed; l is the length (m) of the source; r is the distance (m) from the receptor site to the source point; and β is a road coefficient (μm s^{-1}). And the integral part in the equation represents a road constant (s m^{-2}) at the given location.

For any ambient species j,

$$e_{ij} = E_i \times F_{ij} \tag{4.5}$$

where E_i is the $PM_{2.5}$ emission factor (μg m^{-1}) of vehicle type i, and F_{ij} is the fraction quantity (dimensionless) of the j^{th} species in the emissions from the i^{th}-type vehicles.

When the distance (d) between the receptor site and the road is much smaller than the length of the roadway source (L), r^2 is approximately the sum of d^2 and l^2 (refer to Appendix D2 for detailed derivation of the geometric relation), as illustrated in Figure 4.4. Hence Equation 4.4 can be expressed as follows: θ

$$c_j = \frac{2s\sum k_i E_i F_{ij}}{\beta(2\pi)^{3/2}} \int_{l=0}^{L} \frac{1}{d^2+l^2} dl \tag{4.6}$$

where d is the distance between the receptor site and I-895, and L is effective length of road where the road remains heading downhill to the receptor site. After integration, Equation 4.6 gives:

$$c_j = \frac{2s\sum k_i E_i F_{ij}}{(2\pi)^{3/2}} \times \frac{atan(L/d)}{\beta \cdot d} \quad (4.7)$$

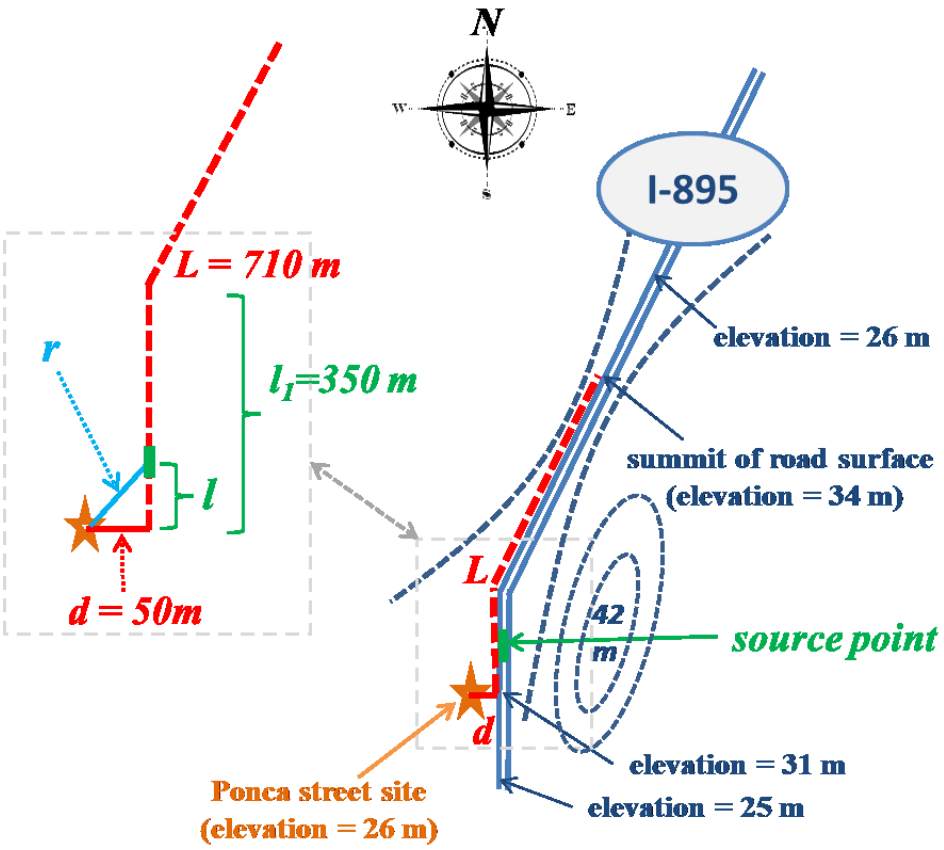

Figure 4.4 Schematic representation of the I-895 roadway near the receptor site as a line source.

For calculation of $PM_{2.5}$ emission factors, Equation 4.4 can be simplified as:

$$c_{PM} = \frac{2s\sum k_i E_i}{(2\pi)^{3/2}} \times \frac{atan(L/d)}{\beta \cdot d} \quad (4.8)$$

where c_{PM} is the concentration (μg m^{-3}) of $PM_{2.5}$.

Using the ruler function available in Google earth, *d* and *L* were estimated to be 50 and 710 m, respectively, in this study. The total traffic flux and fractions of different

vehicle types were obtained from the hourly traffic statistics recorded in the I-895 tunnel.

Since k_i and E_i are constants specific to an individual vehicle type i in a given scenario, the product of k_i and E_i represents a weighted emission factor of vehicle type i. When the vehicle composition is constant and the contribution from one type of vehicles is dominant over those from others, Equation 4.7 can be approximately expressed as:

$$c_j = \frac{2s \cdot \overline{E} \cdot \overline{F}_j}{(2\pi)^{3/2}} \times \frac{atan(L/d)}{\beta \cdot d} \tag{4.9}$$

where $\overline{E}$ is a weighted average of $PM_{2.5}$ emission factor (μg m^{-1}) and $\overline{F_j}$ is the observed abundance (μg per μg of $PM_{2.5}$) of species j in the average profile of motor vehicle emissions.

In this case, 2-axle gasoline type light-duty vehicles were dominant and diesel vehicles with 3 or more axles only represented a very small fraction (~ 3 %) of the morning traffic on the 20th. In addition, the variations in the fraction of gasoline type vehicles was limited (i.e., < 3 %) throughout the $PM_{2.5}$ excursion. Hence Equation 4.9 can be re-written as:

$$c_{jk} = K \cdot s_k \cdot F_j \tag{4.10}$$

where c_{jk} is the ambient concentration of species j in the k^{th} hourly observation, s_k is the traffic flux (s^{-1}) in the k^{th} observation made at the I-895 tunnel, and the road coefficient $K = \frac{2 \cdot \overline{E} \cdot atan(L/d)}{(2\pi)^{3/2} \cdot \beta \cdot d}$ is a constant for this modeling period (μg s m^{-3} per

vehicle). Thus, the values of $K \cdot F_j$ can be solved by linear regression of c_{jk}s against s_ks. Here, a separate linear regression was implemented using the k = 7 windless observations for each of the 137 species, c_{jk}s, including NO, NO_2, NO_x, CO, TEOM $PM_{2.5}$ mass, EC, OC, sulfate, nitrate, 11 SEAS metals, and 117 SVOCs (individually, and after grouping into 19 categories). In addition, 69 linear regressions were implemented for the seven hourly-averaged observation intervals prepared from the particle number concentrations versus size data by treating the concentration of particles in each size channel as a separate size species (i.e., one species for each of the 69 size channels from 9.65 nm to 2.5 µm). The regressions were performed in MATLAB using the standard expression.

$$c_{jk} = \left(\mathrm{M}_j \pm \sigma_{Mj}\right) \cdot s_k + \left(\mathrm{r}_{jk} \pm \sigma_{rjk}\right) \tag{4.11}$$

where slopes, M_js, are the products $K \cdot F_j$ (µg s m^{-3} $vehicle^{-1}$) in Equation 4.10, r_{jk}s are the residual concentrations (µg m^{-3}), and σ_{Mj} and σ_{rjk} are the uncertainties in the slopes and residuals, respectively.

The abundance (µg per µg of $PM_{2.5}$) of ambient species j was obtained by normalization of B_j with respect to the corresponding fitting coefficient of $PM_{2.5}$, $\mathrm{M}_{PM2.5}$, as follows.

$$F_j = \frac{\mathrm{M}_j}{\mathrm{M}_{PM2.5}} \tag{4.12}$$

The uncertainty (µg per µg of $PM_{2.5}$) associated with the abundance of ambient species j, σ_{Fj}, was determined as the deviation propagation of measurement uncertainties and fitting uncertainties, as follows.

$$\sigma_{Fj} = F_j \sqrt{\left(\frac{\sum_{k=1}^{m}\left(\sigma_{jk}/c_{jk}\right)}{m}\right)^2 + \left(\frac{\sigma_{Bj}}{B_j}\right)^2} \qquad (4.13)$$

where m = 7, i.e., the total number of windless observations, and σ_{jk} is the measurement uncertainty (μg m^{-3}) of species j in the k^{th} observation.

4.3.3 Receptor Modeling

The modeling period was extended to 24 hours (0000 ~ 2400 LT) on November 20th, 2002, to avoid unacceptable total degrees of freedom in these multivariate analyses. Both the mass concentrations of $PM_{2.5}$ as well as its constituents (i.e., EC, OC, sulfate, nitrate, and SEAS metals) and the particle number concentrations in different size channels from 10 nm to 2.5 μm were used in each modeling. Two criteria gaseous pollutants that are present in motor vehicles emissions, NO_x and CO, were also included in each modeling. SVOCs were excluded from the modeling because hourly SVOC concentrations could not be obtained by the decomposition of 3-hour data, as described in Equation 4.2, for the periods (e.g., the windy afternoon) when ambient pollutants were poorly correlated with the traffic. Strategically, the UNMIX was applied first and the PMF modeling was then run with the number of sources specified from the former.

4.3.3.1 UNMIX

The EPA UNMIX 6.0 model was used as described in the user's manual for EPA UNMIX 6.0 (U.S.EPA 2007). Due to the inability of UNMIX to handle more than 50 variants, 22 selected size bins that were evenly distributed (i.e., median particle sizes for the 22 channels were: 12.9, 24.6, 35.2, 47, 54.2, 67.3, 77.7, 83.5, 89.8, 104, 129,

160, 198, 246, 305, 835, 965, 1197, 1486, 1843, 1981, and 2458 nm, respectively), instead of all the size channels, were used. The number of sources in this study was five, as determined by UNMIX. Source contribution edge plots (Appendix D3) were employed to ensure the distinct nature of sources and the bootstrap method was used to estimate the variability in the source profiles. The standard deviations in the UNMIX-derived profiles were those output by the model itself.

4.3.3.2 PMF

The EPA PMF v3.0 program was used in accordance with the user guide for EPA PMF v3.0 (U.S.EPA 2008). Compared with the UNMIX modeling, more size channels were included in the PMF modeling (i.e., median particle sizes for the 60 size channels used for PMF were: 19.8, 21.3, 22.9, 24.6, 26.4, 28.4, 30.5, 32.8, 35.2, 37.9, 40.7, 43.7, 47, 50.5, 54.2, 58.3, 62.6, 67.3, 72.3, 77.7, 83.5, 89.8, 96.5, 104, 111, 120, 129, 138, 149, 160, 172, 184, 198, 213, 229, 246, 264, 284, 305, 328, 352, 379, 583, 626, 673, 723, 777, 835, 898, 965, 1037, 1114, 1197, 1286, 1382, 1486, 1596, 1715, 1843, and 1981 nm, respectively). Note that the first 9 size channels (< 18.4 nm) were excluded from modeling as their scaled residuals (e_{ij}/s_{ij}) always exceeded the criterion (i.e., $e_{ij}/s_{ij} \leq 4$) in the initial modeling trials. Different numbers of factors from 3 to 9 were tested but a factor number of 5 was adopted in the present solution to be most consistent with the UNMIX modeling results. It was found that further increasing of the number of factors resulted only in decomposing one of the factors and did not significantly affect the fit quality. In addition, different values (-0.3 to 0.3) of the rotational parameter, FPEAK, were tested (Paatero et al. 2005). The estimates

of standard deviations in the PMF profiles were based on the variability in three FPEAK solutions (FPEAK = -0.3, 0, and 0.3).

4.4 Results and Discussion

4.4.1 Traffic Analysis

The tunnel traffic counts of I-895 and I-95 were well correlated ($r^2 = 0.985$) with each other during the period from November 19th through 22nd (Appendix D4). However, considering that the receptor site is closer to I-895 than I-95 and the impact of motor vehicle emissions often falls rapidly with increasing off-road distance (Hitchins et al. 2000), only the I-895 tunnel traffic was included in the analysis. As shown in Figure 4.5, the I-895 traffic counts exhibited a bimodal daily pattern with two traffic rush-hours observed, one in early morning and the other in late afternoon, respectively (Figure 4.5). In contrast, heavy-duty diesel vehicles (HDDV, > 3 axles) showed only one daily peak at noon. During this episode, $PM_{2.5}$ concentrations were in a temporal pattern similar to the traffic density of I-895 with several exceptions (Figure 4.5): the blurred peaks in the morning of the 19th and the afternoon of the 20th were due to strong winds (> 3 m s^{-1}), and those in the afternoon of 22nd were due to rain wash.

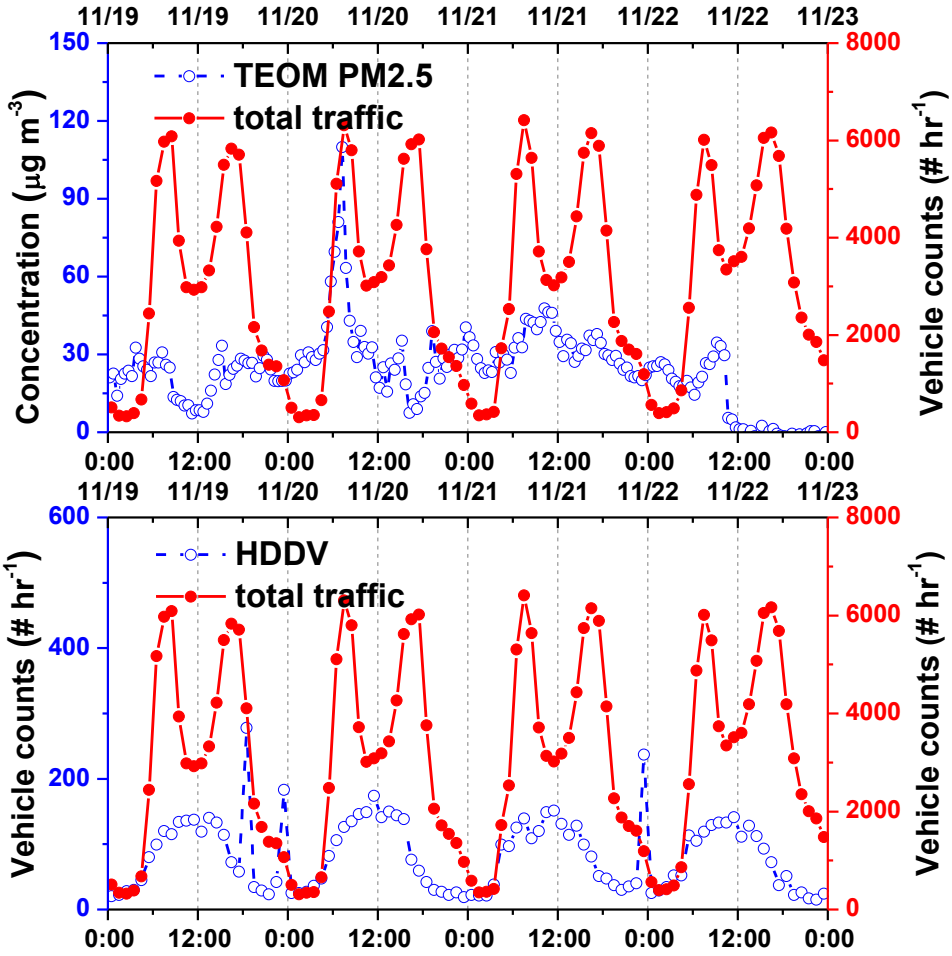

Figure 4.5 Time series $PM_{2.5}$ mass and I-895 tunnel traffic counts from November 19th through 22nd, 2002.

During the large, 7-hour $PM_{2.5}$ excursion in the morning (i.e., 0100 ~ 0800 LT) of November 20th, excellent linear relations between ambient pollutants (i.e., $PM_{2.5}$, EC, and OC) and the total traffic flux were revealed (Figure 4.6). Further MLR of ambient pollutants against the counts of light duty gasoline vehicles (LDGV) and HDDV recorded in the I-895 tunnel during this period afforded the following relationships:

$$[PM_{2.5}] = (0.010 \pm 0.001) \times [LDGV] + (0.015 \pm 0.042) \times [HDDV] + (24.54 \pm 1.32) \quad (4.14)$$

$$[EC] = (0.001 \pm 0.0005) \times [LDGV] + (0.014 \pm 0.032) \times [HDDV]$$

$$+(1.42 \pm 0.99) \qquad (4.15)$$

where concentrations of $PM_{2.5}$ and EC are in μg m^{-3}, and the vehicle densities of LDGV and HDDV are in vehicle hr^{-1}. The regression equations 4.14 and 4.15 had correlation coefficients of 0.999 ($p < 0.001$) and 0.985 ($p < 0.001$), respectively. Note that the residual of $PM_{2.5}$ in this bivariate linear regression (i.e., 24.54 ± 1.32 μg m^{-3}) was nearly identical to that (i.e., 24.70 ± 0.29 μg m^{-3}) obtained from the simple linear regression (Figure 4.6), confirming the validity of Equation 4.9 in which the observed average emission factor of $PM_{2.5}$ was assumed to be little affected by temporal variations in the vehicle composition in this study.

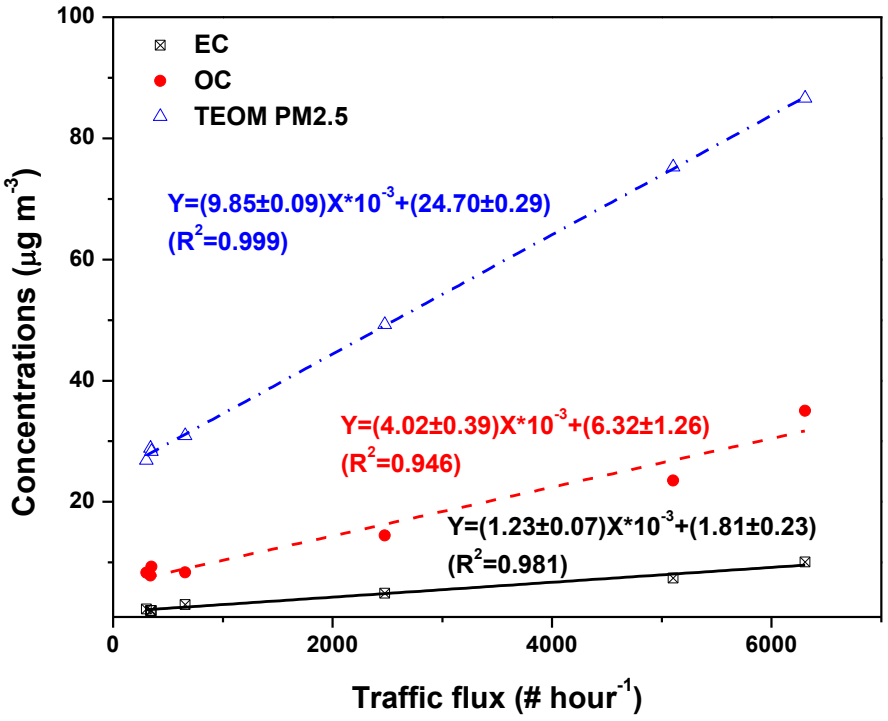

Figure 4.6 Concentrations of EC, OC, and $PM_{2.5}$ mass as a function of the I-895 tunnel traffic flux during the morning period from 0100 to 0800 LT on November 20th, 2002.

Although a wide variety of receptor-modeling studies have concluded that diesel powered vehicles are the major source of on-road PM (Schauer et al. 1996, Landis et al. 2007), it has been argued that PM contributions from gasoline powered vehicles (i.e., light-duty vehicles) may be underestimated (Gertler et al. 2002, Gertler 2005). During this $PM_{2.5}$ excursion, LDGV and HDDV contributed 45 % and 2.1 % of $PM_{2.5}$ mass, respectively, which supports this contention, as did by Gertler's *in-situ* measurements in a highway tunnel and a series of crossroad sites (Gertler et al. 2002, Gertler 2005). Nevertheless, LDGV and HDDV contributed 48 % and 20 % of EC, respectively, in this study suggesting that HDDV was still an important source of EC despite the small fraction of this type of vehicles.

The road coefficient K in Equation 4.10 determined from the simple linear regression of $PM_{2.5}$ against the total traffic flux of I-895 was 35.48 ± 0.42 μg s m^{-3} per vehicle in this study. Note that in the windless model, this coefficient K is co-determined by traffic characteristics (e.g., type and age composition of the fleet of vehicles, and the corresponding vehicle emission factors), road features (i.e., location of receptor site, road surface condition, terrain, and nearby buildings), and meteorological conditions (i.e., wind speed, temperature, humidity, and atmospheric stability). That is, $\overline{E}/\beta$ in Equation 4.9 (or $\sum k_i E_i /\beta$ in Equation 4.8) is a constant at a given site (i.e., 2.58 ± 0.03 μg s m^{-2} for the Ponca street site in this study). Herein, vehicle emission factors, $\overline{E}$ or E_is, are the core terms of interest and have been used as input in the EPA's MOBILE model to evaluate the pollution from highway vehicles and decide air pollution policy (e.g., vehicle emission standards) at the local, state, and national level (Pollack et al. 2004, Parrish 2006). Instead of expensive tailpipe

measurements of a substantial number of vehicles, measurements of ambient pollutants and traffic statistics at the same receptor site can be used to calculate $\overline{E}/\beta$ values during different windless periods as done above. Since the road coefficient β is deemed constant for the given site based on the windless model assumption, changes in emission factors, E_is, over time for a given vehicle category could be conveniently estimated by the comparison of the E_i/β values.

In Gertler's tunnel study (Gertler et al. 2002) where all vehicles were operating under hot-stabilized conditions with a limited speed of 55 mph, the $PM_{2.5}$ emission factor for light-duty gasoline vehicles was determined to be 10 ± 3 μg m^{-1}. Using the traffic counts of different vehicle types measured in the I-895 tunnel, this emission factor was adjusted as 10.2 ± 3.1 μg m^{-1} per vehicle. The β coefficient observed at the Ponca street site was then determined as 3.95 ± 1.20 m s^{-1}, which is the effective transport speed of the I-895 road section under the conditions described. Note that this effective transport speed is the sum of the wind speed and the traffic-induced air flow rate. The wind speed measured at 5 m above the I-895 roadway was 0.81 ± 0.24 m s^{-1} during the $PM_{2.5}$ excursion, and likely above the turbulent wake of the vehicles. In addition, given that the high traffic volume were likely moving substantially more slowly than the posted speed limit of 50 mph (i.e., 22.35 m s^{-1}), the wind speed measured probably reflected only the meteorological wind speed. Thus, the vehicle-induced speed was about 3.14 ± 1.22 m s^{-1}, which seems reasonable compared with the average speed (i.e., 0.5 ~ 1.2 m s^{-1}) of tunnel traffic-induced wind in Jiang's study (Jiang and Chen 2002). In any event, I argue that this value of β is likely applicable for this particular roadway when similar traffic and meteorological conditions prevail.

4.4.2 Correlation of Ambient Pollutants

As shown in Figure 4.8a, $PM_{2.5}$ mass was dominated by EC and OC throughout the 3-day episode. In particular, large fractions of EC (11.6%) and OC (56.6%) in $PM_{2.5}$ observed at the Ponca street site in the morning rush hour (0700 ~ 0800 LT) of the 20th resembled those reported for a gasoline-vehicle type tunnel (21.0% and 62.2%, respectively) (Landis et al. 2007) rather than a diesel-vehicle type tunnel (47.6%, and 56.1%, respectively) (Landis et al. 2007) or a residential area in Baltimore (3.0%, and 33.7%, respectively, as determined by (Landis et al. 2001)). As shown in Figure 4.8a, sulfate remained at low levels without notable fluctuations throughout the study period, except a minor increase during the traffic rush hour of the 20th. In contrast, gradual accumulations of nitrates (Figure 4.8a) were observed in a temporal pattern slightly lagged (i.e., one to two hours) behind that of $PM_{2.5}$, presumably as a result of NO_x chemistry.

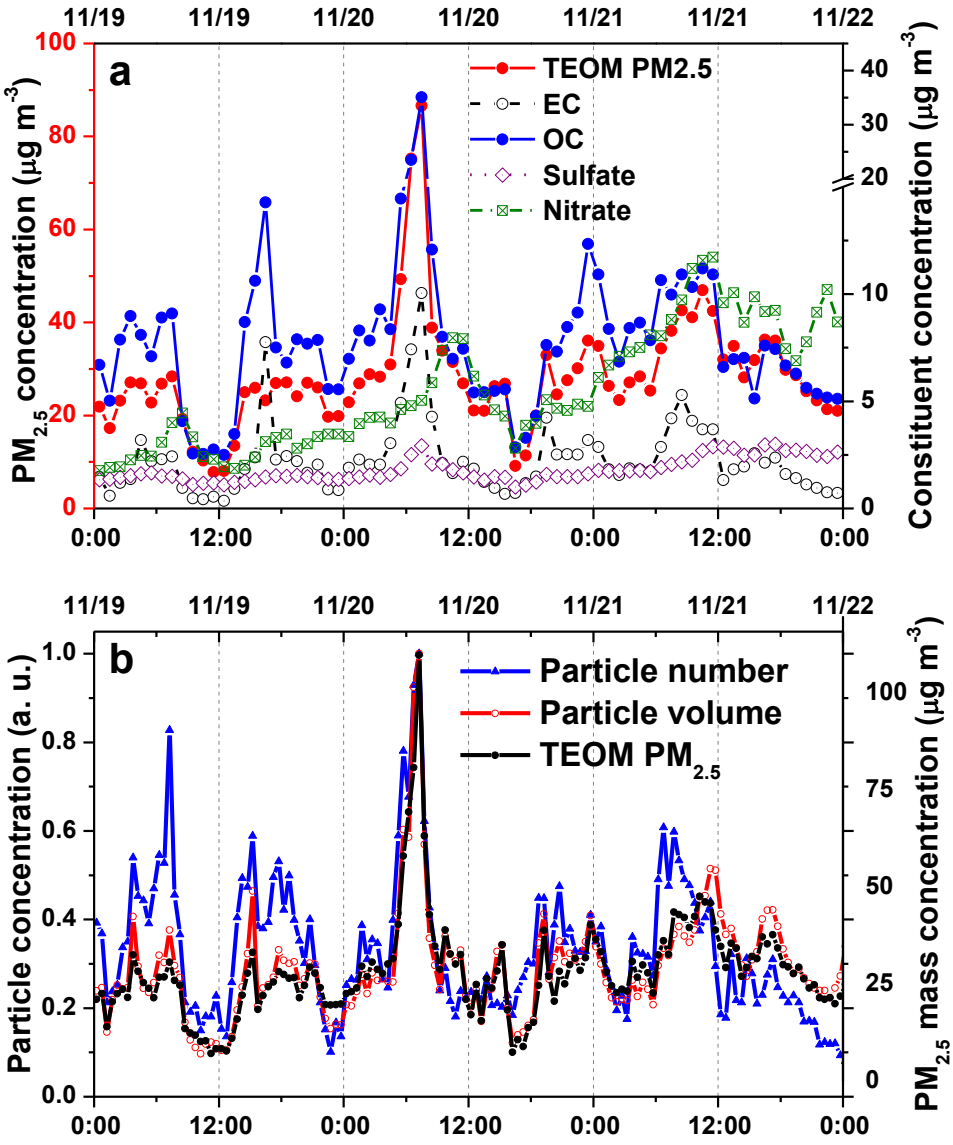

Figure 4.8 Time series of a) mass concentrations of $PM_{2.5}$ and its major constituents (EC, OC, sulfate, and nitrate); and b) particle number and volume concentrations (normalized to the corresponding maximum concentration) from November 19th through 22nd, 2002.

The time series number (PN), volume (PV), and mass concentrations of $PM_{2.5}$ particles in 30-minute intervals during the episode are compared in Figure 4.8b. Both PN and PV concentrations showed fair correlations with mass concentrations (r^2 = 0.445 for PN concentrations, and 0.539 for PV concentrations, respectively). As shown in Figure 4.8b, the PN/PV ratios in the morning of the 19th and 21st were

greater than that in the morning of the 20th, in agreement with smaller mean particle diameters and the relatively heavier influence from other anthropogenic sources in the former cases. In addition, it was found that particle number concentrations in all size channels with the median sizes > 30 nm were well correlated ($r^2 > 0.8$) with $PM_{2.5}$ mass in the early morning (0100 ~ 0800 LT) of the 20th (refer to Appendix D5), indicating there was little influence from aerosol sources other than traffic during this period.

The eleven SEAS metals were divided into four groups based on the similarity of their temporal patterns on November 20th (Figure 4.9). According to the time of the observation maxima, Fe, Al, Zn, Mn, and probably some of the Cu were deemed to be associated with the morning traffic (i.e., Zn and Ni from fuel oil additives (Osan et al. 2000), and Al, Fe, Mn, and Cu from motor engine and brake wear (Rubin et al. 2006)). Among all metals, concentrations of Al, and Mn increased dramatically in the evening of the 20th. Cd, Ni, and Zn showed very similar temporal patterns throughout the afternoon. Pb and Cu were grouped because of their high concentrations in the late afternoon. Se, As, and Cr showed low concentrations all the day. Linear regression (refer to Appendix D5) revealed that Se, As, and Cd were generally poorly correlated ($r^2 < 0.4$) with $PM_{2.5}$ mass in the early morning (0100 ~ 0800 LT), suggesting that these species could not be detected in motor vehicle emissions.

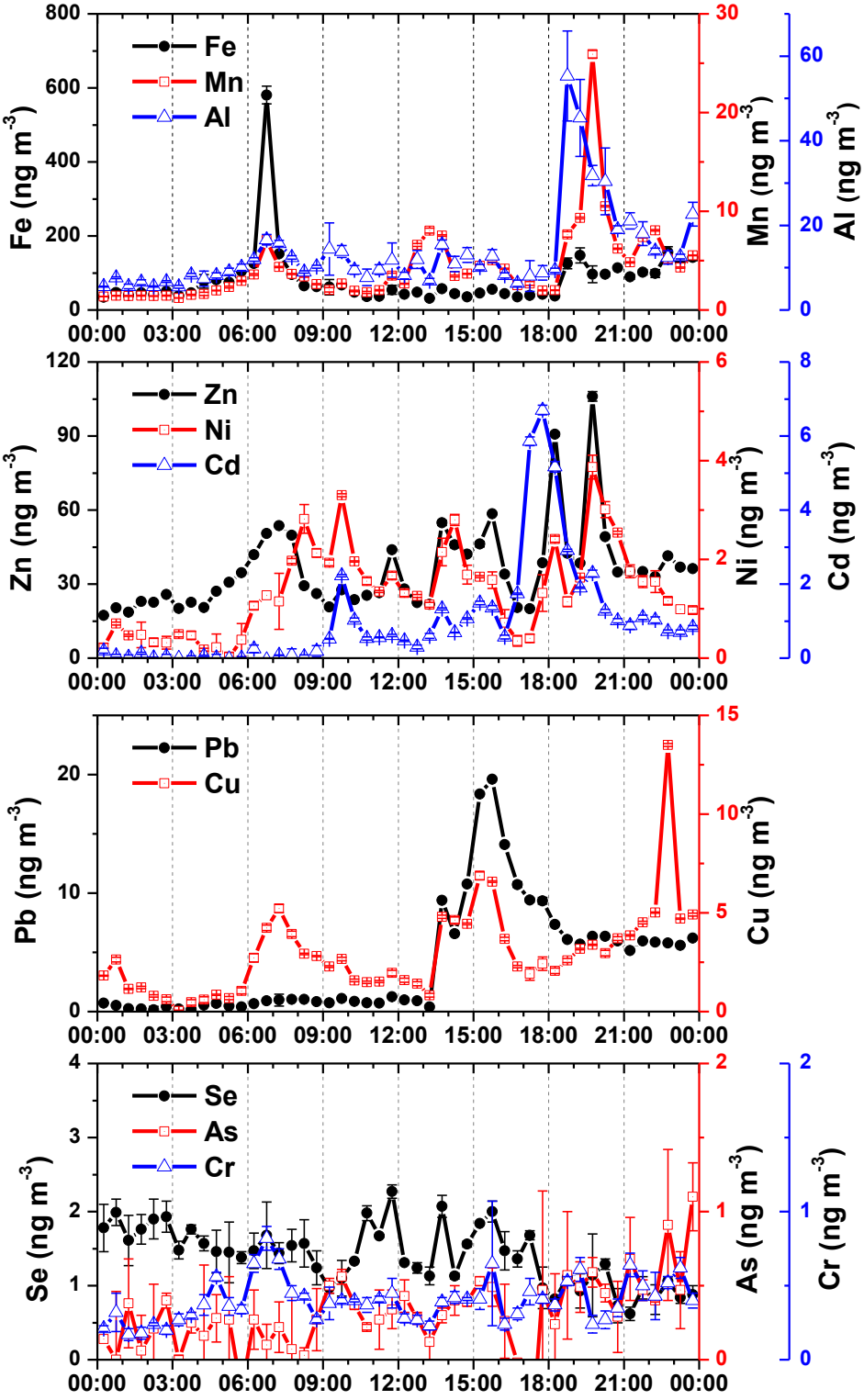

Figure 4.9 SEAS metal concentrations on November 20th, 2002.

The 3-hour measurements and the deconvoluted 1-hour data in selected SVOC categories (refer to Appendix D6 for a complete list) are plotted in Figure 4.10.

Among these different SVOC categories, n-alkanes, PAHs, oxy-PAHs, alkylcyclohexanes, and pentacyclic triterpanes are all well-known tracers of motor vehicle exhaust (Rogge et al. 1993b). As shown in Figure 4.10, the temporal profiles of both the 3-hour and the 1-hour concentrations of these species were in good agreement with those of the I-895 tunnel traffic and the concentrations of TC (i.e., the sum of EC and OC). In contrast, both 3-hour and one-hour SVOC concentrations of thiazoles, steroids, sugars, phenolic wood markers, secondary biogenic oxidation products, and aliphatic dicarboxylic acids exhibited temporal patterns different from those of the I-895 tunnel traffic and the concentrations of TC. Thiazoles are known tracers of road dust (Rogge et al. 1993c) but they were poorly correlated with traffic, possibly because the road was wet with dew in that early morning or tire wear particles may not have been formed/re-suspended under the windless and probably slow traffic conditions. Steroids are well-known markers of meat cooking operations (Rogge et al. 1991). Sugars and phenolic wood markers are unique tracers of biomass burning (Simoneit et al. 1993, Simoneit et al. 1999). Secondary biogenic oxidation products and aliphatic dicarboxylic acids are known tracers of vegetation debris (Rogge et al. 1993d). For those SVOCs that are less relevant to motor vehicle exhaust, the deconvolution of 3-hour data into one-hour sets appeared to barely improve their correlations with the traffic flux, as shown in Figure 4.10.

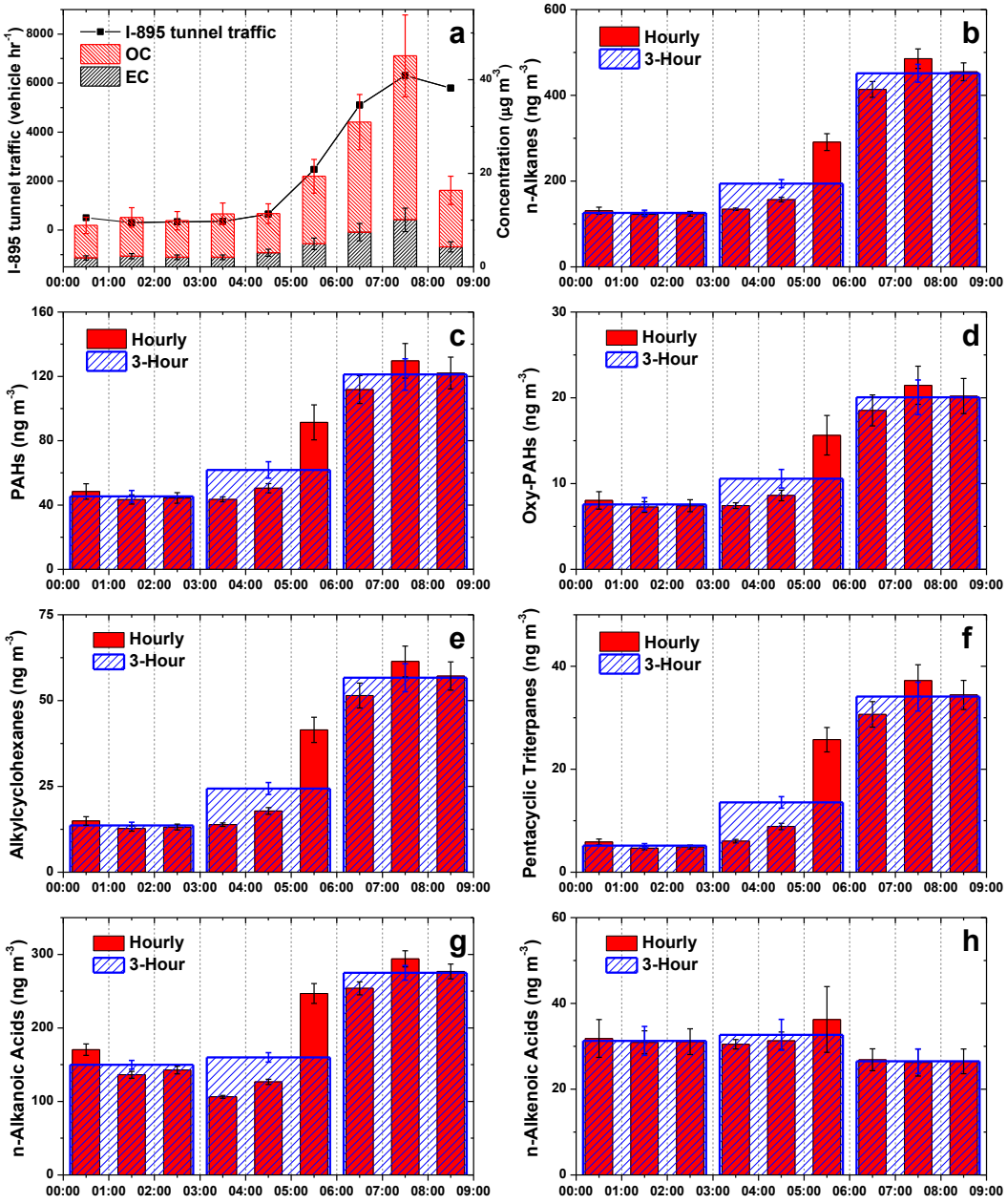
a
I-895 tunnel traffic
OC
EC
I-895 tunnel traffic (vehicle hr-1)
Concentration (μg m-3)
b
Hourly
3-Hour
n-Alkanes (ng m-3)
c
PAHs (ng m-3)
d
Oxy-PAHs (ng m-3)
e
Alkylcyclohexanes (ng m-3)
f
Pentacyclic Triterpanes (ng m-3)
g
n-Alkanoic Acids (ng m-3)
h
n-Alkenoic Acids (ng m-3)
00:00 01:00 02:00 03:00 04:00 05:00 06:00 07:00 08:00 09:00

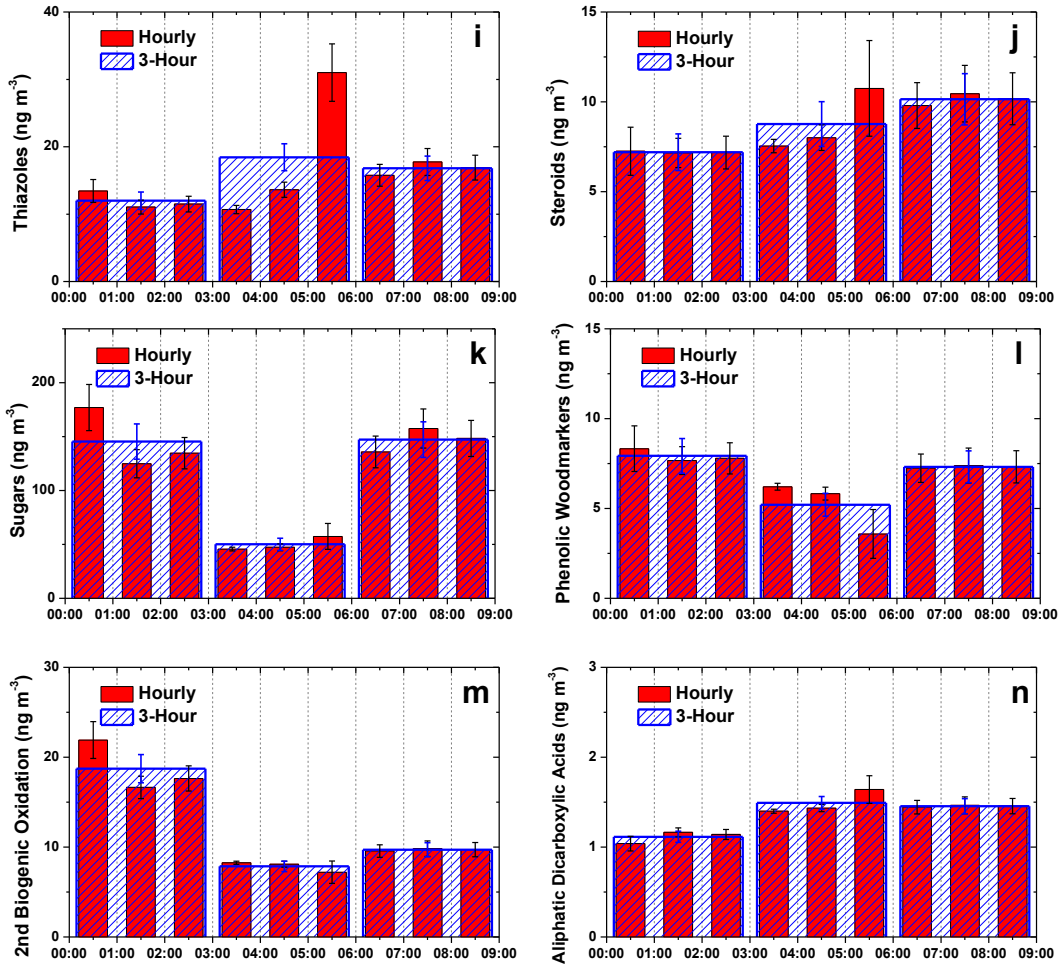

Figure 4.10 3-Hour and hourly estimates of aggregate concentrations in 13 classes of SVOCs in the early morning (0000 ~ 0900 LT) of November 20th, 2002 (temporal profiles of the I-895 tunnel traffic and the concentrations of EC and OC are shown in panel a for comparison purpose).

Both n-Alkanoic acids and n-alkenoic acids are tracers of motor vehicle emissions (Rogge et al. 1993b). These species are not present in gasoline or diesel but present in vehicle exhaust as they are formed during the fuel combustion and catalytic oxidation process in the engines (Laresgoiti and Springer 1977). In particular, the measured n-alkanoic acids (i.e., C9 to C34) are expected to be released from both gasoline and diesel vehicles but the two measured n-alkenoic acids (i.e., C17 and C18) can only arise from diesel vehicles because gasoline fuels only contain compounds lower than

C10 (Rogge et al. 1993b). As shown in Figure 4.10, the former species were highly correlated with the traffic but the latter were not, indicating that the influence of gasoline vehicles was predominant over diesel vehicles in this study.

4.4.3 Profiles of Motor Vehicle Emissions

The abundance profiles of motor vehicle emissions obtained are compared in Table 4.1. In general, these four, independently obtained profiles were differed little. Note that negative abundances for certain species (e.g., As and Se) were generated in the DPO profile, because the concentrations of these species in the peak observation of $PM_{2.5}$ were smaller than those in the background. This emphasized that an appropriate background correction is critical in the DPO analysis to properly subtract the contributions from sources other than motor vehicles from the peak observation interval. Another problem of the DPO method is that the abundances of certain species could be inflated in the resulted profile of motor vehicle emissions, if a minor source contributed significantly to these species during the peak observation but not in the background observation. In contrast, background correction was not required in the windless model analysis as contributions from non-traffic sources were determined as the residual terms in Equation 4.11. As shown in Table 4.1, the abundances of sulfate, nitrate, EC, and OC in the WMA profile were smaller than the corresponding values in the DPO profile, which were arguably the result of more effective removal of the contributions from non-traffic sources in the former.

Table 4.1 Comparison of the abundance profiles of motor vehicle emissions obtained direct peak observation, windless model linear regression, UNMIX, and PMF in this study [1] (unit: μg per μg of $PM_{2.5}$; metal abundances were amplified by a factor of 1000).

Species	DPO	WMA	UNMIX	PMF
Sulfate	**0.024 ± 0.022**	0.023 ± 0.009	0.030 ± 0.010	0.024 ± 0.004
Nitrate	**0.018 ± 0.008**	0.016 ± 0.004	0.038 ± 0.024	0.027 ± 0.012
EC	0.130 ± 0.043	**0.125 ± 0.033**	0.115 ± 0.031	0.108 ± 0.008
OC	0.448 ± 0.151	**0.408 ± 0.114**	0.373 ± 0.106	0.350 ± 0.002
Al	**0.130 ± 0.029**	0.140 ± 0.031	0.130 ± 0.064	0.190 ± 0.023
As	-0.001 ± 0.001	**0.000 ± 0.002**	0.001 ± 0.002	0.001 ± 0.000
Cd	0.000 ± 0.000	**0.001 ± 0.001**	0.000 ± 0.006	0.000 ± 0.000
Cr	0.007 ± 0.003	**0.007 ± 0.003**	0.007 ± 0.002	0.006 ± 0.001
Cu	**0.057 ± 0.020**	0.063 ± 0.020	0.040 ± 0.021	0.027 ± 0.016
Fe	**1.400 ± 0.085**	3.100 ± 1.800	3.000 ± 1.100	2.400 ± 0.360
Mn	**0.043 ± 0.018**	0.057 ± 0.020	0.038 ± 0.027	0.067 ± 0.004
Ni	0.018 ± 0.017	**0.019 ± 0.008**	0.005 ± 0.009	0.008 ± 0.003
Pb	0.013 ± 0.017	**0.011 ± 0.005**	0.014 ± 0.009	0.005 ± 0.001
Se	-0.003 ± 0.009	**0.000 ± 0.003**	0.000 ± 0.027	0.000 ± 0.002
Zn	**0.520 ± 0.230**	0.510 ± 0.110	0.460 ± 0.200	0.400 ± 0.079

[1] Boldfaced type indicates the best result for each species.

The abundances of the SVOCs in 19 categories between the DPO and the WMA profiles are listed in Table 4.2 (refer to Appendix D7 for detailed abundances of 117 individual species). In the WMA solution, the tracers of motor vehicle exhaust (i.e., alkylcyclohexanes, pentacyclic triterpanes, n-alkanes, PAHs, and oxy-PAHs) were well correlated ($r^2 > 0.9$) with the I-895 traffic flux. In contrast, other SVOCs were poorly correlated with the traffic flux ($r^2 < 0.3$). Compared with DPO, the WMA method attributed extra uncertainties stemming from the fitting quality of linear regression. As a result, large uncertainties were associated with the abundances of

those latter other species in the WMA profile, indicating their irrelevance with motor vehicle emissions. In other words, the WMA profile is arguably more accurate than the DPO profile, at least for the species that were poorly correlated with traffic flux.

Table 4.2 SVOC abundance profiles of motor vehicle emissions obtained by direct peak observation and windless model linear regression in this study (unit: ng per μg of $PM_{2.5}$).

Species	DPO	WMA		
	Abundance	Abundance	r^2 [1]	p [2]
n-Alkanes	6.080 ± 0.390	6.07 ± 1.07	0.992	*
n-Alkanoic Acids	2.640 ± 0.199	2.84 ± 0.65	0.878	0.002
PAHs	1.440 ± 0.186	1.46 ± 0.36	0.971	*
Sugars	0.547 ± 0.375	1.06 ± 1.06	0.298	0.205
Alkylcyclohexanes	0.814 ± 0.076	0.815 ± 0.147	0.961	*
Pentacyclic Triterpanes	0.545 ± 0.052	0.541 ± 0.102	0.940	*
Oxy-PAHs	0.237 ± 0.039	0.239 ± 0.075	0.960	*
S-Hetero-PAH	0.122 ± 0.019	0.124 ± 0.030	0.977	*
Thiazoles	0.112 ± 0.038	0.111 ± 0.154	0.149	0.392
Resin Acids	0.101 ± 0.016	0.103 ± 0.033	0.846	0.003
Steroids	0.055 ± 0.030	0.053 ± 0.109	0.692	0.020
Iso- and Antiso-Alkanes	0.039 ± 0.017	0.042 ± 0.021	0.823	0.005
2-Alkanones	0.034 ± 0.007	0.035 ± 0.019	0.558	0.054
Aromatic Polycarboxylic Acids	0.008 ± 0.002	0.009 ± 0.003	0.857	0.003
Phenolic Wood-markers	-0.005 ± 0.021	0.005 ± 0.035	0.007	0.855
Aliphatic Dicarboxylic	0.005 ± 0.002	0.004 ± 0.004	0.253	0.250

Acids				
N-Hetero-PAH	0.001 ± 0.000	0.001 ± 0.000	0.786	0.008
n-Alkenoic Acids	-0.079 ± 0.069	0.000 ± 0.120	0.349	0.163
Secondary Biogenic Oxidation Products	-0.114 ± 0.025	0.000 ± 0.101	0.132	0.423

[1] Correlation coefficients between ambient concentrations of SVOC species and traffic flux.

[2] *p*-value.

* $p < 0.001$.

The traffic factor obtained for both UNMIX and PMF modeling were recognized in each solution by its largest contribution to $PM_{2.5}$ and EC during the day as well as its temporal correlation with the traffic flux in the morning (detailed receptor modeling results were described in the next section). The temporal contributions to $PM_{2.5}$ from the traffic factor were well correlated to the hourly traffic flux (i.e., $r^2 = 0.981$ and $p < 0.001$ for the UNMIX solution; and $r^2 = 0.954$ and $p < 0.001$ for the PMF solution) during this early morning (i.e., 0100 ~ 0800 LT). But these correlations were worse than that obtained by linear regression of ambient $PM_{2.5}$ concentrations against the hourly traffic fluxes (i.e., $r^2 = 0.999$ and $p < 0.001$), suggesting factor contamination in these receptor model solutions, especially for PMF. As shown in Table 4.1, factor cross-contamination in the UNMIX and PMF solutions was also indicated by the larger abundances of nitrate and smaller abundances of EC and OC in these profiles of motor vehicle emissions, compared with the DPO and WMA profiles. The former is a secondary species and its concentrations during the morning $PM_{2.5}$ excursion were lower than the average level of the day (Figure 4.8). Hence factor cross contamination with other sources probably lead to an overestimated abundance of nitrate in the profile of motor vehicle emissions. In

contrast, this morning traffic contributed more than 50 % of EC and OC and a result of mixing of factor contributions was the underestimated abundances of these species in the traffic profiles predicted by UNMIX and PMF. The smaller abundances of Cu, Ni, and Zn in the UNMIX and PMF profiles than their corresponding values in the DPO and WMA profiles were probably due to this same reason.

The particle size distribution profiles of motor vehicle emissions obtained from the four methods are compared in Figure 4.11. In general, a median particle size of about 50 ~ 60 nm for the traffic factor was predicted in all solutions, suggesting its nature of primary emissions. However, the UNMIX- and PMF-predicted median particle sizes of this factor was about 10 nm smaller than that obtained by the DPO or WDA method, which again suggested the interferences from other sources in the UNMIX and PMF solutions.

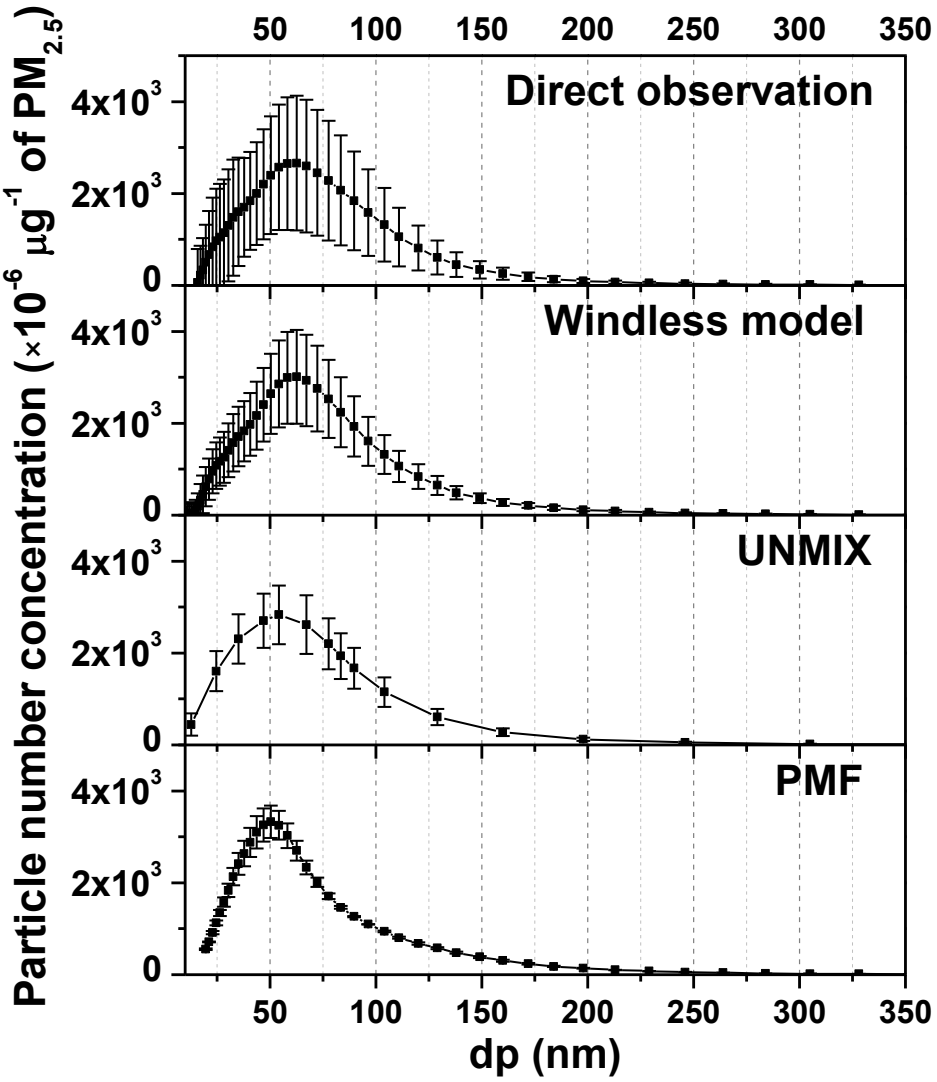

Figure 4.11 Comparison of particle size distribution profiles of motor vehicle emissions obtained by direct observation, windless-model based linear regression, UNMIX, and PMF.

The WDA profile of motor vehicle emissions is compared with those retrieved from the SPECIATE database (Table 4.3). As shown in Table 4.3, the WDA profile agrees better in EC and Pb with gasoline vehicle exhaust (i.e., SPECIATE light-duty gasoline vehicle exhaust) than diesel vehicle emissions (i.e., SPECIATE light-duty diesel vehicle exhaust). The OC/TC ratio (i.e., 0.77) of the WDA profile represents a mixture of those of gasoline vehicle exhaust (i.e., 0.82) and diesel vehicle emissions

(i.e., 0.42), but more resembles the former, implying a gasoline-type traffic as indicated by the I-895 tunnel traffic statistics. Nevertheless, the abundances of OC and Zn in the WDA profile were lower than those of gasoline vehicle exhaust and more like those of diesel tailpipe emissions, probably because these SPECIATE profiles of light-duty vehicles were derived from tailpipe emissions without contributions from brake lining and tire wear. The most abundant SEAS metals in the WDA profile are Fe, Zn, and Al, in good agreement with the SPECIATE composite transportation profile. The SPECIATE mixed motor vehicle, tunnel motor vehicle, and light-duty diesel vehicle exhausts show significantly higher abundances of Pb and Se than those in the WDA profile, which could be attributed to the fact that all these SPECIATE profiles were measured twenty years ago when leaded fuels and higher sulfur diesel fuels were still in use. Moreover, the WDA profile showed a better precision as its abundance uncertainties for most species except OC were generally smaller than those corresponding values in any of these SPECIATE profiles.

Table 4.3 Comparison of the abundance profile of motor vehicle emissions obtained in this study with selected SPECIATE profiles of various vehicular emissions (unit: μg per μg of $PM_{2.5}$; metal abundances were amplified by a factor of 1000).

Species	Motor vehicle emissions in this study [1]	Light-duty vehicle exhaust – gasoline [2]	Light-duty vehicles – unleaded [3]	Light-duty vehicles – diesel [4]	Mixed motor vehicle exhaust [5]	Tunnel motor vehicle exhaust [6]	Transportation – composite [7]
Sulfate	0.023 ± 0.009	0.003 ± 0.001	n.a.	n.a.	0.023 ± 0.010	0.041 ± 0.006	0.023 ± 0.018
Nitrate	0.016 ± 0.004	0.003 ± 0.001	n.a.	n.a.	0.030 ± 0.022	0.010 ± 0.006	0.002 ± 0.001
EC	0.125 ± 0.033	0.128 ± 0.019	0.143 ± 0.095	0.606 ± 0.175	0.184 ± 0.063	0.287 ± 0.064	0.127 ± 0.102
OC	0.408 ± 0.114	0.600 ± 0.044	0.511 ± 0.206	0.441 ± 0.114	0.326 ± 0.094	0.379 ± 0.082	0.212 ± 0.053
Al	0.14 ± 0.03	0.32 ± 0.59	5.07 ± 4.73	1.05 ± 0.90	3.52 ± 1.56	0.00 ± 0.37	3.81 ± 7.15
As	0.00 ± 0.00	0.00 ± 0.02	0.00 ± 0.00	0.01 ± 0.07	0.02 ± 0.27	0.01 ± 0.10	0.00 ± 0.00
Cd	0.00 ± 0.00	0.20 ± 1.08	0.00 ± 0.00	0.00 ± 0.00	0.10 ± 0.55	0.06 ± 0.47	0.00 ± 0.00
Cr	0.01 ± 0.00	0.02 ± 0.23	0.12 ± 0.18	0.07 ± 0.06	0.12 ± 0.09	0.03 ± 0.15	0.00 ± 0.00
Cu	0.06 ± 0.02	0.49 ± 0.12	0.16 ± 0.28	0.06 ± 0.05	0.59 ± 0.48	0.72 ± 0.36	0.38 ± 0.30
Fe	3.10 ± 1.90	0.83 ± 0.14	3.57 ± 3.53	0.84 ± 0.56	5.53 ± 3.18	14.8 ± 8.11	10.9 ± 12.5
Mn	0.06 ± 0.02	0.01 ± 0.17	0.14 ± 0.25	0.10 ± 0.08	0.81 ± 0.27	0.09 ± 0.08	0.45 ± 0.22
Ni	0.02 ± 0.01	0.02 ± 0.10	0.05 ± 0.15	0.04 ± 0.04	0.08 ± 0.07	0.03 ± 0.04	0.05 ± 0.06
Pb	0.01 ± 0.01	0.19 ± 0.20	3.54 ± 3.91	0.79 ± 0.41	1.20 ± 0.55	0.64 ± 0.25	148.0 ± 37.8
Se	0.00 ± 0.01	0.00 ± 0.03	0.03 ± 0.15	0.05 ± 0.05	0.01 ± 0.07	0.02 ± 0.05	0.14 ± 0.10
Zn	0.51 ± 0.11	2.37 ± 0.22	3.20 ± 2.63	0.56 ± 0.29	2.20 ± 1.70	1.86 ± 0.49	1.51 ± 1.84

[1] Obtained with the windless model analysis.

[2] SVOC (e.g., hopanes, PAHs) in both PM and gaseous phases were combined and analyzed together (average of SPECIATE profiles 4933 to 4942).

[3] Vehicle exhaust gases sampled with a dilution sampler and constant volume sampling system (average of SPECIATE profiles 31202 and 31203).

[4] Vehicle exhaust gases sampled with a dilution sampler and constant volume sampling system (average of SPECIATE profiles 32102 and 32103).

[5] Composite of 25 % diesel and 75 % gasoline (SPECIATE profile 3519).

[6] Tunnel exhaust material composited from 24 out of 27 tunnel samples collected on the southward lanes at Oakland, CA; collected 12/92 (SPECIATE profile 3684).

[7] Includes emissions from leaded and unleaded gasoline, diesel, and tire wear (SPECIATE profile 33020).

4.4.4 Source Apportionment by Receptor Modeling Using the 24-Hour Data Set of November 20th, 2002

The chemical compositions and size distributions of the five factors obtained with UNMIX and PMF are compared in Figure 4.12 and Figure 4.13, respectively. The time series contributions from the five factors are shown in Figure 4.14. In general, the predictions for the first three factors were comparable.

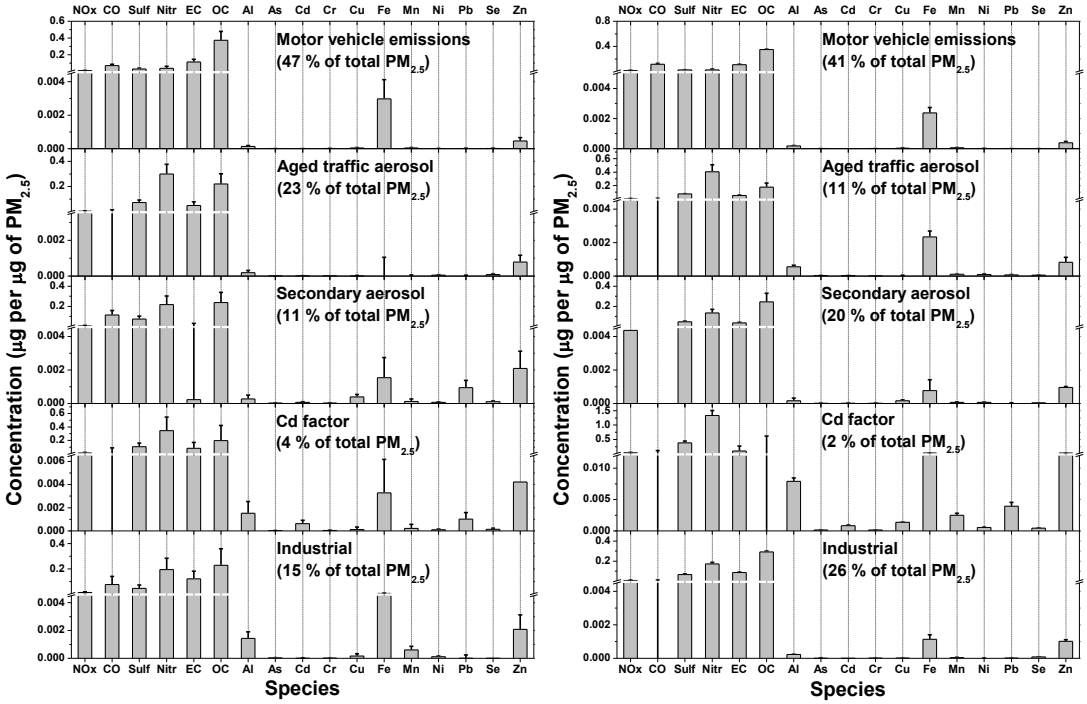

Figure 4.12 Factor profiles of chemical compositions determined by UNMIX (left column of panels) and PMF (right column of panels).

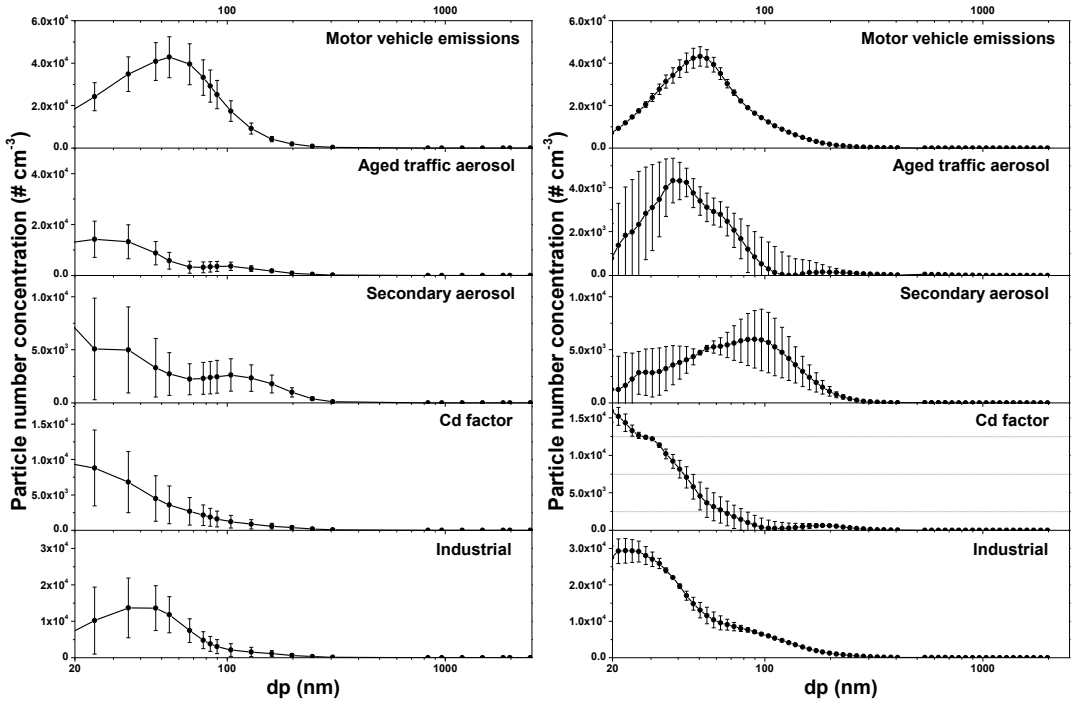

Figure 4.13 Factor profiles of particle number size distributions determined by UNMIX (left column of panels) and PMF (right column of panels).

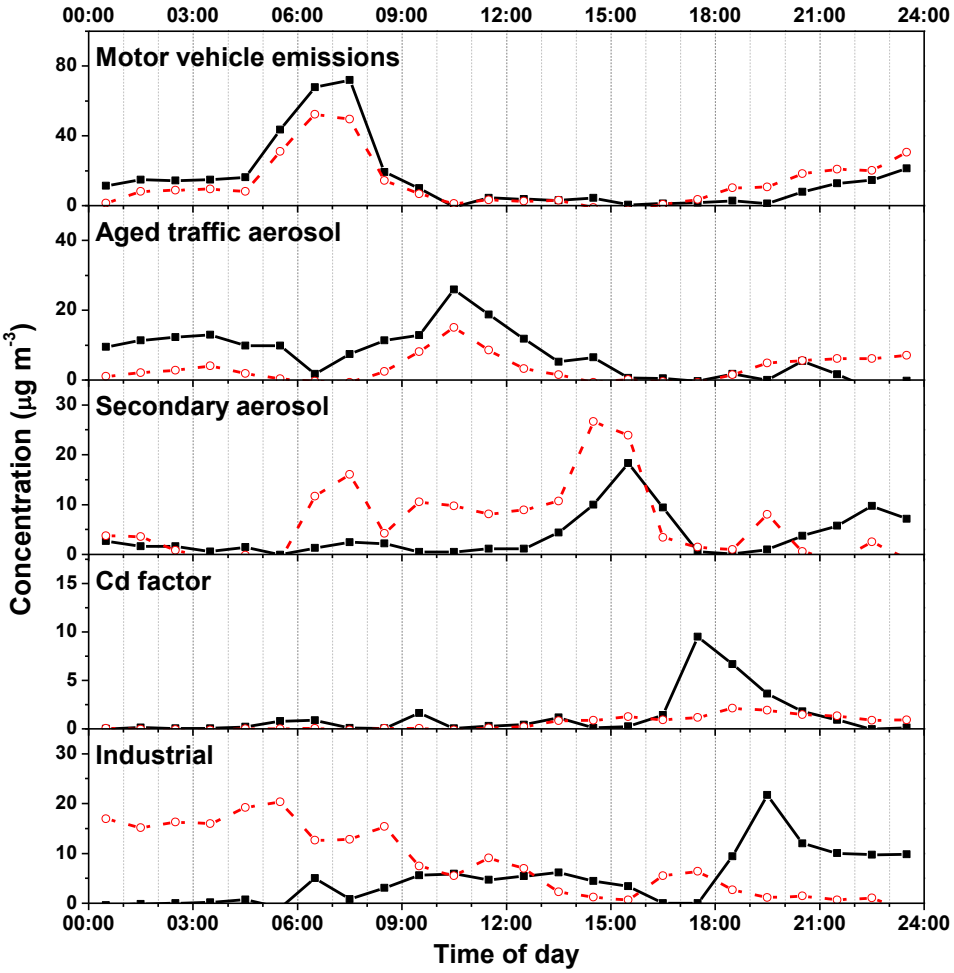

Figure 4.14 Resolved factor contributions by UNMIX (black solid line) and PMF (red dash line).

As discussed earlier, the factor with the largest contributions to $PM_{2.5}$ mass was recognized as motor vehicle emissions in both model solutions. This motor vehicle emission factor was also characterized by its high abundances of NO_x, CO, EC, and OC as well as its unique temporal pattern of factor strengths that was identical to the traffic density. In general, the two model solutions showed quite good agreement. UNMIX and PMF attributed 47 and 42 % of $PM_{2.5}$ mass; 55 and 49 % of $PM_{2.5}$ particles in number; 62 and 55 % of EC; 60 and 50 % of OC; 58 and 60 % of NO_x; and 58 and > 99 % of CO, respectively.

The second factor exhibited some traffic-related features (i.e., high abundances of NO_x, EC OC, and Zn). However, this factor showed a larger (i.e., 20 ~ 45 fold) ratio of nitrate/NO_x than the vehicular emission factor and its largest contribution was observed at 1030 LT, asynchronous with the traffic rush hour. Another gas pollutant, CO, was completely absent in this factor, suggesting its little relevance to fresh fuel combustion. Compared with the primary vehicular emissions, enrichment of Ni in the profile of this factor was found (i.e., enrichment factors of 10 for the UNMIX profile and 13 for the PMF profile), which indicated that this factor probably contained a contribution from an oil-fired power plant. The BGE Wagner Station (station angle = 172° with respect to the Ponca street site) located in the upwind direction during the late morning (0900 ~ 1200 LT) and could be responsible for the elevated level of Ni in this factor profile. Besides, the resolved size distributions of this factor showed an additional accumulation mode compared with the factor of motor vehicle emissions (Figure 4.13). All of this evidence attributes this factor to aged traffic aerosol. Overall, substantial amounts of nitrate (44 % by UNMIX, and 29 % by PMF) and $PM_{2.5}$ mass (23 % by UNMIX, and 11 % by PMF) were apportioned to this factor. It is noteworthy that differences in Fe and Mn were found despite the general similarity of the profiles from the two receptor models. That is, the abundances of these species in the PMF profile were much greater than those in the UNMIX profile.

The third factor was identified as secondary aerosol by its large abundances of sulfate, nitrate and OC, which resembled the aged traffic aerosol but was distinguished from the latter as its largest contribution was found at around 1500 LT (Figure 4.14). This secondary aerosol factor exhibited some industrial characteristics

(i.e., large abundances of Fe, Pb, and Zn). Considering that the prevailing wind was from southerly directions during the afternoon, this factor was finally attributed to secondary aerosol transported from the Dundalk area. This factor was less significant than aged traffic aerosol and its major contributions were limited to nitrate (16 % by UNMIX, and 18 % by PMF) and sulfate (17 % by UNMIX, and 18 % by PMF).

There was discrepancy of the two receptor modeling in resolving the remaining sources. UNMIX decomposed the rest of the contributions into two individual events at 1730 LT and 1930 LT, respectively. In contrast, PMF resolved two background-type factors (Figure 4.14). In both cases, a nucleation mode was predominant in either factor. Both factors were then identified as industrial factors and most of Cd, Al, Mn, and Zn of the day were attributed to these factors, despite their small contributions (i.e., < 25 % totally) to $PM_{2.5}$. In particular, the one with large contribution to Cd (69 % by UNMIX, and 74 % by PMF) was assigned as a Cd factor.

Both model predictions effectively reproduced the measured particle numbers (i.e., slope = 0.997 and r^2 = 0.997 for the UNMIX solution; and slope = 0.921 and r^2 = 0.995 for the PMF solution). Most of the variations in both solutions were due to the low-end (< 30 nm) and high-end (> 1.1 μm) of particle size channels.

The performance of the two models was evaluated (Table 4.4) using a series of statistical tools including mean fraction bias (MFB), normalized mean square error (NMSE), the fraction of predicted concentrations lying within a factor of 2 of the measured ambient concentrations (Fa2), and the Pearson's correlation coefficients (*r*). According to Kumar et al. (Kumar et al. 1993), model performance is deemed acceptable if NMSE $\leq$ 0.5, -0.5 $\leq$ MFB $\leq$ 0.5, and Fa2 $\geq$ 0.8. In addition, the

correlation between predicted and measured values is considered satisfactory in this study if $r > 0.8$. As shown in Table 4.4, the fit statistics for the major $PM_{2.5}$, constituents (i.e., sulfate, nitrate, EC, and OC) were generally acceptable for both model solutions. The predictions of NO_x and CO were also acceptable except that the NMSE value for CO was slightly unsatisfactory in the PMF solution. In contrast, the predictions of metals were generally poor except for Al, Fe and Zn.

Table 4.4 Performance statistics [1] of the UNMIX and PMF modeling.

	UNMIX				PMF			
	MFB	NMSE	Fa2	*r*	MFB	NMSE	Fa2	*r*
NO_x	-0.005	0.006	1	0.991	-0.004	0.016	1	0.973
CO	**0.254**	**0.143**	**0.792**	**0.883**	**-0.227**	**0.053**	**0.792**	**0.939**
$PM_{2.5}$	0.015	0.006	1	0.989	-0.012	0.006	1	0.987
Sulfate	0.015	0.008	1	0.934	0.018	0.011	1	0.925
Nitrate	0.049	0.028	1	**0.792**	0.007	0.02	1	0.841
EC	0.051	0.069	0.958	0.935	0.017	0.028	0.958	0.962
OC	0.016	0.04	1	0.958	-0.005	0.022	1	0.968
Al	0.07	0.12	1	0.898	0.047	0.038	1	0.929
As	0.199	0.235	0.833	**0.723**	-0.091	0.118	0.875	**0.783**
Cd	**0.182**	**1.269**	**0.875**	**0.614**	**-0.495**	**0.025**	**0.583**	**0.985**
Cr	0.066	0.051	1	**0.745**	-0.003	0.032	1	0.811
Cu	0.175	0.353	0.875	**0.596**	-0.063	0.07	0.958	0.892
Fe	0.086	0.261	0.958	0.814	-0.018	0.116	1	0.854
Mn	0.124	0.37	0.875	**0.735**	0.126	0.082	0.833	0.897
Ni	0.117	0.159	0.958	**0.764**	-0.167	0.112	0.833	**0.785**
Pb	**0.25**	**0.725**	**0.792**	**0.68**	**-0.443**	**0.042**	**0.625**	**0.974**

Se	0.046	0.042	1	**0.635**	0.024	0.052	1	**0.576**
Zn	-0.006	0.015	1	0.95	-0.003	0.034	1	0.865

[1] Boldfaced type indicates unacceptable performance.

4.5 Concluding Remarks

The calm winds, constant RHs and temperatures, and thus extreme atmospheric stability in the early morning of November 20th, 2002, provided an excellent opportunity to extract a little-contaminated profile of motor vehicle emissions on the near-road receptor site at Ponca street. It was revealed that ambient concentrations of $PM_{2.5}$ as well as EC and OC were in excellent linear correlations with the traffic flux under the windless period of the morning pollutant excursion. The characteristic ratio of EC and OC at the peak observation and the bivariate linear regression of ambient contributions against two different types of vehicles indicated that light-duty gasoline vehicles were the predominant source of $PM_{2.5}$ emissions in this episode. Composite profiles of motor vehicle emissions were obtained by four independent methods, which are well accordant for traffic-related species and may be applied to represent the primary vehicular emissions in the Mid-Atlantic area. In particular, the profiles of SVOC emissions were obtained in the DPO and WMA solutions. Compared with the DPO profile, the profile from the WMA-based linear regressions is arguably more accurate for species that are irrelevant to motor vehicle emissions. The WMA profile was deemed better than the profiles obtained by UNMIX and PMF in this study, as profile contaminations were indicated in the latter due to the very limited number of samples involved in the receptor modeling. Another important output of this study is that a paradigm of tracking changes in vehicle emission factors over time by

comparing E/β values obtained during different windless periods at the same site was developed.

Chapter 5: The Study on Seasonal Variations in Emissions of Carbonaceous Particulate Matter and Other Air Pollutants in Baltimore

5.1 Background

Carbonaceous particulate matter (PM), including black carbon (BC or EC) and organic carbon (OC), is an important component of emissions from combustion of fossil fuels and biomass and can exert carcinogenic and other adverse health effects (Bocskay et al. 2005, Schnelle-Kreis et al. 2009, Valavanidis, Fiotakis and Vlachogianni 2010). In the Baltimore area, the major sources of carbonaceous PM were motor vehicle exhaust, local industrial sources, and biomass burning (Ogulei et al. 2005, Park et al. 2005a, Ogulei et al. 2006). Particle-borne metals have been widely employed to assist source contribution estimates (SCE) by receptor modeling, e.g., zinc and iron for vehicular emissions (Ondov, Zoller and Gordon 1982a, Huang et al. 1994), vanadium and nickel for residual oil combustion (Mroz 1976), selenium for coal combustion (Ondov et al. 1979, Ondov et al. 1989), and potassium for biomass burning (Silva et al. 1999). Nevertheless, ambiguous source identifications have resulted in some circumstances, as elemental tracers are often source non-specific (Sheffield and Gordon 1986, Watson et al. 2002, Hopke et al. 2005).

Organic molecules, owing to their large variety, provide more flexible options as source-specific tracers than metals. For example, levoglucosan has been used as a unique tracer of biomass burning (Simoneit et al. 1999). Despite their wide use in

source diagnostics (Rogge et al. 1991, Rogge et al. 1993a, Rogge et al. 1993b, Rogge et al. 1993c, Rogge et al. 1993d, Simoneit et al. 1993, Rogge et al. 1994, Rogge et al. 1996, Schauer et al. 1996, Rogge et al. 1998, Simoneit et al. 1999, Simoneit 2002), quantitative applications of organic tracers in air quality studies have met limited success (Jaeckels, Bae and Schauer 2007), partially because organic species are usually depleted more rapidly than elemental tracers due to their reactivity with ozone and numerous free radicals.

In contrast to volatile organic compounds (VOCs) which are emitted and remain entirely in the gas phase, semi-volatile organic compounds (SVOCs) are in partition equilibrium between the gas and aerosol phases under ambient conditions (Grieshop et al. 2009, Pye and Seinfeld 2010). Volatilization and re-deposition of SVOCs with diurnal and seasonal changes in ambient temperatures often introduce extra uncertainties into applications of these tracers (Krupa et al. 2008), as their absorptive processes in fine aerosol show strong temperature dependence (Pankow 1994, Odum et al. 1996).

Recently, Lambe et al. (Lambe et al. 2009) reported bi-hourly measurements of SVOCs in Pittsburgh from February to April 2008 with a Thermal Desorption Aerosol GC-MS (TAG), with which ambient concentrations of BC and 28 SVOC markers were apportioned to diesel vehicles, gasoline vehicles, and a regional factor by both PMF and CMB. In Lambe's modeling, some important source categories such as secondary organic aerosol were excluded because TAG measurements are limited to low-molecular weight nonpolar molecules. Moreover, seasonal variations

in emissions of organic markers (e.g., PAHs and n-alkanes) from those traffic sources were barely considered because of the short term of the sampling campaign.

As part of the Baltimore supersite project (Ondov et al. 2006), 3-hourly SVOC samples were acquired with a traditional method using filter and polyurenthane foam plug pairs at the Ponca street site between July 2002 and February 2003, and > 110 SVOC species with various polarities were analyzed by GC-MS (Rogge et al. 2011). In this chapter, these high-quality highly time-resolved SVOC data were exploited to apportion NO_x, EC, OC, and other pollutants using multiple linear regression and PMF. In particular, we aimed to investigate seasonal and diurnal variations in emission characteristics of major sources such as motor vehicles, coal burning, biomass burning, and space heating.

5.2 Data Description

5.2.1 Site and Meteorology

Baltimore has a typical Mid-Atlantic climate with four distinguished seasons. High humidity is often observed in Baltimore because of its coastal location. Air quality at the Ponca street supersite (refer to Chapter 4 for site description) was subject to the impacts from motor vehicle exhaust and nearby industries perennially (Park et al. 2005a, Park et al. 2006a), as the receptor site was in close proximity to two main roads (I-95 and I-895) in the east and the Dundalk industrial area in the south which contains > 40 facilities. Besides, a large local utility power plant complex, the Brandon Shores and Wagner Station, was only 12 km south of the receptor site. In summer, secondary sulfate transported from several distant electricity and industrial

facilities in the Ohio Valley region is another important category of pollution (Gordon 1988, Suarez and Ondov 2002). In addition, other seasonal emission sources, such as urban residential heating in cold season and vegetation release in spring and summer, affected air quality at this site.

The measurements of SVOCs were carried out at the Ponca street site in four different months from 2002 to 2003, for periods of 7, 7, 11, and 3 days for July, August, November, and February, respectively (July 2002: 17 to 22, and 24 to 25; August 2002: 4 to 12; November 2002: 7 to 9, 14 to 16, 19 to 22, and 24 to 26; and February 2003: 21 to 24). Ambient temperatures and relative humidity (RH) during these sampling periods are listed in Table 5.1. As shown in Table 5.1, ambient temperatures spanned over a broad range, i.e., the highest of 38.4 °C in August 2002 and the lowest of -10.7 °C in February in 2003, although the average RHs were comparable in these different months.

Table 5.1 Seasonal variations of ambient temperature and relative humidity (RH) at the Baltimore Ponca street supersite during the SVOC measuring periods.

	Temperature (°C)				RH (%)			
	lowest	highest	average	σ [4]	lowest	highest	average	σ [4]
Summer [1]	15.2	38.4	27.1	3.5	16	98.4	58.1	12.6
November [2]	-2.6	22.4	8.5	3.7	27.7	100.7	67.8	14.8
February [3]	-10.7	10.4	0.1	3.4	26.4	102	69.2	17.9

[1] July & August 2002. [2] November 2002. [3] February 2003. [4] Daily variations (standard deviation of daily average temperature or RH).

As shown in Figure 5.1, winds were mostly from southerly and westerly directions in July. The prevailing winds were either from northwesterly or from southerly in

August and November. And in February, winds were either mild (wind speed < 2 m s^{-1}) from northeasterly or very strong (wind speed > 5 m s^{-1}) from westerly directions most of the time. Note that these wind rose plots in Figure 5.1 only represent the statistics during the SVOC sampling campaigns.

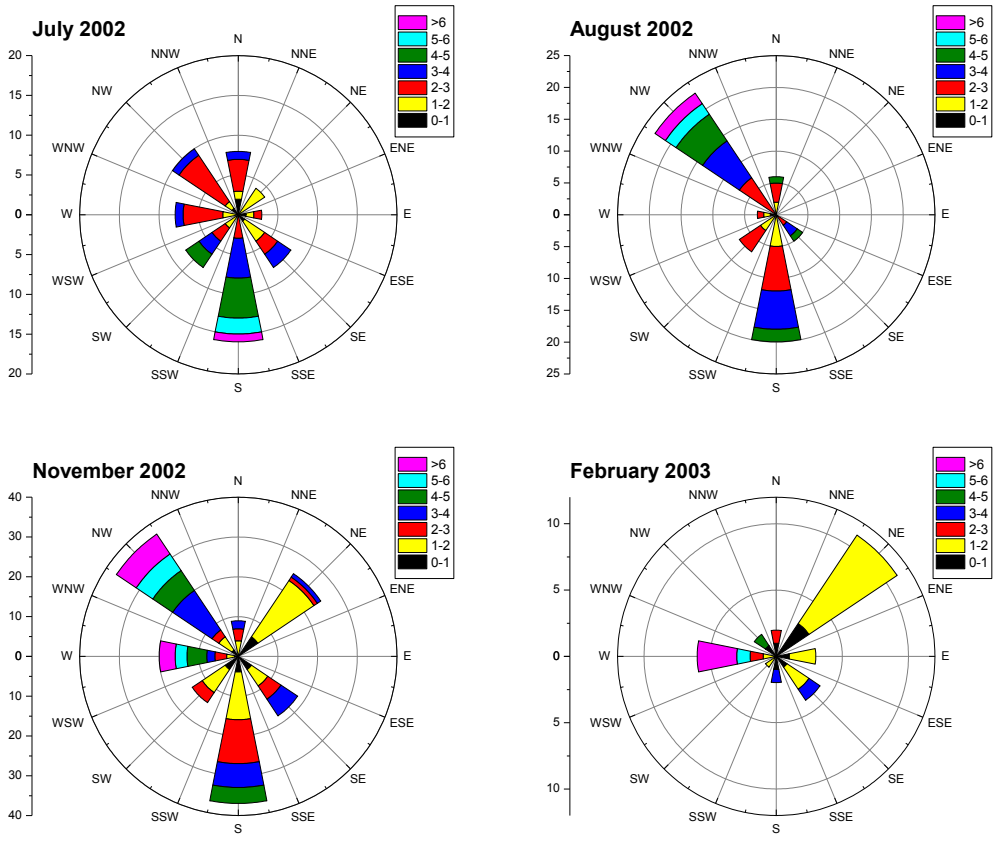

Figure 5.1 Wind rose plots during the periods of SVOC measurements in 2002 - 2003.

5.2.2 Ambient Pollutants

The quantitation of 3-hour SVOC samples was described by Rogge et al. (Rogge et al. 2011). In particular, PAHs and n-alkanes were the most abundant SVOCs in those samples. In this study, 21 PAHs, and 15 n-alkanes (C19-C29, C31, C33, C34, and C36) were grouped, as follows. PAHs were sub-divided into four categories by molecular weight and oxidation states: low molecular weight PAHs (LMWPAHs),

high molecular weight PAHs (HMWPAHs), low molecular weight oxy-PAHs (LMWOPAHs), and high molecular weight oxy-PAHs (HMWOPAHs), as shown in Table 5.2. The n-alkanes were divided into three groups: C19-C28 as low molecular weight (LMW) n-alkanes; C29, C31, and C33 as high molecular weight (HMW) odd-carbon n-alkanes; and C34 plus C36, as HMW even-carbon n-alkanes. Past studies have revealed that most of PAHs in metropolitan areas arise from motor vehicle exhaust (Khalili et al. 1995, Harrison, Smith and Luhana 1996, Yunker et al. 2002). LMW n-alkanes are well-known markers of fossil fuel combustion. The distribution patterns of these analogues have been used to identify fuel types (Kotianova et al. 2008, Zhang et al. 2008). For example, C20 and C21 are most abundant in gasoline combustion exhaust while high portions of C22, C23, and C25 indicate coal combustion exhaust (Zhang et al. 2008). HMW even-carbon n-alkanes are known markers of tire-wear dust (Rogge et al. 1993c). In contrast, HMW odd-carbon n-alkanes are often associated with atmospheric vegetative detritus and biomass burning (Rogge et al. 1993d).

Table 5.2 Categories of PAHs by molecular weight and oxidation state.

Category	Criterion	Species
Low molecular weight PAHs (LMWPAHs)	MW < 210	Phenanthrene, Anthracene, 4H-Cyclopenta-[def]-phenanthrene, Fluoranthene, and Pyrene
High molecular weight PAHs (HMWPAHs)	MW > 220	Benz[a]anthracene, Chrysene/Triphenylene, Benz[e]acephenanthrylene, Benzo[k]fluoranthene, Benzo[j]fluoranthene, Benzo[e]pyrene, Benzo[a]pyrene, Perylene, Indeno[1,2,3-cd]pyrene, Benzo[ghi]perylene, Dibenz[a,h]anthracene, and Coronene

Low molecular weight oxy-PAHs (LMWOPAHs)	MW < 210	9H-Fluorene-9-one, and 9,10-Anthracenedione
High molecular weight oxy-PAHs (HMWOPAHs)	MW > 220	7H-Benz[de]anthracene-7-one, and Benz[a]anthracene-7,12-dione

Twelve alkylcyclohexanes (ACHs) and eight pentacyclic triterpanes (PCTTs) were grouped, respectively, as two types of traffic tracers. The former is ubiquitously found in refinery petroleum products (Hostettler and Kvenvolden 2002) and the latter is exclusively present in lubricating oil (Rogge et al. 1993b). Benzothiazole is a pyrolysis product of vulcanization accelerator and thus has been used as a tracer of tire-wear dust (Kim et al. 1990). Nevertheless, our previous study (refer to Chapter 4) found that this road dust tracer was poorly correlated with primary vehicular traffic.

Other SVOCs that are less relevant to motor vehicle emissions were grouped into iso- and antiso-alkanes, n-alkanoic acids, n-alkenoic acids, aliphatic dicarboxylic acids (ADCAs), aromatic polycarboxylic acids (APCAs), 2-alkanones, resin acids, sugars, steroids, N-hetero-PAHs, S-hetero-PAH, secondary biogenic oxidation products (2^{nd} biogenic), and phenolic wood markers, accordingly. Iso-alkanes are enriched in the waxes of tobacco plants and detectable in cigarette smoke (Rogge et al. 1994). Steroids, n-alkanoic acids (i.e., palmitic acid, and stearic acid), and n-alkenoic acids (i.e., oleic acid) have been used as tracers of cooking (Rogge et al. 1991) or biomass burning (Oros and Simoneit 1999, Simoneit et al. 1999). Resin acids are often found in conifer wood (Simoneit et al. 1993), and phenolic compounds are markers of hardwood combustion (Rogge et al. 1998).

Hourly data of TEOM $PM_{2.5}$ mass, EC, OC, sulfate, nitrate, NO_x, CO, and ozone were retrieved from the Baltimore supersite (http://www2.chem.umd.edu/supersite/) database, and combined into 3-hour intervals. In addition, 30-minute data of 11 SEAS metals (i.e., Al, As, Cd, Cr, Cu, Fe, Mn, Ni, Pb, Se, and Zn) were available in the Baltimore supersite database for part of the study periods in July and November 2002 and treated likewise.

5.3 Methods

5.3.1 Linear Regression

As discussed in Chapter 2, NO_x is a criteria pollutant gas that can be generated from multiple types of combustion sources, e.g., motor vehicle exhaust, coal burning, residual oil combustion, and biomass burning. In this study, linear regressions between NO_x and organic molecular tracers of various combustion sources were performed, to apportion the contributions from these sources. In particular, seasonal and diurnal variations in those source emissions were studied by comparing the linear regressions between the summer and the November measuring periods and between morning and afternoon measuring periods. Note that the linear regressions only used the available data in July, August, and November 2002, as NO_x concentrations were not measured in 2003. The linear regression results as well as the corresponding statistics were obtained using a least-square linear regression function available in the MATLAB software (MathWorks, Inc., version 7.8).

5.3.2 PMF

PMF analyses were carried out for the four measuring periods individually. Totally 224 valid 3-hour observations were used as listed in Table 5.3. The EPA PMF v3.0 program (U.S.EPA 2008) was used and up to 30 individual or grouped species (sulfate and nitrate measurements in November and February, and CO and NO_x in February were unavailable) were selected for the modeling, including $PM_{2.5}$ mass, EC, OC, sulfate, nitrate, 117 SVOCs in 23 categories, and two criteria gases (i.e., NO_x and CO). Specifically, EC, OC, NO_x, and organic tracers of motor vehicle exhaust (i.e., ACHs, PCTTs, LMWPAHs, HMWPAHs, LMWOPAHs, HMWOPAHs, and LMW n-alkanes) were set as "strong" species, and all other species were set as "weak" species in the modeling. All concentrations of HMW even-carbon n-alkanes were below the detection limits in July 2002, and were therefore excluded from the corresponding modeling.

Table 5.3 Statistics of 3-hourly SVOC observations by time of the day during different months.

Time of day	July	August	November	February
1:30	8	7	13	3
4:30	6	7	13	3
7:30	6	7	13	3
10:30	6	6	13	3
13:30	6	6	11	3
16:30	6	6	11	3
19:30	7	7	11	2
22:30	7	7	11	3
total	52	53	96	23

Different numbers of factors (3 to 8) were tested until an optimal fit in the robust mode was reached, which sufficiently explained the observed mass and yielded a result without any scaled residual (i.e., e_{ij}/s_{ij}) greater than 4 for any species. In addition, different values (-0.2 to 0.2) of the rotational parameter, FPEAK, were used (Paatero et al. 2005) and the optimality of the solution was confirmed by the degree to which $Q(E)$ was insensitive to changes in the FPEAK parameter. Each PMF factor profile was normalized to the corresponding $PM_{2.5}$ concentration apportioned by PMF to generate the abundance profile with respect to $PM_{2.5}$.

5.4.1 Seasonal and Diurnal Variations of Ambient Pollutants

The seasonal averages of major PM constituents (i.e., EC, OC, sulfate, and nitrate) as well as two most abundant SVOCs, PAHs and n-alkanes, are listed in Table 5.4. In the winter, ambient concentrations of EC, OC, and n-alkanes were higher than those in the summer. In contrast, the average levels of PAHs showed insignificant seasonal variations. Close inspection revealed that ambient concentrations of HMWPAHs were generally greater in the winter than those the summer, in contrast to an opposite trend for LMWPAHs except anthracene. The former agreed with the greater OC concentrations observed in the winter, which was partially due to the enhanced partitioning of SVOCs into the aerosol particle phase at low temperature. The latter indicated an extra source with high abundances of LMWPAHs in the summer, which probably represented enhanced vegetation release (Simonich and Hites 1994, Wilcke et al. 2004).

Table 5.4 Seasonal variations of selected $PM_{2.5}$ constituents (average ± σ).

	$PM_{2.5}$ ($\mu g\ m^{-3}$)	EC ($\mu g\ m^{-3}$)	OC ($\mu g\ m^{-3}$)	Sulfate ($\mu g\ m^{-3}$)	Nitrate ($\mu g\ m^{-3}$)	PAHs ($\mu g\ m^{-3}$)	HMW-PAHs ($ng\ m^{-3}$)	n-alkanes ($ng\ m^{-3}$)
Summer[1]	24.6±14.8	0.51±0.55	3.87±1.57	5.39±6.16	0.83±0.76	46.7±29.3	0.90±1.26	80.5±34.8
November[2]	22.3±9.8	1.44±1.13	6.11±3.47	1.60±0.61	3.76±2.34	40.5±17.2	5.3±3.7	109±59
February[3]	22.5±12.3	1.35±1.52	6.74±5.39	n.a.	n.a.	44.9±29.3	6.1±5.8	150±127
Average[4]	23.4±13.7	0.98±1.05	5.10±3.23	3.97±5.23	1.90±2.09	44.0±25.2	3.2±3.8	98.6±63.0

[1] July & August 2002. [2] November 2002. [3] February 2003. [4] 3-hourly average for all study periods.

The correlation coefficients of NO_x with other ambient pollutants are listed in Table 5.5. In general, EC and OC showed fair correlations ($r^2 \geq 0.6$) with NO_x, except in the summer. Sulfate and nitrate showed poor correlations ($r^2 < 0.5$) with NO_x in any period. 8 of the 12 HMWPAHs showed excellent correlations ($r^2 \geq 0.8$) with NO_x, except Benzo[j]fluoranthene ($r^2 = 0.744$), benzo[a]pyrene ($r^2 = 0.792$), perylene ($r^2 = 0.764$), and dibenz[a,h]anthracene ($r^2 = 0.637$). The two HMWOPAHs showed excellent correlations with NO_x ($r^2 = 0.890$ and 0.840 for 7-*H*-benz[de]anthracen-7-one and benz[a]anthracene-7,12-dione, respectively) as well. In contrast, all the LMWPAHs and LMWOPAHs were poorly correlated ($r^2 < 0.5$) with NO_x, except anthracene ($r^2 = 0.530$). Furthermore, these correlations were investigated season by season and all species except fluoranthene, which exhibited at least a moderate correlation ($r^2 \geq 0.6$) with NO_x in the winter, in contrast to their poor correlations ($r^2 < 0.4$) in the summer. These differences indicated that either there was an additional non-combustion source of SVOCs or enhanced oxidation chemistry degraded their correlations in the summer.

The correlations between NO_x and traffic-related species (i.e., EC, OC, n-alkanes, PAHs, and ACHs) in the mornings were in general better than those in the afternoons (e.g., r^2 for n-alkanes were 0.749 and 0.268 for the mornings and afternoons, respectively), suggesting a stronger influence from motor vehicle emissions in the former. Besides, NO_x showed very poor correlations ($r^2 < 0.2$) with all SEAS metals, even including Ni and Zn. Hence the use of those elemental tracers for source apportionment of NO_x may be infeasible.

Table 5.5 Seasonal and diurnal variations in the correlation (r^2) between NO_x and various organic molecular tracers or other ambient pollutants.

Species	All[1]	Summer[2]	Winter[3]	Morning[4]	Afternoo[5]
Criteria gases:					
Ozone	0.303	0.142	0.242	0.308	0.361
CO	**0.714**	0.085	**0.704**	**0.830**	**0.747**
$PM_{2.5}$ constituents:					
$PM_{2.5}$ mass	0.071	0.003	**0.704**[6]	0.199	0.005
Sulfate	0.065	0.020	0.090	0.039	0.117
Nitrate	0.427	0.031	0.141	0.426	0.434
EC	**0.716**	0.378	**0.729**	**0.743**	**0.661**
OC	**0.641**	0.131	**0.714**	**0.716**	0.514
LMW PAHs:					
Phenanthracence	0.025	0.282	**0.727**	0.046	0.001
Anthracene	0.530	0.263	**0.791**	0.473	**0.636**
4-*H*-Cyclopenta[def]phenanthrene	0.031	0.255	**0.633**	0.045	0.011
Fluoranthene	0.048	0.148	0.394	0.025	0.084
Pyrene	0.211	0.273	0.592	0.270	0.118
HMW PAHs:					
Benz[a]anthracene	**0.871**	0.277	**0.840**	**0.883**	**0.849**
Chrysene and Triphenylene	**0.851**	0.360	**0.822**	**0.876**	**0.811**
Benz[e]acephenanthrylene	**0.846**	0.254	**0.803**	**0.827**	**0.872**
Benzo[k]fluoranthene	**0.817**	0.206	**0.780**	**0.791**	**0.856**
Benzo[j]fluoranthene	**0.744**	0.135	**0.705**	**0.698**	**0.818**
Benzo[e]pyrene	**0.840**	0.267	**0.811**	**0.833**	**0.849**
Benzo[a]pyrene	**0.792**	0.147	**0.783**	**0.744**	**0.872**
Perylene	**0.764**	0.143	**0.793**	**0.710**	**0.857**

Indeno[1,2,3-cd]pyrene	**0.811**	0.186	**0.808**	**0.779**	**0.860**
Benzo[ghi]perylene	**0.843**	0.236	**0.826**	**0.833**	**0.861**
Dibenz[a,h]anthracene	**0.637**	0.165	0.479	**0.690**	0.588
Coronene	**0.811**	0.229	**0.744**	**0.818**	**0.821**
LMW Oxy-PAHs:					
9-*H*-Fluoren-9-one	0.337	0.351	**0.698**	0.364	0.268
9,10-Anthracencedione	0.033	0.107	**0.709**	0.011	0.084
HMW Oxy-PAHs:					
7-*H*-Benz[de]anthracene-7-one	**0.890**	0.507	**0.843**	**0.910**	**0.877**
Benz[a]anthracence-7,12-dione	**0.840**	0.527	**0.743**	**0.868**	**0.799**
n-Alkanes	0.545	0.157	**0.755**	**0.749**	0.268
Iso- and anteiso-alkanes	**0.682**	0.194	0.591	**0.654**	**0.754**
n-Alkanoic acids	0.000	0.033	0.415	0.000	0.001
n-Alkenoic acids	0.462	0.008	0.345	0.378	0.702
n-Aliphatic dicarboxylic acids	0.171	0.012	0.099	0.120	0.269
Aromatic polycarboxylic acids	0.052	0.095	0.111	0.054	0.052
2-Alkanones	0.104	0.046	0.047	0.116	0.113
Alkylcyclohexanes	**0.664**	0.302	**0.713**	**0.763**	0.494
Resin acids	0.460	0.096	0.308	0.586	0.397
Sugars (Levoglucosan)	0.332	0.010	0.238	0.304	0.393
Steriods	0.230	0.000	0.285	0.193	0.323
Thiazoles	0.123	0.091	0.277	0.112	0.157
Pentacyclic triterpanes	**0.657**	0.449	0.561	**0.686**	**0.748**
N-Hetero PAH	0.044	0.016	0.238	0.030	0.059
S-Hetero PAH	0.092	0.305	**0.640**	0.149	0.017

Secondary biogenic oxy-products	0.001	0.048	0.005	0.000	0.003
Phenolic wood markers	0.398	0.146	0.225	0.323	0.596

[1] For the measuring periods in July, August, and November 2002.

[2] July & August 2002.

[3] November 2002.

[4] Including all the a.m. measuring periods in July, August, and November 2002.

[5] Including all the p.m. measuring periods in July, August, and November 2002.

[6] Numbers in boldfaced type indicate at least a fair correlation ($r^2 > 0.6$).

5.4.2 MLR Results

In this study, LMWPAHs, HMWPAHs, LMW n-alkanes, ACHs, PCTTs, n-alkanoic acids, and sugars, which are tracers for various fossil fuel combustions or biomass burning (i.e., ACHs and PCTTs are unique tracers of motor vehicle emissions; levoglucosan is a unique tracer of biomass burning; and other tracers are source non-specific), were selected as the candidates for use as independent variables for the MLR analysis. Using all the datasets in 2002, a best-fit relationship ($r^2 = 0.905$, and $p < 0.001$) between NO_x and combination of tracers is given as follows:

$$[NO_x] = (16.90 \pm 1.02) \times [HMWPAHs] + (3.00 \pm 0.82) \times [ACHs] + (3.59 \pm 1.38) \times [PCTTs] + (0.12 \pm 0.05) \times [sugars] + (-0.20 \pm 5.24) \quad (5.1)$$

where concentrations of NO_x are in ppb, and SVOCs in ng m^{-3}. The small residual compared with the average NO_x concentration (i.e., 89.9 ppb) and the good recovery of predicted NO_x concentrations indicated these four tracers could well represent major sources of combustions in the study.

Similar, the MLR of EC against those four tracers was obtained as:

$$[EC] = (0.168 \pm 0.018) \times [HMWPAHs] + (0.067 \pm 0.012) \times [ACHs] - (0.038 \pm 0.020) \times [PCTTs] - (0.0002 \pm 0.0008) \times [sugars] - (0.167 \pm 0.082) \quad (5.2)$$

where concentrations of EC are in μg m^{-3}, and SVOCs in ng m^{-3}. The regression equation had a correlation coefficient of 0.757 ($p < 0.001$).

Accordingly, motor vehicle exhaust (i.e., ACHs and PCTTs as its tracers) contributed 53 % of EC and 39 % of NO_x during the measuring periods. In contrast, biomass burning (levoglucosan as its tracer) contributed 2.5 % of NO_x and negligible EC (< 0.1%).

Note that attempts to include LMWPAHs or n-alkanes into the MLR analyses turned void, as either large unexplained residuals or poor fits (i.e., unsatisfactory r^2 or negative slopes) were obtained. This suggested that substantial amounts of these species were relevant to non-combustion processes, e.g., evaporative emissions from motor vehicles or vegetation release. Also, as we discussed, there is a stronger temperature effect here that would need to be considered.

5.4.3 PMF Results

In general, a five- or six- factor solution was obtained for each modeling period. The common factors for all modeling periods included traffic, coal burning, sulfate (secondary aerosol), and biomass burning. A vegetation factor was resolved only in July and August and a heating factor was resolved only in November and February. In addition, a road dust factor was resolved only in August. The attributions of these factors are described below.

5.4.3.1 Traffic Factor

The traffic factor was recognized by its largest abundances of traffic-related tracers (Table 5.6), e.g., ACHs and PCTTs, among all factors. Besides, as listed in Table 5.7, this factor was further identified as maximum factor contributions of the day occurred within the traffic rush hours (i.e., 0730 or 1630 LT) for 18 of the 29 days with complete daily records, and only slightly off rush hours in the other 11 days.

Table 5.6 Abundance profiles of motor vehicle emissions obtained by PMF [1] and WMA [2] analyses (unit: μg per μg of $PM_{2.5}$ for CO, NO_x, sulfate, nitrate, EC, and OC; and ng per μg of $PM_{2.5}$ for SVOCs).

Species	Jul	Aug	Nov	Feb	WMA	
					average	σ
CO	59.44	28.48	n.a.	n.a.	46.44	± 16.07
NO_x	27.51	33.04	26.33	n.a.	19.59	± 4.81
Sulfate	0.000	0.000	n.a.	n.a.	0.023	± 0.009
Nitrate	0.133	0.122	n.a.	n.a.	0.016	± 0.004
EC	0.227	0.362	0.166	0.134	0.125	± 0.033
OC	0.640	0.516	0.471	0.365	0.408	± 0.114
n-Alkanes	17.70	5.436	5.111	10.85	6.072	± 1.068
LMW n-alkanes	16.70	5.146	4.967	10.511	5.881	± 0.870
HMW odd-n-alkanes	1.008	0.280	0.144	0.267	0.127	± 0.096
HMW even-n-alkanes	n.a.	0.009	0.000	0.075	0.021	± 0.307
PAHs	14.71	3.878	1.738	2.578	1.457	± 0.357
LMWPAHs	14.45	3.592	1.382	2.256	1.212	± 0.291
HMWPAHs	0.258	0.286	0.355	0.323	0.245	± 0.086
Oxy-PAHs	1.685	0.732	0.248	0.370	0.239	± 0.075
LMWOPAHs	1.644	0.697	0.213	0.335	0.197	± 0.072
HMWOPAHs	0.042	0.035	0.035	0.035	0.042	± 0.017
Alkylcyclohexanes	1.862	0.531	0.796	1.418	0.815	± 0.147
Pentacyclic triterpanes	0.370	0.266	0.397	0.660	0.541	± 0.102
Iso- and antiso-alkanes	0.000	0.088	0.000	0.000	0.042	± 0.021
n-Alkanoic acids	0.000	0.000	0.766	5.818	2.843	± 0.647

n-Alkenoic acids	0.091	0.036	0.072	0.375	0.000 ± 0.086
Aliphatic dicarboxylic acids	0.015	0.010	0.028	0.051	0.004 ± 0.004
Aromatic polycarboxylic acids	0.186	0.132	0.007	0.046	0.009 ± 0.003
2-Alkanones	1.277	0.952	0.000	0.049	0.035 ± 0.019
Resin acids	0.132	0.003	0.000	0.068	0.103 ± 0.033
Sugars	0.061	0.024	0.161	1.261	1.059 ± 1.057
Steroids	0.342	0.000	0.045	0.097	0.053 ± 0.109
Thiazoles	1.150	1.661	0.000	0.584	0.111 ± 0.154
N-Hetero-PAH	0.011	0.017	0.001	0.001	0.001 ± 0.000
S-Hetero-PAH	0.986	0.201	0.107	0.170	0.124 ± 0.030
Secondary biogenic oxidation products	1.776	0.928	0.063	0.083	0.000 ± 0.093
Phenolic wood markers	0.048	0.060	0.068	0.070	0.005 ± 0.034

[1] Obtained with PMF analyses using the 3-hour data in four different months from 2002 to 2003.

[2] Obtained with windless model analysis based linear regression, using the hourly data on November 20th, 2002, as presented in Chapter 4.

Table 5.7 Statistics of the time of the day for the maximum contribution from the traffic factor.

Time of the day	Date
0430 LT	7/22, 8/9, 8/10, 11/8, 11/9,
0730 LT	7/17, 7/18, 7/20, 7/24, 8/5, 8/8, 8/11, 8/12, 11/7, 11/14, 11/19, 11/20, 11/21, 11/22, 11/25, 2/23, 2/24
1030 LT	7/19, 7/21, 8/7, 11/24, 2/21
1630 LT	11/26
1930 LT	11/15

As shown in Table 5.6, the four PMF-resolved profiles of the traffic factor in the different months are compared with that obtained in the previous study of a traffic

episode in November 2002 by the windless model analysis based linear regression (refer to Chapter 4), which was denoted as the WMA profile. The OC/TC ratios were 0.74, 0.59, 0.74, and 0.73 for July, August, November, and February, respectively, compared with a ratio of 0.77 in the WMA profile of the morning of November 20th. The relative emissions of CO and NO_x in the months for which criteria gas data were available (i.e., July, August, and November) were also in rough agreement with the WMA profile.

In general, the November profile is the most consistent with the WMA profile. The February profile showed higher abundances (i.e., about twice) for all SVOC species than those in the WMA profile, which was attributed to enhanced partitioning into aerosol particle phase at low temperature as discussed above. The summer profiles, especially the July profile, showed higher OC contents than the WMA profile. In particular, the abundances of those small SVOCs with low boiling points (e.g., LMWPAHs, LMWOPAHs, LMW n-alkanes, and alkycyclohexanes) in the July profile were much greater than the winter profiles. In contrast, the abundances of SVOCs with high boiling points (e.g., HMWPAHs, HMWOPAHs, and pentacyclic triterpanes) showed little discrepancy among all these profiles. Considering the high summer temperatures, the higher contents of OC and small SVOC molecules in the summer profiles could be partially resulted from enhanced volatilization of organic species from gasoline and diesel fuels.

This traffic factor was found to be a primary source of EC at the receptor site during any study period. As shown in Figure 5.2, it was nearly the sole EC source (e.g., 98 % in July) in the summer, and contributed the majority of EC (i.e., 54 ~ 73

% of EC) in the winter even though heating added a substantial amount of contributions to ambient EC. Moreover, the relative contributions from motor vehicle emissions during the afternoon rush hours were significantly lower than those during the mornings (Figure 5.2). In particular, the percentage contributions to OC and low molecular weight SVOCs (i.e., LMW n-alkanes, LMWPAHs, and LMWOPAHs) from this factor were less significant in the summer afternoons than in the winter afternoons (Figure 5.2b). This suggested substantial contributions from non-traffic sources (e.g., secondary organic aerosol) in the summer afternoons compared with the winter afternoons, considering that the abundances of these species in the summer profiles of motor vehicle emissions were higher than those in the winter profiles (Table 5.6).

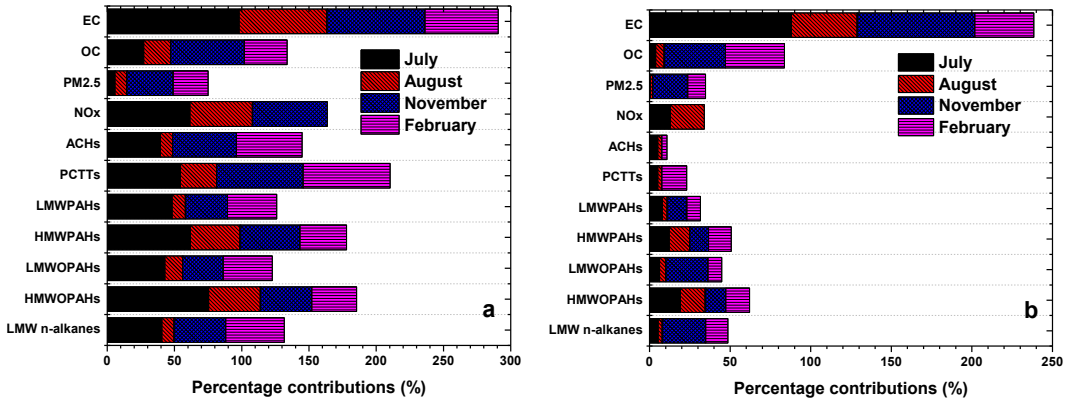

Figure 5.2 The percentage contributions (%) of the traffic factor to ambient concentrations during traffic rush hours: a) in the morning; and b) in the afternoon.

5.4.3.2 Coal Burning

The ratio of indeno[1,2,3-*cd*]pyrene and EC has been used to identify coal burning (Simoneit 2002). In this study, an excellent linear relationship ($r^2 = 0.980$, $p < 0.001$) was revealed between HMWPAHs and indeno[1,2,3-*cd*]pyrene (Figure 5.3), and thus we used the ratio of HMWPAHs and EC as a surrogate. The coal burning factor was

recognized by its largest HMWPAHs/EC ratio among all factors. Note that the HMWPAHs/EC ratio may be unreliable in the summer when EC concentrations appeared to be underestimated by PMF (i.e., only 59 % EC mass reconstructed). Nevertheless, the ratios of two most abundant SVOCs, i.e., LMW n-alkanes and LMWPAHs, were nearly identical in those profiles of different months, as shown in Figure 5.4, inferring that these are the same source by assuming the temperature effects on partitioning were similar for these two types of species with low boiling points. Overall, this factor contributed 9.0 ~ 13.2 % of the total $PM_{2.5}$ in the summer, and 22.0 ~ 24.5 % in the winter.

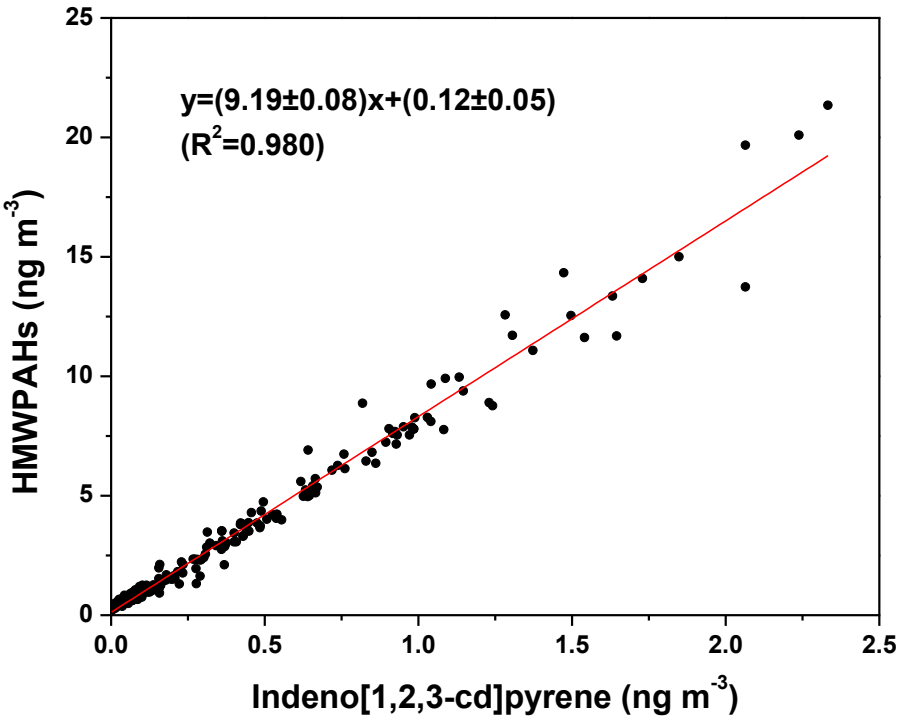

Figure 5.3 Correlation between measured HMWPAHs and Indeno[1,2,3-*cd*]pyrene.

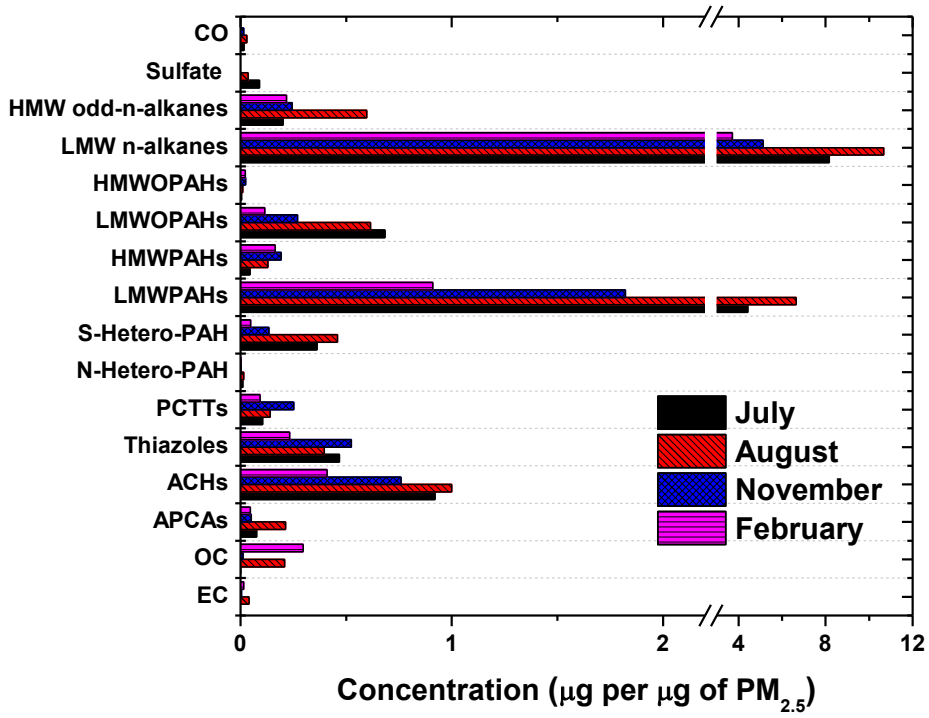

Figure 5.4 PMF-derived profiles of the coal burning factor during different months (SVOC abundances were multiplied by a factor of 1,000).

Because mobile emissions and coal combustion were the two major concerns of air pollution in Baltimore (Ogulei et al. 2005, Ondov et al. 2006), we used LMW n-alkane tracers to compare seasonal variations of these two factors (Zhang et al. 2008). As shown in Table 5.8, enhancements in the corresponding tracers of both factors were observed in the cold season. Nevertheless, the ratios of the tracers for these two factors were fairly constant in the different months, implying insignificant seasonal changes in the relative emissions from these factors with reference to each other.

Table 5.8 Seasonal variations of selected low molecular weight n-alkane tracers.

	Vehicle exhaust tracers ($ng\ m^{-3}$)		Coal combustion tracers ($ng\ m^{-3}$)			Ratio *
	n-eicosane	n-heneicosane	n-docosane	n-tricosane	n-pentacosane	
Average	19.649	13.406	10.410	7.239	3.766	1.544

Summer [1]	17.263	10.921	9.475	6.288	2.487	1.544
November [2]	19.864	14.335	10.113	7.408	5.905	1.522
February [3]	31.401	22.298	16.467	11.424	5.368	1.604

[1] July & August 2002. [2] November 2002. [3] February 2003. * Ratio of total vehicle exhaust tracers and total coal combustion tracers.

5.4.3.3 Biomass Burning and Vegetation Release

Local Biomass Burning in the Winter

Local biomass burning in the Baltimore area includes defoliation combustion and wood burning which mostly occurs in the fall and winter. Simoneit et al. (Simoneit 2002) found that biomass burning had the highest ratio of levoglucosan/EC among all types of combustions. As shown in Figure 5.5, the highest presence of levoglucosan observed in the winter, as well as phenolic wood markers, resin acids, and iso-alkanes, attributed this factor to biomass burning. It is noteworthy that a substantial contribution from this factor occurred on November 25th 2002, a windless day. Levoglucosan concentrations were extremely high (i.e., > 1000-fold of its background level) in that early morning, and 67.0 % of phenolic wood marker, 74.9 % of resin acids, 74.9 % of sugars, and 15.0 % of NO_x of the 11-day measurements in November were emitted on that day.

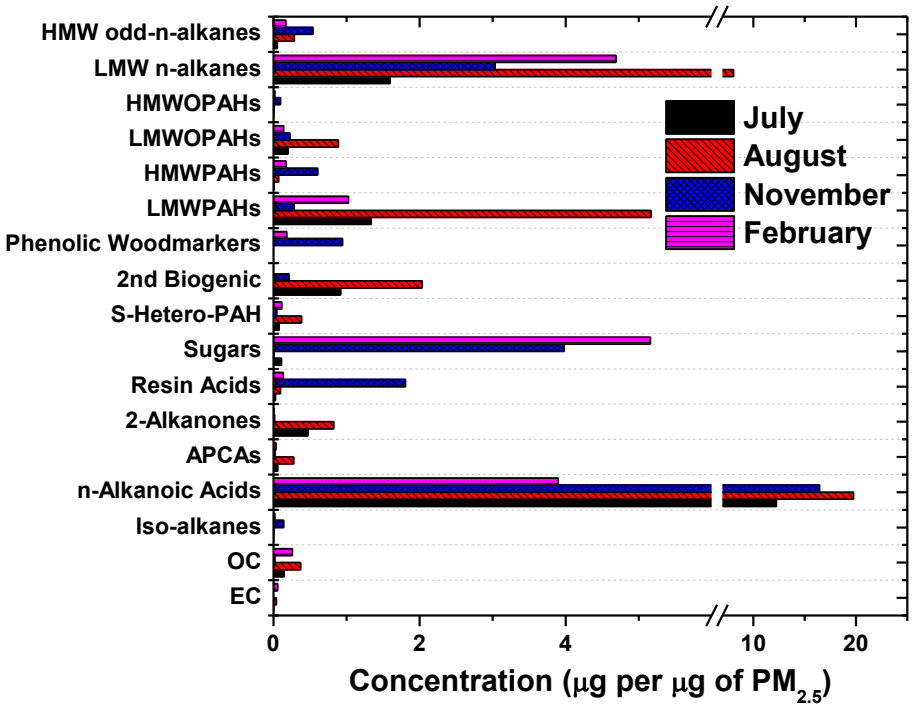

Figure 5.5 PMF-derived profiles of the biomass combustion factor during different months (SVOC abundances were multiplied by a factor of 1,000).

Transported Distant Biomass Burning in the Summer

In North America, the 2002 wildfire season (June to September) was one of the worst in the past 10 year with the acres burned nearly twice the 10-year average, according to the National Interagency Fire Center (http://www.ncdc.noaa.gov/oa/climate/research/fire02.html). Most of the large fires of this year occurred in Arizona, Colorado, Mexico, and Canada but air quality in other regions of the US was impacted (DeBell 2004). For example, during early July 2002, dramatic increases (i.e., > 30-fold) in ambient PM and PAH levels were observed in Baltimore due to the forest fire in Quebec, Canada (Sapkota et al. 2005). The SVOC sampling in July at the Baltimore supersite was carried out one week after the smoke from this fire event was detected in Baltimore and a substantial contribution (i.e., 13.8 ~ 27.9 % of $PM_{2.5}$ mass, 6.1 ~ 21.3 % of EC, 27.8 ~ 28.7 % of

OC, and 21.5 ~ 28.3 % of PAHs) from biomass burning was still resolved. In contrast to the biomass burning profile in the winter, this factor in the summer showed little presence of levoglucosan. Instead, large abundances of alkanoic acids as well as oxidation products such as 2-alkanones and secondary biogenic oxidation products were observed, as shown in Figure 5.5. These differences could be attributed to photo-degradation of levoglucosan during the long-distance plume transport (Hennigan et al. 2011).

Vegetation Release

The vegetation release factor was identified by its large abundance of secondary biogenic oxidation products and high fractions of low molecular weight SVOCs (i.e., LMW n-alkanes, and LMWPAHs) among all factors, as shown in Figure 5.6. Besides, this factor had low abundances of EC and NO_x, indicating its non-combustion nature. Vegetation release was an important source of OC and $PM_{2.5}$ in the summer (i.e., 15.9 ~ 21.2 % of OC and 15.3 ~ 20.0 % of $PM_{2.5}$ mass), and it was not resolved in the winter.

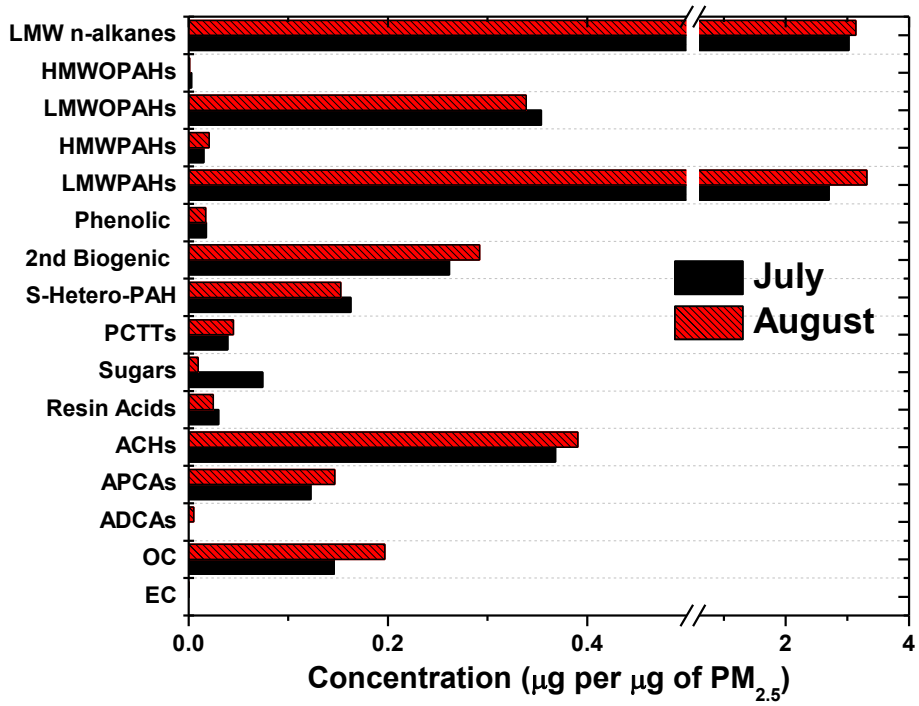

Figure 5.6 PMF-derived profiles of the vegetation release factor in the summer of 2002 (SVOC abundances were multiplied by a factor of 1,000).

5.4.3.4 Sulfate Factor (Secondary Aerosol)

In the summer, the sulfate factor accounted for 48.6 ± 5.1% of sulfate, 31.9 ± 4.2 % of OC, and 44.7 ± 0.5 % of $PM_{2.5}$ mass on average. In addition, it contributed a substantial amount of PAHs (6.3 to 29.2 %) as well as other SVOC species. It was difficult to confidently identify the sulfate factor in the winter due to the lack of sulfate data. However, this secondary aerosol factor was still recognized by its presumably high OC/EC ratio, considerable contribution to $PM_{2.5}$ (i.e., 6.8 ~ 27.5 % of total $PM_{2.5}$ mass), and large abundances of oxidized organic species due to chemical aging (Fuzzi et al. 2006). Figure 5.7 shows the profiles of this secondary aerosol factor. It is noteworthy that the ratios of LMW n-alkanes and LMWPAHs remained fairly constant (i.e., LMW-n-alkanes/LMWPAHs = 2.17 ~ 2.73) in August,

November, and February, although SVOC abundances were generally several fold higher than those in the winter.

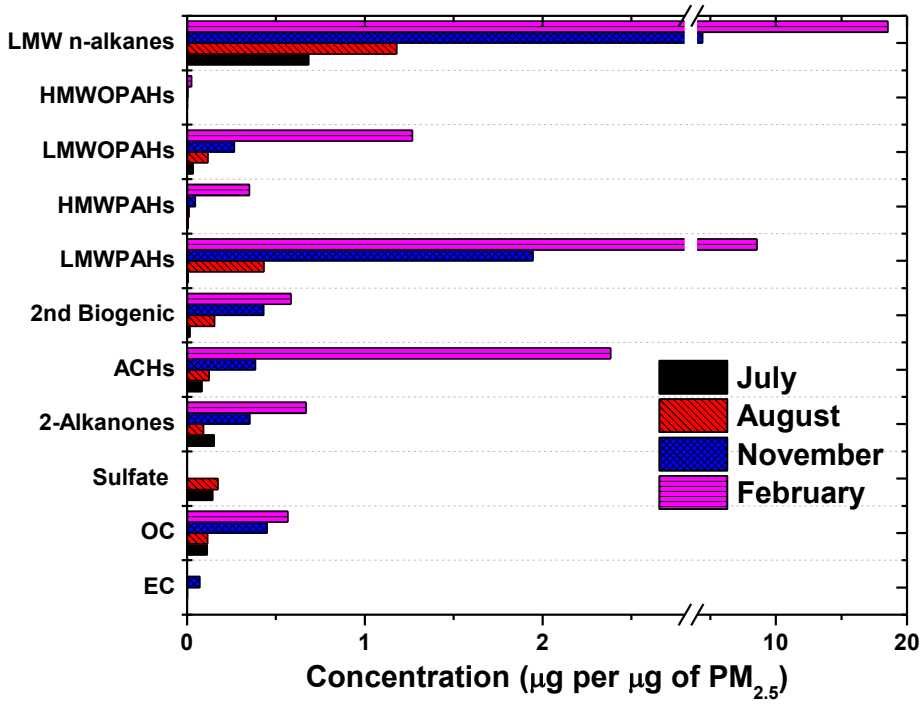

Figure 5.7 PMF-derived profiles of the secondary aerosol factor during different months (SVOC abundance values were multiplied by a factor of 1,000).

5.4.3.5 Heating

Heating was an important source of EC, OC and PAHs in the cold season. In November, the heating factor was identified by its large abundances of EC, CO, NO_x, n-alkanes, and PAHs. In particular, the low presence of resin acids and sugars made this factor distinguished from biomass burning. This factor exhibited a unique diurnal pattern with its maximum contribution of the day in the period from midnight to early morning. NO_x and CO data were unavailable in February 2003 but this factor was still recognized by its great similarity to that in November (Figure 5.8). Moreover, this factor showed enhanced contributions in February than November (i.e., 33.3 % of the

total EC in February, compared to 18.6 % in November), consistent with the greater demand for heating in the former.

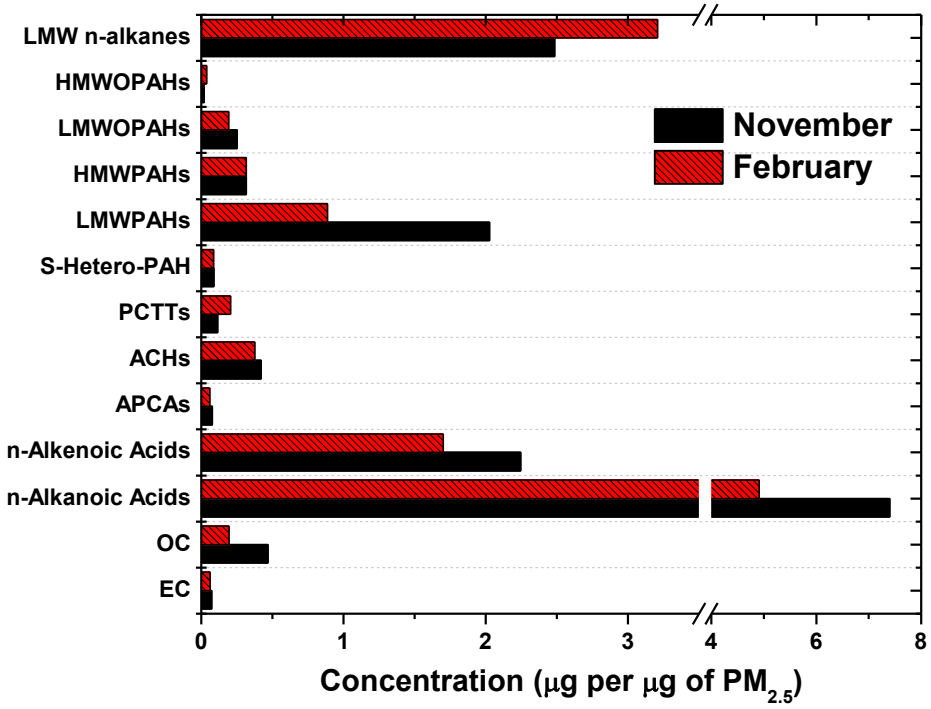

Figure 5.8 PMF-derived profiles of the heating factor in the winter of 2002-2003 (SVOC abundances were multiplied by a factor of 1,000).

5.4.3.6 Road Dust

A road dust factor was identified by its large abundances of HMW even-carbon n-alkanes and benzothiazole in August 2002. This was a minor factor overall which only represented 5.1 % of the total $PM_{2.5}$ and small fractions (< 10 %) of all species except HMW even-carbon n-alkanes during the study period. Most of the contribution (> 80 %) from this factor was made in the evening of August 8th. A northwesterly gale (wind speed > 4 m s^{-1}) lasted several hours in that afternoon and calmed down during the evening, and this episodic contribution was probably related to dust settlement. Indeed, particle size distributions measured on August 8th, 2002, at the Ponca street site (Appendix E) revealed a sudden increase of particles in an

accumulation mode (i.e., median particle size ~ 250 nm) during the evening (i.e., 1930 ~ 2130 LT), in agreement with the attribution of this road dust factor.

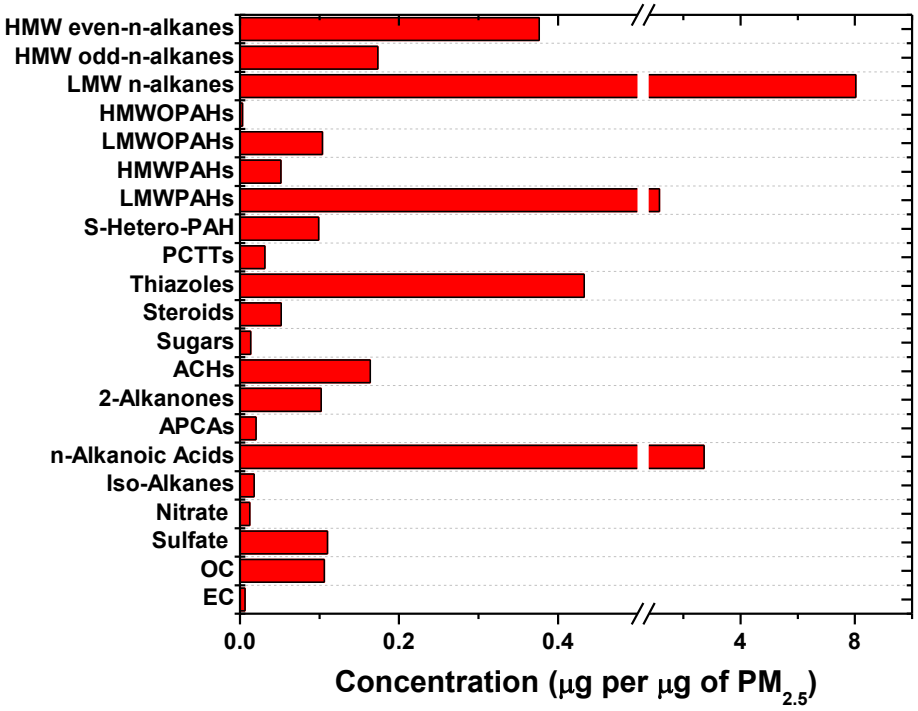

Figure 5.9 PMF-derived profile of the road dust factor in August 2002 (SVOC abundances were multiplied by a factor of 1,000).

5.4.3.7 Summary of PMF Apportionments

Figure 5.10 shows the apportioned $PM_{2.5}$ mass, NO_x, EC, and OC by PMF during different measuring periods. The contributions from both motor vehicle emissions and coal burning in the winter were greater than those in the summer. In contrast, the contributions from the sulfate factor declined from the summer to the winter. Biomass burning showed its highest contribution to $PM_{2.5}$ but lowest contribution to NO_x in July, 2002, because it in fact likely originated from the distant Canadian boreal wildfires. Two other seasonal factors, vegetation release in the summer and heating in winter, exhibited reasonable contributions in the corresponding season: the former contributed remarkable amounts of OC but very little NO_x and EC, and the latter

made a larger contribution to EC in February than in November. Road dust, as a minor source to $PM_{2.5}$ in August, had very little contributions to both EC and OC.

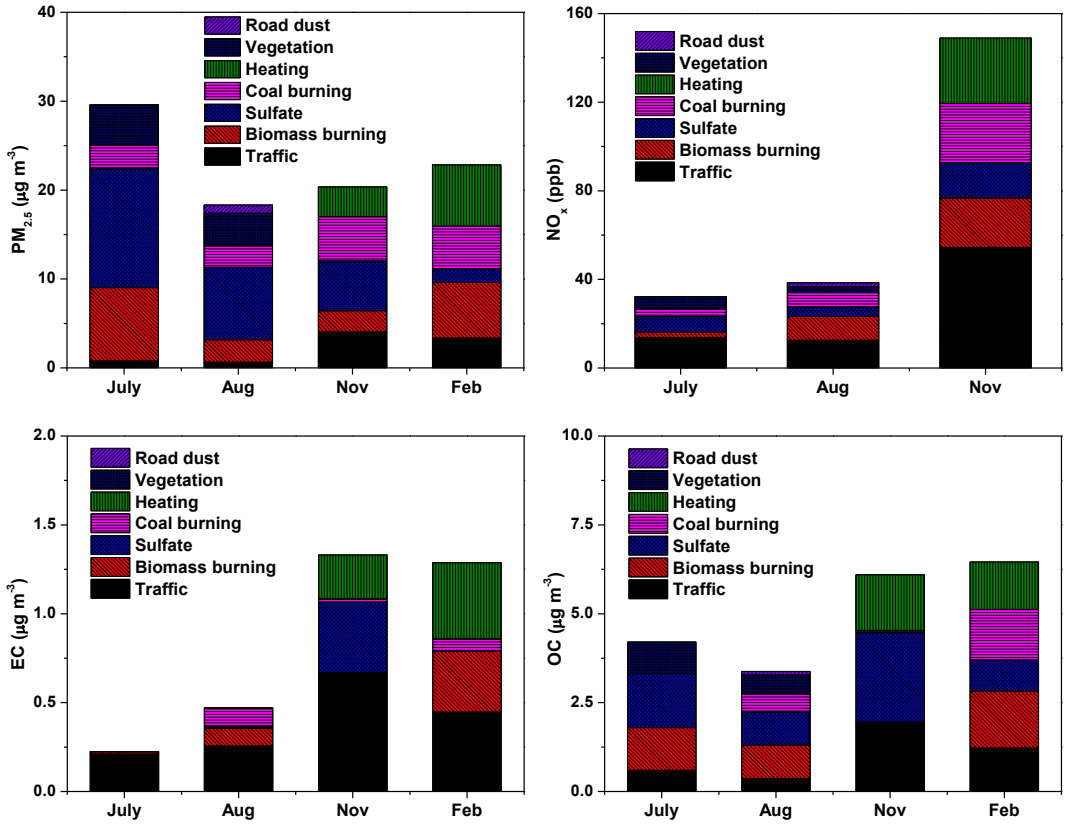

Figure 5.10 PMF apportioned mass contributions of $PM_{2.5}$, NO_x, EC, and OC.

According to the PMF apportionment, motor vehicle emissions contributed 33 ~ 42 % of NO_x in the summer and about 37 % of NO_x in the winter, which were in good agreement with the MLR prediction (i.e., 39 % of NO_x from motor vehicles). The PMF-predicted EC contributions from vehicular emissions were 54 ~ 93 % and 35 ~ 50 % in the summer and winter, respectively, which were consistent with its average contribution to EC (i.e., 55 %) determined by MLR.

SVOC tracers were apportioned, as shown in Figure 5.11. Both the traffic factor and the coal burning factor showed much larger contributions to HMWPAHs and HMWOPAHs in the winter than in the summer. Besides, heating and biomass

burning were two other major sources of HMWPAHs and HMWOPAHs in the winter. As shown in Figure 5.11, secondary aerosol contributed more significantly to low molecular weight species (i.e., LMWPAHs, LMWOPAHs, and LMW n-alkanes) in the winter than in the summer, despite its reduced contributions to $PM_{2.5}$ in the winter. In the summer, vegetation release is an important source of low molecular weight species and the HMW odd-carbon n-alkanes.

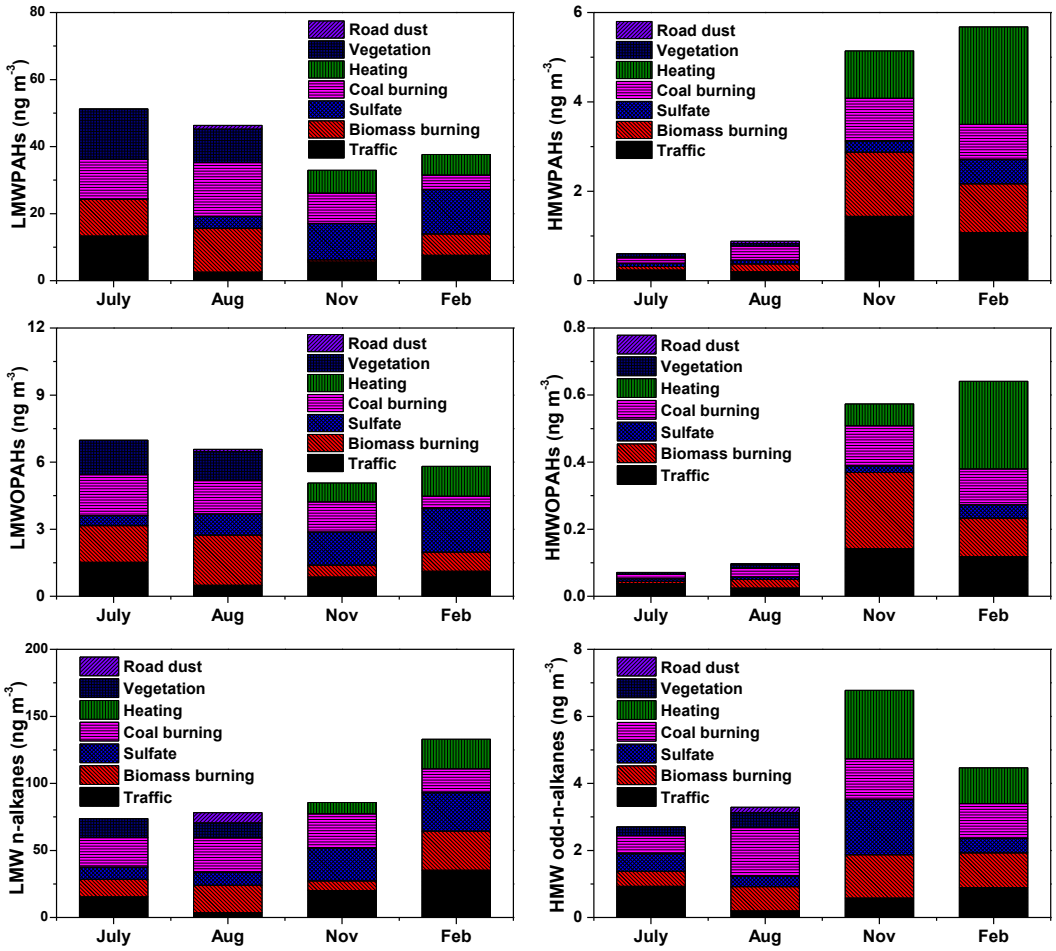

Figure 5.11 PMF apportioned contributions of LMWPAHs, HMWPAHs, LMWOPAHs, HMWOPAHs, LMW n-alkanes, and HMW odd-carbon n-alkanes.

The source apportionment of PAHs in this study was compared with two other urban studies that were carried out in Chicago (Simcik, Eisenreich and Lioy 1999) and Baltimore (Larsen and Baker 2003), respectively (Table 5.9). Simcik's study was

performed in another urban area with some different features of pollution composition from Baltimore. As shown in Table 5.9, coal burning was the primary source of pollution in Chicago, while motor vehicle exhaust was an additional source of major concern in Baltimore. Larsen's study was accomplished for the same area of our interest four years prior to the Baltimore supersite project. In specific, 24-hour measurements of PAHs were conducted in downtown Baltimore from March 1997 to December 1998, and three modeling methods (i.e., principal component analysis with multiple linear regression analysis, PCA/MLR; UNMIX; and PMF) were employed to apportion PAHs in their study (Larsen and Baker 2003). Larsen's PCA/MLR analysis assumed that CO and NO_x were exclusively from motor vehicle exhaust and thus contributions from motor vehicle emissions could have been overestimated, as implied from the smaller contributions of motor vehicles in his other two model solutions. In general, the PMF analyses in my study were in agreement with Larsen's PMF results. Some substantial differences in the "other" category were observed: in Larsen's PMF study, the factor labeled as "other" was unidentified due to the lack of any particular marker in that factor (Larsen and Baker 2003) and possibly represented a mixed factor of fitting residuals; in contrast, one to two "other" factors (i.e., sulfate, heating, vegetable release, and road dust) in different measuring periods were clearly identified by their SVOC tracers in this study. The emissions from those "other" sources in this study were presumably well apportioned using SVOC tracers and their total contribution was generally larger than that in Larsen's study. Moreover, a thorough investigation into seasonal variations of source emissions was made in our

study. As shown in Table 5.9, such a seasonal variation was that biomass burning in the winter was a less important factor than it was in the summer.

Table 5.9 Comparison of source contributions to ambient PAHs in several urban studies.

Source	Contribution in Baltimore, MD (Larsen and Baker 2003) (%)			Contribution in Chicago, IL (Simcik et al. 1999) (%)	Contribution in this PMF study (%)		
	PCA/MLR	UNMIX	PMF		Average[1]	Summer[2]	Winter[3]
Vehicle	26	23	16	9	17	15	19
Coal	28	29	36	48	26	28	23
Oil/heating	22	23	15	26	9	0	20
Wood burning	24	23	21	17	17	24	8
Other	n.a.	n.a.	14	n.a.	30	30	30

[1] Weighted daily average for all measuring periods.

[2] Weighted daily average for the July and August measuring periods.

[3] Weighted daily average for the November and February measuring periods.

5.4.3.8 Modeling Performance

In general, the reconstructed mass of most species in the winter measuring periods (i.e., November 2002 and February 2003) well agreed ($r^2 > 0.7$) with the measured values, compared to their poor correlations in the summer (Table 5.10). Secondary biogenic oxidation products were the only category of SVOCs with better predictions in the summer than in the winter. The PMF performance was evaluated using several statistical measures including mean fraction bias (MFB), normalized mean square error (NMSE), and the fraction of predicted concentrations lying within a factor of 2 of the measured ambient concentrations (Fa2), as shown in Table 5.11. According to Kumar et al. (Kumar et al. 1993), model performance is deemed acceptable if NMSE

≤ 0.5, -0.5 ≤ MFB ≤ 0.5, and Fa2 ≥ 0.8. The predictions for most traffic-related species (e.g., EC, OC, NO_x, LMW n-alkanes, PAHs, ACHs, and PCTTs) were generally acceptable during all measuring periods, except that the NMSE values of predicted EC, PCTTs, and HMWPAHs in July exceeded the criteria. The predictions for n-alkanoic acids, 2-alkanones, APCAs, resin acids, phenolic wood markers, and HMW odd-carbon n-alkanes, were generally good in all measuring periods as well. In contrast, the predictions for CO, nitrate, iso- and anti-iso n-alkanes, n-alkenoic acids, ADCAs, sugars, steroids, and thiazoles were generally poor, especially in the summer periods.

Table 5.10 Correlation coefficients (r^2) [1] between the PMF-modeling reconstructed mass and the observed mass in different measuring periods.

Species	Jul 2002	Aug 2002	Nov 2002	Feb 2003
EC	**0.683**[1]	0.524	**0.844**	**0.898**
OC	**0.607**	**0.880**	**0.862**	**0.889**
$PM_{2.5}$ mass	**0.637**	0.424	**0.830**	**0.837**
Sulfate	0.423	0.397	n.a.	n.a.
Nitrate	0.008	**0.659**	n.a.	n.a.
CO	0.512	0.390	0.315	n.a.
NO_x	**0.728**	**0.842**	**0.902**	n.a.
Iso- & antiso-alkanes	0.007	0.447	0.582	**0.819**
n-Alkanoic acids	**0.662**	0.567	**0.829**	**0.848**
n-Alkenoic acids	0.137	0.200	**0.727**	**0.989**
Aliphatic dicarboxylic acids	0.296	0.478	0.306	**0.959**
Aromatic polycarboxylic acids	**0.659**	**0.690**	0.286	**0.932**
2-Alkanones	0.494	**0.720**	**0.666**	**0.970**
Alkylcyclohexanes	**0.786**	**0.871**	**0.961**	**0.985**
Resin acids	0.391	0.219	**0.897**	**0.927**
Sugars (levoglucosan)	0.255	0.108	**0.628**	**0.965**
Steroids	0.066	0.239	0.592	**0.849**

Thiazoles (benzothiazole)	**0.631**	0.297	0.547	**0.694**
Pentacyclic triterpanes	0.236	0.507	**0.881**	**0.850**
N-Hetero-PAH	0.451	0.268	**0.735**	0.597
S-Hetero-PAH	**0.893**	**0.803**	**0.892**	**0.915**
Secondary biogenic oxidation products	**0.691**	**0.688**	0.081	0.113
Phenolic wood markers	0.508	0.462	**0.667**	**0.906**
LMWPAHs	**0.896**	**0.880**	**0.937**	**0.958**
HMWPAHs	0.385	**0.818**	**0.876**	**0.900**
LMWOPAHs	**0.900**	**0.855**	**0.941**	**0.955**
HMWOPAHs	**0.653**	**0.848**	**0.937**	**0.959**
LMW n-alkanes	**0.830**	**0.895**	**0.933**	**0.961**
HMW odd-n-alkanes	0.281	0.205	**0.638**	**0.820**
HMW even-n-alkanes	n.a.	1.000	0.029	**0.702**

[1] Boldfaced type indicates fair correlation ($r^2 > 0.6$) between reconstructed and observed concentrations.

Table 5.11 Performance statistics of the PMF modeling [1].

	July 2002			August 2002			November 2002			February 2003		
	NMSE [2]	MFB [3]	Fa2 [4]	NMSE	MFB	Fa2	NMSE	MFB	Fa2	NMSE	MFB	Fa2
EC	**0.75**	**0.18**	**0.69**	0.38	0.15	0.87	0.08	0.02	0.92	0.06	0.05	0.83
OC	0.05	0.02	0.98	0.02	0.04	1	0.04	0.07	0.96	0.05	0.06	1
$PM_{2.5}$ mass	0.07	0.02	1	0.24	0.09	0.87	0.04	0.06	0.97	0.12	-0.17	0.87
Sulfate	**0.54**	**0.2**	**0.77**	0.44	0.18	0.83	n.a.	n.a.	n.a.	n.a.	n.a.	n.a.
Nitrate	**1.66**	**0.37**	**0.71**	**0.72**	**0.34**	**0.72**	n.a.	n.a.	n.a.	n.a.	n.a.	n.a.
CO	0.14	0.1	0.87	**0.29**	**0.26**	**0.66**	**0.18**	**0.36**	**0.7**	n.a.	n.a.	n.a.
NO_x	0.13	0.14	0.96	0.04	0.05	1	0.04	0	0.99	n.a.	n.a.	n.a.
Iso-&Antiso-Alkanes	**3.37**	**0.34**	**0.5**	**0.5**	**0.37**	**0.68**	**0.23**	**0.79**	**0.7**	0.21	0.08	0.87
n-Alkanoic Acids	0.15	0.05	0.98	0.4	0.09	0.96	0.05	0.11	0.95	0.07	0.04	1
n-Alkenoic Acids	**1.09**	**0.37**	**0.73**	**1.4**	**0.52**	**0.58**	**0.33**	**0.34**	**0.76**	0.02	0.02	1
ADCAs	**3.8**	**0.28**	**0.79**	**0.39**	**0.18**	**0.66**	**0.4**	**0.32**	**0.74**	0.11	0.06	1
APCAs	0.11	0.09	0.96	0.07	0.07	0.98	0.23	0.14	0.92	0.07	0.06	1

2-Alkanones	0.05	0.07	1	0.05	0.06	1	0.1	0.08	0.96	0.01	0.01	1
ACHs	0.04	0.03	0.98	0.01	0.01	1	0.01	0.02	1	0.01	0.01	1
Resin Acids	0.45	0.18	0.88	0.55	0.24	0.85	0.05	0.03	0.96	0.11	0.1	0.91
Sugars	**3.69**	**0.43**	**0.6**	**3.04**	**19.51**	**0.47**	**3.23**	**0.69**	**0.38**	0.03	0.03	1
Steroids	**1.08**	**0.32**	**0.73**	**1.16**	**0.44**	**0.62**	0.14	0.31	0.85	0.13	0.12	0.96
Thiazoles	**0.79**	**0.17**	**0.92**	**0.62**	**0.22**	**0.83**	0.14	0.17	0.85	0.28	0.12	0.91
PCTTs	**1.22**	**0.06**	**0.98**	0.19	0.07	0.94	0.17	0.07	0.96	0.11	0.04	1
N-Hetero-PAH	0.44	0.23	0.87	0.16	0.16	0.87	0.05	0.07	1	0.14	0.15	0.96
S-Hetero-PAH	0.03	0.04	1	0.06	0.04	1	0.04	0.04	1	0.04	0.07	1
2nd Biogenic	0.15	0.13	0.96	0.27	0.13	0.91	**3.55**	**0.47**	**0.67**	**2.02**	**0.41**	**0.65**
Phenolic	0.53	0.19	0.88	0.34	0.01	0.6	0.34	0.42	0.79	0.08	0.08	0.96
LMWPAHs	0.02	0.03	1	0.02	0.02	1	0.01	0.02	1	0.01	0.03	1
HMWPAHs	**3.31**	**0.1**	**0.94**	0.04	0.04	1	0.04	0.07	0.97	0.06	0.1	0.96
LMWOPAHs	0.02	0.03	1	0.04	0.04	1	0.01	0.02	1	0.01	0.02	1
HMWOPAHs	0.45	0.08	0.96	0.04	0.03	1	0.02	0.05	0.96	0.03	0.06	1
LMW n-alkanes	0.02	0.02	1	0.02	0.02	1	0.02	0.03	1	0.03	0.03	1
HMW odd-n-alkanes	0.23	0.1	0.96	0.22	0.1	0.94	0.11	0.12	0.95	0.1	0.2	0.83
HMW even-n-alkanes	n.a.	n.a.	n.a.	**0**	**-0.05**	**0.7**	**2125**	**-0.06**	**0**	**0.28**	**-0.09**	**0.7**

[1] Boldfaced type indicates unacceptable performance.

[2] MFB: mean fractional bias ($= \left(\frac{2}{N}\right)\sum_{i=1}^{N}[(O_i - P_i)/(O_i + P_i)]$).

[3] NMSE: normalized mean square error ($= \left[\left(\frac{1}{N}\right)\sum_{i=1}^{N}(O_i - P_i)^2\right] / \left[\left(\frac{1}{N}\right)\sum_{i=1}^{N}(O_i \times P_i)\right]$).

[4] Fa2: fractions of the predictions within a factor of 2 of the observed values ($0.5 \leq C_{pred}/C_{obs} \leq 2.0$).

5.5 Concluding Remarks

Benefiting from highly time-resolved SVOC measurements, sources of organic aerosol in the Baltimore area were investigated. Motor vehicle exhaust was found to be the primary source of EC at the receptor site during the sampling periods. In particular, its influence on air quality appeared the most remarkable in the winter,

morning periods. The apportioned contributions of EC and NO_x from motor vehicles by PMF were largely in agreement with those determined by MLR. And the PMF apportionment of PAHs was in good agreement with a past 2-year study (1997 ~ 1998) carried out in downtown Baltimore.

The PMF-resolved profiles of motor vehicle emissions in different seasons showed larger discrepancies in SVOCs than the routine species (e.g., NO_x, and EC). As implied from these seasonal variations, the influences of ambient temperatures were in two aspects. On one hand, enhanced volatilization in the summer gave rise to elevated amounts of those volatile, light molecules from the source (e.g., fossil fuels), but had less effect on those species with high molecular weights. On the other hand, enhanced partitioning into the aerosol particle phase in the winter resulted in promoted abundances of all SVOCs species.

Substantial amounts of PAHs, n-alkanes, and other SVOCs were emitted from non-traffic sources including coal-burning, biomass-burning, and two seasonal sources (i.e., vegetation release and heating). Other essential findings include: 1) the sulfate factor (secondary aerosol) was the largest $PM_{2.5}$ source (i.e., 45 % of $PM_{2.5}$) in the summer, while heating (i.e., 16 ~ 34 % of $PM_{2.5}$), coal-combustion (i.e., 24 % of $PM_{2.5}$), biomass burning (i.e., 12 ~ 31 % of $PM_{2.5}$), and motor vehicle exhaust (i.e., 16 ~ 20 % of $PM_{2.5}$) were the four primary sources of $PM_{2.5}$ in the winter; 2) vegetation release contributed substantial amounts of SVOCs (i.e., 13 ~ 21 % of OC), especially low molecular weight PAHs and n-alkanes (i.e., 19 ~ 29 % of LMWPAHs; and 15 ~ 19 % of LMW n-alkanes), in the summer; 3) heating was an important source of EC (i.e., 19 ~ 32 % of EC) in the winter; and 4) the impact of wildfires on air quality in

Baltimore was significant during the summer of 2002, owing to Canadian Boreal wildfires.

Chapter 6: Conclusions

With the increasing interest on health outcomes of short-term exposures to large PM concentrations, the need to identify and apportion sources with ambient monitoring at a comparable time scale is increasing as well. However, a common problem for factor analyses (e.g., PMF, and UNMIX) is that factor cross contamination in the modeling results is inevitable as too few observations are involved within a typical several-hour campaign. Besides, while they make use of correlations between species, those receptor models do not make use of the actual atmospheric physics of transport and dispersion. In contrast, the pseudo-deterministic receptor model (PDRM) uses meteorological data to constrain dispersion factors (χ/Qs) required to obtain solutions for pollutant emission rates. In the Tampa study (Park, Pancras and Ondov 2005) in which several point sources had CEMs for SO_2, the χ/Qs were tuned so that its dependence on meteorological modeling was attenuated. Park's first prototype PDRM used oversimplified straight-line trajectories and loose constraints on the compositions of particles emitted from the sources. Moreover, background in the region of source influence (i.e., peaks in source-specific tracer species) was assumed to be equal to low concentration periods immediately before and after the peaks in the modeling period. Thus, collinear sources were not efficiently resolved. This situation was improved by Beachley (Beachley 2009, Beachley and Ondov 2012) in his reanalysis of the Tampa data by introducing two major updates: i.e., curvilinear plume trajectories at different aloft heights for different sources to correct the actual plume arrival times, and CMB terms to account

for the contributions from background area sources whose contributions could interfere with the targeted point sources.

Despite its unique advantage for short-term high time resolution studies, PDRM applications have not been extended to other supersites except Pittsburgh (Park et al. 2006) until recently due to two reasons: first, either ambient concentrations of SO_2 at the receptor site or CEM data of SO_2 at the sources of interest were not measured; and second, contributions from non-point sources (e.g., motor vehicle emissions, and secondary aerosol), for which the Gaussian dispersion model does not work well, were often significant.

In my study, the PDRM modeling strategy was further improved specifically for those above-mentioned issues. A key feature of the update is that preliminary PMF analysis was utilized to ascertain major sources and obtain rough estimates of source contributions to seed PDRM. Based on the PMF results, not only the feasibility to use alternative tracer species (i.e., NO_x, and metals) to condition χ/Qs was confirmed in both presence and absence of CEM data, but also a convenient removal of contributions from those non-targeted sources in the absence of source information was transplanted into PDRM. This approach surpasses Beachley's PDRM-II which, since it was based on CMB terms, requires a detailed knowledge of background sources and the composition of their emissions (i.e., their source profiles). Moreover, the plume trajectories in my two case-studies, i.e., Baltimore and St. Louis, were simulated based on 5- or 10-minute resolution wind data. This should better depict the variations of χ/Qs compared with Beachley's 30-minute trajectories, especially

considering the plume transport times from the sources of interest to the receptor site were typically less than one hour in both of my modeling studies.

In Chapter 2, the PMF modeling of the episodic emissions in three consecutive afternoons (7 hours each afternoon) in September 2001 at the Baltimore supersite resolved two power plants in close proximity (i.e., distance < 200 m), but their inexplicable chemical signatures (i.e., Se and Ni) indicated a mixing of these factors. In the absence of SO_2 data, NO_x was used as a tracer gas to condition the χ/Qs for industrial stack units in this power plant complex. With the PMF preliminary results, the PDRM was able to well resolve individual stack units with appropriate ratios of chemical signatures compared with the solutions from either PMF or PDRM alone. Moreover, the emission rates of NO_x predicted by the PMF-seeded PDRM well agreed with the National Emission Inventory (NEI) annual average, and those of metals were arguably more accurate than the rough estimates from the Toxics Release Inventory (TRI). Therefore I conclude that this combinative modeling approach can better resolve point sources (i.e., even individual stacks).

The study in Chapter 3 was focused on resolving emissions from different stack units in the Big River Zinc and Cerro Copper plants in St. Louis during two metal episodes in November 2001 and March 2002. The absence of a tracer gas (i.e., SO_2 or NO_x) with CEM data at those facilities excluded the possibility to apply the same approach as used in Chapter 2. Nevertheless, a group of highly definitive metal tracers (i.e., Cu, Zn, Cd, and Pb) were available in emissions from the four distinct types of metal processing units. Preliminary source contributions and pollutant abundance profiles were obtained with PMF analysis of a Cu, Zn, Cd, and Pb episode

in March 2002, which were used to seed PDRM and condition the χ/Qs of the individual units. Again, the PMF-seeded PDRM approach well resolved those different types of metal production units and the factor cross contamination of Cu in the PMF solution was eliminated.

It may be concluded as well that this combinative modeling approach will show promising success in the following two applications. First, this approach can be used for remote determination of emission rates of non-criteria species such as heavy metals from industrial sources, which are difficult to be accurately monitored. Second, this approach should prove to be successful when applied to extract source emission profiles which can be used for source apportionment using the CMB method.

In the future, high quality 3-D wind measurements should be utilized to better constrain plume transport and dispersion by improving the quality of plume trajectory simulations and predictions of χ/Qs. Besides, efforts towards incorporating the beneficial aspect of PDRM (i.e., constraining the solution of source emissions with Gaussian dispersion factors that are based on highly time-resolved meteorological observations) into other receptor models such as CMB should also be worthwhile.

Compared with industrial point sources, accurate determination of contributions from motor vehicle emissions is more challenging due to the lack of appropriate abundance profiles. In Chapter 4, a detailed profile of on-road motor vehicle emissions was extracted through the analysis of a winter morning traffic episode at the Ponca street supersite with four independent methods (i.e., direct peak observation, linear regression, PMF, and UNMIX). The resultant profiles are generally consistent with each other. Arguably, the profile derived from the linear regression of ambient

concentrations against I-895 traffic counts is the most comprehensive to date, as it included 117 SVOCs in 19 categories in addition to routine aerosol components (EC, OC, sulfate, and nitrate), criteria gases in motor vehicle emissions (NO_x and CO), and SEAS metals (Al, As, Cd, Cr, Cu, Fe, Mn, Ni, Pb, Se, and Zn). As this profile is the average for the high-volume highway traffic over a 7-hour windless period when there was little interference from non-traffic sources, it should well represent Mid-Atlantic traffic (and may represent much of the traffic in Eastern US as well). And there is no doubt that it can be widely used for studies in which vehicular emissions are a major concern. Besides, as a byproduct of the windless data analysis, the ratio of the average motor emission factor (E) and a road coefficient (β; that depends on the traffic-induced wind speed at the receptor site) was also derived. The same approach can be applied to other windless periods at the same site, to extract the corresponding E/β values. As β is approximately a constant at the given site, I conclude that the comparison of E/β values will allow tracking the evolution of motor vehicle emission factors and thus permit evaluations of the achievements of emission control policy.

In Chapter 5, carbonaceous particulate matter (e.g., EC, OC, PAHs, etc.) was apportioned using highly time-resolved SVOC data in Baltimore. Due to the close proximity between the Ponca street site and the I-895 road, motor vehicle exhaust was the major source of EC especially during the morning traffic rush-hours. In contrast, substantial amounts of SVOCs (e.g., PAHs, n-alkanes) were from non-traffic sources such as secondary aerosol, coal burning, and biomass burning. Seasonal and diurnal variations of SVOC emissions from different sources indicated that temperature affects both volatility of source emissions (e.g., enhanced fuel evaporation and

vegetation release at high temperature) and gas/particle partitioning of the emitted species (i.e., enhanced adsorption in the aerosol phase at low temperature). Moreover, seasonal sources (e.g., vegetation release in the summer, and heating in the winter) have shown characteristic contributions to certain categories of organic species rather than the total $PM_{2.5}$ mass. Accordingly, this study is an important advance in the attribution of SVOCs in Baltimore.

Appendices

Appendix A

This section reproduced from Park (Park et al. 2005b) on the calculation of effective plume height, *H*.

The effective plume height is given as the sum of the stack physical height (h_s) and the plume rise (ΔH)

$$H = h_s + \Delta H \tag{1}$$

The plume rise (ΔH) is computed from the Briggs algorithm (Briggs 1969, Briggs 1971, Briggs 1972, Briggs 1975) which is adapted as part of the ISCST3 model (U.S.EPA 1995) and described below.

In general, there are two types of plume rise: buoyancy rise and momentum rise (Seinfeld and Pandis 2006). The buoyancy flux parameter, F_b (m^4 s^{-3}), is expressed by:

$$F_b = g v_s d_s^2 \left(\frac{\Delta T}{4T_s}\right) \tag{2}$$

where g is gravitational acceleration (m s^{-2}), v_s is the stack gas exit velocity (m s^{-1}), d_s is the stack inner diameter (m), T_s is the stack gas exit temperature (K), and ΔT is the difference (K) between the stack gas exit temperature and ambient temperature (T_a).

The momentum flux parameter, F_m (m^4 s^{-3}), is given by:

$$F_b = {v_s}^2 d_s^2 \left(\frac{T_a}{4T_s}\right) \tag{3}$$

In order to determine whether the plume rise is dominated by buoyancy or momentum, a critical temperature, T_c, is defined: (1) Under stable atmospheric conditions,

$$T_c = 0.019582 \times T_s \times v_s \times \sqrt{s} \tag{4}$$

where s (= $g(\partial\theta/\partial z)T_a$) is a stability parameter indicating the potential temperature gradient with height.

(2) Under neutral or unstable atmospheric conditions,

$$T_c = \begin{cases} 0.0297 \times T_s \times \dfrac{v_s^{1/3}}{d_s^{2/3}}, & F_b < 55 \\ 0.00575 \times T_s \times \dfrac{v_s^{2/3}}{d_s^{1/3}}, & F_b \geq 55 \end{cases} \tag{5}$$

If $\Delta T \geq T_c$, the plume rise is assumed as buoyancy dominated. Otherwise, it is presumably momentum dominated.

The Pasquill atmospheric stability classes are determined using surface wind speed and solar radiation (or cloud cover), as shown in Table A1 (Seinfeld and Pandis 2006).

Table A1 Atmospheric stability classification.*

Surface wind speed (m s^{-1})	Day-time solar insolation			Night-time cloud cover	
	Strong (> 700 W m^{-2})	Moderate (350 ~ 700 W m^{-2})	Slight (< 350 W m^{-2})	Thin overcast or > ½ low cloud	<= ½ cloudiness
< 2	A	A – B	B	E	F
2 – 3	A – B	B	C	E	F
3 – 5	B	B – C	C	D	E
5 – 6	C	C – D	D	D	D
> 6	C	D	D	D	D

* A: extremely unstable; B: moderately unstable; C: slightly unstable; D: neutral; E: slightly stable; and F: moderate stable.

If the plume rise is buoyancy dominated, the plume rise under stable atmospheric conditions is given by:

$$\Delta H = 2.60 \times \left(\frac{F_b}{u_s s}\right)^{1/3} \quad (6)$$

where u_s is the mean wind speed (m s^{-1}) at stack height, and.

Under neutral or unstable atmospheric conditions, the calculation of buoyancy plume rise is upon buoyancy flux: (1) For $F_b < 55$,

$$\Delta H = 21.425 \times \left(\frac{F_b}{u_s}\right)^{3/4} \quad (7)$$

(2) For $F_b \geq 55$,

$$\Delta H = 38.71 \times \frac{F_b^{3/5}}{u_s} \quad (8)$$

If the plume rise is momentum dominated, the plume rise under stable atmospheric conditions is given by:

$$\Delta H = 1.5 \times \left(\frac{F_m}{u_s \times \sqrt{s}}\right)^{1/3} \quad (9)$$

Under neutral or unstable atmospheric conditions, the momentum plume rise is calculated as:

$$\Delta H = 3.0 \times d_s \times \frac{v_s}{u_s} \quad (10)$$

Appendix B

B1 Calculation of mixed layer depth (MLD)

The algorithms were adapted from the AERMET pre-processor of the EPA AERMOD model (U.S.EPA 2004a). The AERMET inputs include wind speed, wind direction, ambient temperature, surface albedo, solar radiation and cloud cover, surface roughness, and Bowen ratio (Cimorelli et al. 2005). Surface roughness and Bowen ratio are surface characteristics that are determined by land use and those published values for the area of interest were used in our study (Oke 1982, Ching 1985, Hjelmfelt 1982). Surface albedo, solar radiation and cloud cover were measured at the nearest airport and retrieved from the National Solar Radiation Database (NSRDB).

Sensible heat flux (H_f) in the convective boundary layer (CBL) was derived using a simple energy balance approach (Oke 1987):

$$H_f = \frac{0.9R_n}{\left(1+{}^{1}/_{B_o}\right)} \tag{11}$$

where B_o is the Bowen ratio (dimensionless) and R_n is the net radiation (W m^{-2}). R_n was estimated from the insolation and the thermal radiation balance at ground following the method of Holtslag and Van ulden (Holtslag and Van Ulden 1983):

$$R_n = \frac{(1-r)R+c_1T_{ref}^6-\sigma_{SB}T_{ref}^4+c_2n}{1+c_3} \tag{12}$$

where $c_1 = 5.31\times10^{-13}$ W m^{-2} K^{-6}, $c_2 = 60$ W m^{-2}, $c_3 = 0.12$, σ_{SB} is Stefan Boltzman Constant (5.67×10^{-8} W m^{-2} K^{-4}), T_{ref} is ambient air temperature at reference height for temperature (K), r is Albedo, and R is solar radiation (W m^{-2}).

AERMET computes the surface friction velocity, u_*, and the Monin-Obukhov length, L, in the CBL using an iterative method, since the friction velocity and the Monin Obukhov length are inter-correlated as shown in Equations 13 to 18 (Panofsky and Dutton 1984, Venkatram and Wyngaard 1988). Our MATLAB script initialized u^* by using the surface wind speed and assuming neutral conditions, to calculate L, and iteratively solved for u_* and L until convergence (i.e., less than a 1 % relative change between successive iterations) was reached.

$$L = -\frac{\rho c_p T_{ref} u_*^3}{kgH_f} \tag{13}$$

where ρ is the density of air (kg m^{-3}), k is von Karman's constant (0.4), c_p is specific heat of air at constant pressure (kJ kg^{-1} K^{-1}), and g is the acceleration due to gravity (9.8 m s^{-2}).

$$u_* = \frac{k u_{ref}}{ln\left(z_{ref}/z_o\right) - \varphi_m\left\{z_{ref}/L\right\} + \varphi_m\left\{z_o/L\right\}} \tag{14}$$

where:

$$\varphi_m\left\{z_{ref}/L\right\} = 2ln\left(\frac{1+\mu}{2}\right) + ln\left(\frac{1+\mu^2}{2}\right) - 2tan^{-1}\mu + \pi/2 \tag{15}$$

$$\mu = \left(1 - 16\frac{z_{ref}}{L}\right)^{1/4} \tag{16}$$

$$\varphi_m\left\{z_o/L\right\} = 2ln\left(\frac{1+\mu_o}{2}\right) + ln\left(\frac{1+\mu_o{}^2}{2}\right) - 2tan^{-1}\mu_o + \pi/2 \tag{17}$$

$$\mu_o = \left(1 - 16\frac{z_o}{L}\right)^{1/4} \tag{18}$$

The reference height, z_{ref}, to determine u_* and L is optimized to be representative of the surface layer in the AERMET processor. For those areas with large surface

roughness (i.e., z_0 > 1 m), AERMET constrains the range of vertical height between $7z_o$ and 100 m. In the supersite study, the wind and temperature measurements were carried out at a height of 10 m, which was used as the reference height for the PDRM modeling.

The convective velocity (ω_*) was given by its definition (Venkatram and Wyngaard 1988) as follows:

$$\omega_* = \left(\frac{gH_f L}{\rho c_p T_{ref}}\right)^{1/3} \tag{19}$$

An algorithm based on Benkley and Schulman's method (Benkley and Schulman 1979), as recommended by EPA, was used to calculate the hourly values of the mixed layer depth (MLD). As Benkley's method was originally designed for daytime MLD estimates, we applied another simple diurnal-mode calculation of MLD proposed by Stull (Stull 1989) meanwhile and used whichever MLD value was greater from the two methods (denoted as *MixHm* for Benkley's method and *MixHc* for Stull's method).

Benkley's algorithm of MLD calculation is as follows:

$$MixHm = 0.185 \times \frac{u'}{Cor} \tag{20}$$

where convective velocity scale, *u'*, is estimated as:

$$u' = 0.35 \times \frac{u}{\ln(ht/z_o)} \tag{21}$$

and the Coriolis factor, *Cor*, was obtained according to its definition:

$$Cor = 2\Omega \times sin(f) \tag{22}$$

where u is the surface wind speed (m s^{-1}), ht is the Anemometer height, Ω is the angular velocity of the earth (0.0000727 rad s^{-1}) and f is the latitude (rad) of the site.

Stull's method requires inputs of u_*, ω_*, and L as obtained earlier. Under unstable atmospheric conditions, the MLD is described as:

$$MixHc = -k \times L \times \left(\frac{\omega_*}{u_*}\right)^3 \quad (23)$$

Under neutral and stable atmospheric conditions, an correction by Arya's (Arya 1981) is used as follows.

$$MixHc = 113 + 0.34 \times \left(L \times \frac{u_*}{Cor}\right)^{1/2} \quad (24)$$

EPA reported the effective stack heights of the stack units in the BRZ and Cerro Copper plants based on their daytime measurements. Considering that variations could be resulted from different meteorological conditions, our calculations of effective plume heights with the Brigg's plume rise model were compared with the EPA's reference values. In the PDRM modeling, we used our calculated effective stack height if its discrepancy from the EPA reported value was insignificant (i.e., < 10%). Otherwise, the EPA reported value was used and a flag message of warning was stored.

B2 Calculation of Gaussian dispersion parameters (σ_y and σ_z) based on the ISCST3 model

The EPA Industrial Source Complex Short Term plume model 3, ISCST3 (U.S.EPA 1995), computes lateral and vertical dispersion parameters, σ_y and σ_z, based upon the following equations.

$$\sigma_y = 465.11628 \times x \times \tan(0.017453293 \times [c - d \times \ln(x)]) \quad (25)$$

$$\sigma_z = ax^b \quad (26)$$

The coefficients in above equations (i.e., a, b, c, and d) are dependent on the atmospheric stability (i.e, Pasquill stability classes A to F) and plume downwind distance (x), as shown in Table C2 and C3.

Table B1 Parameters used to calculate Pasquill-Gifford σ_y.

Pasquill stability class	*c*	*d*
A	24.1670	2.5334
B	18.3330	1.8096
C	12.5000	1.0857
D	8.3330	0.72382
E	6.2500	0.54287
F	4.1667	0.36191

Table B2 Parameters used to calculate Pasquill-Gifford σ_z.

Pasquill stability class	x (km)	a	b	Pasquill stability class	x (km)	a	b
A	< 0.10	122.8	0.9447	E	< 0.10	24.26	0.8366
	0.10 - 0.15	158.08	1.0542		0.10 - 0.30	23.331	0.81956
	0.16 - 0.20	170.22	1.0932		0.31 - 1.00	21.628	0.7566
	0.21 - 0.25	179.52	1.1262		1.01 - 2.00	21.628	0.63077
	0.26 - 0.30	217.41	1.2644		2.01 - 4.00	22.534	0.57154
	0.31 - 0.40	258.89	1.4094		4.01 - 10.00	24.703	0.50527
	0.41 - 0.50	346.75	1.7283		10.01 - 20.00	26.97	0.46713
	0.51 - 3.11	453.85	2.1166		20.01 - 40.00	35.42	0.37615
	> 3.11	*	*		> 40	47.618	0.29592
B	< 0.2	90.673	0.93198	F	< 0.2	15.209	0.81558
	0.21 - 0.40	98.483	0.98332		0.21 - 0.70	14.457	0.78407
	> 0.4	109.3	1.0971		0.71 - 1.00	13.953	0.68465
C	All	61.141	0.91465		1.01 - 2.00	13.953	0.63227
D	< 0.3	34.459	0.86974		2.01 - 3.00	14.823	0.54503
	0.31 - 1.00	32.093	0.81066		3.01 - 7.00	16.187	0.4649
	1.01 - 3.00	32.093	0.64403		7.01 - 15.00	17.836	0.41507
	3.01 - 10.00	33.504	0.60486		15.01 - 30.00	22.651	0.32681
	10.01 - 30.00	36.65	0.56589		30.01 - 60.00	27.074	0.27436
	> 30	44.053	0.51179		> 60	34.219	0.21716

* σ_z is set to 5000 m.

B3 Error analysis of the trajectory-driven GPM dispersion parameters

In the study, uncertainty estimates were based on the measurement uncertainties of wind directions using a MATLAB script. For each successive trajectory, the downwind distance (x), mean wind direction (θ_w), the propagated uncertainties associated with the mean wind direction (σ_w), and the average atmospheric stability were obtained from the plume trajectory simulation and meteorological calculations.

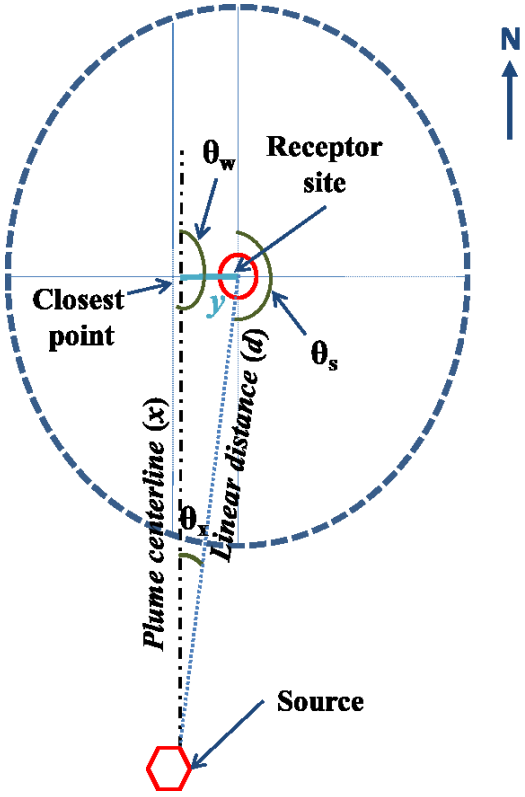

Figure B1 Simplified trajectory and the representation of the closest point approach.

The intercrossing angle (θ_x) of the station angle (θ_s) and the mean wind direction is defined as:

$$\theta_x = abs(\theta_w - \theta_s) \tag{27}$$

When $\theta_x < 15°$, by small-angle approximation, the off-centerline distance (y) is equal to:

$$y = d \times tan(\theta_x) \tag{28}$$

where d is the linear distance (km) between the source and the receptor site.

As θ_x is perturbated by the wind direction uncertainty, the uncertainty of the off-centerline distance (dy) is estimated as:

$$dy = d \times max\left(abs\left(sin(\theta_x) - sin(\theta_x - \sigma_w)\right), abs\left(sin(\theta_x) - sin(\theta_x + \sigma_w)\right)\right) \tag{29}$$

Similar, the uncertainty associated with the plume travel distance (dx) is approximately equal to:

$$dx = d \times max\left(abs\left(cos(\theta_x) - cos(\theta_x - \sigma_w)\right), abs\left(cos(\theta_x) - cos(\theta_x + \sigma_w)\right)\right) \tag{30}$$

and the relative uncertainty of the plume travel distance ($dx\_\%$) is given as:

$$dx\_\% = \frac{max\left(abs\left(cos(\theta_x) - cos(\theta_x - \sigma_w)\right), abs\left(cos(\theta_x) - cos(\theta_x + \sigma_w)\right)\right)}{cos(\theta_x)} \tag{31}$$

Considering the $d \times ln(x)$ term is negligible with respect to the c term in Equation 25 when $x < 20$ km, the relative error of σ_y, $d(\sigma_y)\_\%$, is given by:

$$d(\sigma_y)\_\% = dx\_\% \tag{32}$$

According to Equation 25 the relative error of σ_z, $d(\sigma_z)\_\%$, is given by:

$$d(\sigma_z)\_\% = (dx\_\%)^b \tag{33}$$

where the exponent b can be determined by the lookup of Table C3 based on the known atmospheric stability and x.

According to Equation 2.6, the relative uncertainty of χ/Q is determined as the standard propagation of relative errors of its five components: σ_y, σ_z, mean transport velocity (u), the y exponential and the z exponential.

$$d(\chi/Q)\_\% = \sqrt{\left(d(\sigma_y)\_\%\right)^2 + (d(\sigma_z)\_\%)^2 + (du\_\%)^2 + (d(y\_exp)\_\%)^2 + (d(z\_exp)\_\%)^2} \quad (34)$$

The relative error of the mean transport velocity ($du\_\%$) is calculated as the quotient of the standard deviation of aloft wind speeds (u_i) during all trajectory segments and mean aloft wind speed ($\bar{u}$).

$$du\_\% = \frac{\sqrt{\sum(u_i - \bar{u})^2}}{\bar{u}} \quad (35)$$

Without perturbation by the wind direction error, the *y* exponential term (*y_exp*) in Equation 2.6 is given by:

$$y\_exp = exp\left(-\frac{1}{2} \times \left(\frac{d \times \tan(\theta_x)}{\sigma_y}\right)^2\right) \quad (36)$$

where the σ_y value is obtained as:

$$\sigma_y = 465.11628 \times x \times \tan(0.017453293 \times [c - d \times \ln(x)]) \quad (37)$$

With perturbation by the wind direction error, the lower and upper bounds of the *y* exponential term are given by:

$$LB(y\_exp) = exp\left(-\frac{1}{2} \times \left(\frac{d \times \tan(\theta_x + \sigma_w)}{\sigma_y}\right)^2\right) \quad (38)$$

$$UB(y\_exp) = exp\left(-\frac{1}{2} \times \left(\frac{d \times \tan(\theta_x - \sigma_w)}{\sigma_y}\right)^2\right) \quad (39)$$

Note that in the MATLAB script, UB(*y_exp*) is set to 1 if $\theta_w < \sigma_w$.

The standard deviation of the *y* exponential term and its lower and upper bounds is calculated and the relative error of the *y* exponential term is estimated as the quotient of this standard deviation and the calculated *y* exponential term.

As σ_z is independent of horizontal wind direction, the relative uncertainty of the z exponential term is based on the propagated error as:

$$d(z\_exp)\_\% = \sqrt{2} \times d(\sigma_z)\_\% \quad (40)$$

For the Baltimore Clifton Park supersite, the propagated uncertainties of χ/Qs for individual stacks in the two BGE power plants were listed in Table 2.11 as well as the uncertainties for individual components.

For the St. Louis supersite, the propagated uncertainties of χ/Qs for the representative units in the BRZ and Cerro Copper plants during the two episodes were listed in Table 3.3 as well as the uncertainties for individual components.

Appendix C

C1 Stack parameters of the BRZ and Cerro Copper units

Note that the stack parameters based on the National Emission Trends (NET) database differ slightly from those published in the NEI 2002, as the former were historical data acquired in an earlier date (1996) prior to the St. Louis study in 2002. However, these NET data are listed herein for reference purpose, as they provided useful information to assist the classification of stacks (i.e., primary metal, secondary metal). In our study, the updated stack information retrieved from the NEI 2002 (Table 3.1) was actually applied to the PDRM modeling if any inconsistence between the two databases was found.

Table C1 Stack parameters of the BRZ and Cerro Copper units based on the National Emission Trends Data (1996).

Stack	Eff Hgt (ft)	Height (ft)	Dia (ft)	Temp (F)	Flow (cfs)	Velocity (ft s^{-1})	Latitude	Longitude	SCC
BRZ zinc units:									
1	245	85	3	300	956.4	135.3	38.6017	90.1706	Pri Metal
2	52	22	2	600	61.6	19.6	38.6017	90.1706	Sec Metal
3	116	46	4	240	399.6	31.8	38.6017	90.1706	Pri Metal
4	136	88	6.9	104	957.3	25.6	38.6017	90.1706	Pri Metal
5*	180	88	6.9	160	957.3	25.6	38.6017	90.1706	Pri Metal
6	111	75	1.5	230	171.6	97.1	38.6017	90.1706	Pri Metal
7	111	75	1.5	230	171.6	97.1	38.6017	90.1706	Pri Metal
8	149	97	4.11	135	594.9	44.8	38.6017	90.1706	Pri Metal
9	149	97	4.11	135	594.9	44.8	38.6017	90.1706	Pri Metal
10	78	22	1.5	1150	105.7	59.8	38.6017	90.1706	Sec Metal
11	111	75	1.5	230	171.6	97.1	38.6017	90.1706	Pri Metal
12*	43	25	1.7	140	132.6	58.4	38.6017	90.1706	Sec Metal
13	62	25	2	240	166.5	53.0	38.6017	90.1706	Sec Metal
14	46	30	1.7	135	126.4	55.7	38.6017	90.1706	Sec Metal
15	74	55	2	150	133.2	42.4	38.6017	90.1706	Sec

									Metal
16	38	30	1.5	180	33.2	18.8	38.6017	90.1706	Pri Metal
17	226	150	5	180	628.3	32.0	38.6017	90.1706	Chem Mfg.; H_2SO_4
Cerro Copper units:									
1	88	45	2.8	180	295.6	48.0	38.5931	90.1744	Pri Metal
2	62	40	3.5	110	286.7	29.8	38.5931	90.1744	Pri Metal
3*	148	95	5.5	500	147.3	6.2	38.5931	90.1744	Pri Metal
4	436	261	9.25	184	1850.0	27.5	38.5931	90.1744	Pri Metal
5	36	36	3.2	70	293.6	36.5	38.5931	90.1744	Degreasing
6	75	60	1.5	430	31.5	17.8	38.5931	90.1744	NG Boiler
7	49	45	0.8	250	7.9	15.7	38.5931	90.1744	NG Boiler
8	85	55	6	112	418.5	14.8	38.5931	90.1744	Pri Metal
9	115	55	6	173	480.7	17.0	38.5931	90.1744	Pri Metal
10	112	55	6	163	494.8	17.5	38.5931	90.1744	Pri Metal
11	38	33	1.9	118	32.6	11.5	38.5931	90.1744	Pri Metal
12	71	36	3.3	174	235.2	27.5	38.5931	90.1744	Pri Metal
13	165	68	4.27	396	390.5	27.3	38.5931	90.1744	NG Boiler
14	238	95	5.18	413	635.0	30.1	38.5931	90.1744	Oil Boiler
15	108	50	2	1000	116.9	37.2	38.5931	90.1744	Pri Metal
16	146	52	3.54	367	398.7	40.5	38.5931	90.1744	Sec Metal
17	59	25	2	300	121.9	38.8	38.5931	90.1744	NG Boiler
18	6	6	0.3	70	1.7	23.3	38.5931	90.1744	Sec Metal

* Representative unit in each category.

C2 Carryover correction of SEAS metal concentrations

Within a 30 minute SEAS sampling period, typically about 10-mL slurry was collected. Filtered compressed air was used to purge the sample collector at the end of each sampling. However, a small volume of sample residual, known as a dead volume (~ 0.2 mL), was inevitably left in the sampler in each run (Pancras et al. 2005), which led to a carryover to the following sample. The correction of carryover effect is especially essential at a large excursion of metals which could cause the broadening of the time series concentration peaks and thus blur the temporal information that peaks convey. In our study, the correction of SEAS metal concentrations was carried out with a MATLAB script prior to the receptor modeling, using the following mass-balance algorithm:

$$c_{i,j}{}' = \frac{c_{i,j} \times V_{s,i} + c_{i,j} \times V_r - c_{i-1,j} \times V_r}{V_{s,i}} \quad (41)$$

where $c_{i,j}{}'$ is the corrected concentration (ng m^{-3}) of the j^{th} metal for the i^{th} observation, $c_{i,j}$ is the uncorrected concentration of the j^{th} metal for the i^{th} observation (ng m^{-3}), $c_{i-1,j}$ is the uncorrected concentration (ng m^{-3}) of the j^{th} metal for the $(i\text{-}1)^{th}$ observation, $V_{s,i}$ is the SEAS sample volume (mL) collected during the i^{th} observation, and V_r is the dead volume (mL) of the sample collector.

C3 Hierarchical steps of PMF-seeded PDRM modeling

Figure C1 Flow chart showing hierarchical steps of PMF-seeded PDRM modeling.

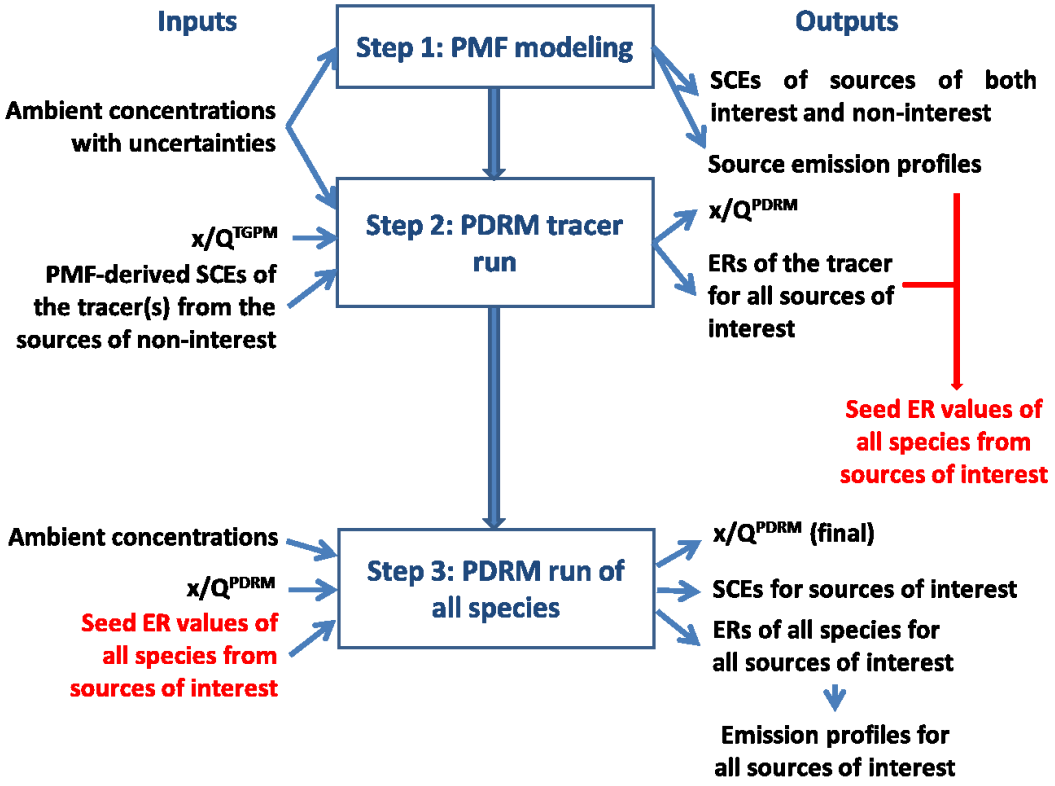

C4 PMF analyses of episode A at the St. Louis supersite

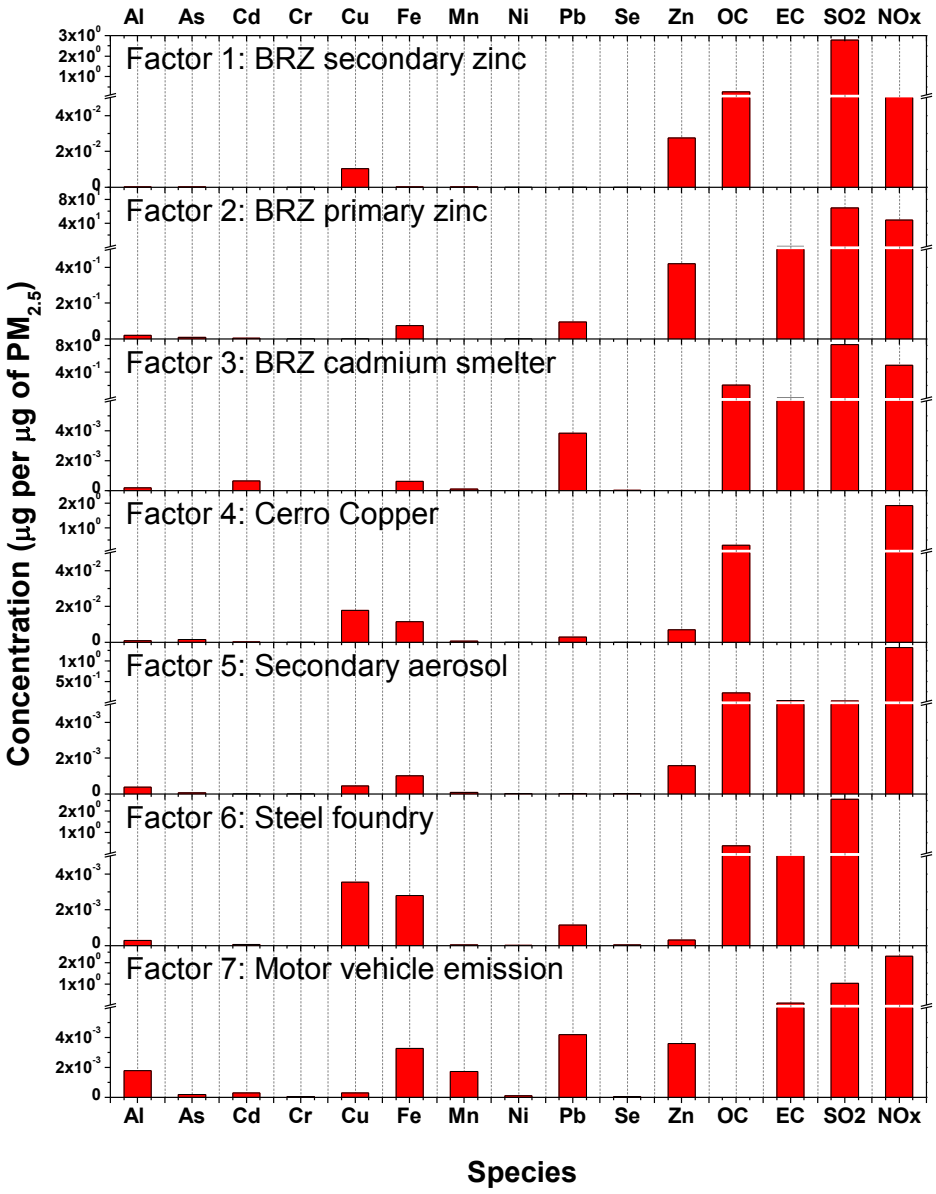

Figure C2 PMF-resolved source profiles for the zinc episode (episode A).

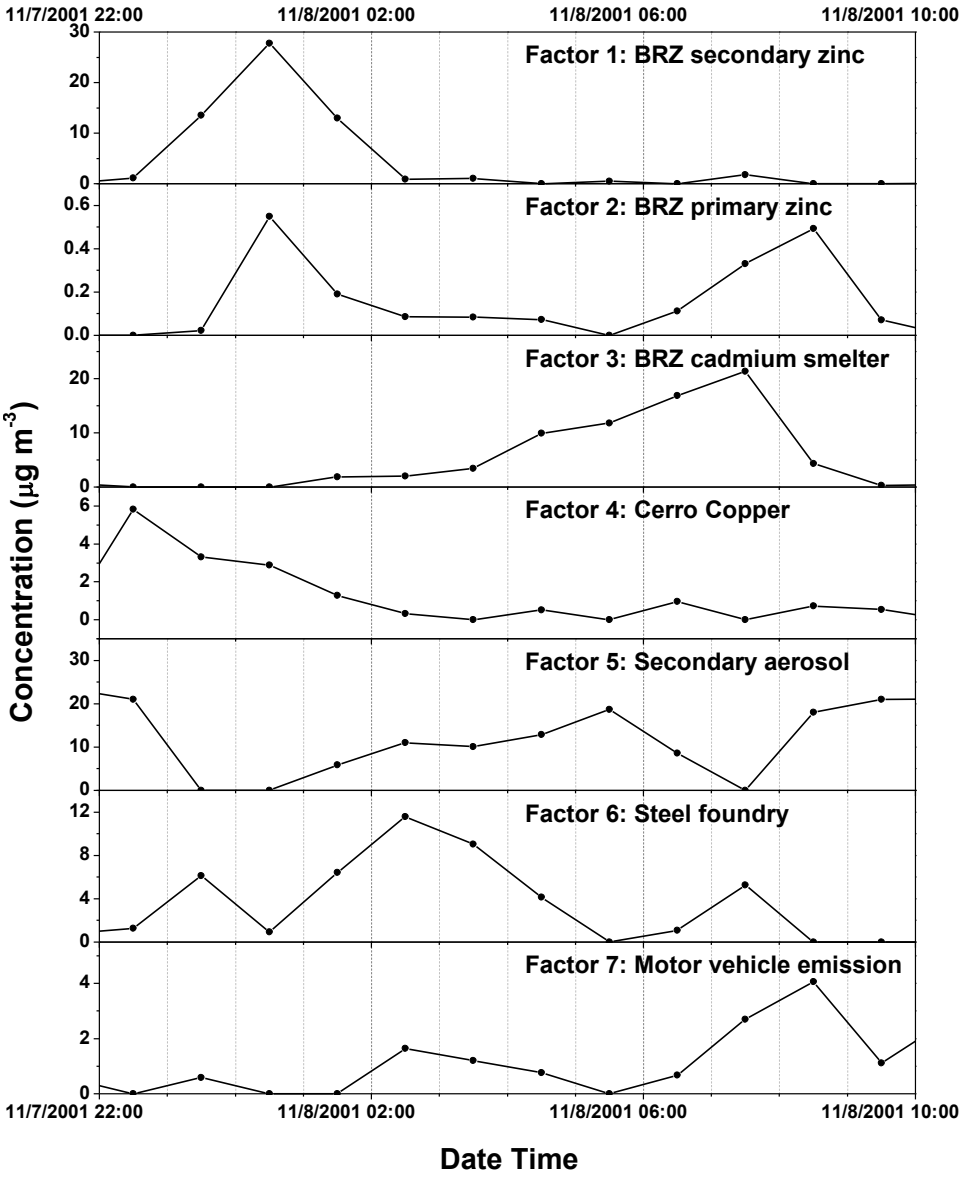

Figure C3 Time series source contributions in episode A predicted by PMF.

C5 PDRM-predicted emission rates of the marker species from the BRZ and Cerro Copper units during the two episodes

Table C2 Comparison of PDRM-predicted emission rates of selected metals from the BRZ and Cerro Copper plants with their annual average emission rates according to TRI 2002.

	Episode A				Episode B				TRI 2002			
	Cu	Zn	Cd	Pb	Cu	Zn	Cd	Pb	Cu	Zn	Cd	Pb
BRZ Unit 1	8.6	67	<0.001	0.07	<0.001	1.2	<0.001	<0.001	n.a.	n.a.	n.a.	n.a.
BRZ Unit 2	<0.001	107	<0.001	24	1.8	3.7	0.17	<0.001	n.a.	n.a.	n.a.	n.a.
BRZ Unit 3	<0.001	<0.001	0.13	0.78	0.46	<0.001	0.05	0.74	n.a.	n.a.	n.a.	n.a.
BRZ composite	**8.6**	**174**	**0.13**	**25**	2.3	4.9	0.22	0.74	2.6	214	4.7	15
Cerro Copper	13	5.2	<0.001	<0.001	**85**	**0.7**	**0.03**	**3.9**	135	1.9	n.a.	1.7

Appendix D

D1 Deconvolution of 3-hourly SVOC measurements on a basis of hourly traffic

Previous investigations (Section 4.4.1) suggested that ambient pollutant concentrations were generally linearly dependent on the traffic density during the windless morning (0100 ~ 0800 LT) of November 20th, 2002, which allowed the extraction of the SVOC abundance profile of motor vehicle emissions with the windless model analysis. As multiple (> 5) hourly observations of SVOCs were needed for the analysis, the 3-hour SVOC datasets were reallocated into 1-hour subsets on a traffic flux basis with a MATLAB script, as follows.

```
%% Interpolate hourly SVOC data based on hourly traffic flux
% ------------------------------------------------------------------
-
% load data:
SVOCc=csvread('EpF_SVOCc.csv',2,1); % SVOC concentrations, 4-by-117
matrix, unit in ng m^-3
SVOCu=csvread('EpF_SVOCu.csv',2,1); % uncertainties of SVOC
concentrations, 4-by-117 matrix, unit in ng m^-3
traf=csvread('EpF_SVOCt.csv',1,1); % 9 hourly traffic data of I-895
tunnel
tf=sum(traf,2); % hourly traffic flux from 00:00 to 09:00 (9 hours),
1-by-9 vector, unit in vehicles/hour
% ------------------------------------------------------------------
-
% background correction of SVOC data
Sc=SVOCc(2:4,:)-repmat(SVOCc(1,:),3,1); %
Su=SVOCu(2:4,:); %
% ------------------------------------------------------------------
-
```

```
% interpolate:
nsv=length(Sc(1,:)); % # of SVOC species (include categorized data)
sc=zeros(9,nsv); % pre-allocate the matrix of hourly SVOC
concentrations, 9-by-117 matrix
su=zeros(9,nsv); % pre-allocate the matrix of hourly SVOC
uncertainties, 9-by-117 matrix
for i=1:9 ;% 9 rows for 9 1-hr periods from 00:00 to 09:00
    nt= floor((i-1)/3)+1;% a temperate variable represent the index
# of the 3-hr period
    fra=tf(i,1)/sum(tf(3*nt-2:3*nt,1)); % hourly fraction of total
vehicle counts in the corresponding 3-hr period
    sc(i,:)=3*fra*Sc(nt,:); % *3 because it is not the sum but
averaging
    su(i,:)=3*fra*Su(nt,:);
end
% ------------------------------------------------------------------
```

The deconvolution of SVOC data was consisted of three steps. First, a preliminary baseline correction was carried out using the SVOC observation at midnight of November 20th, 2002 as the background. Second, the fraction of each hourly traffic volume in a 3-hour period of SVOC measurements was calculated using the hourly traffic statistics of the I-895 tunnel. And lastly the hourly SVOC concentrations were reallocated as three times the products of the corresponding 3-hourly concentrations and the hourly traffic fractions. Note that there is no blending of data in different 3-hourly periods in above data processing so that the temporal information of the 3-hourly data was retained.

D2 Derivation of the geometric relation in the windless model

In the windless model application at the Ponca street site, the line mobile source (I-895) was comprised of two roadway segments (i.e., northbound segment and north eastbound segment), as shown in Figure D1. Accordingly, the overall influence of I-895 during the windless period was the sum of their emission contributions, as follows.

$$c_j = \frac{2s \cdot \sum k_i e_{ij}}{\beta \cdot (2\pi)^{3/2}} \left(\int_{l=0}^{l_1} \frac{1}{r^2} dl + \int_{l=l_1}^{L} \frac{1}{r^2} dl \right) \quad (42)$$

where L is the total length (m) of the roadway source; l_1 is the length (m) of the northbound roadway segment; and other terms in Equation 42 are the same as those demonstrated in Equation 4.4. In particular, the former integral in Equation 42 represents the roadway coefficient (m^{-1}) of the northbound segment and the latter integral represents the roadway coefficient of the north eastbound segment.

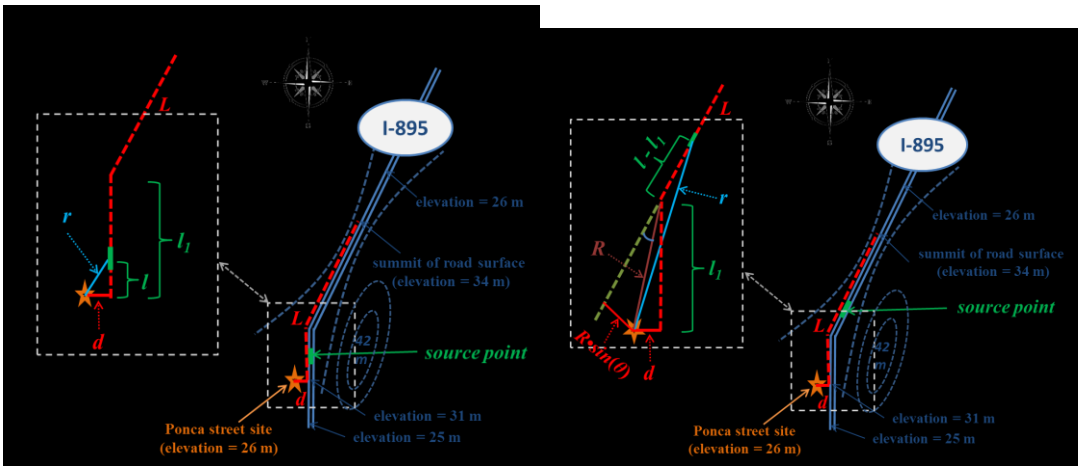

Figure D1 Schematic representation of the geometric relation between the Ponca street site and the I-895 roadway: a) northbound segment; and b) north eastbound segment.

As illustrated in Figure D1a, the roadway coefficient of the northbound segment was expressed as:

$$\int_{l=0}^{l_1} \frac{1}{r^2}\,dl = \int_{l=0}^{l_1} \frac{1}{d^2+l^2}\,dl \tag{43}$$

As illustrated in Figure D1b, the roadway coefficient of the north eastbound segment was expressed as:

$$\int_{l=l_1}^{L} \frac{1}{r^2}\,dl = \int_{l=l_1}^{L} \frac{1}{(R\cdot\sin(\theta))^2+(R\cdot\cos(\theta)+l-l_1)^2}\,dl \tag{44}$$

where R is the length (m) of the link line between the receptor site and the turning point of the I-895 roadway (i.e., $R^2 = d^2 + l_1^2$), and θ is the intersection angle between north eastbound segment and that link line. Reorganization of Equation 44 gives as follows.

$$\int_{l=l_1}^{L} \frac{1}{r^2}\,dl = \int_{l=l_1}^{L} \frac{1}{R^2+2(l-l_1)\cdot R\cdot\cos(\theta)+(l-l_1)^2}\,dl \tag{45}$$

In this case, the intersection angle between the northbound I-895 segment and the extension of the north eastbound segment (i.e., the green dashed line in Figure D1b) was small (i.e., < 45°), and the Ponca street site was only slightly off the center line of this section. Hence R•cos(θ) is approximately equal to l_1 and Equation 46 can be rewritten as follows.

$$\int_{l=l_1}^{L} \frac{1}{r^2}\,dl = \int_{l=l_1}^{L} \frac{1}{d^2+{l_1}^2+2(l-l_1)\cdot l_1+(l-l_1)^2}\,dl \tag{46}$$

The final derivation of Equation 42 is then obtained as follows, which is the same as Equation 4.6 in Chapter 4.

$$c_j = \frac{2s\cdot\sum k_i e_{ij}}{\beta\cdot(2\pi)^{3/2}}\left(\int_{l=0}^{l_1} \frac{1}{d^2+l^2}\,dl + \int_{l=l_1}^{L} \frac{1}{d^2+l^2}\,dl\right) \tag{47}$$

D3 Edge plot diagnostic of the UNMIX solution in this study

In case that PMF and UNMIX do not agree, it is often controversial to conclude which approach can provide more plausible results. Choosing the model that merely gives the better fits is a biased approach and Henry proposed to use the diagnostic edge plots to determine the preference (Henry and Christensen 2010). In this study, the edge plots of the five sources in the UNMIX solution showed clearly defined edges, suggesting that UNMIX might be a more suitable model than PMF.

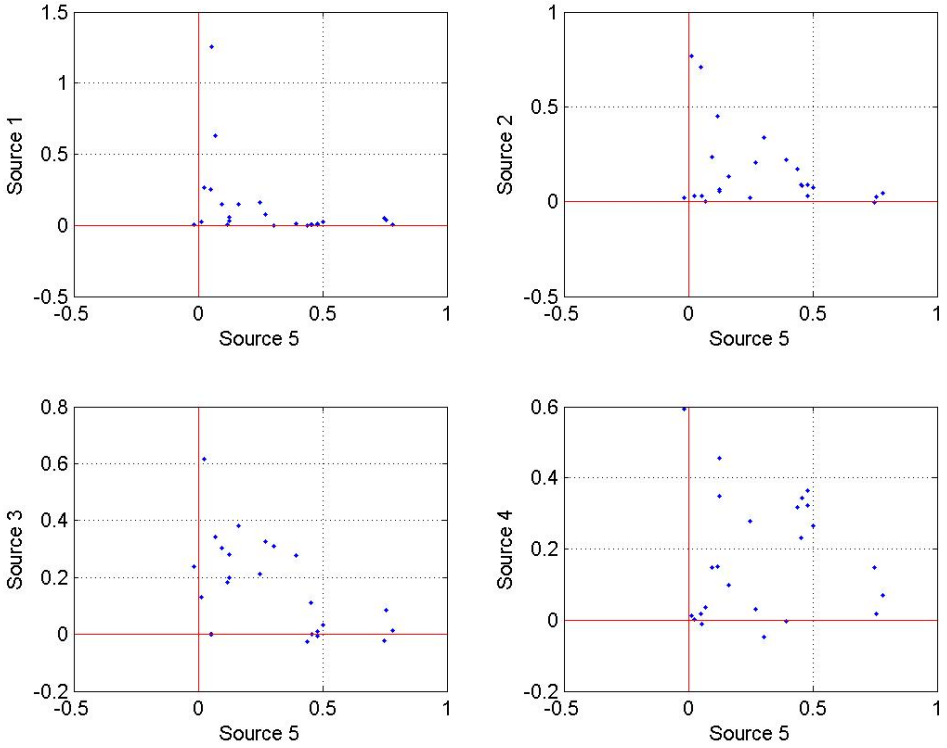

Figure D2 Diagnostic plots showing edges by UNMIX (Source 5 is the traffic factor).

D4 Correlation of traffic between the Fort McHenry (FTMC) tunnel and the I-895 tunnel

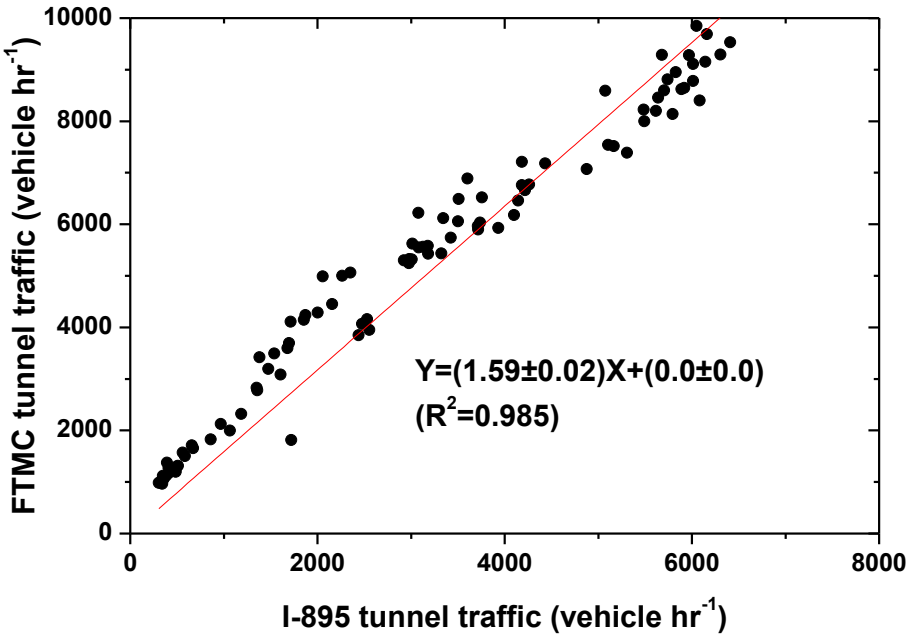

Figure D3 Linear correlation between the Fort McHenry (FTMC) tunnel traffic and the I-895 tunnel traffic during the period from November 19th through 22nd, 2002.

D5 Correlation between ambient species with $PM_{2.5}$ mass during the morning $PM_{2.5}$ excursion (0100 ~ 0800 LT) on November 20th, 2002.

Table D1 Correlation coefficients (r^2) and *p*-values of ambient species or particle number concentrations with $PM_{2.5}$ mass concentrations during the morning $PM_{2.5}$ excursion (0100 ~ 0800 LT) of November 20th, 2002.

	R^2	*p-value*
NOx	0.983	0.000
CO	0.990	0.000
Sulfate	0.985	0.000
Nitrate	0.884	0.002
EC	0.981	0.000
OC	0.952	0.000
Al	0.964	0.000
As	0.099	0.491
Cd	0.378	0.142
Cr	0.680	0.023
Cu	0.892	0.001
Fe	0.494	0.078
Mn	0.856	0.003
Ni	0.785	0.008
Pb	0.803	0.006
Se	0.240	0.264
Zn	0.996	0.000
9.65	0.049	0.635
10.4	0.062	0.591
11.1	0.055	0.613
12	0.027	0.725
12.9	0.004	0.889
13.8	0.004	0.895
14.9	0.070	0.567
16	0.165	0.366
17.2	0.242	0.262
18.4	0.357	0.157
19.8	0.542	0.059
21.3	0.681	0.022
22.9	0.768	0.010
24.6	0.793	0.007
26.4	0.784	0.008

28.4	0.791	0.007
30.5	0.828	0.004
32.8	0.863	0.002
35.2	0.881	0.002
37.9	0.888	0.001
40.7	0.898	0.001
43.7	0.911	0.001
47	0.928	0.000
50.5	0.943	0.000
54.2	0.952	0.000
58.3	0.957	0.000
62.6	0.961	0.000
67.3	0.966	0.000
72.3	0.970	0.000
77.7	0.976	0.000
83.5	0.983	0.000
89.8	0.988	0.000
96.5	0.989	0.000
104	0.989	0.000
111	0.993	0.000
120	0.997	0.000
129	0.994	0.000
138	0.992	0.000
149	0.992	0.000
160	0.989	0.000
172	0.984	0.000
184	0.972	0.000
198	0.955	0.000
213	0.948	0.000
229	0.936	0.000
246	0.927	0.001
264	0.924	0.001
284	0.937	0.000
305	0.914	0.001
328	0.912	0.001
352	0.929	0.000
379	0.898	0.001
407	0.880	0.002
542	0.984	0.000
583	0.980	0.000

626	0.975	0.000
673	0.971	0.000
723	0.963	0.000
777	0.970	0.000
835	0.968	0.000
898	0.973	0.000
965	0.976	0.000
1037	0.973	0.000
1114	0.982	0.000
1197	0.981	0.000
1286	0.949	0.000
1382	0.973	0.000
1486	0.980	0.000
1596	0.954	0.000
1715	0.973	0.000
1843	0.978	0.000
1981	0.986	0.000
2129	0.900	0.001
2288	0.973	0.000
2458	0.973	0.000

D6 Supplemental 3-hour and decomposed 1-hour sets of SVOC concentrations

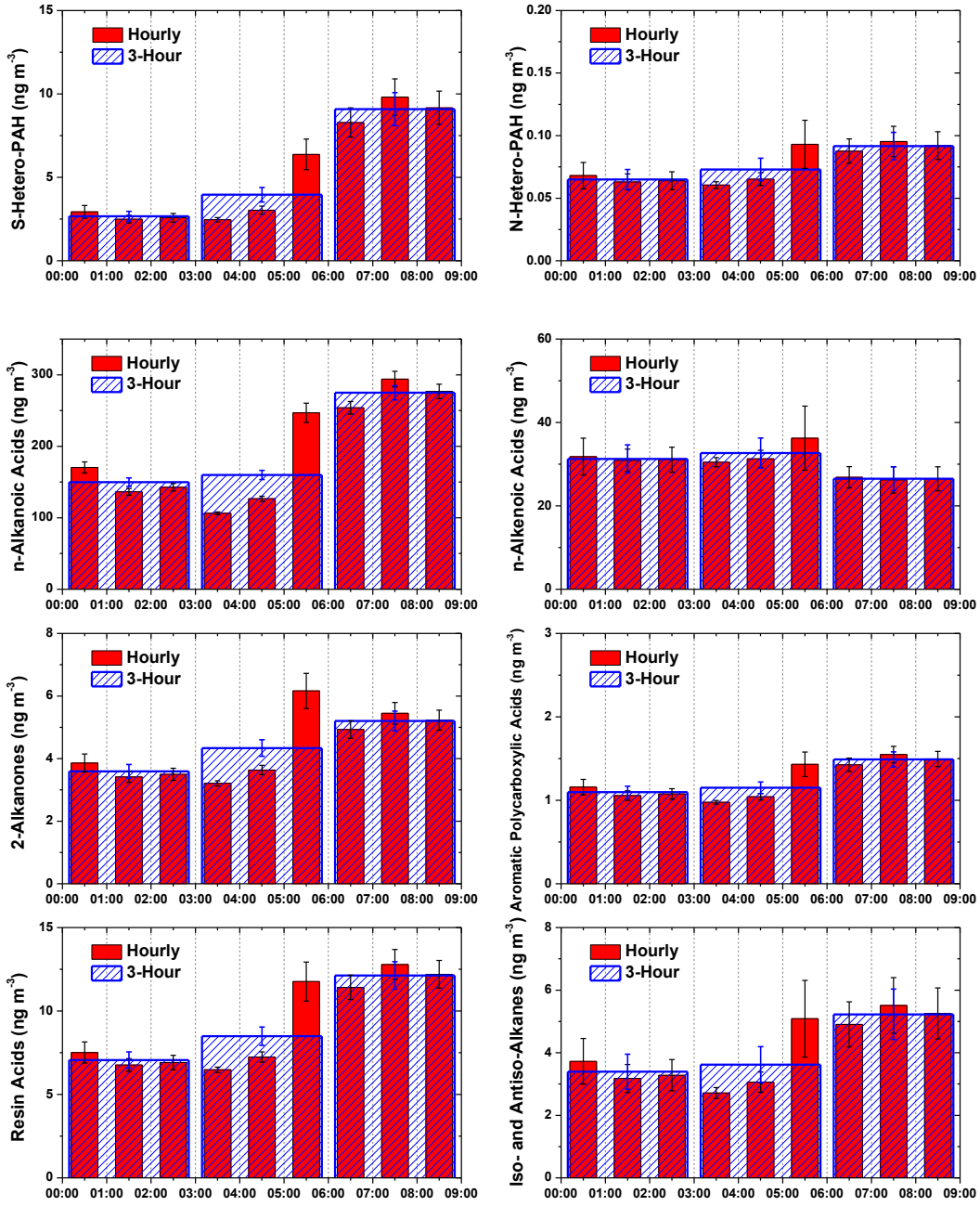

Figure D4 3-Hour and disassembled hourly concentrations of selected SVOC categories in the early morning (0000 ~ 0900 LT) of November 20th, 2002.

D7 Supplemental abundance profiles of motor vehicle emissions

Table D2 Supplemental abundance profiles of motor vehicle emissions obtained by direct peak observation (DPO) and windless model analysis (WMA) in the study of November 20th, 2002 (unit: μg per μg of $PM_{2.5}$ for criteria gases, and ng per μg of $PM_{2.5}$ for SVOCs).

Species	DPO	WMA		
	Abundance	Abundance	r^2	p
Criteria gases				
NO	11.08 ± 4.20	11.94 ± 3.01	0.980	0.000
NO2	1.29 ± 0.62	1.28 ± 0.32	0.930	0.000
NOx	12.37 ± 4.82	13.22 ± 4.81	0.980	0.000
CO	43.30 ± 16.65	46.44 ± 16.07	0.990	0.000
n-Alkanes				
Nonadecane	1.250 ± 0.064	1.270 ± 0.139	0.983	0.000
Eicosane	1.180 ± 0.052	1.190 ± 0.120	0.984	0.000
Heneicosane	1.100 ± 0.064	1.110 ± 0.130	0.981	0.000
Docosane	0.895 ± 0.040	0.905 ± 0.116	0.960	0.000
Tricosane	0.643 ± 0.038	0.650 ± 0.102	0.943	0.000
Tetracosane	0.354 ± 0.023	0.359 ± 0.057	0.947	0.000
Pentacosane	0.250 ± 0.027	0.245 ± 0.129	0.987	0.000
Hexacosane	0.114 ± 0.012	0.107 ± 0.039	0.825	0.005
Heptacosane	0.041 ± 0.010	0.027 ± 0.055	0.073	0.557
Octacosane	0.033 ± 0.008	0.020 ± 0.047	0.058	0.604
Nonacosane	0.067 ± 0.014	0.060 ± 0.064	0.230	0.276
Triacontane	0.050 ± 0.009	0.044 ± 0.028	0.470	0.089
Hentriacontane	0.053 ± 0.016	0.050 ± 0.024	0.643	0.030
Dotriacontane	0.022 ± 0.008	0.021 ± 0.317	0.933	0.000
Tritriacontane	0.017 ± 0.008	0.017 ± 0.014	0.652	0.028
Tetratriacontane	0.000 ± 0.000	0.000 ± N.A.	N.A.	N.A.
Pentatriacontane	0.000 ± 0.000	0.000 ± N.A.	N.A.	N.A.
Hexatriacontane	0.000 ± 0.000	0.000 ± N.A.	N.A.	N.A.
Iso- and antiso-alkanes				
Isohentriacontane	0.017 ± 0.006	0.017 ± 0.012	0.491	0.079
Isotritriacontane	-0.009 ± 0.002	0.000 ± 0.010	0.866	0.002

Hentriacontane, 3-methyl-	0.031 ± 0.010	0.034 ± 0.014	0.962	0.000
n-Alkanoic acids				
Octanoic Acid	0.286 ± 0.012	0.298 ± 0.033	0.974	0.000
Nonanoic Acid	0.285 ± 0.011	0.296 ± 0.019	0.995	0.000
Decanoic Acid	0.088 ± 0.006	0.093 ± 0.023	0.856	0.003
Undecanoic Acid	0.012 ± 0.002	0.014 ± 0.014	0.265	0.237
Dodecanoic Acid	0.125 ± 0.007	0.125 ± 0.032	0.847	0.003
Tridecanoic Acid	0.028 ± 0.002	0.027 ± 0.006	0.883	0.002
Tetradecanoic Acid	0.113 ± 0.008	0.111 ± 0.073	0.434	0.108
Pentadecanoic Acid	0.046 ± 0.003	0.042 ± 0.043	0.243	0.262
Hexadecanoic Acid	0.664 ± 0.033	0.711 ± 0.206	0.802	0.006
Heptadecanoic Acid	0.049 ± 0.005	0.051 ± 0.012	0.876	0.002
Octadecanoic Acid	0.778 ± 0.046	0.880 ± 0.168	0.907	0.001
Nonadecanoic Acid	0.013 ± 0.002	0.014 ± 0.003	0.911	0.001
Eicosanoic Acid	0.028 ± 0.004	0.031 ± 0.010	0.799	0.007
Heneicosanoic Acid	0.008 ± 0.002	0.009 ± 0.004	0.704	0.018
Docosanoic Acid	0.031 ± 0.008	0.036 ± 0.019	0.568	0.050
Tricosanoic Acid	0.010 ± 0.003	0.011 ± 0.007	0.473	0.088
Tetracosanoic Acid	0.044 ± 0.016	0.051 ± 0.040	0.373	0.145
Pentacosanoic Acid	0.005 ± 0.003	0.006 ± 0.006	0.269	0.233
Hexacosanoic Acid	0.019 ± 0.010	0.024 ± 0.019	0.354	0.159
Heptacosanoic Acid	0.003 ± 0.002	0.004 ± 0.003	0.351	0.161
Octacosanoic Acid	0.005 ± 0.005	0.006 ± 0.010	0.092	0.509
Nonacosanoic Acid	0.001 ± 0.001	0.001 ± 0.002	0.146	0.398
Triacontanoic Acid	0.002 ± 0.007	0.003 ± 0.005	0.127	0.433
Hentriacontanoic Acid	0.002 ± 0.001	0.002 ± 0.003	0.967	0.000
Dotriacontanoic Acid	-0.003 ± 0.002	0.000 ± 0.003	0.317	0.188
Tritriacontanoic Acid	0.000 ± 0.000	0.000 ± N.A.	N.A.	N.A.
Tetratriacontanoic Acid	0.000 ± 0.000	0.000 ± N.A.	N.A.	N.A.
n-Alkenoic acids				
9-Hexadecenoic Acid	0.010 ± 0.002	0.002 ± 0.068	0.000	0.970
9-Octadecenoic Acid	-0.088 ± 0.067	0.000 ± 0.203	0.918	0.001
Aliphatic dicarboxylic acids				
Butanedioic Acid	0.001 ± 0.000	0.001 ± 0.000	0.908	0.001

Pentanedioic Acid	0.001 ± 0.001	0.000 ± 0.004	0.064	0.586
Hexanedioic Acid	0.000 ± 0.000	0.000 ± 0.000	N.A.	N.A.
Nonanedioic Acid	0.003 ± 0.001	0.004 ± 0.002	0.564	0.052
Aliphatic polycarboxylic acids				
1,2-Benzenedicarboxylic Acid	0.009 ± 0.002	0.009 ± 0.004	0.783	0.008
1,4-Benzenedicarboxylic Acid	-0.001 ± 0.000	0.000 ± 0.002	0.151	0.388
1,3-Benzenedicarboxylic Acid	0.000 ± 0.000	0.000 ± 0.000	0.509	0.072
1,2-Benzenedicarboxylic acid, 4-methyl-	0.000 ± 0.000	0.000 ± 0.000	N.A.	N.A.
2-Alkanones				
2-Pentadecanone, 6,10,14-trimethyl-	0.034 ± 0.007	0.035 ± 0.019	0.558	0.054
Alkylcyclohexanes				
Cyclohexane, undecyl-	0.139 ± 0.016	0.142 ± 0.026	0.968	0.000
Cyclohexane, dodecyl-	0.086 ± 0.007	0.087 ± 0.012	0.984	0.000
Cyclohexane, tridecyl-	0.069 ± 0.006	0.069 ± 0.013	0.977	0.000
Cyclohexane, tetradecyl-	0.054 ± 0.004	0.054 ± 0.009	0.980	0.000
Cyclohexane, pentadecyl-	0.075 ± 0.006	0.075 ± 0.013	0.954	0.000
Cyclohexane, hexadecyl-	0.084 ± 0.007	0.084 ± 0.015	0.943	0.000
Cyclohexane, heptadecyl-	0.104 ± 0.009	0.103 ± 0.020	0.934	0.000
Cyclohexane, octadecyl-	0.085 ± 0.008	0.085 ± 0.015	0.959	0.000
Cyclohexane, nonadecyl-	0.062 ± 0.007	0.062 ± 0.012	0.954	0.000
Cyclohexane, eicosyl-	0.033 ± 0.004	0.033 ± 0.010	0.866	0.002
Cyclohexane, heneicosyl-	0.017 ± 0.002	0.017 ± 0.003	0.996	0.000
Cyclohexane, docosyl-	0.005 ± 0.001	0.005 ± 0.002	0.905	0.001
Resin acids				
1-Phenanthrenecarboxylic acid	0.005 ± 0.001	0.004 ± 0.003	0.486	0.082
1-Phenanthrenecarboxylic acid, 7-ethenyl-1,2,3,4,4a,4b,5,6,7,9,10,10a-dodecahydro-1,4a,7-	0.003 ± 0.001	0.004 ± 0.001	0.822	0.005

trimethyl-, (1R,4aR,4bS,7R,10aR)-				
1-Phenanthrenecarboxylic acid, 7-ethenyl-1,2,3,4,4a,4b,5,6,7,8,10,10a-dodecahydro-1,4a,7-trimethyl-, (1R,4aR,4bS,7S,10aR)-	0.011 ± 0.000	0.011 ± 0.002	0.863	0.002
1-Phenanthrenecarboxylic acid, 1,2,3,4,4a,9,10,10a-octahydro-1,4a-dimethyl-7-(1-methylethyl)-, (1R,4aS,10aR)-	0.054 ± 0.009	0.052 ± 0.040	0.646	0.029
1-Phenanthrenecarboxylic acid, 1,2,3,4,4a,9,10,10a-octahydro-1,4a-dimethyl-7-(1-methylethyl)-9-oxo-, (1R,4aS,10aR)-	0.028 ± 0.005	0.034 ± 0.009	0.843	0.003
Phenolic wood markers				
Benzaldehyde, 4-hydroxy-3,5-dimethoxy-	-0.016 ± 0.015	0.000 ± 0.026	0.048	0.635
Ethanone, 1-(4-hydroxy-3,5-dimethoxyphenyl)-	0.000 ± 0.004	0.002 ± 0.006	0.041	0.662
Benzoic acid, 4-hydroxy-3,5-dimethoxy-	0.011 ± 0.002	0.012 ± 0.009	0.732	0.014
Sugars				
.beta.-D-Glucopyranose, 1,6-anhydro-	0.547 ± 0.375	1.060 ± 1.057	0.298	0.205
Steroids				
Cholest-5-en-3-ol (3.beta)-	0.036 ± 0.013	0.034 ± 0.043	0.538	0.061
Stigmast-5-en-3-ol, (3.beta)-	0.019 ± 0.016	0.019 ± 0.081	0.967	0.000
Thiazoles				
Benzothiazole	0.112 ± 0.038	0.111 ± 0.154	0.149	0.392
Pentacyclic triterpanes				
20,29,30-Trinorlupane, (17.alpha.)-	0.048 ± 0.006	0.048 ± 0.011	0.929	0.000
A'-Neo-22,29,30-	0.049 ± 0.005	0.048 ± 0.011	0.896	0.001

trinorgammacerane, (17.alpha.)-				
A'-Neo-30-norgammacerane, (17.alpha.)-	0.205 ± 0.019	0.203 ± 0.037	0.946	0.000
A'-Neogammacerane, (17.alpha.)-	0.104 ± 0.009	0.103 ± 0.019	0.934	0.000
A'-Neo-30-norgammacerane, 22-ethyl-, (17.alpha.,22S)-	0.052 ± 0.005	0.052 ± 0.009	0.955	0.000
A'-Neo-30-norgammacerane, 22-ethyl-, (17.alpha.,22R)-	0.039 ± 0.004	0.039 ± 0.007	0.965	0.000
A'-Neo-30-norgammacerane, 22-propyl-, (17.alpha.,22S)-	0.028 ± 0.003	0.028 ± 0.005	0.943	0.000
A'-Neo-30-norgammacerane, 22-propyl-, (17.alpha.,22R)-	0.020 ± 0.002	0.020 ± 0.004	0.920	0.001
PAHs				
Phenanthrene	0.862 ± 0.100	0.873 ± 0.186	0.979	0.000
Anthracene	0.077 ± 0.010	0.077 ± 0.020	0.976	0.000
4H-Cyclopenta[def]phenanthrene	0.027 ± 0.003	0.027 ± 0.010	0.988	0.000
Fluoranthene	0.086 ± 0.010	0.086 ± 0.032	0.984	0.000
Pyrene	0.149 ± 0.015	0.149 ± 0.044	0.998	0.000
Benz[a]anthracene	0.028 ± 0.004	0.028 ± 0.006	0.940	0.000
Chrysene and Triphenylene	0.041 ± 0.007	0.041 ± 0.011	0.961	0.000
Benz[e]acephenathrylene	0.033 ± 0.006	0.033 ± 0.010	0.905	0.001
Benzo[k]fluoranthene	0.009 ± 0.002	0.009 ± 0.003	0.913	0.001
Benzo[j]fluoranthene	0.004 ± 0.001	0.005 ± 0.002	0.823	0.005
Benzo[e]pyrene	0.024 ± 0.004	0.024 ± 0.008	0.932	0.000
Benzo[a]pyrene	0.020 ± 0.005	0.021 ± 0.008	0.783	0.008
Perylene	0.003 ± 0.001	0.003 ± 0.001	0.808	0.006
Indeno[1,2,3-cd]pyrene	0.025 ± 0.005	0.025 ± 0.011	0.699	0.019
Benzo[ghi]perylene	0.037 ± 0.008	0.037 ± 0.015	0.784	0.008
Dibenz[a,h]anthracene	0.001 ± 0.000	0.001 ± 0.001	0.434	0.107
Coronene	0.018 ± 0.005	0.017 ± 0.010	0.622	0.035
Oxy-PAHs				
9H-Fluoren-9-one	0.165 ± 0.024	0.166 ± 0.057	0.991	0.000

9,10-Anthracenedione	0.030 ± 0.009	0.031 ± 0.015	0.697	0.019
7H-Benz[de]anthracen-7-one	0.036 ± 0.005	0.036 ± 0.010	0.911	0.001
Benz[a]anthracene-7,12-dione	0.006 ± 0.001	0.006 ± 0.006	0.910	0.001
N-Hetero-PAHs				
Benzo[h]quinoline	0.001 ± 0.000	0.001 ± 0.000	0.787	0.008
S-Hetero-PAHs				
Dibenzothiophene	0.122 ± 0.019	0.124 ± 0.030	0.977	0.000
Secondary biogenic oxidation products				
Bicyclo[3.1.1]heptan-2-one, 6,6-dimethyl-	-0.048 ± 0.012	0.000 ± 0.028	0.562	0.052
Cyclobutanecarboxylic acid, 3-acetyl-2,2-dimethyl-	-0.004 ± 0.002	0.001 ± 0.000	0.003	0.904
Cyclobutaneacetic acid, 3-acetyl-2,2-dimethyl-, (1R,3R)-rel-	-0.063 ± 0.012	0.000 ± 0.313	0.049	0.633

Appendix E

Particle size distribution measured at Ponca Street site on August 8th, 2002

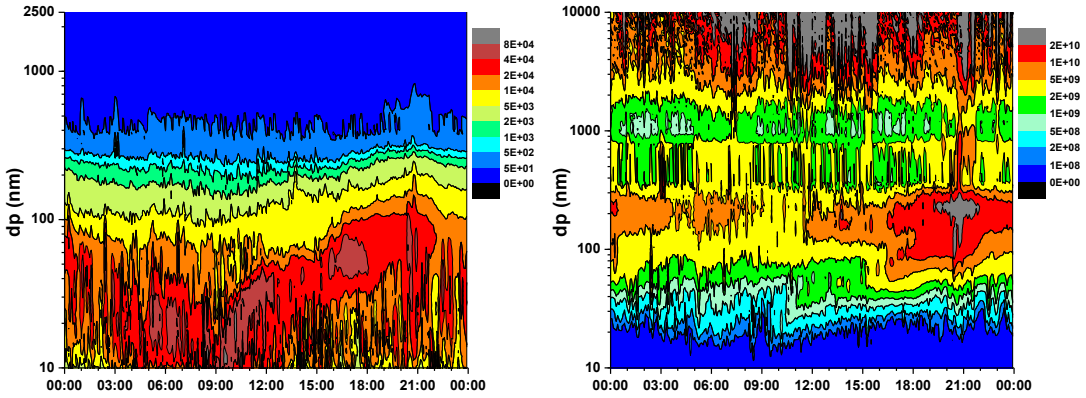

Figure E1 Contour plot of $PM_{2.5}$ particle size distribution at the Ponca street supersite on August 8th, 2002 (left panel: number size distribution; and right: volume size distribution).

Figure E1 shows the 5-minute $PM_{2.5}$ particle size distribution measured with SMPS and APS at the Ponca street supersite on August 8th, 2002. The SMPS and APS measurements and the data processing have been described in Chapter 4.

As shown in Figure E1, an Aitken mode with a maximum at ~ 80 nm in the contour plot of number size distribution (NSD) and a corresponding accumulation mode with a maximum at ~ 250 nm in the volume size distribution (VSD) were observed in the evening (i.e., 1930 ~ 2130 LT).

Glossary

χ/Q: Gaussian plume dispersion factors (s m^{-3})

ABL: Atmospheric Boundary Layer

ACH: Alkylcyclohexanes

ADCA: n-Aliphatic dicarboxylic acid

APCA: Aromatic polycarboxylic acid

APS: Aerodynamic Particle Sizer

BRZ: Big River Zinc Corporation

BS: Brandon Shores

CAMMS: Continuous Ambient Mass Monitoring System

CAMx: Comprehensive Air-quality Model with Extensions

CBL: Convective Boundary Layer

CEM: Continuous Emissions Monitor

CFPP: Coal-fired Power Plant

CMAQ: Community Multi-scale Air Quality Model

CMB: Chemical Mass Balance

COPREM: Constrained Physical Receptor Model

DPO: Direct peak observation

EC: Elemental carbon

EPA: United States Environmental Protection Agency

ESP: Electrostatic Precipitator

FA: Factor Analysis

Fa2: Fractions of the predictions within a factor of 2 of the observed values

GPM: Gaussian Plume Model

HDDV: Heavy-duty diesel vehicle

HMW: How molecular weight

HMWOPAHs: How molecular weight oxy-PAH

HMWPAHs: How molecular weight PAH

LB: Lower bound

LMW: Low molecular weight

LMWOPAHs: Low molecular weight oxy-PAH

LMWPAHs: Low molecular weight PAH

ISCST3: Industrial Source Complex Short Term Plume Model 3

MAGE: Mean Absolute Gross Error

MB: Mean Bias

MC: Multiple Cyclone

MDE: Maryland Department of Environment

ME: Multilinear Engine

MFB: Mean Fractional Bias

MLR: Multiple Linear Regression

MLD: Mixed layer depth

MNB: Mean Normalized Bias

MNGE: Mean Normalized Gross Error

NAAQS: National Ambient Air Quality Standard

NEI: National Emission Inventory

NET: National Emission Trends (precursor to NEI)

NMSE: Normalized Mean Square Error

NSD: Number size distribution

NSRDB: National Solar Radiation Database

OC: Organic carbon

OFPP: Oil-fired Power Plant

PAH: Polycyclic aromatic hydrocarbon

PCA: Principle Component Analysis

PCTT: Pentacyclic triterpane

PDRM: Pseudo-Deterministic Receptor Model

PM: Particulate matter

$PM_{2.5}$: Particulate matter with an aerodynamic diameter < 2.5 μm

PMF: Positive Matrix Factorization

RH: Relative humidity

RMSE: Root Mean Square Error

RSMS: Rapid Single-particle Mass Spectrometer

SCC: Source Classification Code

SCE: Source Contribution Estimates

SCR: Selective Catalytic Reduction

SEAS: Semi-continuous Elements in Aerosol Sampler

SMPS: Scanning Mobility Particle Sizer

SPECIATE: EPA SPECIATE database of source emission profiles

SVOC: Semi-volatile organic carbon

TAG: Thermal Desorption Aerosol GC-MS

TC: Total carbon

TEOM: Tapered Element Oscillating Microbalance

TGPM: Trajectory-driven Gaussian Plume Model

TRI: Toxics Release Inventory

WS: Wagner Station

VOC: Volatile organic compound

VSD: Volume size distribution

UB: Upper bound

UFP: Ultrafine particles with an aerodynamic diameter < 0.1 μm

UNMIX: EPA UNMIX Model

WMA: Windless model analysis

Bibliography

Adachi, K. & Y. Tainosho (2004) Characterization of heavy metal particles embedded in tire dust. *Environment International,* 30**,** 1009-1017.

Adam, M. (2004) Aerosol optical characterization by nephelometer and lidar: The Baltimore Supersite experiment during the Canadian forest fire smoke intrusion. *Journal of Geophysical Research,* 109.

Amato, F. & P. K. Hopke (2012) Source apportionment of the ambient PM2.5 across St. Louis using constrained positive matrix factorization. *Atmos. Environ.,* 46**,** 329-337.

Amato, F., M. Pandolfi, M. Viana, X. Querol, A. Alastuey & T. Moreno (2009) Spatial and chemical patterns of PM10 in road dust deposited in urban environment. *Atmospheric Environment,* 43**,** 1650-1659.

Arya, S. P. S. (1981) Parameterizing the height of the stable atmospheric boundary layer. *J. Appl. Meteor.,* 20**,** 1192-1202.

Ban-Weiss, G. A., M. M. Lunden, T. W. Kirchstetter & R. A. Harley (2010) Size-resolved particle number and volume emission factors for on-road gasoline and diesel motor vehicles. *Journal of Aerosol Science,* 41**,** 5-12.

Beachley, G. M. (2009) An improved pseudo-deterministic receptor model (iPDRM) to apportion ambient PM constituents to sources in Tampa, FL. *Ph.D. dissertation,* Department of chemistry and biochemistry, University of Maryland College Park.

Beachley, G. M. & J. M. Ondov (2012) Improved apportionment of ambient PM constituents to sources in Tampa, FL, with Pseudo-Deterministic Receptor Model-II. *Science of the Total Environment*.

Benkley, C. W. & L. L. Schulman (1979) Estimating hourly mixing depths from historical meteorological data. *J. Appl. Meteor.,* 18**,** 772-780.

Bevington, P. R. (1969) Data reduction and error analysis for the physical sciences. McGraw-Hill, New York.

Binkowski, F. S. (1979) A simple semi-empirical theory for turbulence in the atmospheric surface layer. *Atmos. Environ.,* 13**,** 247-253.

Bocskay, K. A., D. L. Tang, M. A. Orjuela, X. H. Liu, D. P. Warburton & F. P. Perera (2005) Chromosomal aberrations in cord blood are associated with prenatal exposure to carcinogenic polycyclic aromatic hydrocarbons. *Cancer Epidemiology Biomarkers & Prevention,* 14**,** 506-511.

Brauer, M. (2002) Air Pollution from Traffic and the Development of Respiratory Infections and Asthmatic and Allergic Symptoms in Children. *American Journal of Respiratory and Critical Care Medicine,* 166**,** 1092-1098.

Briggs, G. A. (1969) Plume rise. *U.S. Atomic Energy Commission Critical Review Series,* T/D 25075.

--- (1971) Some recent analyses of plume rise observations. *Proc. 2nd Int. Clean Air Congress,* Academic Press, New York**,** 1029-1032.

--- (1972) Discussion on Chimney Plumes in Neutral and Stable Surroundings. *Atmos. Environ.,* 6**,** 507-510.

--- (1974) Diffusion estimation for small emissions. *Air Resources Atmospheric Turbulence and Diffusion Laboratory 1973 Annual Report,* Environmental Research Laboratories**,** USAEC Rep. ATDL-106, NOAA, Washington, D. C.

--- (1975) Plume rise predictions. *In Lectures on Air Pollution and Environmental Impact Analysis,* American Meteorological Society, Boston, Massachusetts.

Byun, D. & K. L. Schere (2006) Review of the governing equations, computational algorithms, and other components of the Models-3 Community Multiscale Air Quality (CMAQ) modeling system. *Appl. Mech. Rev.,* 59**,** doi:10.1115/1.2128636.

Chang, S. N., P. K. Hopke, G. E. Gordon & S. W. Rheingrover (1988) Target-transformation factor analysis of airborne particulate samples selected by wind-trajectory analysis. *Aerosol Science and Technology,* 8**,** 63-80.

Chen, L. C. & M. Lippmann (2009) Effects of metals within ambient air particulate matter (PM) on human health. *Inhalation Toxicology,* 21**,** 1-31.

Ching, J. K. S. (1985) Urban-scale variations of turbulence parameters and fluxes. *Boundary-Layer Meteorology,* 33**,** 335-361.

Chuang, K. J., C. C. Chan, T. C. Su, C. T. Lee & C. S. Tang (2007) The Effect of Urban Air Pollution on Inflammation, Oxidative Stress, Coagulation, and Autonomic Dysfunction in Young Adults. *American Journal of Respiratory and Critical Care Medicine,* 176**,** 370-376.

Cimorelli, A. J., S. G. Perry, A. Venkatram, J. C. Weil, R. J. Paine, R. B. Wilson, R. F. Lee, W. D. Peters & R. W. Brode (2005) AERMOD: A dispersion model for industrial source applications. Part I: General model formulation and boundary layer characterization. *J. Appl. Meteor.,* 44**,** 682-693.

Cinoco, R. (1965) A mathematical model for air flow in a vegetative canopy. *J. Appl. Met.,* 4**,** 517-522.

Claiborn, C., A. Mitra, G. Adams, L. Bamesberger, G. Allwine, R. Kantamaneni, B. Lamb & H. Westberg (1995) Evaluation of PM10 emission rates from paved and unpaved roads using tracer techniques. *Atmos. Environ.,* 29**,** 1075-1089.

Cohen, D. D., E. Stelcer, D. Garton & J. Crawford (2011) Fine Particle characterisation, source apportionment and long range dust transport into the Sydney basin: A long term study between 1998 and 2009. *Atmospheric Pollution Research,* 2**,** 182-189.

Cooper, D. W. (1982) Receptor-oriented source-receptor analysis. *Specialty Conference on Receptor Models Applied to Contemporary Pollution Problems***,** Northeast Atl. Int. Sect. of the Air Pollut. Control Assoc., Danvers, Mass., 17–20 Oct.

Costabile, F., W. Birmili, S. Klose, T. Tuch, B. Wehner, A. Wiedensohler, U. Franck, K. Konig & A. Sonntag (2009) Spatio-temporal variability and principal components of the particle number size distribution in an urban atmosphere. *Atmos. Chem. Phys.,* 9**,** 3163-3195.

DeBell, L. J. (2004) A major regional air pollution event in the northeastern United States caused by extensive forest fires in Quebec, Canada. *Journal of Geophysical Research,* 109.

Draxler, R. R. (1976) Determination of atmospheric diffusion parameters. *Atmos. Environ.,* 10**,** 99-105.

Finkelstein, M. M., M. Jerrett & M. R. Sears (2004) Traffic Air Pollution and Mortality Rate Advancement Periods. *American Journal of Epidemiology,* 160**,** 173-177.

Fuzzi, S., M. O. Andreae, B. J. Huebert, M. Kulmala, T. C. Bond, M. Boy, S. J. Doherty, A. Guenther, M. Kanakidou, K. Kawamura, V. M. Kerminen, U. Lohmann, L. M. Russell & U. Poschl (2006) Critical assessment of the current state of scientific knowledge, terminology, and research needs concerning the role of organic aerosols in the atmosphere, climate, and global change. *Atoms. Chem. Phys.,* 6**,** 2017-2038.

Gertler, A. W. (2005) Diesel vs. gasoline emissions: Does PM from diesel or gasoline vehicles dominate in the US? *Atmospheric Environment,* 39**,** 2349-2355.

Gertler, A. W., M. Abu-Allaban, W. Coulombe, J. A. Gillies, W. Pierson, C. F. Rogers, J. C. Sagebiel, L. Tarnay & T. A. Cahill (2002) Measurements of mobile source particulate emissions in a highway tunnel. *International Journal of Vehicle Design,* 27**,** 86-93.

Gifford, F. A. (1961) Use of routine meteorological observations for estimating atmospheric dispersion. *Nucl. Safety,* 2**,** 47-51.

Gladney, E. S., J. A. Small, G. E. Gordon & W. H. Zoller (1976) Composition and size distribution of in-stack particulate material at a coal-fired power plant. *Atmos. Environ.,* 10**,** 1071-1077.

Glaser, B., A. Dreyer, M. Bock, S. Fiedler, M. Mehring & T. Heitmann (2005) Source apportionment of organic pollutants of a highway-traffic-influenced urban area in Bayreuth (Germany) using biomarker and stable carbon isotope signatures. *Environ. Sci. Technol.,* 39**,** 3911-3917.

Gordon, G. E. (1988) Receptor models. *Environ. Sci. Technol.,* 22**,** 1132-1142.

Gordon, G. E. & W. H. Zoller (1974) Normalization and interpretation of atmospheric trace element concentration patterns. *Proceedings of the First Annual NSF Trace Contaminants Conference,* U.S. Atomic Energy Commission, Oak Ridge, TN**,** 314-325.

Grieshop, A. P., M. A. Miracolo, N. M. Donahue & A. L. Robinson (2009) Constraining the volatility distribution and gas-particle partitioning of combustion aerosols using isothermal dilution and thermodenuder measurements. *Environ. Sci. Technol.,* 43**,** 4750-4756.

Gu, J., M. Pitz, J. Schnelle-Kreis, J. Diemer, A. Reller, R. Zimmermann, J. Soentgen, M. Stoelzel, H. E. Wichmann, A. Peters & J. Cyrys (2011) Source apportionment of ambient particles: Comparison of positive matrix factorization analysis applied to particle size distribution and chemical composition data. *Atmospheric Environment,* 45**,** 1849-1857.

Habre, R., B. Coull & P. Koutrakis (2011) Impact of source collinearity in simulated PM2.5 data on the PMF receptor model solution. *Atmospheric Environment,* 45**,** 6938-6946.

Harrison, R. M., D. J. T. Smith & L. Luhana (1996) Source apportionment of atmospheric polycyclic aromatic hydrocarbons collected from an urban location in Birmingham, U.K. *Environ. Sci. Technol.,* 30**,** 825-832.

Hartley, D. & R. Prinn (1993) Feasibility of determining surface emissions of trace gases using an inverse method in a three-dimensional chemical transport model. *Journal of Geophysical Research,* 98**,** 5183-5197.

Hays, M. D., L. Beck, P. Barfield, R. D. Willis, M. S. Landis, R. K. Stevens, W. Preston & Y. Dong (2009) Physical and chemical characterization of residual oil-fired power plant emissions. *Energy & Fuels,* 23**,** 2544-2551.

Hennigan, C. J., M. A. Miracolo, G. J. Engelhart, A. A. May, A. A. Presto, T. Lee, A. P. Sullivan, G. R. McMeeking, H. Coe, C. E. Wold, W. M. Hao, J. B. Gilman, W. C. Kuster, J. de Gouw, B. A. Schichtel, J. L. Collett, S. M. Kreidenweis & A. L. Robinson (2011) Chemical and physical transformations of organic aerosol from the photo-oxidation of open biomass burning emissions in an environmental chamber. *Atmospheric Chemistry and Physics,* 11**,** 7669-7686.

Henry, R. C. (1992) Dealing with near collinearity in chemical mass balance receptor models. *Atmos. Environ.,* 26A**,** 933-938.

--- (2000) UNMIX theory and applications. *Final Report of Workshop on UNMIX and PMF as Applied to PM2.5,* Publ. EPA/600/A-00/48**,** edited by R. D. Willis, pp. 4 –6, U.S. Environ. Prot. Agency, Washington, D. C.

Henry, R. C. & E. R. Christensen (2010) Selecting an appropriate multivariate source apportionment model result. *Environ. Sci. Technol.,* 44**,** 2474-2481.

Hirshon, J. M., M. Shardell, S. Alles, J. L. Powell, K. Squibb, J. Ondov & C. J. Blaisdell (2008) Elevated Ambient Air Zinc Increases Pediatric Asthma Morbidity. *Environmental Health Perspectives,* 116**,** 826-831.

Hitchins, J., L. Morawska, R. Wolff & D. Gilbert (2000) Concentrations of submicrometer particles from vehicle emissions near a major road. *Atmos. Environ.,* 34**,** 51-59.

Hjelmfelt, M. R. (1982) Numerical simulation of the effects of St. Louis on mesoscale boundary-layer airflow and vertical air motion: simulations of urban vs non-urban effects. *Journal of Applied Meteorology,* 21**,** 1239-1257.

Holtslag, A. A. M. & A. P. Van Ulden (1983) A simple scheme for daytime estimates of the surface fluxes from routine weather data. *J. Clim. Appl. Meteorol.,* 22**,** 517-529.

Hopke, P. K. & D. D. Cohen (2011) Application of receptor modeling methods. *Atmospheric Pollution Research,* 2**,** 122-125.

Hopke, P. K., K. Ito, T. Mar, W. F. Christensen, D. J. Eatough, R. C. Henry, E. Kim, F. Laden, R. Lall, T. V. Larson, H. Liu, L. Neas, J. Pinto, M. Stölzel, H. Suh, P. Paatero & G. D. Thurston (2005) PM source apportionment and health effects: 1. Intercomparison of source apportionment results. *Journal of Exposure Science and Environmental Epidemiology,* 16**,** 275-286.

Hopke, P. K., Z. Ramadan, P. Paatero, G. A. Norris, M. S. Landis, R. W. Williams & C. W. Lewis (2003) Receptor modeling of ambient and personal exposure samples: 1998 Baltimore Particulate Matter Epidemiology-Exposure Study. *Atmospheric Environment,* 37**,** 3289-3302.

Hostettler, F. D. & K. A. Kvenvolden (2002) Alkylcyclohexanes in environmental geochemistry. *Environmental Forensics,* 3**,** 293-301.

Huang, C. H. (1979) A theory of dispersion in turbulent shear flow. *Atmos. Environ.,* 13**,** 453-463.

Huang, X., I. Olmez, N. K. Aras & G. E. Gordon (1994) Emissions of trace elements from motor vehicles: potential marker elements and source composition profile. *Atmos. Environ.,* 28**,** 1385-1391.

Irwin, J. S. (1979) Scheme for estimating dispersion parameters as a function of release height. *Publ. EPA-600/4-79-062,* U.S. Environ. Prot. Agency, Washington, D. C.

Jacobs, L., T. S. Nawrot, B. de Geus, R. Meeusen, B. Degraeuwe, A. Bernard, M. Sughis, B. Nemery & L. Panis (2010) Subclinical responses in healthy cyclists briefly exposed to traffic-related air pollution: an intervention study. *Environmental Health,* 9**,** 64.

Jaeckels, J. M., M. S. Bae & J. J. Schauer (2007) Positive matrix factorization (PMF) analysis of molecualr marker measurements to quantify the sources of organic aerosols. *Environ. Sci. Technol.,* 41**,** 5763-5769.

Jiang, H. & F. Chen (2002) On the determination of the aerodynamic coefficients of highway tunnels. *Journal of Wind Engineering and Industrial Aerodynamics,* 90**,** 869-896.

Jin, T. & L. Fu (2005) Application of GIS to modified models of vehicle emission dispersion. *Atmospheric Environment,* 39**,** 6326-6333.

Jones, R., T. Lapp & D. Wallce (1993) Locating and estimating air emissions from sources of cadmium and cadmium compounds. *U.S. Environmental Protection Agency,* Office of Air and Radiation Office of Air Quality Planning and Standards**,** EPA-453/R-93-040.

Kang, J. H. & K. S. Kim (2003) Enhanced oligomerization of the alpha-synuclein mutant by the Cu,Zn-superoxide dismutase and hydrogen peroxide system. *Mol. Cells.,* 15**,** 87-93.

Karr, C. J., C. B. Rudra, K. A. Miller, T. R. Gould, T. Larson, S. Sathyanarayana & J. Q. Koenig (2009) Infant exposure to fine particulate matter and traffic and risk of hospitalization for RSV bronchiolitis in a region with lower ambient air pollution. *Environmental Research,* 109**,** 321-327.

Kaur, S. & M. J. Nieuwenhuijsen (2009) Determinants of personal exposure to PM2.5, ultrafine particle counts, and CO in a transport microenvironment. *Environ. Sci. Technol.,* 43**,** 4737-4743.

Kaur, S., M. J. Nieuwenhuijsen & R. N. Colvile (2007) Fine particulate matter and carbon monoxide exposure concentrations in urban street transport microenvironments. *Atmospheric Environment,* 41**,** 4781-4810.

Khalili, N. R., P. A. Scheff & T. M. Holsen (1995) PAH source fingerprints for coke ovens, diesel and gasoline engines, highway tunnels, and wood combustion emissions. *Atmos. Environ.,* 29**,** 533-542.

Kim, E. & P. K. Hopke (2004) Comparison between Conditional Probability Function and Nonparametric Regression for Fine Particle Source Directions. *Atmospheric Environment,* 38**,** 4667-4673.

Kim, E., P. K. Hopke, T. V. Larson & D. S. Covert (2004) Analysis of ambient particle size distributions using UNMIX and positive matrix factorization. *Environ. Sci. Technol.,* 38**,** 202-209.

Kim, M. G., K. Yagawa, H. Inoue, Y. K. Lee & T. Shirai (1990) Measurement of tire tread in urban air by pyrolysis-gas chromatography with flame photometric detection. *Atmos. Environ.,* 24A**,** 1417-1422.

Kleinman, M. T., B. S. Pasternack, M. Eisenbud & T. J. Kneip (1980) Identifying and estimating the relative importance of sources of airborne particulates. *Environ. Sci. Technol.,* 14**,** 62-65.

Knibbs, L. D., T. Cole-Hunter & L. Morawska (2011) A review of commuter exposure to ultrafine particles and its health effects. *Atmospheric Environment,* 45**,** 2611-2622.

Knibbs, L. D. & R. J. de Dear (2010) Exposure to ultrafine particles and PM2.5 in four Sydney transport modes. *Atmospheric Environment,* 44**,** 3224-3227.

Koo, B., G. M. Wilson, R. E. Morris, G. Yarwood & A. M. Dunker (2009) Comparision of PM source apportionment and sensitivity analysis in CAMx. *Presentation at the 8th Annual CMAS Conference,* Chapel Hill, NC, October 19-21.

Kotianova, P., H. Puxbaum, H. Bauer, A. Caseiro, I. Marr & G. Cik (2008) Temporal patterns of n-alkanes at traffic exposed and suburban sites in Vienna. *Atmospheric Environment,* 42**,** 2993-3005.

Krupa, S., F. Booker, V. Bowersox, C. Lehmann, D. Grantz, K. Brown, W. Bouhamra, D. Lamoureux, J. Evans, P. Koutrakis, J. Winebrake, J. Corbett, A. Falzarano, J. Hawker, K. Korfmacher, S. Ketha, S. Zilora, O. Bergersen, K. Haarstad, S. Erdal, L. Berman, D. Hryhorczuk, S. Abolhasani, H. Frey, K. Kim, W. Rasdorf, P. Lewis, S.-H. Pang, A. Chambers, M. Strosher, T. Wootton, J. Moncrieff, P. McCready, L. Wang, J. Hao, K. He, S. Wang, J. Li, Q. Zhang, D. Streets, J. Fu, C. Jang, H. Takekawa, S. Chatani, S. Konopa, J. Mulholland, M. Realff, P. Lemieux, J. Lim, L. Yu, Y. Kostetski, C. Lim, J. Ryu, J. Kim, C. Hogrefe, K. Civerolo, W. Hao, J.-Y. Ku, E. Zalewsky, G. Sistla & R. Hashmonay (2008) Uncertainties in the Current Knowledge of Some Atmospheric Trace Gases Associated with U.S. Agriculture: A Review. *Journal of the Air & Waste Management Association,* 58**,** 986-993.

Kumar, A., J. Luo & G. Bennett (1993) Statistical evaluation of lower flammability distance (LFD) using four hazardous release models. *Process Safety Prog.,* 12**,** 1-11.

Kumar, A., B. K. Singh, I. Ahmad, S. Shukla, D. K. Patel, G. Srivastava, V. Kumar, H. P. Pandey & C. Singh (2012) Involvement of NADPH oxidase and glutathione in zinc-induced dopaminergic neurodegeneration in rats: Similarity with paraquat neurotoxicity. *Brain Research,* 1438**,** 48-64.

Lambe, A. T., J. M. Logue, N. M. Kreisberg, S. V. Hering, D. R. Worton, A. H. Goldstein, N. M. Donahue & A. L. Robinson (2009) Apportioning black carbon to sources using highly time-resolved ambient measurements of organic molecular markers in Pittsburgh. *Atmospheric Environment,* 43**,** 3941-3950.

Landis, M. S., C. W. Lewis, R. K. Stevens, G. J. Keeler, J. T. Dvonch & R. T. Tremblay (2007) Ft. McHenry tunnel study: Source profiles and mercury emissions from diesel and gasoline powered vehicles. *Atmospheric Environment,* 41**,** 8711-8724.

Landis, M. S., G. A. Norris, R. W. Williams & J. P. Weinstein (2001) Personal exposures to PM2.5 mass and trace elements in Baltimore, MD, USA. *Atmos. Environ.,* 35**,** 6511-6424.

Lane, T. E., R. W. Pinder, M. Shrivastava, A. L. Robinson & S. N. Pandis (2007) Source contributions to primary organic aerosol: Comparison of the results of a source-resolved model and the chemical mass balance approach. *Atmospheric Environment,* 41**,** 3758-3776.

Laresgoiti, A. & G. S. Springer (1977) Sulfate and particulate emissions from an oxidation catalyst equipped engine. *Environ. Sci. Technol.,* 11**,** 285-292.

Larsen, R. K. I. & J. E. Baker (2003) Source apportionment of polycyclic aromatic hydrocarbons in the urban atmosphere: a comparison of three methods. *Environ. Sci. Technol.,* 37**,** 1873-1881.

Lee, J. H. & P. K. Hopke (2006) Apportioning sources of PM2.5 in St. Louis, MO using speciation trends network data. *Atmospheric Environment,* 40**,** 360-377.

Lee, J. H., P. K. Hopke & J. R. Turner (2006) Source identification of airborne PM2.5 at the St. Louis-Midwest supersite. *Journal of Geophysical Research,* 111**,** doi:10.1029/2005JD006329.

Lee, J. H., Y. Yoshida, B. J. Turpin, P. K. Hopke, R. L. Poirot, P. J. Lioy & J. C. Oxley (2002) Identification of Sources Contributing to Mid-Atlantic Regional Aerosol. *Journal of the Air & Waste Management Association,* 52**,** 1186-1205.

Li, Z., P. K. Hopke, L. Husain, S. Qureshi, V. A. Dutkiewicz, J. J. Schwab, F. Drewnick & K. L. Demerjian (2004) Sources of fine particle composition in New York city. *Atmospheric Environment,* 38**,** 6521-6529.

Lipfert, F. W., R. E. Wyzga, J. D. Baty & J. P. Miller (2006) Traffic density as a surrogate measure of environmental exposures in studies of air pollution health effects: Long-term mortality in a cohort of US veterans. *Atmospheric Environment,* 40**,** 154-169.

Lough, G. C., J. J. Schauer, J. S. Park, M. M. Shafer, J. T. Deminter & J. P. Weinstein (2005) Emissions of metals associated with motor vehicle roadways. *Environ. Sci. Technol.,* 39**,** 826-836.

MatWeb (2012) Material Property Data. *http://www.matlab.com/*.

McElroy, J. L. & F. Pooler (1968) The St. Louis dispersion study. Volume II-Analysis, U.S. EPA Publication AP-53.

Miller, S. L., M. J. Anderson, E. P. Daly & J. B. Milford (2002) Source apportionment of exposures to volatile orgainc compounds. I. Evaluation of receptor models using simulated exposure data. *Atmos. Environ.,* 36**,** 3629-3641.

Morawska, L., Z. Ristovski, E. R. Jayaratne, D. U. Keogh & X. Ling (2008) Ambient nano and ultrafine particles from motor vehicle emissions: Characteristics, ambient processing and implications on human exposure. *Atmospheric Environment,* 42**,** 8113-8138.

Morawska, L. & J. F. Zhang (2002) Combustion sources of particles. 1. Health relevance and source signatures. *Chemosphere,* 49**,** 1045-1058.

Mroz, E. J. (1976) The study of the elemental composition of particulate emissions from an oil-fired power plant. *Ph.D. dissertation,* University of Maryland.

Nawrot, T. S., L. Perez, N. Kunzli, E. Munters & B. Nemery (2011) Public health importance of triggers of myocardial infarction: a comparative risk assessment. *Lancet,* 377**,** 732-740.

Nicholas, F. W. & J. E. Lewis (1980) Relationships between aerodynamic roughness and land use and land cover in Baltimore, Maryland. *Geological Survey Prof. Paper,* 1099-C**,** U.S. Government Printing Office, Washington, D.C.

Nielsen, T. (1996) Traffic contribution of polycyclic aromatic hydrocarbons in the center of a large city. *Atmos. Environ.,* 30**,** 3481-3490.

Ning, Z., A. Polidori, J. Schauer & C. Sioutas (2008) Emission factors of PM species based on freeway measurements and comparison with tunnel and dynamometer studies. *Atmospheric Environment,* 42**,** 3099-3114.

O'Connor, G. T., L. Neas, B. Vaughn, M. Kattan, H. Mitchell, E. F. Crain, R. Evans, R. Gruchalla, W. Morgan, J. Stout, G. K. Adams & M. Lippmann (2008) Acute respiratory health effects of air pollution on children with asthma in US inner cities. *Journal of Allergy and Clinical Immunology,* 121**,** 1133-1139.e1.

Odum, J. R., T. Hoffmann, F. Bowman, D. Collins, R. C. Flagan & J. H. Seinfeld (1996) Gas/particle partitioning and secondary organic aerosol yields. *Environ. Sci. Technol.,* 30**,** 2580-2585.

Ogulei, D., P. K. Hopke, A. R. Ferro & P. A. Jaques (2007) Factor analysis of submicron particle size distributions near a major United States_Canada trade bridge. *J. Air & Waste Manage. Assoc.,* 57**,** 190-203.

Ogulei, D., P. K. Hopke, L. Zhou, P. Paatero, S. S. Park & J. M. Ondov (2005) Receptor modeling for multiple time resolved species: The Baltimore supersite. *Atmospheric Environment,* 39**,** 3751-3762.

Ogulei, D., P. K. Hopke, L. Zhou, J. Patrick Pancras, N. Nair & J. M. Ondov (2006) Source apportionment of Baltimore aerosol from combined size distribution and chemical composition data. *Atmospheric Environment,* 40**,** 396-410.

Oke, T. B. (1982) The energetic basis of the urban heat island. *Quart. J. Roy. Meteor. Soc.,* 108**,** 1-24.

Oke, T. R. 1987. *Boundary layer climates*. London ; New York: Methuen.

Oliveira, C., C. Pio, A. Caseiro, P. Santos, T. Nunes, H. Mao, L. Luahana & R. Sokhi (2010) Road traffic impact on urban atmospheric aerosol loading at Oporto, Portugal. *Atmospheric Environment,* 44**,** 3147-3158.

Ondov, J., W. H. Zoller & G. E. Gordon (1982a) Trace element emissions on aerosols from motor vehicles. *Environ. Sci. Technol.,* 16**,** 318-328.

Ondov, J. M., T. J. Buckley, P. K. Hopke, D. Ogulei, M. B. Parlange, W. F. Rogge, K. S. Squibb, M. V. Johnston & A. S. Wexler (2006) Baltimore Supersite: Highly time- and size-resolved concentrations of urban PM2.5 and its constituents for resolution of sources and immune responses. *Atmospheric Environment,* 40**,** 224-237.

Ondov, J. M., C. E. Choquette, W. H. Zoller, G. E. Gordon, A. H. Biermann & R. E. Heft (1989) Atmospheric behavior of trace elements on particles emitted from a coal-fired power plant. *Atmos. Environ.,* 23**,** 2193-2204.

Ondov, J. M., J. P. Pancras, S. Gazula, M. Yu, J. Turner, A. Robinson, S. Pandis, N. D. Poor & R. K. Stevens (2003) Highly time-resolved measurements of elemental composition at the Baltimore, St. Louis, Pittsburgh, and Tampa

Supersites using the UM high-frequency aerosol slurry sampler: Unprecedented resolution of the sources of primary atmospheric aerosol. *2003 PM AAAR Meeting, Am. Assoc. for Aerosol Res.,* Pittsburgh, PA, 31 March to 4 April.

Ondov, J. M., R. C. Ragaini & A. H. Biermann (1979) Elemental emissions from a coal-fired power plant: Comparison of a Venturi wet scrubber system with a cold-side electrostatic precipitator. *Environ. Sci. Technol.,* 13**,** 598-607.

Ondov, J. M., W. H. Zoller & G. E. Gordon (1982b) Trace element emissions in aerosols from motor vehicles. *Environ. Sci. Technol.,* 16**,** 318-328.

Oros, D. R. & B. R. T. Simoneit (1999) Identification of Molecular Tracers in Organic Aerosols from Temperate Climate Vegetation Subjected to Biomass Burning. *Aerosol Science and Technology,* 31**,** 433-445.

Orsini, D. A., Y. Ma, A. Sullivan, B. Sierau, K. Baumann & R. J. Weber (2003) Refinements to the particle-into-liquid sampler (PILS) for ground and airborne measurements of water soluble aerosol composition. *Atmospheric Environment,* 37**,** 1243-1259.

Osan, J., S. Torok, J. Fekete & A. Rindby (2000) Case study of the emissions from a heavy-oil-fueled Hungarian power plant. *Energy Fuels,* 14**,** 986-993.

Paatero, P. (1997) Least square formulation of robust non-negative factor analysis. *Chemom. Intel. Lab. Syst.,* 37**,** 23-35.

--- (1999) The multilinear engine: A table-driven, least squares program for solving multilinear problems, including the n-way parallel factor analysis model. *J. Comput. Graph. Stat.,* 8**,** 854-888.

Paatero, P., P. Hopke, B. Begum & S. Biswas (2005) A graphical diagnostic method for assessing the rotation in factor analytical models of atmospheric pollution. *Atmospheric Environment,* 39**,** 193-201.

Paatero, P., P. K. Hopke, X. Song & Z. Ramadan (2002) Understanding and controlling rotations in factor analytic models. *Chemom. Intel. Lab. Syst.,* 60**,** 253-264.

Paatero, P. & U. Tapper (1994) Positive matrix factorization: a non-negative factor model with optimal utilization of error estimates of data values. *Environmentrics,* 5**,** 111-126.

Pancras, J. P., J. M. Ondov & R. Zeisler (2005) Multi-element electrothermal AAS determination of 11 marker elements in fine ambient aerosol slurry samples collected with SEAS-II. *Anal. Chim. Acta.,* 538**,** 303-312.

Pancras, J. P., R. Vedantham, M. S. Landis, G. A. Norris & J. M. Ondov (2011) Application of EPA Unmix and Nonparametric Wind Regression on High Time Resolution Trace Elements and Speciated Mercury in Tampa, Florida Aerosol. *Environmental Science & Technology,* 45**,** 3511-3518.

Pankow, J. F. (1994) An absorption model of gas/particle partitioning of organic compounds in the atmosphere. *Atmospheric Environment,* 28**,** 185-188.

Panofsky, H. A., A. K. Blackadar & G. E. McVehil (1960) The diabatic wind profile, Q. *J. R. Meteorol. Soc.,* 86**,** 390-398.

Panofsky, H. A. & J. A. Dutton (1984) Atmospheric turbulence. *J. Wiley and Sons, New York***,** 397 pp.

Park, J. D., L. J. Akinbami & T. J. Woodruff (2009) Air Pollution and Childhood Respiratory Allergies in the United States. *Environ. Health Perspect.,* 117**,** 140-147.

Park, S. S., D. Harrison, P. J. Pancras & J. M. Ondov (2005a) Highly time-resolved organic and elemental carbon measurements at the Baltimore Supersite in 2002. *Journal of Geophysical Research,* 110**,** D07S06.

Park, S. S., J. Kleissl, D. Harrison, V. Kumar, N. P. Nair, M. Adam, J. Ondov & M. Parlange (2006a) Characteristics of $PM_{2.5}$ episodes revealed by semi-continuous measurements at the Baltimore Supersite at Ponca Street. *Aerosol Science and Technology,* 40**,** 845-860.

Park, S. S., P. J. Pancras & J. M. Ondov (2005b) A new pseudodeterministic multivariate receptor model for individual source apportionment using highly time-resolved ambient concentration measurements. *Journal of Geophysical Research,* 110.

Park, S. S., P. J. Pancras, J. M. Ondov & A. Robinson (2006b) Application of the pseudo-deterministic receptor model to resolve power plant influences on air quality in Pittsburgh. *Aerosol Science and Technology,* 40**,** 883-897.

Parrish, D. D. (2006) Critical evaluation of US on-road vehicle emission inventories. *Atmospheric Environment,* 40**,** 2288-2300.

Pasquill, F. (1979) Atmospheric Dispersion Modeling. *Journal of the Air Pollution Control Association,* 29**,** 117-119.

Pekney, N. J., C. I. Davidson, A. Robinson, L. Zhou, P. Hopke, D. Eatough & W. F. Rogge (2006) Major Source Categories for PM2.5in Pittsburgh using PMF and UNMIX. *Aerosol Science and Technology,* 40**,** 910-924.

Peters, A., v. K. S., M. Heier, I. Trentinaglia, A. Hormann, H. E. Wichmann & H. Lowel (2004) Exposure to traffic and the onset of myocardial infarction. *The New England Journal of Medicine,* 351**,** 1721-1730.

Peters, T. M., H. Chein, D. A. Lundgren & P. B. Keady (1993) Comparison and Combination of Aerosol Size Distributions Measured with a Low Pressure Impactor, Differential Mobility Particle Sizer, Electrical Aerosol Analyzer, and Aerodynamic Particle Sizer. *Aerosol Science and Technology,* 19**,** 396-405.

Pollack, A. K., C. Lindhjem, T. E. Stoeckenius, C. Tran, G. Mansell, M. Jimenez, G. Wilson & S. Coulter-Burke (2004) Evalutation of the U.S. EPA MOBILE6 highway vehicle emission factor model. *CRC Project E-64*.

Pye, H. O. T. & J. H. Seinfeld (2010) A global perspective on aerosol from low-volatility organic compounds. *Atmospheric Chemistry and Physics,* 10**,** 4377-4401.

Ragaini, R. C. & J. M. Ondov (1977) Trace-Element Emissions from Western United-States Coal-Fired Power-Plants. *Journal of Radioanalytical Chemistry,* 37**,** 679-691.

Rogge, W. F., L. M. Hildemann, M. A. Mazurek, G. R. Cass, G. R. Cass & B. R. T. Simoneit (1996) Mathematical modeling of atmospheric fine particle-associated primary organic compound concentrations. *Journal of Geophysical Research,* 101**,** 19379-19394.

Rogge, W. F., L. M. Hildemann, M. A. Mazurek, G. R. Cass & B. R. T. Simoneit (1991) Sources of fine organic aerosol. 1. Charbroilers and meat cooking operations. *Environ. Sci. Technol.,* 25**,** 1112-1125.

--- (1993a) Quantification of organic aerosols at a molecular level: Identification, abundance and seasonal variation. *Atmos. Environ.,* 27A**,** 1309-1330.

--- (1993b) Sources of fine organic aerosol: 2. Non-catalyst and catalyst-equipped automobiles and heavy-duty diesel trucks. *Environ. Sci. Technol.,* 27**,** 636-651.

--- (1993c) Sources of fine organic aerosol: 3. Road dust, tire debris, and organometallic brake lining dust - roads as sources and sinks. *Environ. Sci. Technol.,* 27**,** 1892-1904.

--- (1993d) Sources of fine organic aerosol: 4. Particulate abrasion products from leaf surfaces of urban plants. *Environ. Sci. Technol.,* 27**,** 2700-2711.

--- (1994) Sources of fine organic aerosol. 6. Cigaret smoke in the urban atmosphere. *Environ. Sci. Technol.,* 28**,** 1375-1388.

--- (1998) Sources of fine organic aerosol. 9. Pine, oak, and synthetic log combustion in residential fireplaces. *Environ. Sci. Technol.,* 32**,** 13-22.

Rogge, W. F., J. M. Ondov, A. Bernardo-Bricker & O. Sevimoglu (2011) Baltimore PM2.5 Supersite: highly time-resolved organic compounds—sampling duration and phase distribution—implications for health effects studies. *Analytical and Bioanalytical Chemistry,* 401**,** 3069-3082.

Rubin, J. I., A. J. Kean, R. A. Harley, D. B. Millet & A. H. Goldstein (2006) Temperature dependence of volatile organic compound evaporative emissions from motor vehicles. *Journal of Geophysical Research,* 111.

Russell, A. G. (2008) EPA Supersites Program-Related Emissions-Based Particulate Matter Modeling: Initial Applications and Advances. *Journal of the Air & Waste Management Association,* 58**,** 289-302.

Rönkkö, T., A. Virtanen, K. Vaaraslahti, J. Keskinen, L. Pirjola & M. Lappi (2006) Effect of dilution conditions and driving parameters on nucleation mode particles in diesel exhaust: Laboratory and on-road study. *Atmospheric Environment,* 40**,** 2893-2901.

Sapkota, A., J. M. Symons, J. Kleissl, L. Wang, M. B. Parlange, J. Ondov, P. N. Breysse, G. B. Diette, P. A. Eggleston & T. J. Buckley (2005) Impact of the 2002 canadian forest fires on particulate matter air quality in Baltimore city. *Environ. Sci. Technol.,* 39**,** 24-32.

Sayes, C. M., K. L. Reed & D. B. Warheit (2007) Assessing Toxicity of Fine and Nanoparticles: Comparing In Vitro Measurements to In Vivo Pulmonary Toxicity Profiles. *Toxicological Sciences,* 97**,** 163-180.

Schauer, J. J. & G. R. Cass (2000) Source apportionment of wintertime gas-phase and particle-phase air pollutants using organic compounds as tracers. *Environ. Sci. Technol.,* 34**,** 1821-1832.

Schauer, J. J., W. F. Rogge, L. M. Hildemann, M. A. Mazurek, G. R. Cass & B. R. T. Simoneit (1996) Source apportionment of airborne particulate matter using organic compounds as tracers. *Atmos. Environ.,* 30**,** 3837-3855.

Schnelle-Kreis, J., U. Küpper, M. Sklorz, J. Cyrys, J. J. Briedé, A. Peters & R. Zimmermann (2009) Daily measurement of organic compounds in ambient

particulate matter in Augsburg, Germany: new aspects on aerosol sources and aerosol related health effects. *Biomarkers,* 14**,** 39-44.

Schwartz, J. (2005) Traffic related pollution and heart rate variability in a panel of elderly subjects. *Thorax,* 60**,** 455-461.

Seinfeld, J. H. & S. N. Pandis. 2006. *Atmospheric chemistry and physics : from air pollution to climate change*. Hoboken, N.J.: J. Wiley.

Sheffield, A. E. & G. E. Gordon (1986) Variability of particle composition from ubiquitous sources: Results from a new source-composition library. *Receptor Methods for Source Apportionment: Real World Issues and Applications,* Air Pollution Control Association, Pittsburgh, PA.

Silva, P. J., D. Y. Liu, C. A. Noble & K. A. Prather (1999) Size and chemical characterization of individual particles resulting from biomass burning of local southern california species. *Environ. Sci. Technol.,* 33**,** 3068-3076.

Simcik, M. F., S. J. Eisenreich & P. J. Lioy (1999) Source apportionment and source/sink relationships of PAHs in the coastal atmosphere of Chicago and Lake Michigan. *Atmos. Environ.,* 33**,** 5071-5079.

Simoneit, B. R. T. (2002) Biomass burning - a review of organic tracers for smoke from incomplete combustion. *Applied Geochemistry,* 17**,** 129-162.

Simoneit, B. R. T., W. F. Rogge, M. A. Mazurek, L. J. Standley, L. M. Hildemann & G. R. Cass (1993) Lignin pyrolysis products, lignans, and resin acids as specific tracers of plant classes in emissions from biomass combustion. *Environ. Sci. Technol.,* 27**,** 2533-2541.

Simoneit, B. R. T., J. J. Schauer, C. G. Nolte, D. R. Oros, V. O. Elias, M. P. Fraser, W. F. Rogge & G. R. Cass (1999) Levoglucosan, a tracer for cellulose in biomass burning and atmospheric particles. *Atmos. Environ.,* 33**,** 173-182.

Simonich, S. L. & R. A. Hites (1994) Importance of vegetation in removing polycyclic aromatic hydrocarbons from the atmosphere. *Nature,* 370**,** 49-51.

Singh, S. & V. Prakash (2007) Toxic Environmental Releases from Medical Waste Incineration: A Review. *Environmental Monitoring and Assessment,* 132**,** 67-81.

Song, S., K. Lee, Y.-M. Lee, J.-H. Lee, S. Il Lee, S.-D. Yu & D. Paek (2011) Acute health effects of urban fine and ultrafine particles on children with atopic dermatitis. *Environmental Research,* 111**,** 394-399.

Song, Y., S. Xie, Y. Zhang, L. Zeng, L. G. Salmon & M. Zheng (2006) Source apportionment of PM2.5 in Beijing using principal component analysis/absolute principal component scores and UNMIX. *Science of the Total Environment,* 372**,** 278-286.

Strak, M., H. Boogaard, K. Meliefste, M. Oldenwening, M. Zuurbier, B. Brunekreef & G. Hoek (2009) Respiratory health effects of ultrafine and fine particle exposure in cyclists. *Occupational and Environmental Medicine,* 67**,** 118-124.

Stull, R. B. (1989). *An introduction to boundary layer meteorology,* Kluwer, Dordrecht.

Suarez, A. E. & J. M. Ondov (2002) Ambient aerosol concentrations of elements resolved by size and by source: Contributions of some cytokine-active metals from coal- and oil-fired power plants. *Energy & Fuels,* 16**,** 562-568.

Thai, A., I. McKendry & M. Brauer (2008) Particulate matter exposure along designated bicycle routes in Vancouver, British Columbia. *Science of the Total Environment,* 405**,** 26-35.

Thurston, G. D. & J. D. Spengler (1985) A quantitative assessment of source contributions to inhalable particulate matter pollution in metropolitan Boston. *Atmos. Environ.,* 19**,** 9-25.

Tuncel, S. G., G. E. Gordon, I. Olmez, J. R. Parrington, R. W. Shaw & R. J. Paur (1987) Trace Element Concentrations on Fine Particles in the Ohio River Valley. 349**,** 66-81.

Tuncel, S. G., I. Olmez, J. R. Parrington, G. E. Gordon & R. K. Stevens (1985) Composition of Fine Particle Regional Sulfate Component in Shenandoah Valley. *Environmental Science & Technology,* 19**,** 529-537.

Turner, J. (2007) St. Louis - midwest fine particulate matter supersite final report.

U.S.EPA (1995) User's guide for the Industrial Source Complex (ISC3) dispersion models, vol. II, Description of model algorithms. *EPA-454/B-95-003b,* Research Triangle Park, N.C.

--- (2004a) AERMOD: Description of model formulation. *EPA-454/R-03-004*.

--- (2004b) Air quality criteria for particulate matter. *Research Trigangle Park, NC: National Center for Environmental Assessement-RTP Office,* EPA/600/P-99/002bF.

--- (2004c) EPA-CMB 8.2: user's manual. *EPA/452/R-04-011,* Office of Air Quality Planning and Standards Emissions, Monitoring and Analysis Division, Air Quality Modeling Group.

--- (2005) Federal Register, 40 CFR Part 51. 25 April 2005.

--- (2006) SPECIATE 4.0: Speciation Database Development Documentation Final Report. Office of Research and Development, Research Triangle Park, N. C.

--- (2007) Unmix 6.0: fundamentals and user guide. *EPA/600/R-07/089,* Office of Research and Development: Washington, DC.

--- (2008) EPA Positive Matrix Factorization (PMF) 3.0: fundamentals and user guide. *EPA/600/R-08/108,* Office of Research and Development: Washington, DC.

Valavanidis, A., K. Fiotakis & T. Vlachogianni (2008) Airborne Particulate Matter and Human Health: Toxicological Assessment and Importance of Size and Composition of Particles for Oxidative Damage and Carcinogenic Mechanisms. *Journal of Environmental Science and Health, Part C,* 26**,** 339-362.

--- (2010) The Role of Stable Free Radicals, Metals and PAHs of Airborne Particulate Matter in Mechanisms of Oxidative Stress and Carcinogenicity. 411-426.

Venkatram, A. & J. C. Wyngaard (1988) Dispersion in the stable boundary layer. *Lectures on Air Pollution Modeling,* Amer. Meteor. Soc.**,** 229-265.

Viana, M., M. Pandolfi, M. C. Minguillón, X. Querol, A. Alastuey, E. Monfort & I. Celades (2008) Inter-comparison of receptor models for PM source apportionment: Case study in an industrial area. *Atmospheric Environment,* 42**,** 3820-3832.

Wang, G., P. K. Hopke & J. R. Turner (2011) Using highly time resolved fine particulate compositions to find particle sources in St. Louis, MO. *Atmospheric Pollution Research,* 2**,** 219-230.

Watson, J. G. (1979) Chemical element balance receptor model methodology for assessing the sources of fine and total suspended particulate in Portland, Oregon. *Doctoral Dissertation for the Oregon Graduate Center*.

--- (1984) Overview of Receptor Model Principles. *Journal of the Air Pollution Control Association,* 34**,** 619-623.

Watson, J. G., L. W. Antony Chen, J. C. Chow, P. Doraiswamy & D. H. Lowenthal (2008) Source Apportionment: Findings from the U.S. Supersites Program. *Journal of the Air & Waste Management Association,* 58**,** 265-288.

Watson, J. G. & J. C. Chow (2001) Source characterization of major emission sources in the Imperial and Mexicali Valleys along the US/Mexico border. *Science of the Total Environment,* 276**,** 33-47.

Watson, J. G., J. C. Chow & J. E. Houck (2001) PM2.5 chemical source profiles for vehicle exhaust, vegetative burning, geological material, and coal burning in Northwestern Colorado during 1995. *Chemosphere,* 43**,** 1141-1151.

Watson, J. G., N. F. Robinson, J. C. Chow, R. C. Henry, B. M. Kim, T. G. Pace, E. L. Meyer & Q. Nguyen (1990) The USEPA/DRI chemical mass balance receptor model, CMB 7.0. *Environmental Software,* 5**,** 38-49.

Watson, J. G., T. Zhu, J. C. Chow, J. Engelbrecht, E. M. Fujita & W. E. Wilson (2002) Receptor modeling application framework for particle source apportionment. *Chemosphere,* 49**,** 1093-1136.

Weichenthal, S., A. Dufresne, C. Infante-Rivard & L. Joseph (2008) Determinants of ultrafine particle exposures in transportation environments: findings of an 8-month survey conducted in Montréal, Canada. *Journal of Exposure Science and Environmental Epidemiology,* 18**,** 551-563.

Wilcke, W., M. Krauss, J. Lilienfein & W. Amelung (2004) Polycyclic aromatic hydrocarbon storage in a typical Cerrado of the Brazilian Savanna. *Journal of Environmental Quality,* 33**,** 946-955.

Willis, R. D. (2000) Workshop on UNMIX and PMF as applied to PM2.5. *U. S. Environmental Protection Agency,* 14-16 February, Research Triangle Park, NC.

Wåhlin, P. (2003) COPREM—A multivariate receptor model with a physical approach. *Atmospheric Environment,* 37**,** 4861-4867.

Yamartino, R. J. (1982) Formulation and application of a hybrid receptor model. *Specialty Conference on Receptor Models Applied to Contemporary Pollution Problems,* Northeast Atl. Int. Sect. of the Air Pollut. Control Assoc., Danvers, Mass., 17–20 Oct.

Yue, W., M. Stölzel, J. Cyrys, M. Pitz, J. Heinrich, W. G. Kreyling, H. E. Wichmann, A. Peters, S. Wang & P. K. Hopke (2008) Source apportionment of ambient fine particle size distribution using positive matrix factorization in Erfurt, Germany. *Science of the Total Environment,* 398**,** 133-144.

Yunker, M. B., R. W. Macdonald, R. Vingarzan, R. H. Mitchell, D. Goyette & S. Sylvestre (2002) PAHs in the Fraser River basin: a critical appraisal of PAH

ratios as indicators of PAH source and composition. *Organic Geochemistry,* 33**,** 489-515.

Zhang, Y., J. J. Schauer, Y. Zhang, L. Zeng, Y. Wei, Y. Liu & M. and Shao (2008) Characteristics of particulate carbon emissions from real-world Chinese coal combustion. *Environ. Sci. Technol.,* 42**,** 5069-5073.